Design of Multifunctional Magnetic Nanomaterials for Biomedical Applications

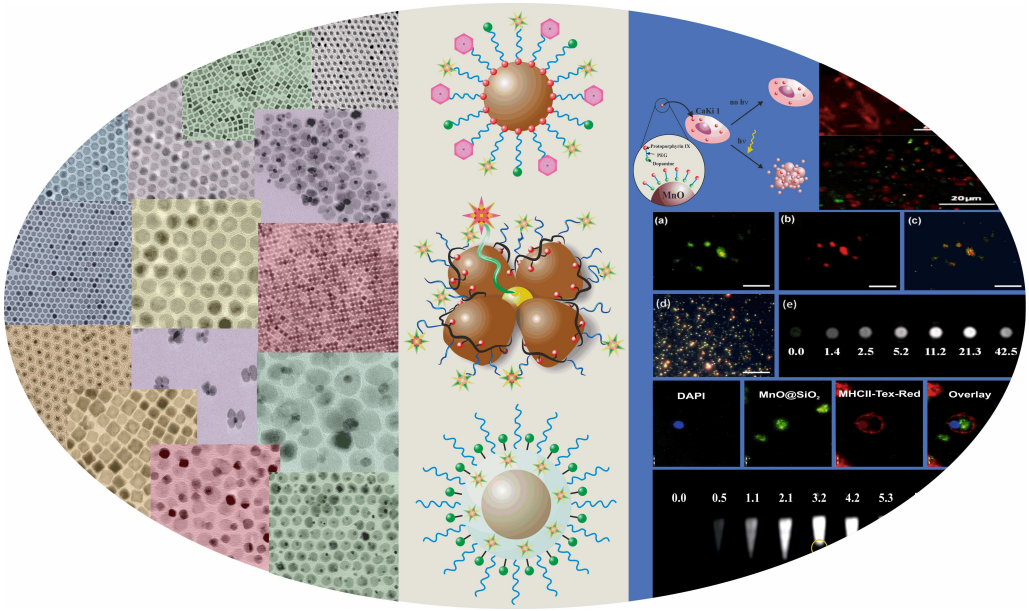

Dissertation zur Erlangung des Grades

"Doktor der Naturwissenschaften"

dem Fachbereich Chemie, Pharmazie und Geowissenschaften

der Johannes-Gutenberg-Universität Mainz

vorgelegt von

Dipl.-Chem. Thomas D. Schladt

geboren in Boppard

Mainz, 2010

Dekan: [redacted]

Erster Berichterstatter: [redacted]

Zweiter Berichterstatter:

Datum der mündlichen Prüfung:

Erklärung

Die vorliegende Arbeit wurde in der Zeit von November 2007 bis August 2010 unter Anleitung von [redacted] an der Johannes-Gutenberg-Universität Mainz, Institut für anorganische Chemie und analytische Chemie angefertigt.

Ich erkläre hiermit, dass ich die vorliegende Arbeit selbständig und ohne fremde Hilfe verfasst habe. Alle verwendeten Quellen und Hilfsmittel sind vollständig angegeben.

Mainz, im September 2010

Abstract

Abstract in English: The present work is a contribution to the rapidly evolving research fields of nano-biotechnology and nanomedicine. It focuses on the specific design of magnetic nanomaterials for different biomedical areas, ranging from application as contrast agents for magnetic resonance imaging (MRI) to "theragnostic" agents for simultaneous optical/MR detection and treatment via photodynamic therapy (PDT).

A variety of magnetic nanoparticles (NPs) with distinct magnetic properties were synthesized and thoroughly characterized. Additionally, a whole series of surface modification strategies were developed to improve both, colloidal and chemical stability, and thus cope with the respective challenges presented by *in vitro* and *in vivo* application. These strategies involve, not only, the use of bi-functional and multifunctional polymeric ligands equipped with catechol anchorgroups for efficient surface attachment, but also the condensation of suitable silane precursors to create a robust, inert and hydrophilic silica shell around the magnetic NPs.

More precisely, the formation mechanism and the magnetic properties of monodisperse MnO NPs were extensively investigated. Due tor their unique magnetic behavior, these NPs serve as (positive) contrast agents to shorten the longitudinal relaxation time T_1, which leads to brightening in the corresponding MR image. In fact, this contrast enhancing potential was confirmed in several studies using different surface ligands. Au@MnO "nanoflowers", on the other hand, are representatives

of another class of nanomaterials that has attracted considerable interest during the last years and is often termed "nano-*hetero*-materials". They combine the individual physical and chemical properties of each component within one nanoparticulate probe and, hence, increase the diversity of possible applications. Both, magnetic features of MnO and optical characteristics of Au, offer the possibility to use these "nanoflowers" for combined MR and optical imaging. In addition to that, two chemically unique surfaces permit the selective attachment of catechol ligands (on MnO) and thiol ligands (on Au) at the same time. Furthermore, the therapeutic potential of magnetic NPs was demonstrated in the case of MnO NPs functionalized with the photosensitizer protoporphyrin IX (PP). PP initiates the production of highly cytotoxic reactive oxygen upon illumination with visible light. We show that kidney cancer cells incubated with PP-functionalized MnO NPs die after irradiation with laser light, whereas they remain unharmed, when no laser light was applied. In a comparable study we investigated the characteristics of silica coated MnO NPs. For this purpose a novel silica coating procedure was developed, that allows further attachment of various ligands and the incorporation of fluorescent dyes via common silane sol-gel chemistry. The particles show excellent stability in a whole range of aqueous solutions, including physiological saline, buffers and human blood serum, and are less prone to manganese ion leaching compared to simply PEGylated MnO NPs. Besides, the presence of a thin silica shell on the MnO NP surface does not change the magnetic properties significantly and, hence, still enables their use as T_1 contrast agents. Finally, we synthesized FePt@MnO nano-*hetero*-particles that combine the individual magnetic properties of a ferromagnetic (FePt) and an antiferromagnetic (MnO) material. We were able to tune the corresponding particle sizes and, therefore, the resulting magnetic behavior of the system by adjustment of the experimental parameters during the synthesis. The magnetic interaction between both materials can be ascribed to spin communication at the interface between both types of NPs.

Kurzfassung in Deutsch: Diese Arbeit ist ein Beitrag zu den schnell wachsenden Forschungsgebieten der Nano-Biotechnologie und Nanomedizin. Sie behandelt die spezifische Gestaltung magnetischer Nanomaterialien für verschiedene biomedizinische Anwendungsgebiete, wie beispielsweise Kontrastmittel für die magnetische Resonanztomographie (MRT) oder "theragnostische" Agenzien für si-

multane optische/MR Detektion und Behandlung mittels photodynamischer Therapie (PDT).

Eine Vielzahl magnetischer Nanopartikel (NP) mit unterschiedlichsten magnetischen Eigenschaften wurden im Rahmen dieser Arbeit synthetisiert und erschöpfend charakterisiert. Darüber hinaus wurde eine ganze Reihe von Oberflächenmodifizierungsstrategien enwickelt, um sowohl die kolloidale als auch die chemische Stabilität der Partikel zu verbessern, und dadurch den hohen Anforderungen der *in vitro* und *in vivo* Applikation gerecht zu werden. Diese Strategien beinhalteten nicht nur die Verwendung bi-funktionaller und multifunktioneller Polymerliganden, sondern auch die Kondensation geeigneter Silanverbindungen, um eine robuste, chemisch inerte und hydrophile Siliziumdioxid- (SiO_2) Schale um die magnetsichen NP auszubilden.

Genauer gesagt, der Bildungsmechanismus und die magnetischen Eigenschaften monodisperser MnO NPs wurden ausgiebig untersucht. Aufgrund ihres einzigartigen magnetischen Verhaltens eignen sich diese NPs besonders als (positive) Kontrastmittel zur Verkürzung der longitudinalen Relaxationszeit T_1, was zu einer Aufhellung im entsprechenden MRT-Bild führt. Tatsächlich wurde dieses konrastverbessernde Potential in mehreren Studien mit unterschiedlichen Oberflächenliganden bestätigt. Au@MnO "Nanoblumen", auf der anderen Seite, sind Vertreter einer weiteren Klasse von Nanomaterialien, die in den vergangenen Jahren erhebliches Interesse in der wissenschaftlichen Welt geweckt hat und oft "Nano-*hetero*-materialien genannt wird. Solche Nano-*hetero*-partikel vereinen die individuellen physikalischen und chemischen Eigenschaften der jeweiligen Komponenten in einem nanopartikulärem System und erhöhen dadurch die Vielseitigkeit der möglichen Anwendungen. Sowohl die magnetischen Merkmale von MnO, als auch die optischen Eigenschaften von Au bieten die Möglichkeit, diese "Nanoblumen" für die kombinierte MRT und optische Bildgebung zu verwenden. Darüber hinaus erlaubt das Vorliegen zweier chemisch unterschiedlicher Oberflächen die gleichzeitige selektive Anbindung von Katecholliganden (auf MnO) und Thiolliganden (auf Au). Außerdem wurde das therapeutische Potential von magnetischen NPs anhand von MnO NPs demonstriert, die mit dem Photosensibilisator Protoporhyrin IX (PP) funktionalisiert waren. Bei Bestrahlung mit sichtbaren Licht initiert PP die Produktion von zytotoxischen reaktivem Sauerstoff. Wir zeigen, dass Nierenkreb-

szellen, die mit PP-funktionaliserten MnO NPs inkubiert wurden nach Bestrahlung mit Laserlicht verenden, während sie ohne Bestrahlung unverändert bleiben. In einem ähnlichen Experiment untersuchten wir die Eigenschaften von SiO_2 beschichteten MnO NPs. Dafür wurde eigens eine neuartige SiO_2-Beschichtungsmethode entwickelt, die einer nachfolgende weitere Anbindung verschiedenster Liganden und die Einlagerung von Fluoreszenzfarbstoffen durch herkömmliche Silan-Sol-Gel Chemie erlaubt. Die Partikel zeigten eine ausgezeichnete Stabilität in einer ganzen Reihe wässriger Lösungen, darunter auch physiologische Kochsalzlösung, Pufferlösungen und humanes Blutserum, und waren weniger anfällig gegenüber Mn-Ionenauswaschung als einfache PEGylierte MnO NPs. Des weiteren konnte bewiesen werden, dass die dünne SiO_2 Schicht nur einen geringen Einfluss auf das magnetische Verhalten der NPs hatte, so dass sie weiterhin als T_1-Kontrastmittel verwendet werden können. Schließlich konnten zusätzlich FePt@MnO NPs hergestellt werden, welche die individuellen magnetischen Merkmale eines ferromagnetischen (FePt) und eines antiferromagnetischen (MnO) Materials vereinen. Wir zeigen, dass wir die jeweiligen Partikelgrößen, und damit das resultierende magnetische Verhalten, durch Veränderung der experimentellen Parameter variieren können. Die magnetische Wechselwirkung zwischen beiden Materialien kann dabei auf Spinkommunikation an der Grenzfläche zwischen beiden NP-Sorten zurückgeführt werden.

Acknowledgments

[redacted]

[redacted]

Contents

List of Figures **xv**

1 Introduction **1**

1.1 References 5

2 Nanomagnetism **9**

2.1 Single-Domain Limit 9

2.2 Superparamagnetic Limit 11

2.3 Surface Effects 12

2.4 Nanomagnetism in Magnetic Resonance Imaging (MRI) 12

2.5 References 18

3 Synthesis of Magnetic NPs **21**

3.1 General Considerations 23

3.2 Co-Precipitation 26

3.3 Solvothermal/Hydrothermal Synthesis 28

3.4 Preparation within Micelles 30

3.5 Thermal Decomposition and/or Reduction 34

3.6 References 38

4 Colloidal Nano-*hetero*-Structures **45**
4.1 Synthesis of Colloidal Nano-*hetero*-Particles 46
4.1.1 Dimer Nanoparticles 48
4.1.2 Core-Shell Nanoparticles 49
4.1.3 *Multi*-mer Nanoparticles 52
4.2 Properties of Nano-*hetero*-Particles 53
4.2.1 Magnetic Properties 54
4.2.2 Optical Properties 55
4.3 Potential Application 56
4.4 References 58

5 Surface Modification of Magnetic NPs **61**
5.1 Amphiphilic Micelles 63
5.2 Polymeric Ligands 66
5.3 Bifunctional Ligands 69
5.4 Silica Coating 74
5.5 References 78

6 Biomedical Applications of Magnetic NPs **87**
6.1 Design Considerations 89
6.2 Passive Cell-Targeting 91
6.3 Active Cell-Targeting 93
6.4 MR Imaging Using Magnetic NPs 96
6.5 Toxicity of Magnetic Nanoparticles 101
6.6 Biodistribution and Clearance 103
6.7 References 104

7 Synthesis of Monodisperse MnO Nanoparticles: Evaluation of the Nucleation and Growth Mechanism **115**
7.1 Abstract 116
7.2 Introduction 116
7.3 Results and Discussion 117
7.4 Conclusion 132
7.5 Experimental Section 133

7.6 References 135

8 Au@MnO Nanoflowers: Hybrid Nanocomposites for Selective Dual Functionalization and Imaging 139

8.1 Abstract 140
8.2 Introduction 140
8.3 Results and Discussion 142
8.4 Conclusion 149
8.5 Experimental Section 150
8.6 References 155

9 Highly Soluble Multifunctional MnO Nanoparticles for Simultaneous Optical and MRI Imaging and Cancer Treatment using Photodynamic Therapy 161

9.1 Abstract 162
9.2 Introduction 162
9.3 Results and Discussion 164
9.4 Conclusion 174
9.5 Experimental 174
9.6 References 179

10 Multifunctional Superparamagnetic MnO@SiO_2 Core/Shell Nanoparticles and their Application for Optical and Magnetic Resonance Imaging 185

10.1 Abstract 186
10.2 Introduction 186
10.3 Results and Discussion 190
10.4 Conclusion 203
10.5 Experimental Section 204
10.6 References 208

11 Synthesis and Magnetic Properties of FePt@MnO Nano-*hetero*-Particles 215

11.1 Abstract 216

11.2 Introduction 216
11.3 Results and Discussion 218
11.4 Conclusion 226
11.5 Experimental Section 227
11.6 References 230

12 Conclusion and Outlook **235**

List of Figures

2.1 Single domain limit 10
2.2 Magnetic surface effects 13
2.3 T_1 and T_2 relaxation mechanisms 14
2.4 Origins of T_1 and T_2 contrast enhancement 16

3.1 Synthetic top-down and bottom-up approach 22
3.2 LaMer plot 23
3.3 Critical nuclei radius 25
3.4 Magnetic NPs synthesized by co-precipitation of metal salts 27
3.5 Magnetic NPs synthesized by hydro-/solvothermal reactions 28
3.6 Reverse micelles as "nanoreactors" 31
3.7 Magnetic NPs synthesized in reverse microemulsions 32
3.8 Experimental setup for the synthesis of monodisperse NPs 34
3.9 Superlattices of monodisperse FePt NPs 36
3.10 Two- and three-dimensional superlattices of monodisperse MnO NPs 37

4.1 Different morphologies of colloidal nano-*hetero*-particles 46
4.2 Epitaxial relationship between Au and MnO 47
4.3 TEM images of Au@Fe_3O_4 nano-*hetero*-dimers 48
4.4 Solvent effect during the synthesis of nano-*hetero*-particles 50

4.5 TEM images of FePt@Fe_3O_4 and FePt@MnO core-shell NPs . . . 51
4.6 Possible reaction pathways leading to nano-*hetero*-particles 52
4.7 Examples of various metal- metal oxide nano-*hetero*-particles . . . 53
4.8 Magnetic properties of nano-*hetero*-particles 54
4.9 Nano-*hetero*-dimers as Janus particles 57

5.1 Illustration of hydrophobic surfactant capped magnetic NP 62
5.2 Different surface functionalization strategies 63
5.3 Magnetic NP coated by an amphiphilic micelle 64
5.4 PEG-phospholipid for the micellar coating of NPs 65
5.5 Chemical structure of a typical multifunctional polymeric ligand . . 67
5.6 Magnetic NP coated with a multidentate polymeric ligand 68
5.7 Surface modification of magnetic NPs using bi-functional ligands . 69
5.8 Different binding coordinations of catechols on metal oxide surfaces 71
5.9 Degradation of NP surface by dopamine 72
5.10 Illustration of a multifunctional silica coated magnetic NP 73
5.11 Silica functionalization of magnetic NPs in a reverse microemulsion 74
5.12 TEM images of silica coated MnO NPs synthesized in a reverse microemulsion 75
5.13 Illustration of a fluorescent core-silica shell NP 76
5.14 Encapsulation of magnetic NPs with mesoporous silica 77

6.1 Fractions of nanomedicine patents from 1993-2003 88
6.2 Illustration of multifunctional magnetic nanoparticle 90
6.3 Illustration of passive targeting of tumor tissue due to the EPR effect 92
6.4 Illustration of active targeting of tumor cells and receptor-mediated cellular uptake 94
6.5 Specifically engineered $M$$Fe_2O_4$ NPs as MRI contrast agents 96
6.6 Fe_3O_4-decorated SiO_2 spheres as MRI imaging agents 99
6.7 MnO NPs as T1 contrast agents 100
6.8 Bimodal imaging using ^{124}I conjugated $MnFe_2O_3$ NPs 101

7.1 Size-dependent powder XRD patterns of MnO nanoparticle samples 118
7.2 TGA-curve of Mn-oleate 119

7.3 In-situ FT-IR spectra of MnO nanoparticle formation 120
7.4 TEM images of MnO NPs at different stages of the reaction 122
7.5 Evolution of MnO particle size with time 123
7.6 MnO nanoparticle size as a function of temperature and solvent . . . 124
7.7 TEM images of MnO NPs prepared in trioctylamine 125
7.8 FT-IR spectra of oleic acid, Mn-oleate and MnO NPs 126
7.9 ^{1}HNMR spectra of oleic acid,manganese oleate, and washed MnO NPs 127
7.10 High-resolution XPS scans of the Mn 2p region. 129
7.11 TGA curve of washed MnO nanocrystals 130
7.12 TEM images of MnO NPs synthesized at different heating rates . . . 131
7.13 FC-ZFC-curves of MnO NPs 132
7.14 Magnetic hysteris loops of MnO NPs 133

8.1 Functionalization scheme for Au@MnO nanoflowers 141
8.2 Au@MnO nanoflowers with different petal sizes 142
8.3 Powder XRD pattern of Au@MnO nanoflowers 143
8.4 Field-dependent and temperature dependent magnetization curves of Au@MnO nanoflowers 144
8.5 UV-Vis absorption spectra of Au@MnO nanoflowers 145
8.6 UV-Vis spectra of NBD functionalized Au@MnO nanoflowers and MTT assay 146
8.7 Surface functionalization scheme for Au@MnO nanoflowers 147
8.8 Fluorescence and MR images of Au@MnO nanoflowers 148
8.9 Scattering spectrum of Au@MnO nanflowers 149
8.10 Theoretical Scattering spectra of Au@MnO nanoflowers 150

9.1 Experimental scheme for DA-PEG-PP functionalized MnO nanoparticles 163
9.2 TEM images of as-prepared and DA-PEG functionalized MnO NPs 165
9.3 Powder XRD pattern and magnetic data of MnO NPs 166
9.4 FT-IR and UV-Vis spectra of DA-PEG-NH_2 and DA-PEG-PP functionalized MnO NPs 167

9.5 MTT assay for DA-PEG-NH_2 and DA-PEG-PP functionalized MnO NPs . . . 169
9.6 Light microscopic pictures of human Caki-1 cells incubated with MnO-DA-PEG-PP . . . 171
9.7 Light microscopic pictures of human Caki-1 cells incubated with MnO-DA-PEG-PP . . . 172
9.8 MRI data for DA-PEG-PP functionalized MnO NPs . . . 173

10.1 Experimental scheme for the preparation of multifunctional silica coated MnO NPs . . . 189
10.2 TEM images of silica coated MnO NPs . . . 191
10.3 FT-IR spectra and powder XRD patterns of silica coated MnO NPs . 192
10.4 Magnetic data of silica coated MnO NPs . . . 194
10.5 Uv-Vis and fluorescence spectra of Atto 465 doped MnO@SiO_2 NPs 195
10.6 Colloidal stability of MnO@SiO_2 NPs in aqueous solution . . . 197
10.7 T_1 weighted images of aqueous solutions containing MnO@SiO_2-PEG/NH_2 NPs . . . 198
10.8 Determination of MR relaxivities r_1 and r_2 and Mn leaching of MnO@SiO_2-PEG/NH_2 NPs . . . 199
10.9 TEM images of DA-PEG functionalized and silica coated MnO NPs after the leaching experiments . . . 200
10.10 Cytoxicity studies on silica coated MnO NPs . . . 201
10.11 Fluorescence microscopic images of cellular uptake of silica coated MnO NPs . . . 202

11.1 TEM images of monodisperse FePt NPs . . . 218
11.2 TEM images of monodisperse FePt@MnO NPs . . . 220
11.3 TEM images flower-like FePt@MnO NPs . . . 221
11.4 Flower-like FePt@MnO NPs synthesized with 13 nm FePt seeds . . 222
11.5 Powder XRD pattern of FePt@MnO nano-*hetero*-particles . . . 223
11.6 Magnetic data of FePt@MnO nano-*hetero*-particles . . . 224
11.7 Illustration of the pinning effect of the antiferromagnetic MnO domain at the FePt-MnO interface . . . 225

CHAPTER 1

Introduction

The evolution of nanotechnology during the past decades has had an enormous impact on our modern world. Looking back over major discoveries and taking a look around today, it is undeniable, that nanotechnology has found its way into our every day life. Whether it is news reports that warn us of possible health risks emanating from airborne nanoparticles, or newspaper ads and television commercials that praise car polish, sun screen lotion or tooth paste that has been improved by nanoparticles.

Today, the development of nanomaterials has moved beyond the discovery of totally new materials and compositions. Instead the focus has shifted to the investigation of more complex, composite systems, in which the recombination of known materials into structures of higher complexity opens new possibilities of functionality.[1–5] While scientific diligence of designing new composite or hybrid materials is speeding up, industrial producers have begun merchandising the earliest discovered nanomaterials, and, in fact, are developing novel applications for them to fit the desired needs. Besides other commercial applications, magnetic nanoparticles (NPs) are intensively being investigated for utilization in many different scientific and industrial fields, ranging from catalysis to mass data storage.[6, 7]

But one of the fastest moving and most exciting research areas is the interface be-

tween nanotechnology, biology and medicine. It has been stated by numerous experts, that the application of nanotechnology in medicine, which is often referred to as "nanomedicine", offers many exciting possibilities for healthcare in the future, and may revolutionize the areas of targeted drug delivery, disease detection and tissue engineering.[8–11] An often used catchphrase in this context is "theragnostics", which, as this word construction implies, comprehends the combination of both, therapy and diagnostics into one powerful tool. In fact, the concept of using magnetic nanoparticles to target tumor cells inside the human body, and applying them to treat cancer, was first conceived in the late 1970's.[12, 13] The key idea was to attach common anticancer drugs to small magnetic spheres outside the body before administering them to the patient. After injection into the blood stream strong external magnetic fields should concentrate the drug-loaded particles inside the tumor tissue. The authors predicted that by this approach the drug payload would be reduced significantly, and thereby the unwanted side effects associated with the systemic distribution of chemotherapeutic agents, including nausea, hair loss and compromised immune system could be avoided. Although not yet fully in clinical use, nanomedicine has come a long way since these initial ideas and is proceeding with remarkable speed.

The present dissertation is an attempt to contribute to these proceedings by exploring the potential of different magnetic nanomaterials for a possible use in nanobiotechnology and nanomedicine. It comprises not only state of the art strategies for the synthesis of magnetic nanoparticles but also different efficient ways to tailor their surfaces in order to address the difficult requirements of biomedical applications.

In principle, this doctorate thesis is divided into two parts. In the first part (chapters 2 through 6) basic principles concerning physical properties, synthesis, surface modification, and biomedical application of magnetic nanoparticles are reviewed. More precisely:

- **Chapter 2** introduces a set of physical phenomena that provide the basis for the use of magnetic NPs in biotechnology and medicine. It briefly explains how different processes lead to the evolution of new magnetic properties in nanoscale materials and, furthermore, focuses on how magnetic NPs can en-

hance the contrast in magnetic resonance imaging (MRI).

- **Chapter 3** surveys the most common synthetic approaches for the preparation of magnetic NPs and explains the basic physico-chemical laws associated with the formation of nanocrystals.

- **Chapter 4** is devoted to a new class of nanomaterials which has lately received considerable attention in the scientific community - nano-*hetero*-materials. Different preparation techniques, as well as new physical properties which arise from the combination of different materials at the nanoscale, are presented.

- **Chapter 5** gives a review of the most applied surface modification strategies to provide magnetic NPs with a high degree of functionality. It comprises simple approaches involving the micellar encapsulation of hydrophobic NPs with amphphilic molecules, but also more sophisticated procedures, in which the NPs are coated with specifically tailored multifunctional polymeric ligands.

- **Chapter 6** gives an overview of how magnetic NPs behave inside living organisms. It introduces basic concepts concerning the application of magnetic NPs in biomedicine and addresses, among other subjects, the most common design considerations, different delivery processes to designated sites inside living organisms, and shows how magnetic NPs have improved MRI during the past years and how they will help to increase the sensitivity and efficiency of this diagnostic method.

The second part (chapters 7 through 11), on the other hand, demonstrates specific examples for the concepts introduced in part 1. That means in particular:

- **Chapter 7** illustrates the concepts introduced in chapters 2 and 3 using MnO nanoparticles as an example. Besides the synthesis and characterization, the nucleation and growth processes of monodisperse MnO NPs are thoroughly investigated by different techniques. It reveals that the formation of monodisperse MnO NPs can be understood as a process in which, according to the

LaMer concept, nucleation and growth are separated from each other. Moreover, MnO NPs show an increase in magnetic moment when the particle size is reduced.[14]

- **Chapter 8** on the other hand, addresses several issues of part 1. It is not only an example for a representative of nano-*hetero*-particles, the new class of materials introduced in chapter 4, but it also shows how the individual surfaces of the materials can selectively be functionalized by different methods mentioned in chapter 5. In the present case, Au@MnO "nanoflowers" were generated by an *in situ* seed-mediated growth technique and subsequently functionalized with two different ligands, which selectively addressed the Au and MnO domains, respectively. Additionally, the potential of these "nanoflowers" as imaging agents for both, optical imaging and MRI is presented.[15]

- **Chapter 9** is a further example for an efficient surface modification strategy (chapter 5) and, in addition to that, demonstrates the use of MnO NPs as "theragnostic" agents (chapter 6). The NPs were functionalized with hydrophilic bi-functional ligand that contained a catechol as anchor group and protoporphyrin IX (PP) as photosensitizer conjugated via a poly(ethylene glycol) (PEG) linker. PP initiates the production of reactive singlet oxygen ($^1O_2$), a molecular entity that is highly toxic for cells, once it is excited with visible light. We demonstrate that PP-functionalized MnO NPs can induce apoptosis in kidney cancer cells upon laser illumination, whereas non-irradiated cells containing MnO-PP NPs show no toxic response. Additionally, by virtue of their magnetic properties, MnO NPs exhibit a strong T_1 contrast in MRI. Consequently, PP functionalized MnO NPs have a great potential as "theragnostic" probes for photodynamic therapy (PDT) and MRI (diagnosis).[16]

- **Chapter 10** is a further example for the principles covered in chapter 5 and 6. It reveals how surface modification of MnO NPs with a shell of silica (MnO@SiO_2) can improve the stability of the magnetic NPs in aqueous environments. A novel synthetic approach was developed to, not only coat MnO NPs with a thin and uniform silica shell, but also to permit further functionalization with different ligands. The resulting particles exhibit almost unaltered

magnetic properties compared to "naked" MnO NPs, making them ideal candidates as MRI contrast agents. Moreover, the use of silica as coating material allows the incorporation of fluorescent dyes and, therefore, offers an extension of their biomedical imaging potential. Additionally, the MnO@SiO_2 NPs have a negligible toxic effect on bone marrow-derived dendritic cells (BMDCs) making them suitable candidates for *in vivo* applications. Another interesting feature, that can be attributed to the excellent stability of SiO_2, is the minor liability of MnO@SiO_2 NPs towards Mn leaching, compared to simply PEGylated MnO NPs.

- **Chapter 11**, on the other hand, illustrates the concepts introduced in chapters 2 and 4. FePt@MnO NPs, as a further example for a nano-*hetero*-material, were synthesized with different sizes and morphologies by a two-step seed-mediated growth procedure, in which monodisperse FePt NPs acted as seeds for the nucleation of MnO domains. The size and morphology were controllable according to the synthetic principles explained in chapter 4. Furthermore, the spin interactions between two different magnetic materials sharing a common interface lead to interesting magnetic properties, e.g. an exchanged biased magnetic hysteresis.

Finally, chapter 12 summarizes the results of this doctorate work and gives conclusions and an outlook to future projects.

1.1 References

[1] Nath, N.; Chilkoti, A. *Analytical Chemistry* **2002**, *74*, 504–509.

[2] Ferrari, M. *Nature Reviews: Cancer* **2005**, *5*, 161–171.

[3] Cheon, J.; Lee, J.-H. *Accounts of Chemical Research* **2008**, *41*, 1630–1640.

[4] Gao, J.; Gu, H.; Xu, B. *Accounts of Chemical Research* **2009**, *42*, 1097–1107.

[5] Hao, R.; Xing, R.; Xu, Z.; Hou, Y.; Gao, S.; Sun, S. *Advanced Materials* **2010**, *22*, 2729–2742.

[6] Pankhurst, Q. A.; Connolly, J.; Jones, S. K.; Dobson, J. *Journal of Physics D: Applied Physics* **2003**, *36*, R167.

[7] Pankhurst, Q. A.; Thanh, N. T.; Jones, S. K.; Dobson, J. *Journal of Physics D: Applied Physics* **2009**, *42*, 224001.

[8] Wagner, V.; Dullaart, A.; Bock, A.-K.; Zweck, A. *Nature Biotechnology* **2006**, *24*, 1211–1217.

[9] Sun, C.; Lee, J. S. H.; Zhang, M. *Advanced Drug Delivery Reviews* **2008**, *60*, 1252–1265.

[10] Davis, M. E.; Chen, Z.; Shin, D. M. *Nature Reviews on Drug Discovery* **2008**, *7*, 771–782.

[11] Shi, J.; Votruba, A. R.; Farokhzad, O. C.; Langer, R. *Nano Letters* **2010**, *10*, 3223–3230.

[12] Widder, K. J.; Senyei, A. E.; Scarpelli, D. G. *Proceedings of the Society for Experimental Biology and Medicine* **1978**, *58*, 141–146.

[13] Senyei, A.; Widder, K.; Czerlinski, G. *Journal of Applied Physics* **1978**, *49*, 3578–3583.

[14] Schladt, T. D.; Graf, T.; Tremel, W. *Chemistry of Materials* **2009**, *21*, 3183–3190.

[15] Schladt, T. D. et al. *Angewandte Chemie International Edition* **2010**, *49*, 3976–3980.

[16] Schladt, T. D.; Schneider, K.; Shukoor, M. I.; Natalio, F.; Bauer, H.; Tahir, M. N.; Weber, S.; Schreiber, L. M.; Schröder, H. C.; Müller, W. E. G.; Tremel, W. *Journal of Materials Chemistry* **2010**, *20*, 8297–8904.

Part I

CHAPTER 2

Nanomagnetism

Magnetic nanoparticles are among the most investigated nanomaterial systems, owing to the fact that their magnetic properties dramatically depend upon their size and their morphology. Several issues are responsible for these unique properties: finite-size effects, which result from the quantum confinement of the electrons inside the material, and surface effects caused by symmetry breaking of the crystal structure at the boundaries of the particles.[1–4]
Concerning finite-size effects, the magnetic properties of (ferro-) magnetic nanoparticles are dominated by two key features: (1) The single domain limit and (2) the superparamagnetic limit, which both lead to individual material-dependent length scales, i.e. the single domain size and the superparamagnetic size. Both features will be discussed briefly.

2.1 Single-Domain Limit

A ferromagnetic bulk material usually consists of many separate areas, in which all magnetic moments of the constituent atoms are pinned in the same direction (see Figure 2.1). The reason for such an arrangement arises from the fact, that the

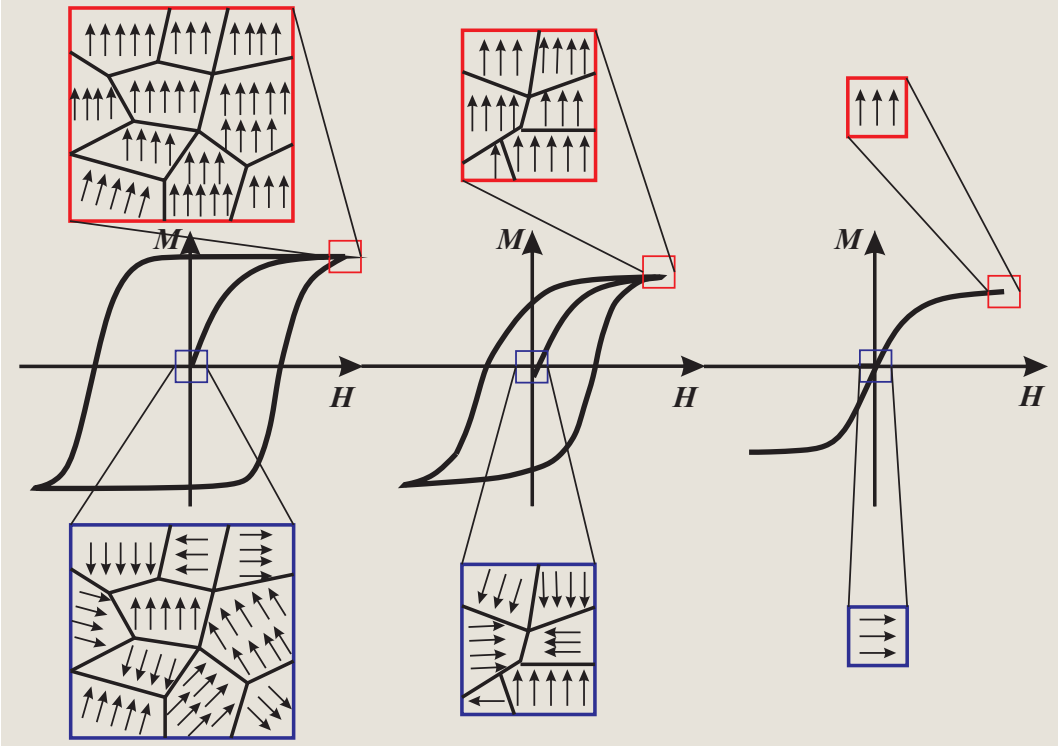

Figure 2.1: Illustration of the single domain limit.

magnetostatic energy (ΔE_{MS}) of the materials is lowered once a large domain is broken up into several smaller domains. However, the formation of new domain walls requires energy (E_D), and therefore, there is a size limit, below which the energy needed for the creation of a smaller domain exceeds the amount of energy gained from decreasing the magnetostatic energy. Consequently, this means, that a magnetic nanoparticle with a diameter comparable to, or lower than the size of the smallest possible magnetic domain, could only consist of a single domain. This critical diameter (D_c) is dependent on the regarding material, but usually lies in the range of a few tens of nm. It can be derived by considering:

$$\Delta E_{MS} \approx E_D \tag{2.1}$$

Since the magnetostatic energy is proportional to the particle volume (i.e. D^3), and the energy density inside a magnetic field follows B^2 (and therefore, M_s^2), ΔE_{MS}

scales with $M_s^2 D^3$. On the other hand, the domain wall formation energy is strongly dependent on the surface area of the domain walls (i.e. D^2) and the effective surface energy γ.[5] This leads to:

$$M_s^2 D^3 \approx \gamma D^2 \tag{2.2}$$

which results in:

$$D_c \approx \frac{\gamma}{M_s^2} \approx 18 \frac{\sqrt{A_{ex} K_a}}{\mu_0 M_s^2} \tag{2.3}$$

in which A_{ex} is the exchange constant, K_a is the anisotropy constant, μ_0 is the vacuum permeability and M_s is the saturation magnetization.[3, 6, 7]

2.2 Superparamagnetic Limit

To understand the super-paramagnetic effect the magnetic anisotropy energy per particle ($E(\Theta)$) which pins the magnetic moments of a single domain particle in a certain direction, has to be considered. $E(\Theta)$ is proportional to $K_a V$ (V is the particle volume), the energy barrier which stops the magnetic moment flipping from one direction to the opposite. $K_a V$ is usually much higher than the thermal energy $k_b T$, however, with decreasing particle size $K_a V$ decreases to values equal to, or below $k_b T$. As a result, the magnetic moments are able to overcome the energy barrier and freely flip in any direction, i.e. for $k_b T \geq K_a V$ the system behaves like a paramagnet. Since the individual atomic moments add up to one (super) moment for every particle, this phenomenon is called superparamagnetism. On the other hand, if the temperature is lowered for a given superparamagnetic particle, the thermal energy of the particle decreases until $k_b T$ is lower than the energy barrier $K_a V$ ($k_b T \leq K_a V$), i.e. the particle undergoes a magnetic transition from a super-paramagnetic to a blocked state, in which the magnetic moments cannot flip freely. The temperature at which $k_b T = K_a V$ is therefore called magnetic blocking temperature T_B.[3, 6, 7]

Experimentally, T_B can be determined by measuring the magnetization of a nanoparticle sample versus increasing temperature under an applied external magnetic field. More precisely, in a so called zero-field-cooled/field-cooled (ZFC/FC) experiment, the sample is first cooled down to a temperature well below the expected

blocking temperature (usually 5 K). Then, an external field (generally 100 Oe) is applied and the sample is slowly heated up while simultaneously measuring the magnetization. Since the particles were "frozen" from room temperature, their magnetic moments are distributed homogeneously, and therefore the net magnetization is zero. However, as the temperature, increases the particles are able to move their moments in the direction of the external field. As a result, the net magnetization rises. As mentioned before, above T_B the thermal energy exceeds K_aV, leading to a decline of the magnetization. As a result, the ZFC curve passes a maximum at T_B.

2.3 Surface Effects

Surface effects are directly dependent on the ratio of surface spins to bulk spins. Therefore, surface effects become more pronounced with increasing surface to volume ratio, i.e. decreasing particle size. The symmetry breaking at the particle boundary can lead to variations in the electronic band structure, lattice constant, and atom coordination and, as a direct result, change the magnetic properties.[6, 7] Furthermore, surface effects can lead to a decrease of the magnetization of small particles, for instance ferromagnetic oxide nanoparticles, with respect to the bulk value. This reduction has been associated with different mechanisms, such as the existence of a magnetic dead layer on the particle surface, or the existence of canted surface spins.[2] Additionally, Bødker et *al.* reported, that the magnetic anisotropy K_a of iron NPs increases with decreasing particle size, due to a higher contribution of the surface anisotropy K_{aS}.[8] As an example, antiferromagnetic NiO and MnO nanoparticles exhibit increasing net magnetization values and higher magnetic blocking temperatures with decreasing particle size, the reason being the larger number of uncompensated surface spins (see Figure 2.2).[1, 9, 10]

2.4 Nanomagnetism in Magnetic Resonance Imaging (MRI)

Their unique physical properties make magnetic NPs especially appealing for biomedical purposes, such as the diagnosis and treatment of diseases or bioanalytical

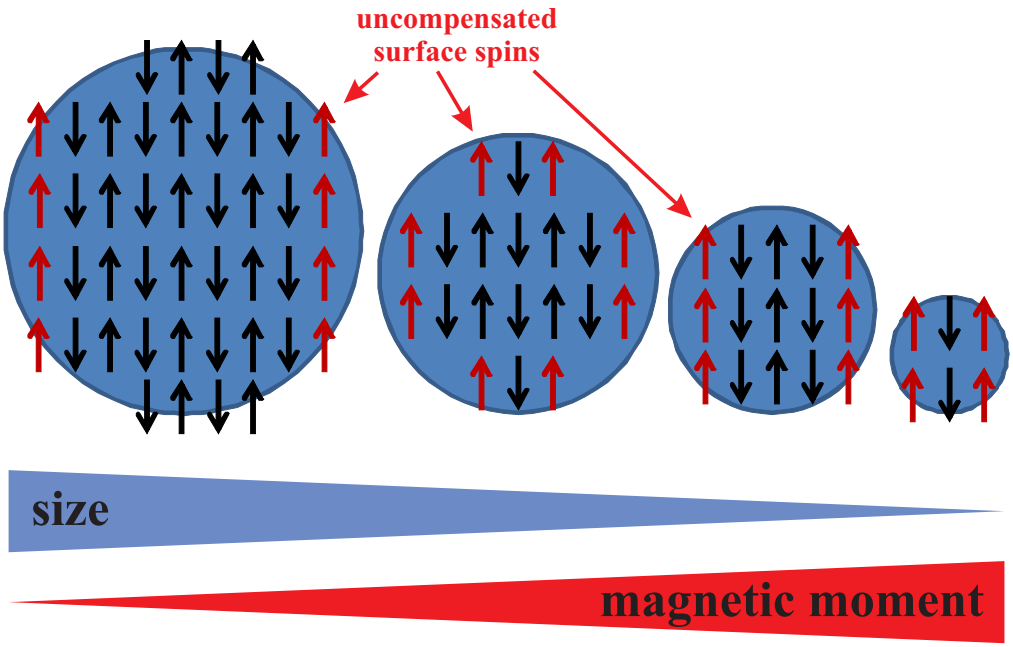

Figure 2.2: Antiferromagnetic materials have a net magnetization of zero, however, uncompensated spins on the particle surface contribute to a measurable magnetic moment. With decreasing particle size the surface-to-volume ratio increases, which leads to higher magnetic moments.

processes. However, this section will solely focus on their utilization as contrast agents for magnetic resonance imaging (MRI).

MR imaging is one of the most powerful non-invasive imaging techniques in clinical use today.[11–13] Just as NMR spectroscopy, it is based on measuring the relaxation of protons in an external magnetic field after they have been excited with a radio-frequency pulse. To be more specific, if a strong magnetic field (B_0) is applied, water protons will align along the main field axis and precess with a field-dependent frequency (the Lamor-frequency ω_0). However, they can align either parallel or anti-parallel to the external field, the latter being energetically a little less favorable. Therefore, there is a slightly larger number of proton spins pointing in field (z-) direction, which leads to a measurable longitudinal magnetization M_z (see Figure 2.3a). Since the energy difference between the parallel and anti-parallel state depends on the strength of the magnetic field, a higher B_0 yields a better signal in-

tensity. By applying an electromagnetic pulse whose frequency corresponds to the Lamor frequency, the spins can be tilted from the z-direction into the xy plane (see Figure 2.3b). As a result M_z becomes zero and a transverse magnetization M_{xy} arises. However, this condition is energetically not stable and the system slowly returns to its initial state.
The process by which this occurs is called relaxation. Basically, there are two different types of relaxation depending on the nature of the corresponding interactions:

- ***T*$_1$: Longitudinal relaxation.** After excitation with a 90° radio frequency pulse M_z is zero and M_{xy} is maximal (see Figure 2.3c). Over time, the magnetization returns to the z-direction and M_{xy} decreases. This process is asso-

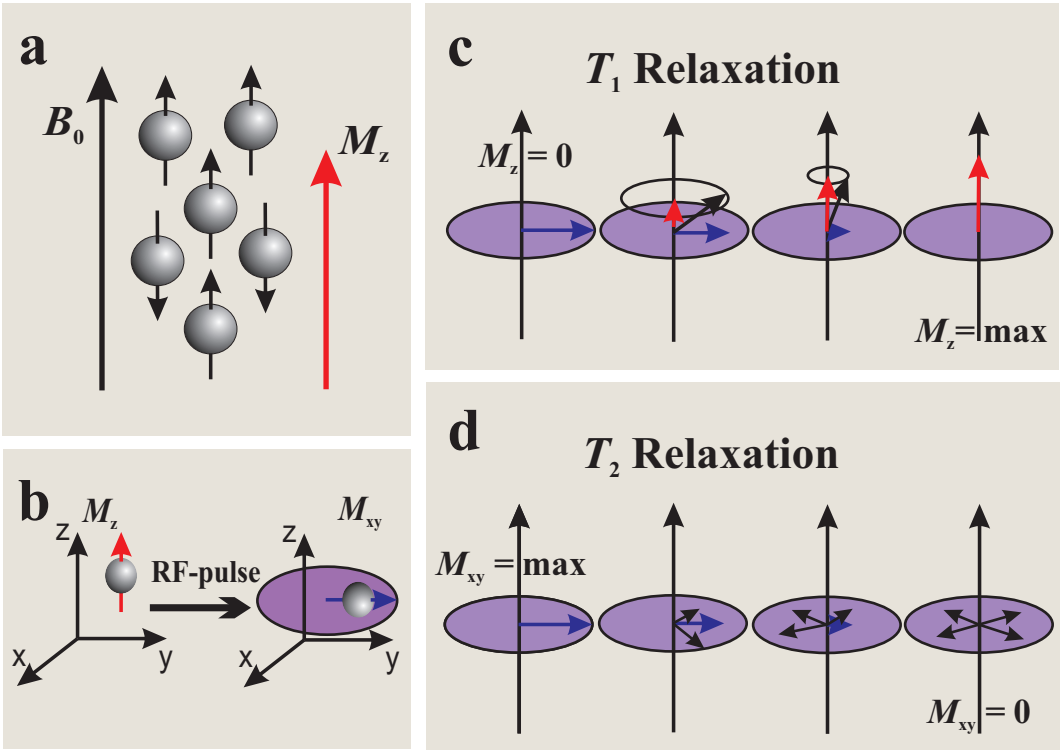

Figure 2.3: (a) Parallel and anti-parallel alignment of proton spins in an external magnetic field B_0, (b) by applying a 90° RF-pulse the spins are tilted into the xy-plane, (c) T_1 relaxation mechanism: over time, energy is transmitted to the environment (lattice), M_z increases, (d) T_2 relaxation mechanism: dephasing of the spins leads to depletion of M_{xy}.[11]

ciated with a release of energy to the environment (the "lattice"), therefore, it is also called *spin-lattice* (or *longitudinal*) relaxation. The time constant, at which the energy is depleted (and M_z increases) T_1, depends on different factors, including B_0, or the nature of the observed tissue.[11, 13]

- ***T_2*: Transverse relaxation.** The loss of the transverse magnetization M_{xy} is also associated with a dephasing of the spins precessing in the xy-plane (see Figure 2.3d). Directly after excitation all spins are in phase and M_{xy} is maximal. In principle, two components determine the dephasing process: On the one hand, an energy exchange between the spins induced by local magnetic field interferences among the spins themselves (*spin-spin* or *transverse* relaxation), leads to a faster and slower precession in the xy-plane. The time constant T_2, with which M_{xy} is depleted is therefore independent of B_0. On the other hand, inhomogeneities of the external magnetic field, arising from the magnetic coils of the MRI scanner itself or the body of the patient, lead to an additional dephasing and a faster decay of M_{xy} with a time constant T_2^*.[11–13]

The contrast in MR images is mainly determined by three different features: the proton density, the T_1 time and the T_2 time of the regarding tissue. While the proton density is given by the chemical and physical nature of the tissue, the use of contrast agents can greatly enhance both T_1 and T_2 contrast. Basically it is desired to shorten the relaxation times because this leads to a greater difference in signal intensity and thus to a better contrast in the MR image. Figure 2.4 demonstrates the basic principles of contrast enhancement. In T_1-weighted images, the signal intensity relies on how fast M_z is restored. Curve A in Figure 2.4a shows the normal T_1 relaxation of a tissue without a contrast agent. After a certain time period t' the longitudinal magnetization has recovered to a value $M_z^{'}$. Curve B corresponds to a T_1 relaxation of the same tissue but using a suitable contrast agent. After the same time period more longitudinal magnetization ($M_z^{''}$) is restored, and since $M_z^{''} > M_z^{'}$ more intensity is measured in the scanner. Therefore, T_1 enhancement leads to a brighter (positive) contrast in the image. On the other hand, in T_2-weighted images the signal intensity is determined by M_{xy}. Curve A in Figure 2.4b shows the original T_2 relaxation of a tissue. After a time t' the transverse magnetization has dropped to a value $M_{xy}^{'}$. By

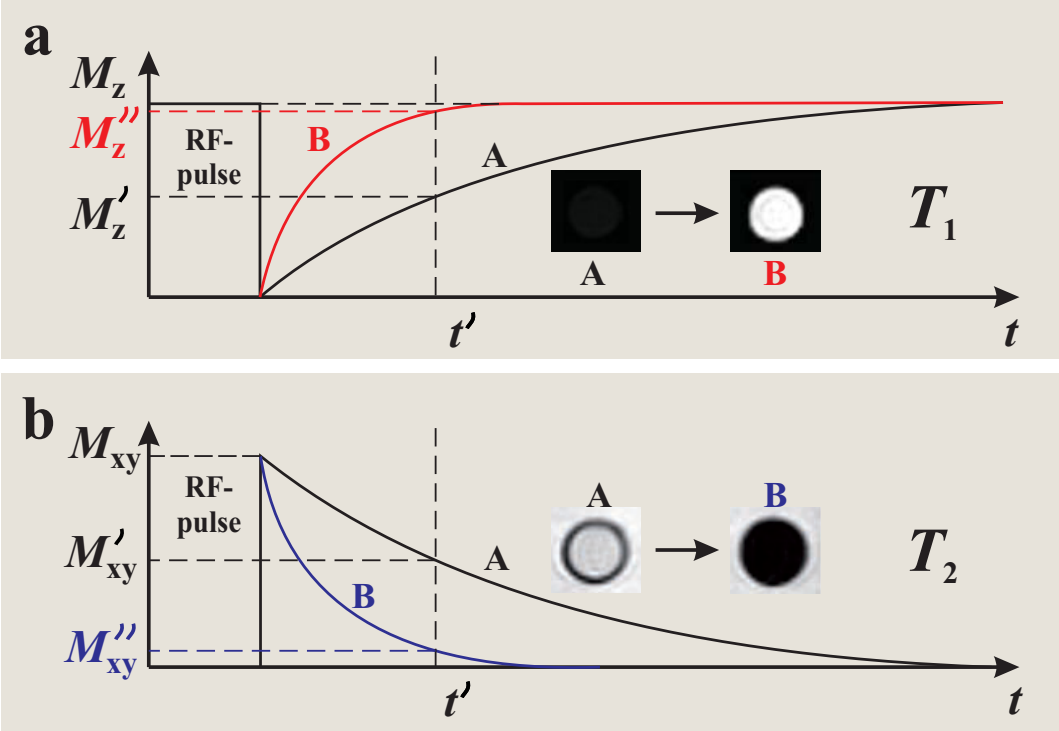

Figure 2.4: (a) Evolution of longitudinal magnetization M_z over time: A without, B with T_1 contrast agent, (b) evolution of the transverse magnetization M_{xy}, A without and B with T_2 contrast agent.

use of a contrast agent the relaxation is accelerated (curve B) and after t the in-plane magnetization is $M_{xy}^{''}$. Since $M_{xy}^{''} < M_{xy}^{'}$, the area in the concerning image appears darker (negative contrast).

In general, the effect of MRI contrast agents is based on influencing the resonance properties of the tissue by changing the local magnetic field inside the body. This change depends on interactions between the protons of the tissue (water, fat, proteins) and the unpaired electrons, and therefore, the magnetic moment of the contrast agent. Consequently, most commercially available contrast agents consist of paramagnetic substances with a high number of unpaired electrons and high magnetic moment (e.g. solutions of metal ions, like Gd^{3+}, Mn^{2+} or Fe^{3+}). Superparamagnetic nanoparticles (see section 2.2) have a much higher magnetic moment (compared to free ions 100-10,000-fold), making them promising candidates for contrast enhancing purposes. In fact, iron oxide NPs are already in clinical use as

T_2 contrast agents.[11]

Unlike X-ray contrast agents for computer tomography, that rely on the direct absorption of X-ray radiation, the effect of (super)paramagnetic substances in MRI is oblique. For example, paramagnetic T_1 contrast agents withdraw the excess energy after proton excitation, and hence, lead to a faster recovery of M_z (see above). However, this effect is strongly related to the ability of water molecules to enter the periphery of the agent. The impact of T_2 agents, on the other hand, arises from the creation of local magnetic fields, which results in increased field-fluctuations, and thus in a faster dephasing of the in-plane spins. As a consequence, T_2 agents need to have a much larger magnetic moment than T_1 agents. The measure, by which the performance of MRI contrast agents is evaluated, is called relaxivity ($r_1 = 1/T_1$ and $r_2 = 1/T_2$, per mol of agent). Additionally, the ratio of T_2 to T_1 relaxivity (r_2/r_1-ratio) can also be used to estimate the contrast enhancing potential (e.g. T_1 agents require a low r_2/r_1 ratio, whereas for T_2 agents it should be large). The degree of performance is strongly dependent on the size, size distribution, composition and crystallinity of the NPs.[14–16] As already stated in the previous sections the particle size and composition mainly determines the magnetization and, therefore, a narrow size distribution is necessary to efficiently exploit the magnetic properties for MRI. Furthermore, it was shown by Weller and coworkers, that the surface characteristics of magnetic NPs (i.e. nature of surface ligands, degree of ligand loading) also play a crucial role for the MRI contrast enhancing abilities.[17] The authors demonstrated that the transverse relaxivity, in particular r_2^*, is greatly higher for micellar coated compared to polymer-functionalized particles using same-sized nanoparticles.

Although superparamagnetic iron oxide NPs (SPIONs) show a strong T_2 effect, there are numerous reports in which they can also be applied as effective agents for the shortening of the T_1 relaxation time, either by applying special measurement techniques, by reducing the particle diameter, and thus the magnetic moment, or by labeling Fe_3O_4 NPs with Gd-complexes.[18–21] Apart from iron oxide NPs, other nanomaterials are also objects of increasing scientific interest as MRI contrast agents. In this respect, gadolinium-based NPs have been extensively investigated as positive (T_1) contrast agents. [22–30] However, superparamagnetic MnO nanoparticles have recently attracted considerable attention as positive (T_1) contrast agents

(see also section 6.4).[31–36]

2.5 References

[1] Kodama, R. H.; Makhlouf, S. A.; Berkowitz, A. E. *Physical Review Letters* **1997**, *79*, 1393–1396.

[2] Kodama, R. H. *Journal of Magnetism and Magnetic Materials* **1999**, *200*, 359–372.

[3] Klabunde, K. J. *Nanoscale materials in chemistry*; Wiley-Interscience: New York, NY, 2001.

[4] Battle, X.; Labarta, A. *Journal of Physics D: Applied Physics* **2002**, *35*, R15.

[5] Leslie-Pelecky, D. L.; Rieke, R. D. *Chemistry of Materials* **1996**, *8*, 1770–1783.

[6] Lu, A.-H.; Salabas, E. L.; Schüth, F. *Angewandte Chemie International Edition* **2007**, *46*, 1222–1244.

[7] Lu, A.-H.; Salabas, E. L.; Schüth, F. *Angewandte Chemie* **2007**, *119*, 1242–1266.

[8] B\o dker, F.; M\o rup, S.; Linderoth, S. *Physical Review Letters* **1994**, *72*, 282.

[9] Ghosh, M.; Biswas, K.; Sundaresan, A.; Rao, C. N. *Journal of Materials Chemistry* **2006**, *16*, 106–111.

[10] Schladt, T. D.; Graf, T.; Tremel, W. *Chemistry of Materials* **2009**, *21*, 3183–3190.

[11] Weishaupt, D.; Köchli, V. D.; Marincek, B. *Wie funktioniert MRI? Eine Einführung in Physik und Funktionsweise der Magnetresonanzbildgebung*, 6th ed.; Springer Berlin Heidelberg: Berlin, Heidelberg, 2009.

[12] Mitchell, D. G.; Cohen, M. S. *MRI principles*, 2nd ed.; Elsevier Saunders: Philadelphia, Pe., 2004.

[13] Brown, M. A.; Semelka, R. C. *MRI: Basic principles and applications*, 4th ed.; Wiley-Blackwell: Hoboken, 2010.

[14] Perez, J.; Josephson, L.; O'Loughlin, T.; Hogemann, D.; Weissleder, R. *Nature Biotechnology* **2002**, *20*, 816–820.

[15] Berret, J.-F.; Schonbeck, N.; Gazeau, F.; El Kharrat, D.; Sandre, O.; Vacher, A.; Airiau, M. *Journal of the American Chemical Society* **2006**, *128*, 1755–1761.

[16] Lee, J.-H.; Huh, Y.-M.; Jun, Y.-w.; Seo, J.-w.; Jang, J.-T.; Song, H.-T.; Kim, S.; Cho, E.-J.; Yoon, H.-G.; Suh, J.-S.; Cheon, J. *Nature Medicine* **2007**, *13*, 95–99.

[17] Tromsdorf, U. I.; Bigall, N. C.; Kaul, M. G.; Bruns, O. T.; Nikolic, M. S.; Mollwitz, B.; Sperling, R. A.; Reimer, R.; Hohenberg, H.; Parak, W. J.; Förster, S.; Beisiegel, U.; Adam, G.; Weller, H. *Nano Letters* **2007**, *7*, 2422–2427.

[18] Eibofner, F.; Steidle, G.; Kehlbach, R.; Bantleon, R.; Schick, F. *Magnetic Resonance in Medicine* **2010**, NA.

[19] Çukur, T.; Yamada, M.; Overall, W. R.; Yang, P.; Nishimura, D. G. *Magnetic Resonance in Medicine* **2010**, *63*, 427–437.

[20] Tromsdorf, U. I.; Bruns, O. T.; Salmen, S. C.; Beisiegel, U.; Weller, H. *Nano Letters* **2009**, *9*, 4434–4440.

[21] Bae, K. H.; Kim, Y. B.; Lee, Y.; Hwang, J.; Park, H.; Park, T. G. *Bioconjugate Chemistry* **2010**, *21*, 505–512.

[22] Evanics, F.; Diamente, P. R.; van Veggel, F. C. J. M.; Stanisz, G. J.; Prosser, R. S. *Chemistry of Materials* **2006**, *18*, 2499–2505.

[23] Bridot, J.-L.; Faure, A.-C.; Laurent, S.; Rivière, C.; Billotey, C.; Hiba, B.; Janier, M.; Josserand, V.; Coll, J.-L.; Elst, L. V.; Muller, R.; Roux, S.; Perriat, P.; Tillement, O. *Journal of the American Chemical Society* **2007**, *129*, 5076–5084.

[24] Fortin, M.-A.; Petoral, R. M., Jr.; Söderlind, F.; Klasson, A.; Engström, M.; Veres, T.; Käll, P.-O.; Uvdal, K. *Nanotechnology* **2007**, *18*, 395501.

[25] Park, J. Y.; Baek, M. J.; Choi, E. S.; Woo, S.; Kim, J. H.; Kim, T. J.; Jung, J. C.; Chae, K. S.; Chang, Y.; Lee, G. H. *ACS Nano* **2009**, *3*, 3663–3669.

[26] Petoral, R. M.; Söderlind, F.; Klasson, A.; Suska, A.; Fortin, M. A.; Abrikossova, N.; Selegard, L.; Käll, P.-O.; Engström, M.; Uvdal, K. *Journal of Physical Chemistry C* **2009**, *113*, 6913–6920.

[27] Esqueda, A. C.; López, J. A.; Andreu-de Riquer, G.; Alvarado-Monzón, J. C.; Ratnakar, J.; Lubag, A. J.; Sherry, A.; de León-Rodríguez, L. M. *Journal of the American Chemical Society* **2009**, *131*, 11387–11391.

[28] Cheng, Z.; Thorek, D. L. J.; Tsourkas, A. *Angewandte Chemie International Edition* **2010**, *49*, 346–350.

[29] Warsi, M. F.; Adams, R. W.; Duckett, S. B.; Chechik, V. *Chemical Communications* **2010**, *46*, 451–453.

[30] Manus, L. M.; Mastarone, D. J.; Waters, E. A.; Zhang, X.-Q.; Schultz-Sikma, E. A.; MacRenaris, K. W.; Ho, D.; Meade, T. J. *Nano Letters* **2010**, *10*, 484–489.

[31] Na, H. B.; Lee, J. H.; An, K.; Park, Y. I.; Park, M.; Lee, S.; Nam, D. H.; Kim, S. T.; Kim, S. H.; Kim, S. W.; Lim, K. H.; Kim, K. S.; Kim, S. O.; Hyeon, T. *Angewandte Chemie International Edition* **2007**, *46*, 5397–5401.

[32] Na, H. B.; Hyeon, T. *Journal of Materials Chemistry* **2009**, *19*, 6267–6273.

[33] Schladt, T. D. et al. *Angewandte Chemie International Edition* **2010**, *49*, 3976–3980.

[34] Schladt, T. D.; Schneider, K.; Shukoor, M. I.; Natalio, F.; Bauer, H.; Tahir, M. N.; Weber, S.; Schreiber, L. M.; Schröder, H. C.; Müller, W. E. G.; Tremel, W. *Journal of Materials Chemistry* **2010**, *20*, 8297–8904.

[35] Yang, H.; Zhuang, Y.; Hu, H.; Du, X.; Zhang, C.; Shi, X.; Wu, H.; Yang, S. *Advanced Functional Materials* **2010**, *20*, 1733–1741.

[36] Huang, J.; Xie, J.; Chen, K.; Bu, L.; Lee, S.; Cheng, Z.; Li, X.; Chen, X. *Chemical Communications* **2010**, *46*, 6684–6686.

CHAPTER 3

Synthesis of Magnetic NPs

For more than 30 years, the preparation of nanocrystals, i.e. crystalline materials with dimensions in the range between 1-100 nm, has been intensively investigated, not only for their fundamental scientific interest, but also for their many possible technological applications. As mentioned in chapter 2, nanomaterials exhibit physical and chemical properties, that are quite different from their bulk counterparts. However, since these properties are strongly dependent on the dimensions of the nanocrystals, the synthesis of uniformly-sized NPs (i.e. monodisperse with a standard deviation of the size distribution $\sigma \leq 5\%$) is of key importance. Especially, nanocrystals composed of semiconductor (so called quantum dots (QDs)) or magnetic materials have attracted considerable interest, in this respect. For applications in optical devices, size uniformity of the QDs is critical for achieving a sharp colored emission at a specific wavelength. On the other hand, monodisperse magnetic nanocrystals are essential for next-generation multiterabite (Tbit in^{-2}) magnetic storage media.[1–5]

In principle, there are two major approaches for the preparation of nanomaterials. The first one is based on physical methods to break down a bulk material, until the crystallite size reaches nano-dimensions.[6, 7] Therefore, it is generally referred to as "top-down" approach. The second strategy is based on the atomic assembly of

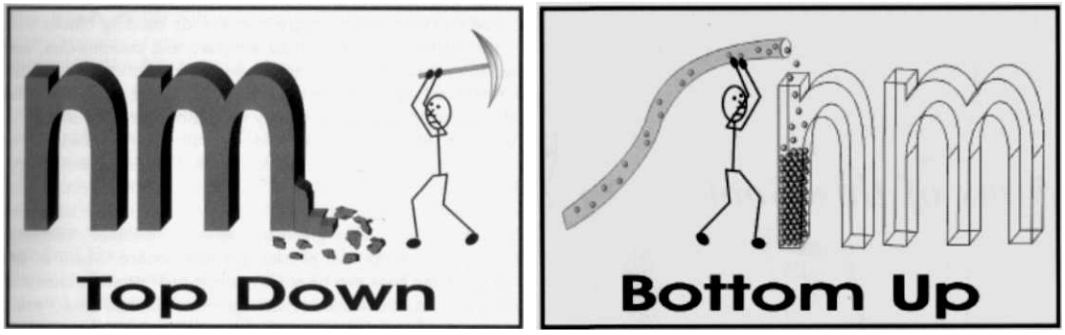

Figure 3.1: Illustration of the "top-down" and "bottom-up" approaches.

individual elements to create nanoparticles of the desired material, hence the name "bottom-up" approach (see Figure 3.1). For industrial, and other large-scale production pathways, physical "top-down" methods are beneficial, since they guarantee the preparation of large quantities of NPs in a short time. The major drawback, however, is the poor control over size, size distribution, and morphology of the resulting particles.[5, 8–10] A better control is achieved by solution-based "bottom-up" strategies, although the yields are comparably low. Since the research interest in the development of magnetic nanomaterials for biomedical applications is focused on nanoparticles with homogeneous size distribution and morphology, only solution-based "bottom-up" methods will be considered in the following.

As magnetic nanoparticles have played a major role in materials research over the past decades, numerous strategies have been developed to synthesize them with different compositions and homogeneous size distributions. The most favorable synthetic approaches usually comprise co-precipitation, hydrothermal synthesis, synthesis in (reverse) micelles, and thermal decomposition and/or reduction of appropriate metal-organic precursors. Simple metal nanoparticles such as iron,[11–13] cobalt[14] and nickel,[15] as well as metal oxides, like Fe_3O_4,[16–18] γ-Fe_2O_3,[11] MnO,[19–25] Mn_3O_4,[26] CoO,[27–30] or NiO,[31, 32] mixed metal oxides with spinel-type structure, such as MFe_2O_4 (M = Mn, Co, Zn),[16, 33–35] or intermetallics such as FePt,[36–41] NiPt,[42, 43] and $CoPt_3$[44, 45] have been prepared by these methods.

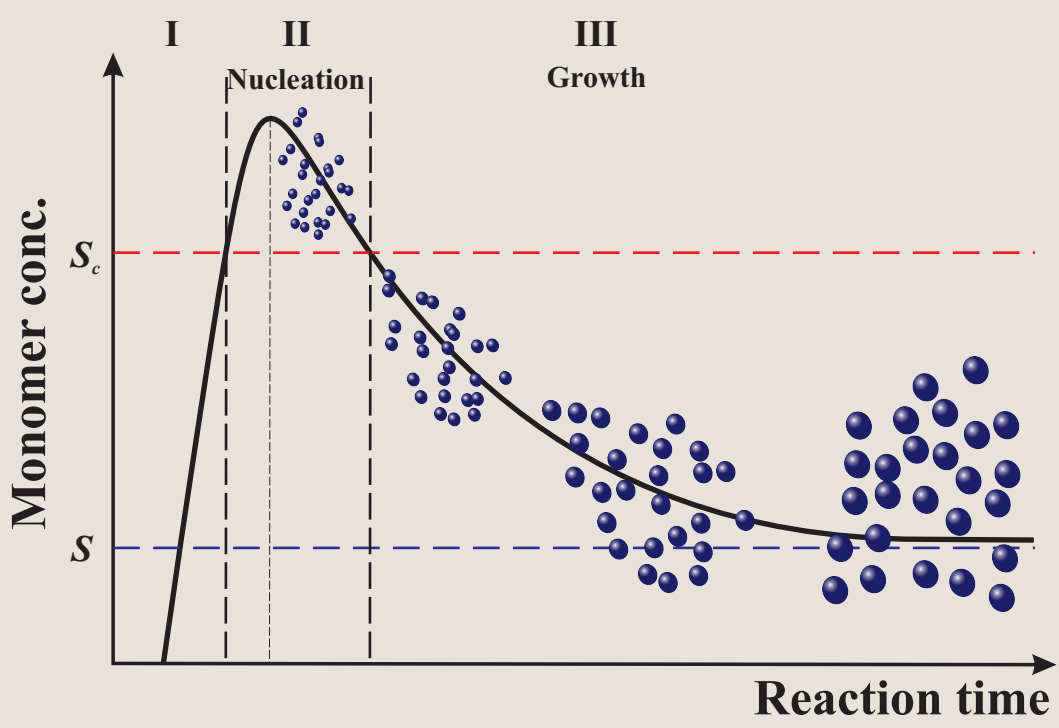

Figure 3.2: LaMer plot illustrating the separation of nucleation and growth during the synthesis of monodisperse NPs. S and S_c are supersaturation and critical supersaturation, respectively.

3.1 General Considerations

A key issue for the preparation of monodisperse magnetic nanoparticles is to understand the basic formation mechanism of nanocrystals in solution. It is in fact surprising, that, although many different synthetic strategies are known today (see above), the comprehensive understanding of nanoparticle generation is still very limited. However, the main factors that determine this process, i.e. nucleation and growth, will be discussed briefly. [23, 46]

The first research efforts associated with the formation of monodisperse colloidal particles were carried out in the 1940's. LaMer and coworkers revealed, that a short nucleation burst followed by slow controlled growth, without further nucleation, is essential to produce colloids with a narrow size distribution.[47, 48] Although this model was actually developed for sulfur hydrosols and oil aerosols, it can easily be

transferred to nanoparticulate systems. According to the LaMer model, the whole nucleation and growth process can be divided into three phases (see Figure 3.2). In the first phase, the monomer concentration increases gradually until it reaches the point of supersaturation (S). If no seeds (like dust particles or small crystallites) are present, which would initiate heterogeneous nucleation, only homogeneous nucleation is possible. However, since the energy barrier for the initiation of a homogeneous nucleation event is considerably high, the monomer concentration can further increase (phase II). The energy barrier can be expressed as the Gibbs free energy of spherical crystal formation with radius r:

$$\Delta G_K = 4\pi r^2\gamma + \frac{4}{3}\pi r^3 \Delta G_\nu \tag{3.1}$$

Herein, γ is the surface free energy per unit area and ΔG_ν is the change of free lattice energy during the generation of the crystallites. Since γ is always positive and ΔG_ν is negative, a plot of ΔG_K versus r passes a maximum at the critical radius r_c (see Figure 3.3). For $r \leq r_c$ the nucleus is too small and will dissolve away. Only for $r \geq r_c$ the formed nucleus is stable and able to grow.

The requirements for homogeneous nucleation to occur can be derived by calculating the critical radius:

$$\frac{\partial(\Delta G_K)}{\partial r} = 0 \tag{3.2}$$

considering $\Delta G_K = (-RT\ln S)/V_m$ with supersaturation S and V_m being the molar volume of the bulk crystal, this leads to:

$$r_c = \frac{-2\gamma}{\Delta G_\nu} = \frac{2\gamma V_m}{RT\ln S} \tag{3.3}$$

As a consequence, equation 3.3 emphasizes the necessary condition for the initiation of homogeneous nucleation, without premature heterogeneous nucleation taking place: only if S is sufficiently high, r_c will be small enough, so that the system can surmount the energy barrier for spontaneous homogeneous nucleation.[49] In phase II, the supersaturation finally reaches a critical value (S_c), which means that the system contains enough energy to overcome the energy barrier (see Figure 3.2 and Figure 3.3). Therefore, homogeneous nucleation throughout the entire reaction solution can take place any time. The critical free energy (ΔG_{Kc}) needed to create

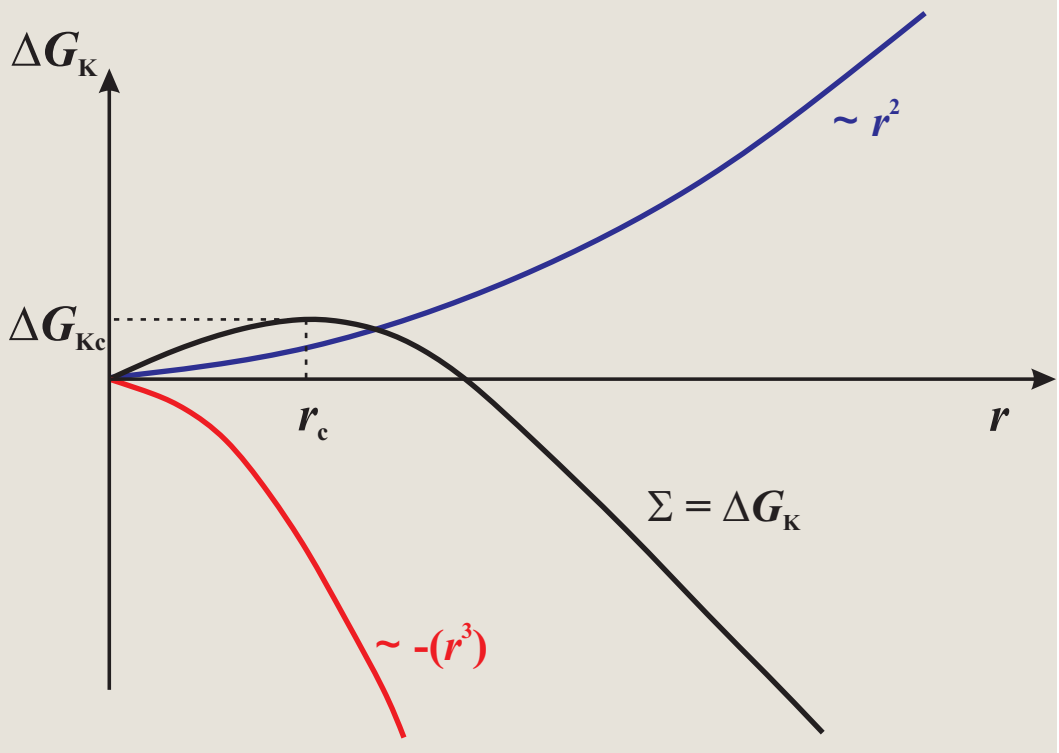

Figure 3.3: Plot of the Gibbs free energy for crystal formation (ΔG_K) versus the nuclei radius (r). Since the surface free energy term scales with r^2 and the free lattice energy term scales with $-r^3$, ΔG_K passes a maximum with the corresponding critical radius r_c.

a stable nucleus can be obtained by combining equations 3.1 and 3.3:

$$\Delta G_{Kc} = \frac{16\pi\gamma^3}{3(\Delta G_\nu)^2} = \frac{16\pi\gamma^3 V_m^2}{3(RT\ln S)^2} \tag{3.4}$$

Eventually, a large number of nuclei are formed simultaneously in a process, that can best be described as a nucleation "burst". As a consequence, the monomer concentration drops drastically below a point where no further nucleation is possible. The rate $\mathrm{d}N/\mathrm{d}t$, at which these nuclei are formed, can be expressed in an Arrhenius form:

$$\frac{\mathrm{d}N}{\mathrm{d}t} = A\exp\left[-\frac{\Delta G_{Kc}}{kT}\right] = A\exp\left[\frac{16\pi\gamma^3 V_m^2}{3(kT)^3(N_A\ln S)^2}\right] \tag{3.5}$$

Finally, in phase III, all nuclei grow at the same time, and, since their growth histories are identical, the NPs will end up having an exceptionally narrow size distribution.
However, it should be noted at this point, that this theory has been derived for microparticle systems and, although it is feasible to apply most of these considerations to nanoparticle models, caution must be taken and the statements must be judged critically, since the surface free energy γ is much higher in this size range, and therefore, cannot be considered to be constant.[50] In fact, the high ratio of surface atoms to bulk atoms in small NPs leads to a extremely high driving force of these particles to minimize the surface energy, which, consequently, results in uncontrolled growth and particle agglomeration.
The most common techniques to prevent these unwanted features use surfactant molecules to stabilize even the smallest NPs in solution. These molecules usually consist of a long hydrophobic hydrocarbon chain with a functional end group, that strongly attaches onto the surface of the regarding nanomaterial. Typical functional endgroups include phosphines, amines, thiols and carboxylates, and, as a result, a hydrophobic shell is formed around each particle, providing, not only, protection against oxidation, but also long-term stability in non-polar solvents.[3, 8, 16, 22, 51, 52]

3.2 Co-Precipitation

One of the most preferred methods to produce magnetite (Fe_3O_4), maghemite (γ-Fe_2O_3), and mixed ferrite (MFe_2O_4) nanoparticles is the co-precipitation of iron(II)-, iron(III), and other metal (M(II)) salts (e.g. chlorides, sulfates, nitrates) in aqueous solution by addition of a base (see Figure 3.4).[8, 55–57] The products of co-precipitation reactions, especially those performed at or near room temperature, are usually poorly crystalline, or even completely amorphous, requiring a subsequent annealing step, which makes particle agglomeration unavoidable. On the other hand, conducting the co-precipitation reaction at higher temperatures (50-100 °C) automatically leads to condensation of the precipitated metal hydroxides to form crystalline metal oxides.[53, 58] Depending on the metals salts used as starting materials, temperature, the Fe^{2+}/Fe^{3+} ratio and the pH, particles of different

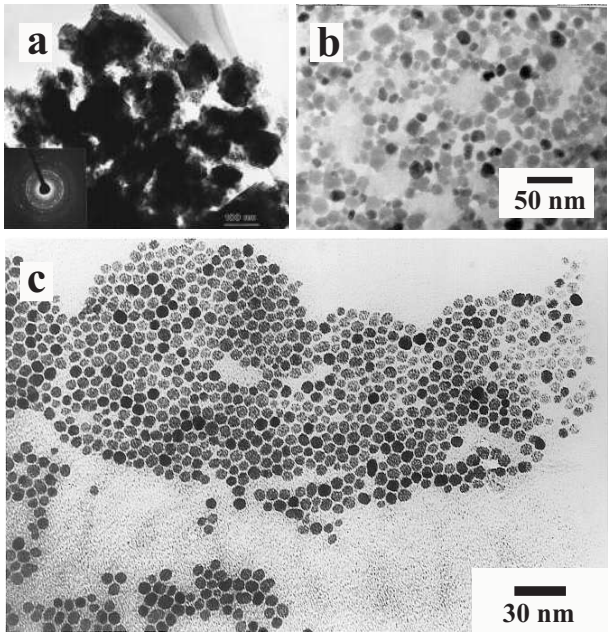

Figure 3.4: Magnetic NPs synthesized by the co-precipitation of metal salts in basic aqueous solution. (a) Mn-ferrite NPs.[53] (b) Co-ferrite NPs.[54] (c) Fe_3O_4 NPs.[55]

size, morphology, and composition can be produced in a highly reproducible fashion. Since Fe_3O_4 nanoparticles are subject to oxidation and dissolution in aqueous environment, controlled oxidation to the more stable maghemite (γ-Fe_2O_3) is often conducted as a follow-up step during nanoparticle synthesis. A better dispersibility in water can be obtained by subsequent acidification of the particle surface with nitric acid or by addition of tartrate ions, making the NPs stable in acidic and basic media over long periods of time.[54] The major advantages of this method are, once all parameters are set, the high reproducibility and high yields that can easily exceed multi kilogram amounts. Therefore, it is especially interesting for industrial scale applications.[9]

The major drawback, however, is a poor control of the size distribution. Since magnetization and blocking temperature strongly depend on nanoparticle size, a narrow size distribution is essential to fully exploit these properties in subsequent applications. Partial control over the size distribution can be achieved by addition of organic stabilizing agents, like polyvinyl pyrrolidone (PVP) or polyvinyl alcohol

(PVA), which cover the surface of the nanoparticles during the synthesis. Other authors have reported that the use of various organic salts like sodium citrate or tartrate can control the dispersity of the product (see Figure 3.4b).[54] The effects of several organic anions, such as carboxylate and hydroxy carboxylate ions, on the formation of iron oxides or oxyhydroxides have been studied extensively.[59] However, oleic acid is by far the most often used stabilizing agent for magnetic NPs.[60, 61]

3.3 Solvothermal/Hydrothermal Synthesis

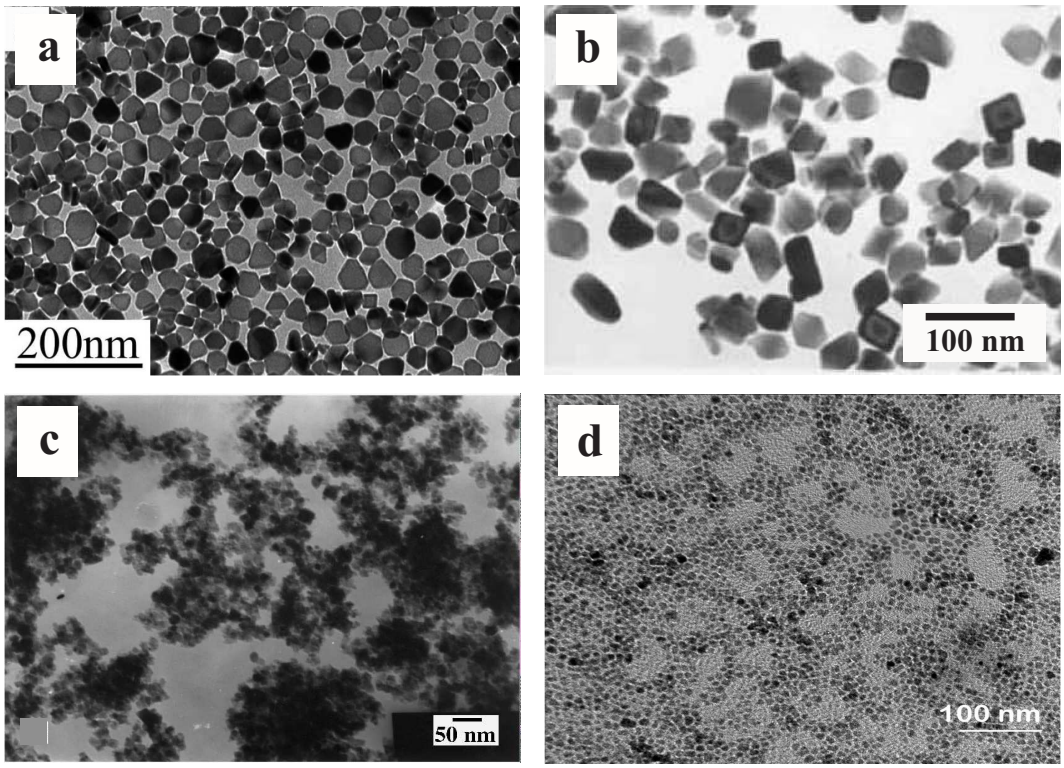

Figure 3.5: Magnetic NPs synthesized by hydro-/solvothermal reaction. (a) γ-Fe_2O_3 nanoplates synthesized from iron nitrate precursors in ethanol[62], (b) Mn_3O_4 NPs prepared from $KMnO_4$ in ethanol/water[63], (c) $ZnFe_2O_4$ NPs synthesized from zinc granules and ferric chloride in aqueous ammonia[64] and nearly monodisperse $NiFe_2O_4$ NPs prepared from the metal nitrates at a water-toluene interface with oleic acid as capping agent.[65]

Solvothermal/hydrothermal strategies have been used to produce a large variety of nanomaterials.[62–69] The key idea behind these processes is to bring the reaction mixture to temperatures well above the boiling point of the respective solvent. This is achieved by placing the mixture inside a sealed high-pressure reaction vessel (autoclave). In some cases the solvent is heated above its critical point, where it becomes a supercritical fluid. Supercritical fluids exhibit very high viscosities and are able to dissolve compounds that have a very low solubility under ambient conditions.[66] However, in most cases it is not necessary to heat the solvent above its critical point, because the solubility and reactivity of metal salts and complexes is high enough, even under more moderate subcritical conditions. In any event, solvothermal processing allows many inorganic materials to be prepared at temperatures well below those required by traditional solid-state reactions. Similar to the co-precipitation process, the addition of stabilizing molecules can control the particle morphology and significantly narrow the size distribution. The main advantage compared to other "low-temperature" procedures, like co-precipitation and sol-gel processing, are the very high crystallinity of the resulting nanomaterials. Detailed descriptions of the theory of solvothermal/hydrothermal processes can be found in recent review articles.[10, 66, 67, 70–72]

The solvothermal synthesis of magnetic metal oxide nanoparticles can be performed starting from different metal precursors. Fe_3O_4 nanoparticles with tunable sizes were prepared under hydrothermal conditions using $FeCl_2 \times 4H_2O$ and ammonia. Here, the size of the NPs could be controlled by variation of the reaction conditions.[73] On the other hand, Lu et *al.*[62] reported the solvothermal synthesis of nearly monodisperse γ-Fe_2O_3 nanoplates (see Figure 3.5a) by reacting a solution of $Fe(NO_3)_3 \times 9H_2O$ in absolute ethanol with PVP as stabilizing agent at 240 °C. Furthermore, monodisperse NPs of $M Fe_2O_4$ (M = Ni, Co, Mn) and γ-Fe_2O_3 were obtained at the water/toluene interface under conventional and microwave-assisted hydrothermal conditions using metal nitrates and chlorides and oleic acid as capping agent (see Figure 3.5d).[65] Monodisperse magnetite nanoparticles with an average size of 39 nm were synthesized by co-precipitation of ferrous Fe^{2+} and ferric Fe^{3+} ions in water with tetramethylammonium hydroxide ($N(CH_3)_4OH$) at 70 °C followed by hydrothermal treatment at 250 °C.[68] The use of hydrothermal techniques also allows the formation of unusual morphologies. Nanorings of

α-Fe_2O_3, γ-Fe_2O_3 and Fe_3O_4 were prepared by hydrothermal treatment of $FeCl_3$ with certain additives, like Na_2HPO_4 and Na_2SO_4, at 220 °C. The preformed α-Fe_2O_3 nanorings could easily be converted into γ-Fe_2O_3 and Fe_3O_4 by reduction in a hydrogen/argon atmosphere.[69] As a further example, larger nanoparticles of hausmannite (Mn_3O_4) and nanorods of manganese oxidehydroxide (MnOOH) were synthesized using $KMnO_4$ as precursor in a solution of water and ethanol (see Figure 3.5b).[53, 54, 58, 63, 69, 74–76] Among the metal complexes cupferronates are the most frequently used compounds. Ghosh et *al.*[32] reported the successful synthesis of 6-14 nm MnO and NiO nanoparticles by decomposing manganese cupferronate $Mn(C_6H_5N_2O_2)_2$ and nickel cupferronate $Ni(C_6H_5N_2O_2)_2$ in the presence of trioctylphosphine oxide (TOPO) as capping agent under solvothermal conditions.

3.4 Preparation within Micelles

Another strategy, that is often applied for the synthesis of magnetic nanoparticles, uses micelles as "nanoreactors" in (reverse) microemulsions. By definition, and in contrast to conventional emulsions, microemulsions are thermodynamically stable isotropic dispersions of two immiscible liquids, in which a mono-layered film of surfactant molecules stabilizes each microdomain of both liquids.[77–79] A special kind of dispersion is the water-in-oil microemulsion, where the aqueous phase is dispersed as microdroplets (typically 1-50 nm in diameter) in a non-polar hydrocarbon phase (e.g. cyclohexane).
As shown in Figure 3.6, the aqueous droplets themselves are surrounded by a stabilizing monolayer of surfactant molecules. Since the size and size distribution of the synthesized nanoparticles strongly depends on the diameter of the micelles, efficient control over the micelle radius is crucial to obtain high quality nanocrystals. It has been shown in the past, that the size of the reverse microdroplets can be adjusted by varying the molar ratio of water to surfactant:[80]

$$\omega_0 = [H_2O]/[S] \tag{3.6}$$

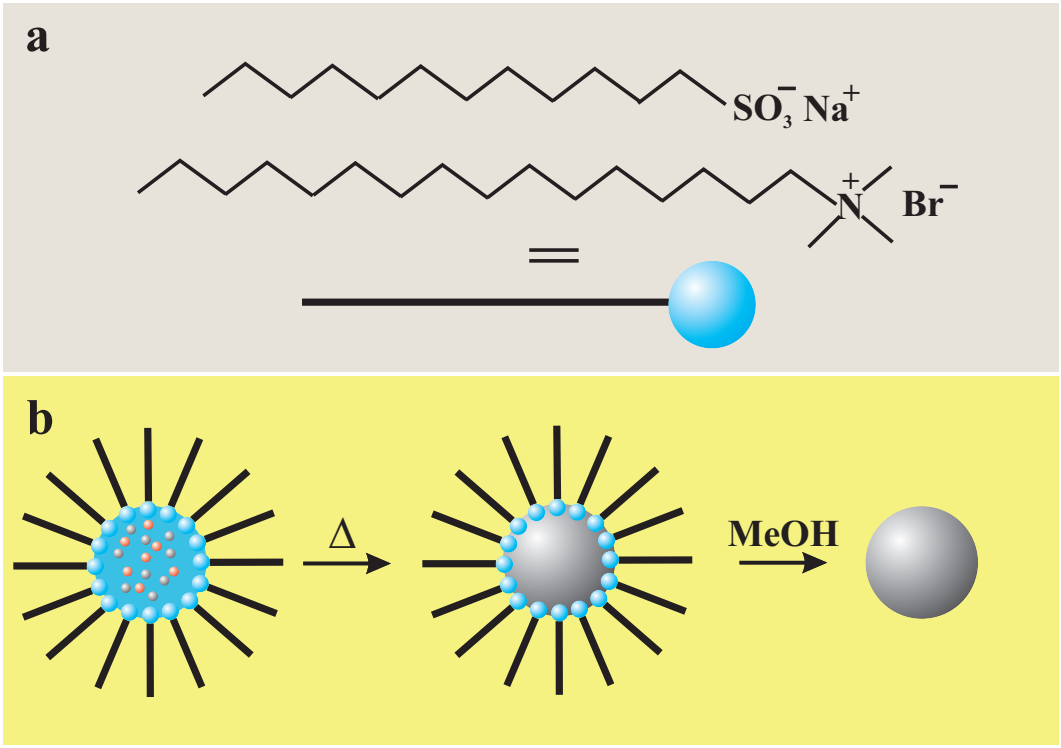

Figure 3.6: (a) Different surfactant molecules, such as SDS or CTAB can be used for the formation of reverse microemulsions. (b) Reaction scheme for the synthesis of NPs inside the micelles of a water-in-oil microemulsion. The micelles act as spatially confined "nanoreactors" in which the NPs are generated. Metal precursors (grey) are reduced by suitable reducing agents (red) at elevated temperatures. The micelles are subsequently disrupted by addition of polar solvents, such as methanol, after which the NPs can be collected by centrifugation.

To derive the micellar radius R_M one first has to consider the volume of each micelle, given by:

$$V = \frac{4\pi R_M^3}{3} = [\mathrm{S}]V_S + [\mathrm{H_2O}]V_W \tag{3.7}$$

in which, V_S and V_W are the volumes of surfactant and water, respectively. Conversion of equations 3.6 and 3.7 gives:

$$R_M = \frac{3V_S}{\Sigma_S} + \frac{3V_W\omega_0}{\Sigma_S} \tag{3.8}$$

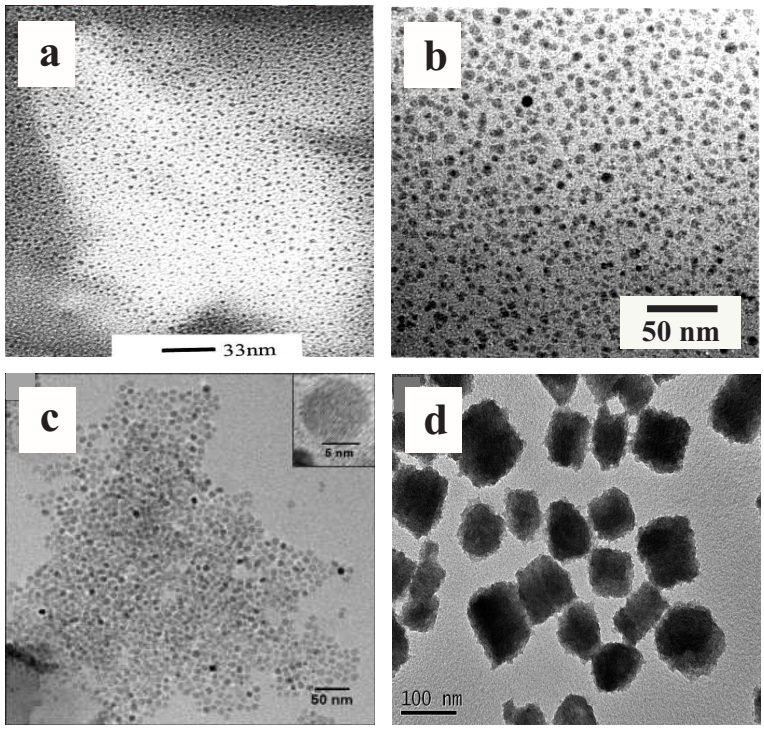

Figure 3.7: Magnetic NPs synthesized using micelles as "nanoreactors". (a) fcc Ni NPs prepared by reduction of nickel(II) chloride with hydrazine using a water-in-oil microemulsion of water/CTAB/*n*-hexanol [81], (b) $CoCrFeO_4$ NPs synthesized in a water/NaDBS/toluene reverse microemulsion using $CoCl_2 \times 6H_2O$, $CrCl_3 \times 6H_2O$ and $Fe(NO_3)_3 \times 9H_2O$ [82], (c) Fe_3O_4 NPs prepared in water/NaDBS/xylene with $FeCl_2 \times 4H_2O$ and $Fe(NO_3)_3 \times 9H_2O$ [83] and manganese-based nanoscale metal-organic frameworks coated with silica prepared through a combination of reverse microemulsion and microwave assisted techniques. [84]

Herein, Σ_S is the effective surface area of the surfactant-terminated micelle. With equation 3.8 a straight proportional relationship between the effective micelle radius R_M and the molar water-to-surfactant ratio ω_0 is evident. With this understanding, a precise control of the micelle size is possible.

In a stirred reverse microemulsion the micelles continuously collide, fuse, and break up again. Therefore, a reaction system containing two or more precursors in individual aqueous droplets will eventually lead to intimate mixing of the reactants and initiation of the reaction.[85] The nanoparticle formation itself is usually conducted at room temperature, but it can also be accelerated by heating the or-

ganic solvent to reflux.[81] After completion, the product can be isolated by breaking up the micelles with different solvents such as methanol or acetone followed by filtration or centrifugation. Commonly used surfactant molecules are either ionic, like cetyltrimethylammonium bromide (CTAB) or sodium dodecylbenzenesulfonate (NaDBS), or non-ionic, like Igepal CO-520 or Triton-X 100. In some cases an additional co-surfactant is also applied.

A vast variety of different nanoparticles have been synthesized using (reverse) micelles, ranging from metallic or intermetallic materials to quaternary metal oxides. Microemulsions, consisting of octane and hydrazine as reducing agent in water, with CTAB as surfactant and 1-hexanol as co-surfactant, were employed to create fcc-structured nickel nanoparticles (see Figure 3.7a).[81] Additionally, the large-scale synthesis of uniform magnetite (Fe_3O_4) nanoparticles was achieved by precipitation from ethanolic $FeCl_2$/$Fe(NO_3)_3$ solution in xylene with NaDBS under reflux conditions (see Figure 3.7c).[83] Ternary 3d metal oxides, $M$$Fe_2O_4$ (M = Mn, Co, Ni, Cu, Zn, Mg, or Cd, etc.), of the spinel structure are among the most important magnetic nanomaterials and have been widely used for various applications. A common approach for the synthesis of spinel ferrites comprises the combination of aqueous solutions of metal nitrates (e.g. $Mn(NO_3)_2$ and $Fe(NO_3)_3$) in toluene with NaDBS as surfactant,[86] and, as mentioned before, the average size of the resulting nanoparticles can be controlled by adjusting the molar ratio of water to surfactant. As shown in Figure 3.7b, even more complex metal oxide systems, like the quaternary $CoCrFeO_4$ could be synthesized by a similar approach using aqueous solutions of $CoCl_2$, $CrCl_3$ and $Fe(NO_3)_3$ in toluene with NaDBS.[82] A more exotic example was given by Xu et *al.*, who prepared $BaFe_{12}O_{19}$ nanocrystals in a microemulsion system consisting of CTAC, n-hexanol, water and cyclohexanol with $(NH_4)_2CO_3$ and NH_4OH as precipitants.[87] In contrast to that, a combination of reverse microemulsion and microwave assisted synthesis was recently used to produce manganese-based nanoscale metal-organic frameworks, which show promising properties for magnetic resonance imaging (MRI) (see Figure 3.7d).[84]

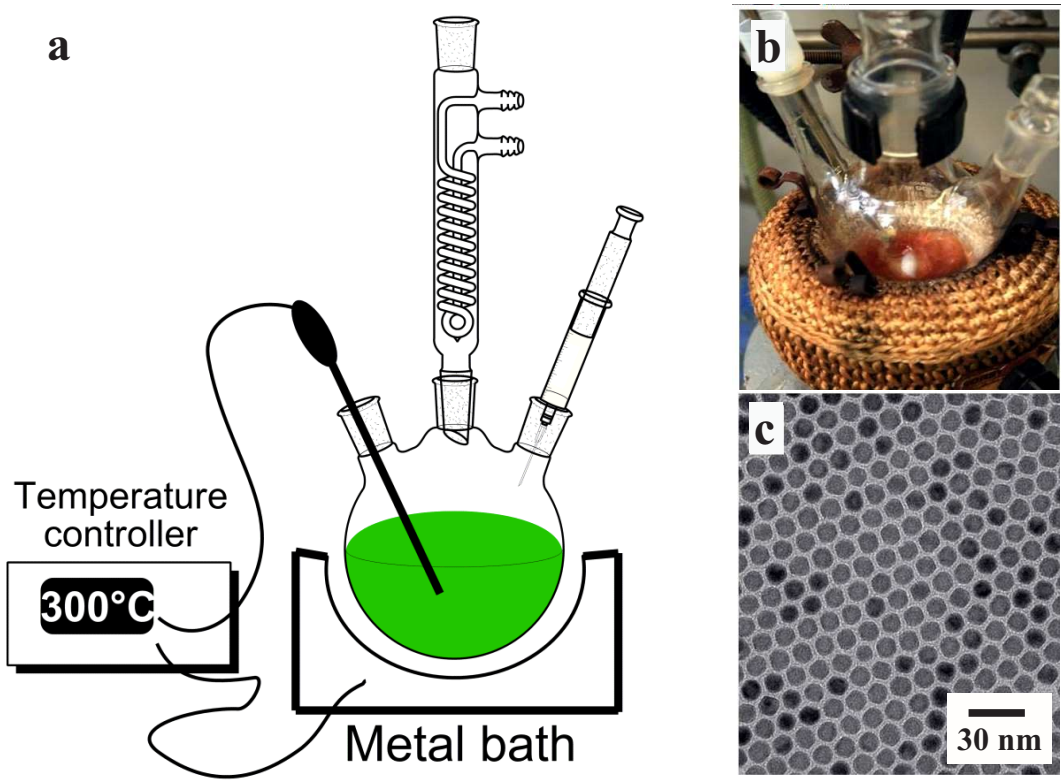

Figure 3.8: (a) Scheme of experimental setup for the synthesis of monodisperse NPs by decomposition of suitable metal precursors using a metal bath with temperature controller. (b) Photograph of laboratory setup using a conventional heating mantle. (c) TEM-image of as-prepared MnO NPs.

3.5 Thermal Decomposition and/or Reduction

The by far best results, for the reproducible synthesis of highly crystalline magnetic nanoparticles with a narrow size distribution, are obtained when metal-organic precursors are decomposed or metal salts are reduced in high-boiling non-polar solvents and in the presence of surfactant molecules. The key issue for the production of monodisperse nanoparticles, the separation of nucleation and growth according to the LaMer concept (see section 3.1),[47] can easily be achieved by controlling the basic experimental parameters like reaction temperature, heating time, heating rate, and concentrations of precursors and surfactants.[3] The required short nucleation burst can basically be initiated in two ways: either by injecting a cold precursor

solution into a hot mixture of solvent and surfactants, or by heating up a mixture of all components at the same time in a controlled fashion. The first method is based on the simultaneous formation of many nuclei when the precursor is injected.[89] In the second procedure, all reactants are mixed at room temperature and subsequently heated at a well defined heating rate, until the decomposition temperature of the precursor is reached. A typical laboratory set-up for the synthesis of monodisperse NPs is illustrated in Figure 3.8. Fortunately, this decomposition does not necessarily lead to the formation of nuclei, because a precise separation of nucleation and growth would be difficult, if not impossible. In some cases, the degradation of the precursor molecules rather leads to the formation of molecular clusters, that can be viewed as monomers for the generation of NPs. As the temperature rises, the concentration of these clusters increases until it reaches a critical point of supersaturation (see section 3.1). As a result, a large number of nuclei are formed, however, since the temperature only increases slowly, no considerable growth occurs. Once the reaction mixture has reached a temperature that allows sufficient growth, all particles grow at the same leading to a homogeneous size distribution.[90] In most cases particle growth can be stopped by rapidly reducing the temperature. For nanoparticles synthesized in this way the standard deviation of the size distribution (σ) is usually around 10%, however, further size selection techniques, like repetitive precipitation, can lower σ below 5%.[3, 90, 91] Some of the most popular precursors and additives for the synthesis of magnetic nanoparticles will be discussed in the following.

Among magnetic nanomaterials, metallic NPs show higher magnetization values than metal oxides. For the synthesis of metal NPs, zero-valent precursors, such as metal carbonyls are preferably used.[11, 92, 93] Fatty acids, long chain amines and thiols are generally used as surfactants to stabilize the as-prepared particles from oxidation and agglomeration.[35, 94, 95] For instance, Alivisatos et *al.*[96] were able to prepare monodisperse ϵ-Co nanoparticles by rapid pyrolysis of dicobalt octacarbonyl ($[Co_2(CO)_8]$) in the presence of a surfactant mixture containing oleic acid, lauric acid, and trioctylphosphine. The size of the particles could be controlled from 3-17 nm by adjusting the precursor/surfactant ratio, the temperature and the injection time. In fact, iron NPs were prepared by a similar method.[12] On the other hand, the reduction of metal salts with suitable reducing agents, like hydrides

or alcohols, can also lead to the formation of metal nanoparticles. Sun and Murray were among the first to synthesize metallic nanoparticles by a variety of methods, e.g. ϵ-Co NPs by injecting superhydride ($LiBEt_3H$) into a hot solution of $CoCl_2$ in octyl ether with oleic acid and trialkylphosphines as surfactants.[97] The size of the particles could be controlled by varying the chain length of the alkyl group in the trialkylphosphines. However, one of the most cited approaches for the synthesis of intermetallic NPs, is the preparation of monodisperse FePt NPs and their self-assembly into two- and three-dimensional superlattices (see Figure 3.9).

Precursors with cationic metal centers are preferably used for the synthesis of magnetic metal oxide nanoparticles. Yet, the preparation of metal nanoparticles followed by mild oxidation is also applied in some cases. For instance, monodisperse maghemite nanoparticles have been synthesized by injecting iron pentacarbonyl ($Fe(CO)_5$) into a hot solution of oleic acid, oleylamine and 1,2-hexadecandiol in octyl ether. The initially formed Fe nanoparticles were subsequently oxidized by addition of trimethylamine oxide ($(CH_3)_3NO$) as mild oxidant.[11] However, metal organic compounds, such as formates,[21] acetates,[20] and acetylacetonates[19]

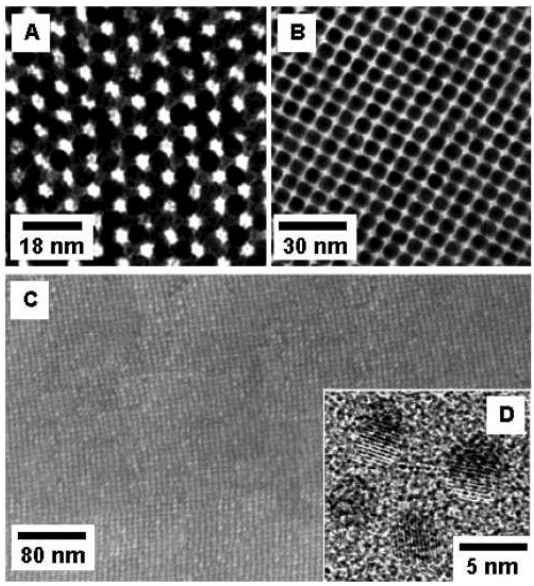

Figure 3.9: (A) and (B) TEM images of three-dimensional assemblies of 6 nm as-synthesized $Fe_{50}Pt_{50}$ NPs. (C) HRSEM image of a $\approx$ 180 nm thick layer of assembled 4 nm $Fe_{52}Pt_{48}$ nanocrystals. (D) HRTEM image of 4 nm $Fe_{52}Pt_{48}$ NPs.[36]

have evolved as the most common precursors for the preparation of metal oxide particles.

Inspired by the idea, that during the heating procedure a complex of the metal ion and the surfactant is formed, a new strategy was recently proposed.[22, 25, 35] By directly using a pre-prepared metal-surfactant complex, a much better control over the reaction process was obtained. In this way, highly crystalline nanoparticles of different metal oxides with exceptionally narrow size distribution ($\sigma \leq 5\%$) were synthesized. As an example, Figure 3.10 shows monodisperse manganese oxide (MnO) NPs synthesized by decomposition of a manganese oleate precursor in 1-octadecene. Due to their exceptionally narrow size distribution they self-assemble to form two-dimensional and even three-dimensional superlattices.

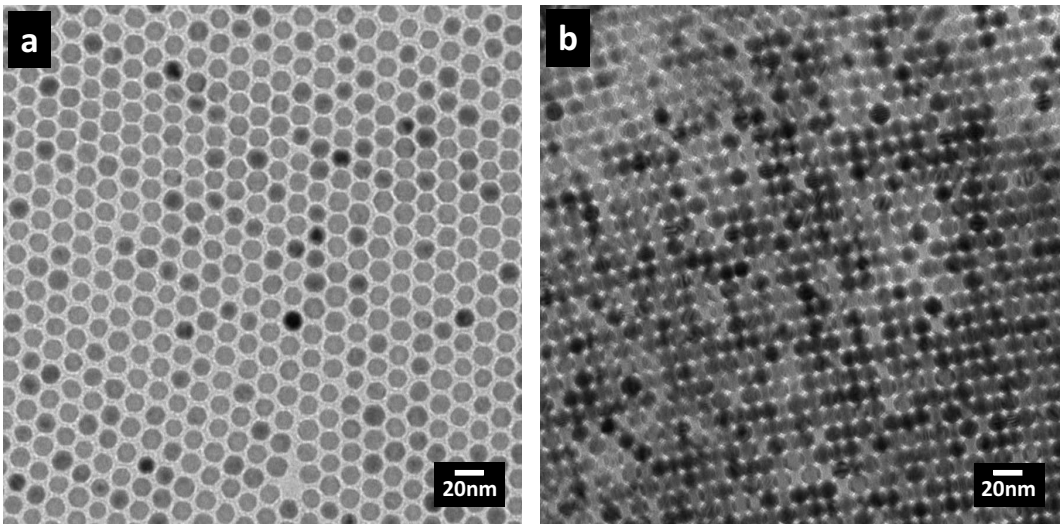

Figure 3.10: (a) Two- and (b) three-dimensional superlattices of monodisperse MnO NPs. the NPs were prepared by the decomposition of Mn oleate in 1-octadecene.

3.6 References

[1] Schmid, G. *Nanoparticles: From theory to application*, 4th ed.; Wiley-VCH: Weinheim, 2006.

[2] Klabunde, K. J. *Nanoscale materials in chemistry*; Wiley-Interscience: New York, NY, 2001.

[3] Hyeon, T. *Chemical Communications* **2003**, 927–934.

[4] O'Handley, R. C. *Modern magnetic materials: Principles and applications*; Wiley: New York, NY, 2000.

[5] Park, J.; Joo, J.; Kwon, S.; Jang, Y.; Hyeon, T. *Angewandte Chemie International Edition* **2007**, *46*, 4630–4660.

[6] Herzer, G. *IEEE Transactions on Magnetics* **1989**, *25*, 3327–3329.

[7] Skorvánek, I.; O'Handley, R. C. *Journal of Magnetism and Magnetic Materials* **1995**, *140-144*, 467–468.

[8] Cheon, J.; Kang, N.-J.; Lee, S.-M.; Lee, J.-H.; Yoon, J.-H.; Oh, S. J. *Journal of the American Chemical Society* **2004**, *126*, 1950–1951.

[9] Lu, A.-H.; Salabas, E. L.; Schüth, F. *Angewandte Chemie International Edition* **2007**, *46*, 1222–1244.

[10] Lu, A.-H.; Salabas, E. L.; Schüth, F. *Angewandte Chemie* **2007**, *119*, 1242–1266.

[11] Hyeon, T.; Lee, S. S.; Park, J.; Chung, Y.; Na, H. B. *Journal of the American Chemical Society* **2001**, *123*, 12798–12801.

[12] Farrell, D.; Majetich, S. A.; Wilcoxon, J. P. *Journal of Physical Chemistry B* **2003**, *107*, 11022–11030.

[13] Peng, S.; Wang, C.; Xie, J.; Sun, S. *Journal of the American Chemical Society* **2006**, *128*, 10676–10677.

[14] Grass, R.; Athanassiou, E.; Stark, W. *Angewandte Chemie International Edition* **2007**, *46*, 4909–4912.

[15] Chen, D.-H.; Hsieh, C.-H. *Journal of Materials Chemistry* **2002**, *12*, 2412–2415.

[16] Sun, S.; Zeng, H.; Robinson, D. B.; Raoux, S.; Rice, P. M.; Wang, S. X.; Li, G. *Journal of the American Chemical Society* **2004**, *126*, 273–279.

[17] Bao, N.; Shen, L.; Wang, Y.; Padhan, P.; Gupta, A. *Journal of the American Chemical Society* **2007**, *129*, 12374–12375.

[18] Yavuz, C. T.; Mayo, J. T.; Yu, W. W.; Prakash, A.; Falkner, J. C.; Yean, S.; Cong, L.; Shipley, H. J.; Kan, A.; Tomson, M.; Natelson, D.; Colvin, V. L. *Science* **2006**, *314*, 964–967.

[19] Seo, W. S.; Jo, H. H.; Lee, K.; Kim, B.; Oh, S. J.; Park, J. T. *Angewandte Chemie International Edition* **2004**, *43*, 1115–1118.

[20] Yin, M.; O'Brien, S. *Journal of the American Chemical Society* **2003**, *125*, 10180–10181.

[21] Zhong, X.; Xie, R.; Sun, L.; Lieberwirth, I.; Knoll, W. *Journal of Physical Chemistry B* **2006**, *110*, 2–4.

[22] Park, J.; An, K.; Hwang, Y.; Park, J. G.; Noh, H. J.; Kim, J. Y.; Park, J. H.; Hwang, N. M.; Hyeon, T. *Nature Materials* **2004**, *3*, 891–895.

[23] Park, J.; Joo, J.; Kwon, S. G.; Jang, Y.; Hyeon, T. *Angewandte Chemie International Edition* **2007**, *46*, 4630–4660.

[24] Chen, Y.; Johnson, E.; Peng, X. *Journal of the American Chemical Society* **2007**, *129*, 10937–10947.

[25] Schladt, T. D.; Graf, T.; Tremel, W. *Chemistry of Materials* **2009**, *21*, 3183–3190.

[26] Jiao, F.; Harrison, A.; Bruce, P. *Angewandte Chemie* **2007**, *119*, 4020–4024.

[27] Verelst, M.; Ely, T. O.; Amiens, C.; Snoeck, E.; Lecante, P.; Mosset, A.; Respaud, M.; Broto, J. M.; Chaudret, B. *Chemistry of Materials* **1999**, *11*, 2702–2708.

[28] He, T.; Chen, D.; Jiao, X.; Wang, Y.; Duan, Y. *Chemistry of Materials* **2005**, *17*, 4023–4030.

[29] Ghosh, M.; Sampathkumaran, E. V.; Rao, C. N. R. *Chemistry of Materials* **2005**, *17*, 2348–2352.

[30] Seo, W. S.; Shim, J. H.; Oh, S. J.; Lee, E. K.; Hur, N. H.; Park, J. T. *Journal of the American Chemical Society* **2005**, *127*, 6188–6189.

[31] Carnes, C. L.; Stipp, J.; Klabunde, K. J.; Bonevich, J. *Langmuir* **2002**, *18*, 1352–1359.

[32] Ghosh, M.; Biswas, K.; Sundaresan, A.; Rao, C. N. R. *Journal of Materials Chemistry* **2006**, *16*, 106–111.

[33] Zeng, H.; Rice, P. M.; Wang, S. X.; Sun, S. *Journal of the American Chemical Society* **2004**, *126*, 11458–11459.

[34] Song, Q.; Zhang, Z. *Journal of the American Chemical Society* **2004**, *126*, 6164–6168.

[35] Jana, N. R.; Chen, Y.; Peng, X. *Chemistry of Materials* **2004**, *16*, 3931–3935.

[36] Sun, S.; Murray, C. B.; Weller, D.; Folks, L.; Moser, A. *Science* **2000**, *287*, 1989–1992.

[37] Shevchenko, E.; Talapin, D.; Kornowski, A.; Wiekhorst, F.; Kötzler, J.; Haase, M.; Rogach, A.; Weller, H. *Advanced Materials* **2002**, *14*, 287–290.

[38] Varanda, L. C.; Jafelicci, M. *Journal of the American Chemical Society* **2006**, *128*, 11062–11066.

[39] Sun, S. *Advanced Materials* **2006**, *18*, 393–403.

[40] Chen, M.; Liu, J.; Sun, S. *Journal of the American Chemical Society* **2004**, *126*, 8394–8395.

[41] Liu, C.; Wu, X.; Klemmer, T.; Shukla, N.; Yang, X.; Weller, D.; Roy, A. G.; Tanase, M.; Laughlin, D. *Journal of Physical Chemistry B* **2004**, *108*, 6121–6123.

[42] Li, Y.; Zhang, X. L.; Qiu, R.; Qiao, R.; Kang, Y. S. *Journal of Physical Chemistry C* **2007**, *111*, 10747–10750.

[43] Song, H. M.; Kim, Y. J.; Park, J. H. *Journal of Physical Chemistry C* **2008**, *112*, 5397–5404.

[44] Shevchenko, E. V.; Talapin, D. V.; Rogach, A. L.; Kornowski, A.; Haase, M.; Weller, H. *Journal of the American Chemical Society* **2002**, *124*, 11480–11485.

[45] Shevchenko, E. V.; Talapin, D. V.; Schnablegger, H.; Kornowski, A.; Festin, A.; Svedlindh, P.; Haase, M.; Weller, H. *Journal of the American Chemical Society* **2003**, *125*, 9090–9101.

[46] van Embden, J.; Sader, J. E.; Davidson, M.; Mulvaney, P. *Journal of Physical Chemistry C* **2009**, *113*, 16342–16355.

[47] LaMer, V. K.; Dinegar, R. H. *Journal of the American Chemical Society* **1950**, *72*, 4847–4854.

[48] Sugimoto, T. *Monodispersed particles*, 1st ed.; Elsevier: Amsterdam, New York, 2001.

[49] Vossmeyer, T.; Katsikas, L.; Giersig, M.; Popovic, I. G.; Diesner, K.; Chemseddine, A.; Eychmueller, A.; Weller, H. *J. Phys. Chem. (Journal of Physical Chemistry)* **1994**, *98*, 7665–7673.

[50] Alivisatos, A. *J. Phys. Chem. (Journal of Physical Chemistry)* **1996**, *100*, 13226–13239.

[51] Rockenberger, J.; Scher, E. C.; Alivisatos, A. P. *Journal of the American Chemical Society* **1999**, *121*, 11595–11596.

[52] Jun, Y.-w.; Choi, J.-s.; Cheon, J. *Chemical Communications* **2007**, *43*, 1203–1214.

[53] Zhang, Z.; Wang, Z. L.; Chakoumakos, B. C.; Yin, J. S. *Journal of the American Chemical Society* **1998**, *120*, 1800–1804.

[54] Neveu, S.; Bee, A.; Robineau, M.; Talbot, D. *Journal of Colloid and Interface Science* **2002**, *255*, 293–298.

[55] Kang, Y. S.; Risbud, S.; Rabolt, J. F.; Stroeve, P. *Chemistry of Materials* **1996**, *8*, 2209–2211.

[56] Kuo, P. C.; Tsai, T. S. *Journal of Applied Physics* **1989**, *65*, 4349–4356.

[57] Hong, C.-Y.; Jang, I. J.; Horng, H. E.; Hsu, C. J.; Yao, Y. D.; Yang, H. C. *Journal of Applied Physics* **1997**, *81*, 4275–4277.

[58] Fried, T.; Shemer, G.; Markovich, G. *Advanced Materials* **2001**, *13*, 1158–1161.

[59] Lu, X.; Niu, M.; Qiao, R.; Gao, M. *Journal of Physical Chemistry B* **2008**, *112*, 14390–14394.

[60] Cushing, B. L.; Kolesnichenko, V. L.; O'Connor, C. J. *Chemical Reviews* **2004**, *104*, 3893–3946.

[61] Willis, A. L.; Turro, N. J.; O'Brien, S. *Chemistry of Materials* **2005**, *17*, 5970–5975.

[62] Lu, J.; Jiao, X.; Chen, D.; Li, W. *Journal of Physical Chemistry C* **2009**, *113*, 4012–4017.

[63] Zhang, W.; Yang, Z.; Liu, Y.; Tang, S.; Han, X.; Chen, M. *Journal of Crystal Growth* **2004**, *263*, 394–399.

[64] Rath, C.; Sahu, K.; Anand, S.; Date, S.; Mishra, N.; Das, R. *Journal of Magnetism and Magnetic Materials* **1999**, *202*, 77–84.

[65] Baruwati, B.; Nadagouda, M. N.; Varma, R. S. *Journal of Physical Chemistry C* **2008**, *112*, 18399–18404.

[66] Cansell, F.; Chevalier, B.; Demourgues, A.; Etourneau, J.; Even, C.; Pessey, V.; Petit, S.; Tressaud, A.; Weill, F. *Journal of Materials Chemistry* **1999**, *9*, 67–75.

[67] Gautam, U. K.; Ghosh, M.; Rajamathi, M.; Seshadri, R. *Pure and Applied Chemistry* **2002**, *74*, 1643–1649.

[68] Daou, T.; Pourroy, G.; Bégin-Colin, S.; Grenéche, J.; Ulhaq-Bouillet, C.; Legare, P.; Bernhardt, P.; Leuvrey, C.; Rogez, G. *Chemistry of Materials* **2006**, *18*, 4399–4404.

[69] Jia, C.-J. et al. *Journal of the American Chemical Society* **2008**, *130*, 16968–16977.

[70] Rajamathi, M.; Seshadri, R. *Current Opinion in Solid State and Materials Science* **2002**, *6*, 337–345.

[71] Demazeau, G. *Journal of Materials Chemistry* **1999**, *9*, 15–18.

[72] Willard, M. A.; Kurihara, L. K.; Carpenter, E. E.; Calvin, S.; Harris, V. G. *International Materials Reviews* **2004**, *49*, 125–170.

[73] Ge, S.; Shi, X.; Sun, K.; Li, C.; Uher, C.; Baker, J. R.; Banaszak Holl, M. M.; Orr, B. G. *Journal of Physical Chemistry C* **2009**, *113*, 13593–13599.

[74] Lee, J.; Isobe, T.; Senna, M. *Colloids and Surfaces A: Physicochemical and Engineering Aspects* **1996**, *109*, 121–127.

[75] Willis, A. L.; Turro, N. J.; O'Brien, S. *Chemistry of Materials* **2005**, *17*, 5970–5975.

[76] Lu, X.; Niu, M.; Qiao, R.; Gao, M. *Journal of Physical Chemistry B* **2008**, *112*, 14390–14394.

[77] Hoar, T. P.; Schulman, J. H. *Nature* **1943**, *152*, 102–103.

[78] Gillberg, G.; Lehtinen, H.; Friberg, S. *Journal of Colloid and Interface Science* **1970**, *33*, 40–53.

[79] Langevin, D. *Annual Review of Physical Chemistry* **1992**, *43*, 341–369.

[80] Paul, B. K.; Moulik, S. P. *Current Science* **2001**, *80*, 990–1001.

[81] Chen, D.-H.; Wu, S.-H. *Chemistry of Materials* **2000**, *12*, 1354–1360.

[82] Vestal, C. R.; Zhang, Z. *Chemistry of Materials* **2002**, *14*, 3817–3822.

[83] Lee, Y.; Lee, J.; Bae, C. J.; Park, J.-G.; Noh, H.-J.; Park, J.-H.; Hyeon, T. *Advanced Functional Materials* **2005**, *15*, 503–509.

[84] Taylor, K. M.; Rieter, W. J.; Lin, W. *Journal of the American Chemical Society* **2008**, *130*, 14358–14359.

[85] Gupta, A. K.; Gupta, M. *Biomaterials* **2005**, *26*, 3995–4021.

[86] Liu, C.; Zou, B.; Rondinone, A. J.; Zhang, Z. *Journal of Physical Chemistry B* **2000**, *104*, 1141–1145.

[87] Xu, P.; Han, X.; Wang, M. *Journal of Physical Chemistry C* **2007**, *111*, 5866–5870.

[88] LaMer, V. K.; Dinegar, R. H. *Journal of the American Chemical Society* **1950**, *72*, 4847–4854.

[89] Murray, C. B.; Norris, D. J.; Bawendi, M. *Journal of the American Chemical Society* **1993**, *115*, 8706–8715.

[90] Puntes, V. F.; Krishnan, K. M.; Alivisatos, A. *Science* **2001**, *291*, 2115–2117.

[91] Stoeva, S.; Klabunde, K. J.; Sorensen, C. M.; Dragieva, I. *Journal of the American Chemical Society* **2002**, *124*, 2305–2311.

[92] Dinega, D. P.; Bawendi, M. *Angewandte Chemie International Edition* **1999**, *38*, 1788–1791.

[93] Redl, F. X.; Black, C. T.; Papaefthymiou, G. C.; Sandstrom, R. L.; Yin, M.; Zeng, H.; Murray, C. B.; O'Brien, S. P. *Journal of the American Chemical Society* **2004**, *126*, 14583–14599.

[94] Murray, C. B.; Kagan, C. R.; Bawendi, M. *Annual Review of Materials Science* **2000**, *30*, 545–610.

[95] Samia, A. C. S.; Hyzer, K.; Schlueter, J. A.; Qin, C.-J.; Jiang, J. S.; Bader, S. D.; Lin, X.-M. *Journal of the American Chemical Society* **2005**, *127*, 4126–4127.

[96] Puntes, V. F.; Krishnan, K. M.; Alivisatos, P. *Applied Physics Letters* **2001**, *78*, 2187–2189.

[97] Sun, S.; Murray, C. B. *Journal of Applied Physics* **1999**, *85*, 4325–4330.

CHAPTER 4

Colloidal Nano-*hetero*-Structures

One of the most exciting aspects of nanoparticle synthesis is the possibility to expand the preparation techniques from single-component NPs to multi-component hybrid nano-*hetero*-structures consisting of several individual domains.[1] Combining different materials on a nanometer length scale opens numerous new opportunities, e.g. the realization of multifunctionality, the combination/enhancement of individual physical and chemical properties, or the presence of separately addressable surfaces, and therefore, directed self-assembly by binding different ligands to the concerning surfaces. As an example, alternating nanoscale layers of metal and magnetic domains gave rise to giant magnetoresistance (GMR), a property which is now intensively employed in hard disk drive read heads.[2] Therefore, integrating separate, intrinsically different, functionalities represents a exceedingly powerful way to create novel functional materials with convergent properties found in neither of the constituents.

4.1 Synthesis of Colloidal Nano-*hetero*-Particles

There are many different ways to prepare nano-*hetero*-structures, including seed mediated growth or heat-induced phase segregation. However, herein the focus will be devoted to the formation of nano-*hetero*-particles through heterogeneous nucleation on suitable seeds. Generally, there are two different approaches to prepare these structures in solution:

- (1) either by a two-step technique, where one of the components is prepared separately in advance and acts as seed material for the nucleation of the second constituent in a second reaction step, or
- (2) by a one-step method, in which the seeds of the first component are generated *in situ* followed by seed-mediated nucleation of the second material in the same reaction solution.[3]

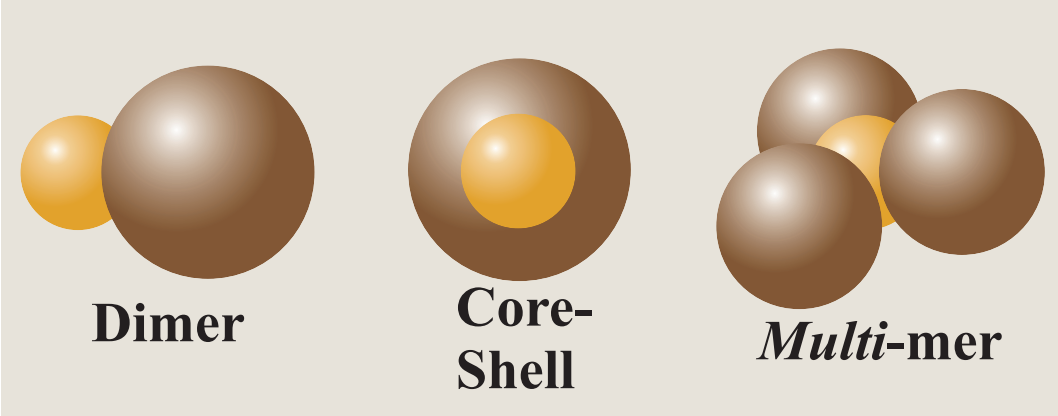

Figure 4.1: By tuning the reaction conditions different morphologies of colloidal nano-*hetero*-particles are possible.

However, the first technique is the most often applied approach. A variety of different *hetero*-morphologies is obtainable with these techniques. Depending on the lattice match and the interfacial energy of the regarding materials the achievable shapes range from symmetric core-shell NPs to non-symmetric *hetero*-dimers, and other multicomponent *hetero*-structures (see Figure 4.1). Although it is generally

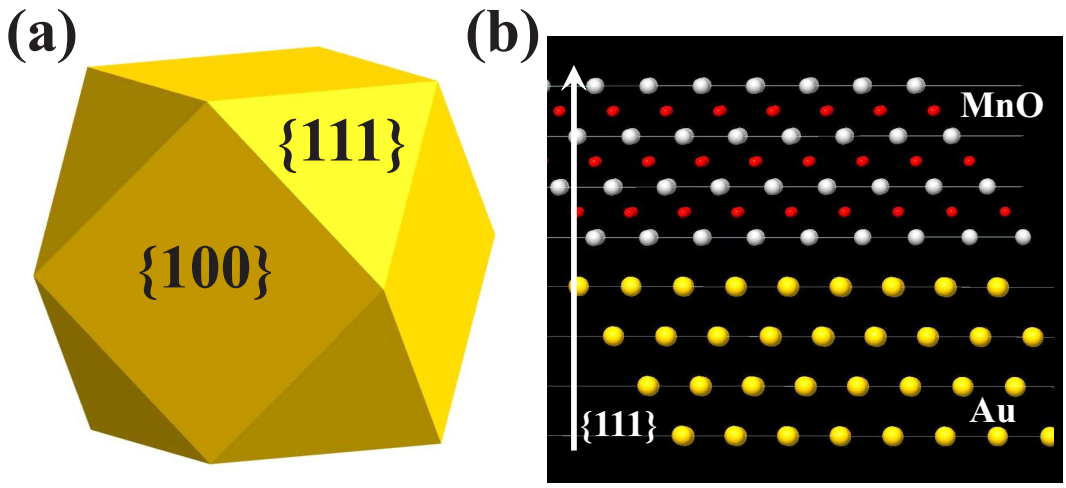

Figure 4.2: (a) The different crystal faces on a Au NP. (b) Epitaxial relationship between Au and MnO along the $\{111\}$ direction.

possible to create nano-*hetero*-particles with a considerable lattice mismatch between the individual constituents, the combination of two materials with sufficient matching of the lattice *d*-spacing is definitely preferred. As an example, Figure 4.2 displays the crystallographic relationship between Au and MnO. Basically, a Au seed particle exhibits definite crystal faces on which a nucleation of MnO can occur, however, only faces with matching d-spacing permit the formation and epitaxial growth of a MnO domain. In the case of Au@MnO, the distance between the $\{111\}$ lattice planes are similar in both materials, allowing nucleation and growth in the corresponding crystallographic direction.

A successful preparation of nano-*hetero*-particles depends substantially on promoting heterogeneous nucleation while at the same time suppressing homogeneous nucleation, since the latter would lead to the formation of separate NPs. Suppression of homogeneous nucleation can be obtained by keeping the precursor concentration under the critical supersaturation value (see section 3.1). This can be achieved by precise control of the precursor ratio, amount of seed particles and the heating profile. Although the exact mechanisms are not yet fully understood, it has to be estimated that an approximate matching between the crystal lattices of the individual constituents is necessary to ensure epitaxial growth of the second component. Furthermore, the seed particles can act as catalysts for the growth of the second

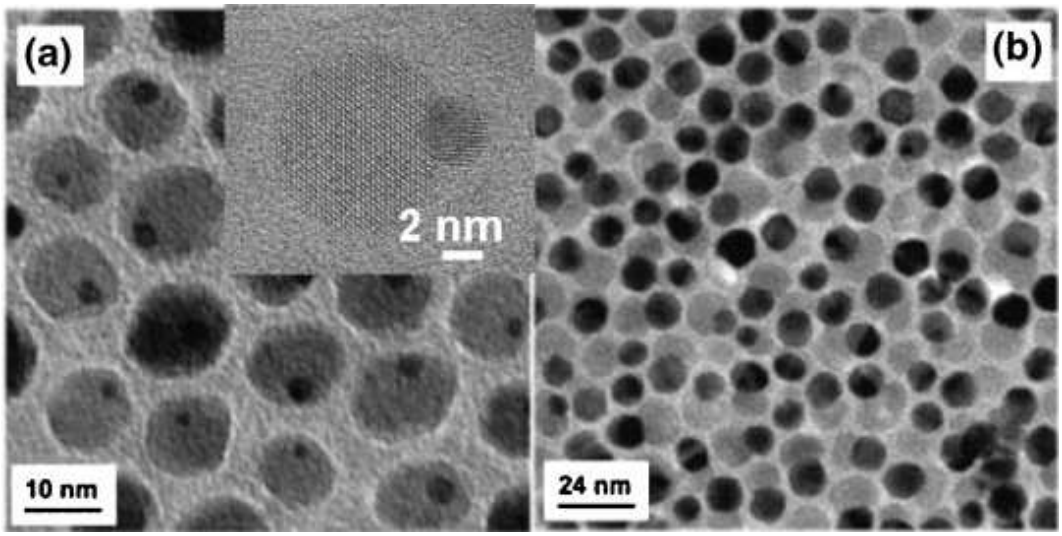

Figure 4.3: TEM images of (a) 3-14 nm and (b) 8-14 nm Au@Fe_3O_4 nano-*hetero*-dimers. The HRTEM image in the sinset of (a) demonstraties the coherent interface between Au and Fe_3O_4.[5]

domain when a transfer of electron density to the newly nucleated components is involved, because in this case, the energy for heterogeneous nucleation is lowered. The general prerequisites and possible reaction pathways leading to colloidal nano-*hetero*-particles are depicted in Figures 4.4 and 4.6.

4.1.1 Dimer Nanoparticles

The simplest conceivable structure consisting of two individual materials is a dimer, in which two joined NPs share a common interface. The question which automatically arises is how to control the formation of only one domain on the seed NP, i.e. how can additional nucleation on the surface of the seed be prevented? In deed, various reports describe the preparation of nano-*hetero*-dimers and emphasize the importance of controlling the experimental parameters.[4–7] A typical example for Au-Fe_3O_4 nanodimers is shown in Figure 4.3. However, the essence of all techniques can be brought down to controlling the polarity of the solvent. In this respect, "polarity" must be equaled to the ability to provide electron density. As mentioned above, a certain amount of electron density is necessary for the heterogeneous nu-

cleation of a second material on the seed NP. During the nucleation process electron density is withdrawn from the metallic core and transferred to the growing nucleus (see Figure 4.4). In fact, this phenomenon can be observed in Au@Fe_3O_4 nano-*hetero*-particles, as a red-shift in the absorption maximum compared to bare Au NPs (see section 4.2.2 for further explanation). As a result, the electron density in the seed is depleted and no further nucleation is possible. This mechanism has been proposed, not only for Au@Fe_3O_4, but also for Au@PbS and Au@MnO nano-*hetero*-particles, where the authors suppose an electron transfer from the Au to the Fe_3O_4, PbS and MnO domain, respectively.[5, 8, 9] As demonstrated in Figure 4.4, if a non-polar (i.e. electron-poor) solvent, such as 1-octadecene or dioctyl ether, is used for the synthesis, the electron deficiency on the Au seed cannot be replenished by the solvent, and therefore, additional nucleation events are prevented leading to nano-*hetero*-dimer NPs. For example, Yu et *al.* prepared Au-Fe_3O_4 dimers by injecting $Fe(CO)_5$ into a hot solution of pre-synthesized Au seeds in 1-octadecene.[5] The size-ratio between both domains could be varied by changing the amount of iron precursor. In a similar way, we were able to produce *hetero*-dimer NPs of Pt@Fe_3O_4, Au@Fe_3O_4, Pt@MnO and FePt@MnO (see Figure 4.7).
Alternative approaches involve the preliminary formation of a metastable core-shell NP structure followed by the generation of dimers by thermal annealing, as demonstrated for FePt@CdS *hetero*-dimers.[10] However, this procedure requires a considerable lattice mismatch between both materials.

4.1.2 Core-Shell Nanoparticles

Although dimers constitute the simplest nano-*hetero*-structures, core-shell NPs are the most extensively studied type of multicomponent NPs. They were initially introduced for semiconductor nanocrystals in the 1990's, by Bawendi, Alivisatos and coworkers,[14–16] but also received a lot of interest for magnetic composites, e.g. consisting of metal cores and metal oxide shells.[7]
The main synthetic principles mentioned above can also be applied for core-shell NPs, however, with the difference that additional nucleation on the seed surface is desired. For this purpose the preparation parameters must be varied to compensate the electron deficiency in the metal seed. The most often used approach is to use a

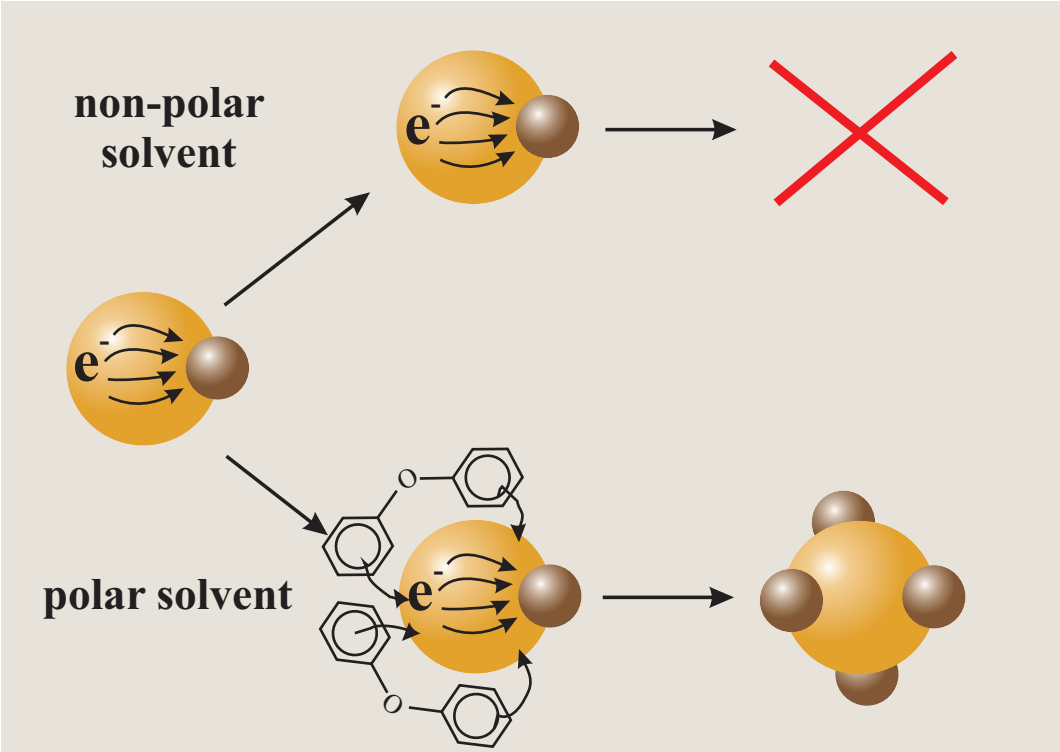

Figure 4.4: The solvent effect during the synthesis of nano-hetero-particles. Non-polar solvents cannot compensate the deficient electron density on the seed metal NP, therefore no further nucleation is possible. Polar (electron rich) solvents can transfer electron density to the metal particle permitting the formation of additional nuclei. Adapted from Ref.[11].

solvent which, by itself, carries a sufficient amount of electron density, that can be transferred to the metal surface (see Figure 4.4). Ideal solvents for this purpose comprise high boiling point compounds with a vast delocalized π-electron system, such as benzyl ether or phenyl ether. As soon as a nucleus is formed on the seed, the withdrawn electron density can be compensated, which then allows further nucleation on the surface. Subsequently, the growth of the nuclei leads to the coalescence of the metal oxide domains and finally to the formation of shell around the metal core.[11] As an example, Zeng et *al.* created bimagnetic FePt@Fe_3O_4 core-shell NPs by decomposing $Fe(acac)_3$ in the presence of preformed FePt seeds using phenyl ether as a solvent (See Figure 4.5a-c).[12] The authors showed, that the shell thickness is tunable by varying the amount of the precursor. In a similar way Kang et al.

were able to create FePt@MnO core-shell nanostructures (see Figure 4.5e-h).[13] Other core-shell nanostructures with a variety of material combinations, ranging from metallic-magnetic Pt@Fe_2O_3, metallic-semiconducting Au@PbS, Au@PbSe and Au@CdS and semiconducting-magnetic PbS@Fe_3O_4, were also prepared by similar approaches.[8, 17]

Alternatively, core-shell NPs with magnetic metal oxide cores and metallic shells have also been prepared. For example, Sun and coworkers synthesized Fe_3O_4@Au core-shell NPs by reducing $HAuCl_4$ onto pre-synthesized Fe_3O_4 NPs in the presence of oleylamine. The key issue here is to prevent the spontaneous homogeneous nucleation of Au. Therefore, the synthesis was carried out at room temperature and oleylamine was used, both as surfactant and as a mild reducing agent.[18]

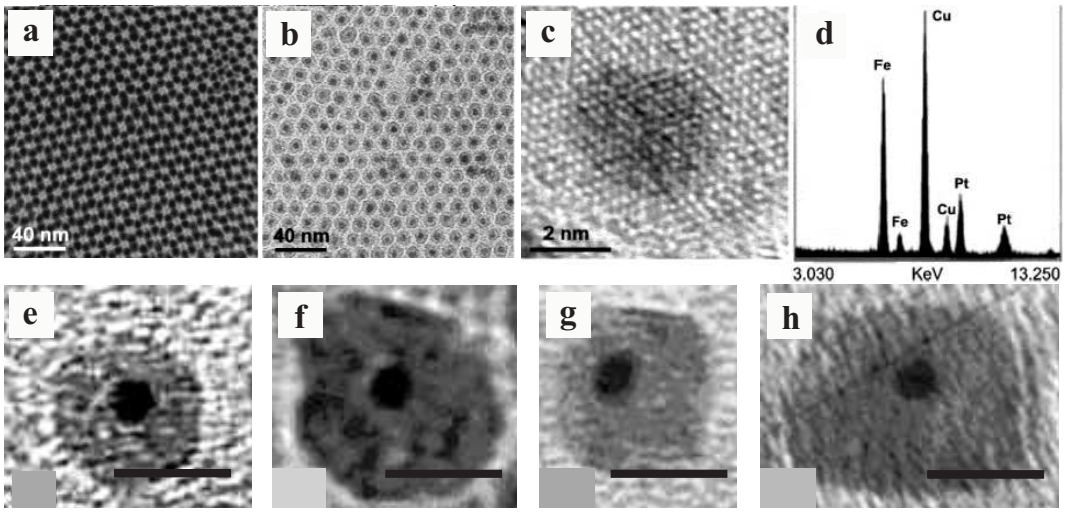

Figure 4.5: (a-d) TEM images of FePt@Fe_3O_4 core-shell NPs, (a) three-dimensional superlattice, (b) two-dimensional self-assembly, (c) HR-TEM image of a single core-shell NP, (d) corresponding EDX spectrum.[12] (e-h) TEM images of FePt@MnO core-shell NPs with different shell thicknesses and shapes (scale bar 10 nm). The particles were prepared via seed mediated growth using preformed FePt NPs as seeds and by growing MnO shells by decomposition of $Mn(acac)_2$. By adjustment of the synthetic parameters the shell thickness and morphology is tunable.[13]

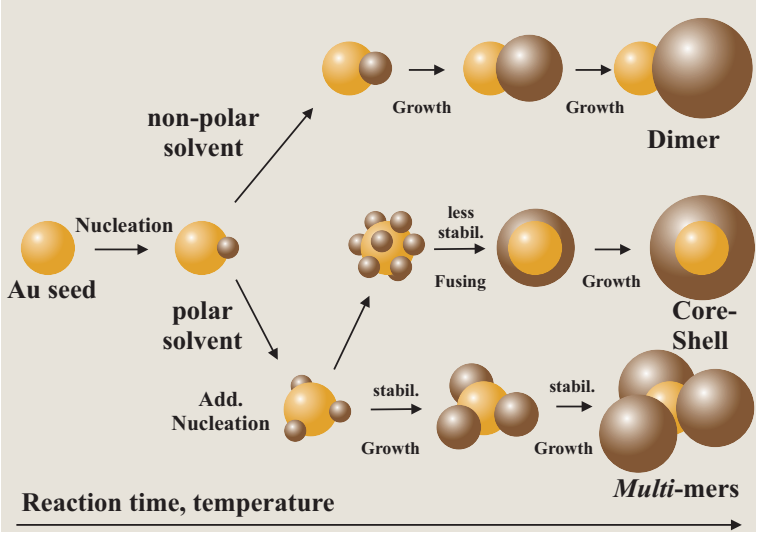

Figure 4.6: Possible reaction pathways leading to different nano-*hetero*-structures. Non-polar solvents yield *hetero*-dimers, whereas polar solvent lead to either core-shell or *multi*-mer structures, depending on the amount of stabilizing agent added.

4.1.3 *Multi*-mer Nanoparticles

As already addressed for core-shell NPs, using a polar solvent is essential to permit additional nucleation on the surface of the seed particle. This approach can be used to create more complex multifunctional nanocomposites that consist of more than two domains. However, the key issue in this case is to avoid the formation of a core-shell-type structure by preventing particle fusing the seed surface. This can be achieved by providing extra stabilization to each nuclei so that it can grow to one individual domain (see Figure 4.6). The most obvious way to accomplish this is to increase the molar amount of surfactant. Indeed, Yu et *al.* reported for Au@Fe_3O_4 NPs, that preferably "flowerlike" morphologies were obtained when phenyl ether was the solvent and a higher amount of oleic acid was used during the synthesis to protect the Fe_3O_4 domains.[5] In a similar way, we were able to prepare Au@MnO "nanoflowers" by decomposing $Mn(acac)_2$ in the presence of *in situ* formed Au seeds, oleic acid and oleylamine in phenyl ether (see section 8.5 and Figure 4.7a).[9]

Another method to prepare more complex *multi*-mer structures was introduced by

Shi et *al.*[8] In this approach preformed nano-*hetero*-dimers of $Au@Fe_3O_4$ were fused together on the Au domain by addition of sulphur as a promoting component. During heating of the reaction solution the sulphur is deposited on the Au surface, leading to an attractive interaction between the Au domains of neighboring $Au@Fe_3O_4$ NPs and eventually a dimerization of two or more hetero-dimers to dumbbells or flowerlike particles.

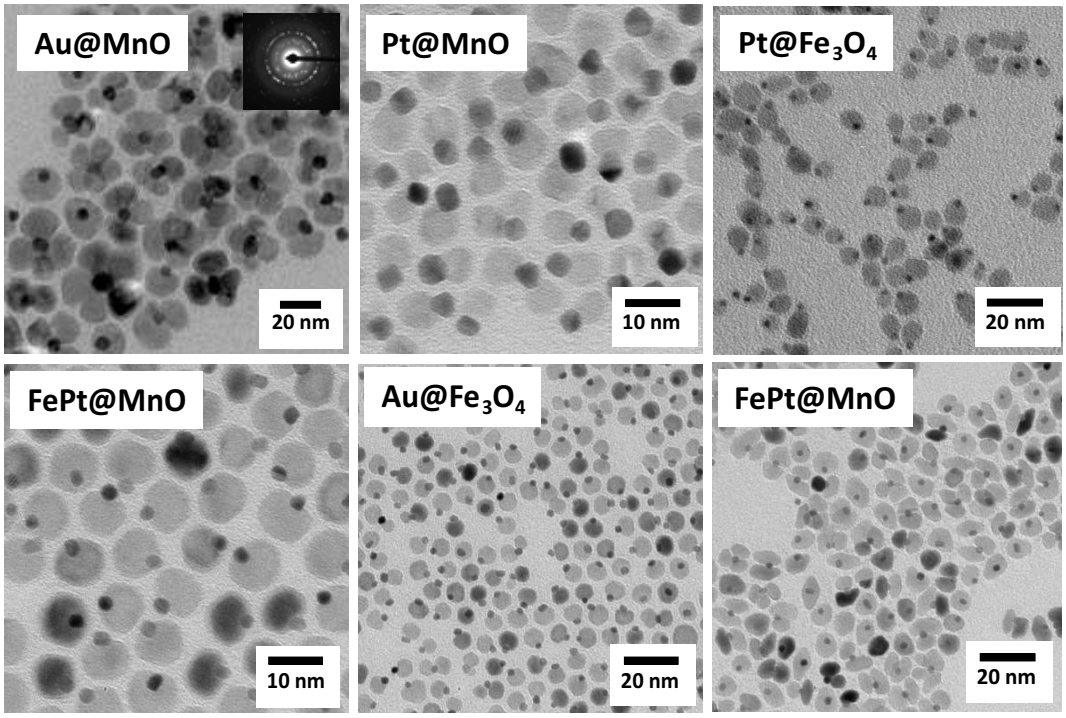

Figure 4.7: Examples of various magnetic metal@metal oxide nano-*hetero*-particles.

4.2 Properties of Nano-*hetero*-Particles

As already mentioned above, multicomponent nano-*hetero*-particles combine the different functionalities and properties of their respective components. Since the individual constituents are attached alongside coherent interfaces, a considerable amount of interactions between both materials must be assumed.

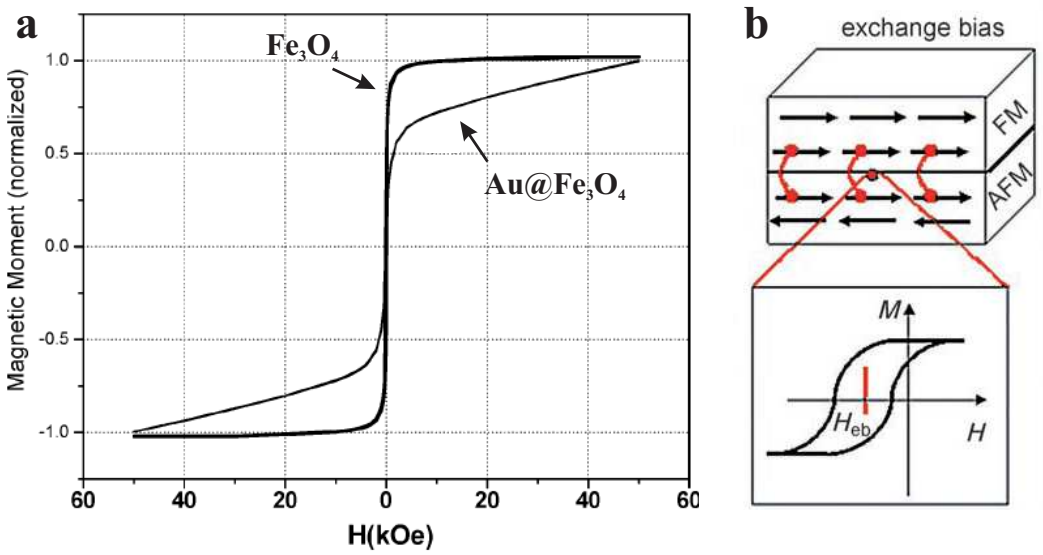

Figure 4.8: (a) Magnetic hysteresis curves for bare Fe_3O_4 NPs and Au@Fe_3O_4 nano-dimers.[5] (b) Magnetic exchange bias at an ferromagnetic/antiferromagnetic interface.[20]

4.2.1 Magnetic Properties

The magnetic properties of multicomponent particles can vary significantly depending on the particular interphase interactions. Sun and coworkers reported on the properties of bimagnetic FePt@Fe_3O_4 core-shell NPs and revealed a direct magnetic coupling through the particle interface.[12, 19] The combination of a magnetically hard material (FePt) and a magnetically soft material (Fe_3O_4) leads to a strong interphase exchange coupling and, therefore, cooperative magnetization switching of the two phases. Furthermore, the authors demonstrated that the nanocomposite exhibited a higher magnetic energy product than the bulk materials.

Additionally, the group of Prasad showed that Au@Fe_3O_4 core-shell nanostructures exhibited higher saturation magnetization and coercivity values compared to common Fe_3O_4 NPs of the same size.[8] It can be assumed that this behavior is due to a higher surface anisotropy caused by the Au-Fe_3O_4 interface. As a result the surface spins in the magnetic Fe_3O_4 domain are canted, which requires a higher magnetic field for the material to become saturated.[11] A similar behavior was observed for Au@Fe_3O_4 nano-hetero-dimers (see Figure 4.8a).[5] Additionally, the

authors observed an increase in the magnetic blocking temperature with increasing Au domain size. This phenomenon can be explained with a higher effective mass of nanocomposites having larger Au components. A higher mass requires more thermal energy for the magnetic moments to freely flip in an external magnetic field, thus the blocked state is already reached at higher temperatures. In fact, the same phenomenon can also be observed in Au@MnO nanoflowers.[9]
Another interesting feature is observed if ferromagnetic materials are combined with antiferromagnetic compounds, as was demonstrated by J. Nogués and coworkers for Co-CoO core-shell NPs.[21] At the interface between both materials, the spins of the antiferromagnetic shell (CoO) pin the magnetization of the ferromagnetic core and increase the magnetic anisotropy, a phenomenon which is called exchange bias and can be observed by a horizontal shift in the magnetic hysteresis curve (see Figure 4.8b).[22]

4.2.2 Optical Properties

One of the most intriguing features of gold NPs is their characteristic color in solution. Depending on the particle size, Au NP solutions exhibit absorption maxima ranging from approximately 500 - 550 nm. This can be attributed to quantisized oscillations of conduction electrons, excited under an external electromagnetic field, a phenomenon which is called surface plasmon resonance (SPR).[23–25] However, the combination of Au NPs with other materials in terms of nano-*hetero*-structures leads to a significant red-shift in the regarding UV/Vis spectrum (see also section 4.1.1). Such a behavior is reasonable, taking into account that the SPR is sensitive to dielectric environments.[26] Since the resonance frequency is proportional to $N^{1/2}$, with N being the number of free electrons in a particle, an electron deficiency will shift the absorption to longer wavelengths.[27–29] This effect becomes even more pronounced with increasing size of the metal oxide domain. In fact, we showed that the absorption maximum in Au@MnO nanoflowers shifts from 525 nm (for bare Au NPs) to 555 nm and 585 nm for a MnO domain size of 10 and 18 nm, respectively (see also chapter 8).[9]

4.3 Potential Application

Nano-*hetero*-particles have been proposed to draw great interest in various fields, ranging from spintronics to nanobiotechnology.[11] The enormous application potential of nano-*hetero*-particles arises, not only from the integration of the different physical properties of the individual domains, but also from the presence of different selectively addressable surfaces.

Indeed, many reports have recently stated the possibility to use multicomponent NPs for biomedical applications.[30–32] As an example, the combination of the unique optical and magnetic properties in Au@Fe_3O_4 or Au@MnO nano-*hetero*-structures make these particles promising candidates for simultaneous optical and MR imaging. Sun and coworkers, developed bio-functionalized Au@Fe_3O_4 nanodimers that were able to attach to and visualize human epithelial carcinoma cells (A431 cell line).[33] The presence of two separate surfaces permitted the selective functionalization with different ligands. A thiol containing poly(ethylene glycol) (PEG) ligand was used to modify the Au domain, whereas a PEG chain with a functional catechol endgroup was attached to the Fe_3O_4 surface. Furthermore, a epidermal growth factor receptor antibody (EGFRA) was conjugated to the catechol-PEG. A431 cells are known to overexpress EGFR and, therefore, the multifunctional Au@Fe_3O_4 nanodimers could selectively attach to the receptors on the cell surface. Another interesting example on how the combination of the individual properties of nano-*hetero*-particles can improve the diagnostic and therapeutic potential of common NPs was demonstrated by Hyeon and coworkers in 2006.[34] The authors deposited a uniform gold shell on silica NPs decorated with small Fe_3O_4 NPs to create a multifunctional probe which acts, both as a T_2 contrast agent for MRI and as activator for photothermal therapy.

Recently, we showed that the individual domains on Au@MnO nanoflowers could selectively be modified using suitable ligand molecules.[9] A multidentate copolymer containing PEG sidechains and several catechol anchorgroups was used to functionalize the MnO NPs, while a thiol-terminated oligonucleotide was conjugated to the Au surface.

On the other hand, core-shell NPs are attractive multifunctional systems for applications in catalysis, data storage, or as advanced permanent magnets.[11, 13, 35]

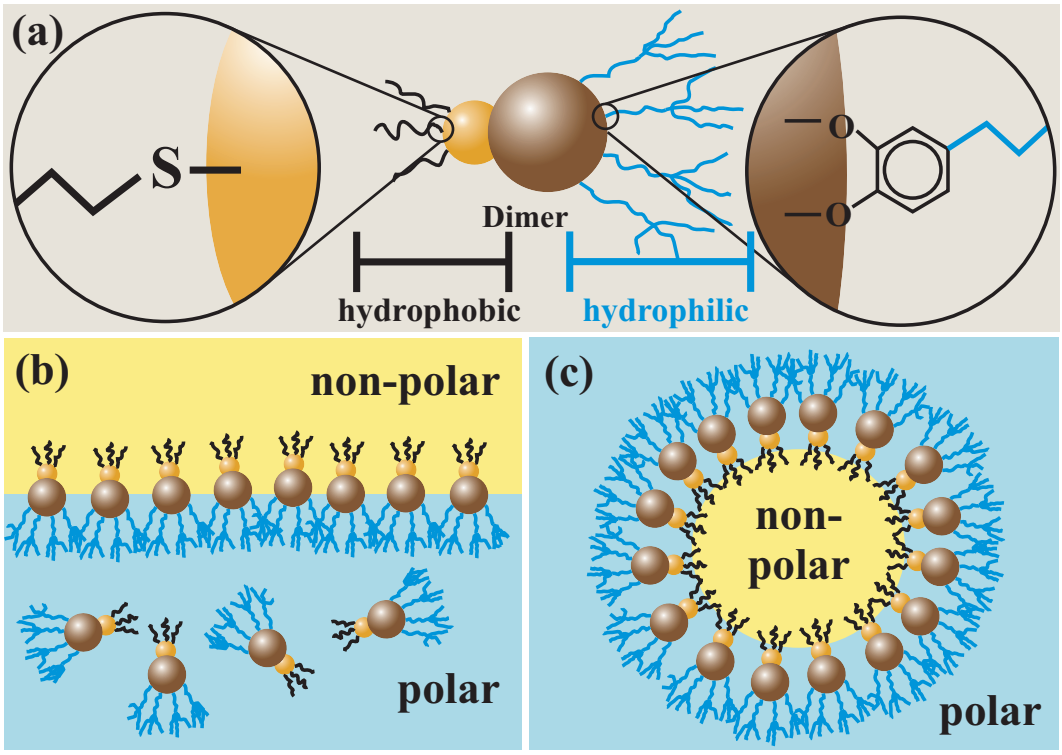

Figure 4.9: (a) A nano-*hetero*-dimer can act as a Janus NP when both surfaces are functionalized with ligands of opposite polarity, thus creating a giant amphiphile. These amphiphiles can self-assemble at a polar/non-polar interface to form e.g. a monolayer (b) or micelles (c).

Another interesting feature concerning *hetero*-dimer NPs is the possibility to create giant inorganic Janus particles. In this context the term "Janus particles" denotes asymmetric building blocks that possess two ends with different polarity and/or chemistry. Janus particles are interesting for a many reasons, e.g. their self-organization into complex and well-defined assemblies.[36–38] By attachment of different ligands with opposite polarity giant amphiphiles can be created which resemble large amphiphilic molecules that can be found in nature. In biological structures, self-assembled architectures formed by such amphiphilic molecules are often hierarchically organized and composed of smaller units (e.g. bilayers or micelles). Synthetic Janus NPs may also exhibit a similar hierarchical self-assembly process and thus provide a new and simple route for a controlled self-assembly

into one-, two-, or even three-dimensional structures. Figure 4.9a illustrates an approach, in which a hydrophobic alkyl thiol is used to attach to the gold domain of a gold@metal oxide dimer, whereas a hydrophilic catechol-PEG ligand is grafted onto the metal oxide domain, thus forming a giant amphiphile. As a result, these composite NPs would behave as amphiphiles which self-assemble at a polar/non-polar interface to form monolayers or even micelles (see Figure 4.9b and c).
No doubt, the toolbox of synthetic techniques for nano-*hetero*-structures is quickly expanding, leading to many fascinating new morphologies and composite materials, which will offer the possibility to create novel functional building block for magnetic, electronic and optoelectronic devices, as well new probes for biomedical purposes.

4.4 References

[1] Lee, D. C.; Smith, D. K.; Heitsch, A. T.; Korgel, B. A. *Annu. Rep. Prog. Chem., Sect. C: Phys. Chem.* **2007**, *103*, 351–402.

[2] Darling, S. B.; Bader, S. D. *ChemInform* **2006**, *37*, DOI: 10.1002/chin.200605242.

[3] Choi, S.-H.; Na, H. B.; Park, Y. I.; An, K.; Kwon, S. G.; Jang, Y.; Park, M.-h.; Moon, J.; Son, J. S.; in Song, C.; Moon, W. K.; Hyeon, T. *Journal of the American Chemical Society* **2008**, *130*, 15573–15580.

[4] Gu, H.; Yang, Z.; Gao, J.; Chang, C.; Xu, B. *Journal of the American Chemical Society* **2005**, *127*, 34–35.

[5] Yu, H.; Chen, M.; Rice, P. M.; Wang, S. X.; White, R.; Sun, S. *Nano Letters* **2005**, *5*, 379–382.

[6] Li, Y.; Zhang, Q.; Nurmikko, A. V.; Sun, S. *Nano Letters* **2005**, *5*, 1689–1692.

[7] Jun, Y.-w.; Choi, J.-s.; Cheon, J. *Chemical Communications* **2007**, *43*, 1203–1214.

[8] Shi, W.; Zeng, H.; Sahoo, Y.; Ohulchanskyy, T. Y.; Ding, Y.; Wang, Z. L.; Swihart, M.; Prasad, P. N. *Nano Letters* **2006**, *6*, 875–881.

[9] Schladt, T. D. et al. *Angewandte Chemie International Edition* **2010**, *49*, 3976–3980.

[10] Gu, H.; Zheng, R.; Zhang, X.; Xu, B. *Journal of the American Chemical Society* **2004**, *126*, 5664–5665.

[11] Zeng, H.; Sun, S. *Advanced Functional Materials* **2008**, *18*, 391–400.

[12] Zeng, H.; Li, J.; Wang, Z.; Liu, J.; Sun, S. *Nano Letters* **2004**, *4*, 187–190.

[13] Kang, S.; Miao, G.; Shi, S.; Jia, Z.; Nikles, D. E.; Harrell, J. *Journal of the American Chemical Society* **2006**, *128*, 1042–1043.

[14] Kortan, A. R.; Hull, R.; Opila, R. L.; Bawendi, M.; Steigerwald, M. L.; Carroll, P. J.; Brus, L. E. *Journal of the American Chemical Society* **1990**, *112*, 1327–1332.

[15] Danek, M.; Jensen, K. F.; Murray, C. B.; Bawendi, M. G. *Chemistry of Materials* **1996**, *8*, 173–180.

[16] Peng, X.; Schlamp, M. C.; Kadavanich, A. V.; Alivisatos, A. *Journal of the American Chemical Society* **1997**, *119*, 7019–7029.

[17] Teng, X.; Black, D.; Watkins, N. J.; Gao, Y.; Yang, H. *Nano Letters* **2003**, *3*, 261–264.

[18] Xu, Z.; Hou, Y.; Sun, S. *Journal of the American Chemical Society* **2007**, *129*, 8698–8699.

[19] Zeng, H.; Sun, S.; Li, J.; Wang, Z. L.; Liu, J. P. *Applied Physics Letters* **2004**, *85*, 792–794.

[20] Lu, A.-H.; Salabas, E. L.; Schüth, F. *Angewandte Chemie International Edition* **2007**, *46*, 1222–1244.

[21] Skumryev, V.; Stoyanov, S.; Zhang, Y.; Hadjipanayis, G.; Givord, D.; Nogues, J. *Nature* **2003**, *423*, 850–853.

[22] Seto, T.; Akinaga, H.; Takano, F.; Koga, K.; Orii, T.; Hirasawa, M. *Journal of Physical Chemistry B* **2005**, *109*, 13403–13405.

[23] Lyon, L. A.; Musick, M. D.; Natan, M. J. *Analytical Chemistry* **1998**, *70*, 5177–5183.

[24] He, L.; Musick, M. D.; Nicewarner, S. R.; Salinas, F. G.; Benkovic, S. J.; Natan, M. J.; Keating, C. D. *Journal of the American Chemical Society* **2000**, *122*, 9071–9077.

[25] Brown, K. R.; Walter, D. G.; Natan, M. J. *Chemistry of Materials* **2000**, *12*, 306–313.

[26] Liz-Marzán, L. M.; Giersig, M.; Mulvaney, P. *Langmuir* **1996**, *12*, 4329–4335.

[27] Aden, A. L.; Kerker, M. *J. Appl. Phys.* **1951**, *22*, 1242–1246.

[28] Toon, O. B.; Ackerman, T. P. *Appl. Opt.* **1981**, *20*, 3657–3660.

[29] Daniel, M.-C.; Astruc, D. *Chemical Reviews* **2004**, *104*, 293–346.

[30] Choi, J.-s.; Jun, Y.-w.; Yeon, S.-I.; Kim, H. C.; Shin, J.-S.; Cheon, J. *Journal of the American Chemical Society* **2006**, *128*, 15982–15983.

[31] Selvan, S.; Patra, P.; Ang, C.; Ying, J. *Angewandte Chemie International Edition* **2007**, *46*, 2448–2452.

[32] Gao, J.; Gu, H.; Xu, B. *Accounts of Chemical Research* **2009**, *42*, 1097–1107.

[33] Xu, C.; Xie, J.; Ho, D.; Wang, C.; Kohler, N.; Walsh, E.; Morgan, J.; Chin, Y.; Sun, S. *Angewandte Chemie International Edition* **2008**, *47*, 173–176.

[34] Kim, J.; Park, S.; Lee, J. E.; Jin, S. M.; Lee, J. H.; Lee, I. S.; Yang, I.; Kim, J. S.; Kim, S. K.; Cho, M. H.; Hyeon, T. *Angewandte Chemie International Edition* **2006**, *45*, 7754–7758.

[35] Li, J.; Zeng, H.; Sun, S.; Liu, J.; Wang, Z. L. *Journal of Physical Chemistry B* **2004**, *108*, 14005–14008.

[36] Perro, A.; Reculusa, S.; Ravaine, S.; Bourgeat-Lami, E.; Duguet, E. *Journal of Materials Chemistry* **2005**, *15*, 3745–3760.

[37] Walther, A.; Müller, A. H. E. *Soft Matter* **2008**, *4*, 663–668.

[38] Wurm, F.; Kilbinger, A. *Angewandte Chemie* **2009**, *121*, 8564–8574.

CHAPTER 5

Surface Modification of Magnetic NPs

Chapter 3 demonstrated that there have been numerous groundbreaking developments in the synthesis of magnetic nanoparticles over the past decades. However, the most important issue, which needs to be accomplished after their preparation, is to provide the nanoparticles with a sufficient degree of stability. It was already pointed out in chapter 3, that the use of surfactant molecules is essential to prevent the particles from aggregation and rapid oxidation (see also Figure 5.1). Especially, pure metal NPs, like Fe, Co and Ni (and their alloys) are extremely sensitive to air, and in fact, their vulnerability toward oxidation becomes more pronounced with smaller particle sizes. Furthermore, the necessity of an efficient coverage of the nanoparticle surface becomes obvious when considering a potential use in biomedical applications. The high chemical reactivity of the NP surface could pose health risk to patients, since the NPs could already influence reaction pathways on the cellular level.

Additionally, the colloidal stability of the NPs under physiological conditions is another important issue, which needs to be addressed if an application in medical or biological respect is anticipated. As mentioned in section 3.5, the synthesis of monodisperse and highly crystalline nanoparticles requires non-hydrolytic synthetic routes and the use of hydrophobic surfactants, that efficiently cover the parti-

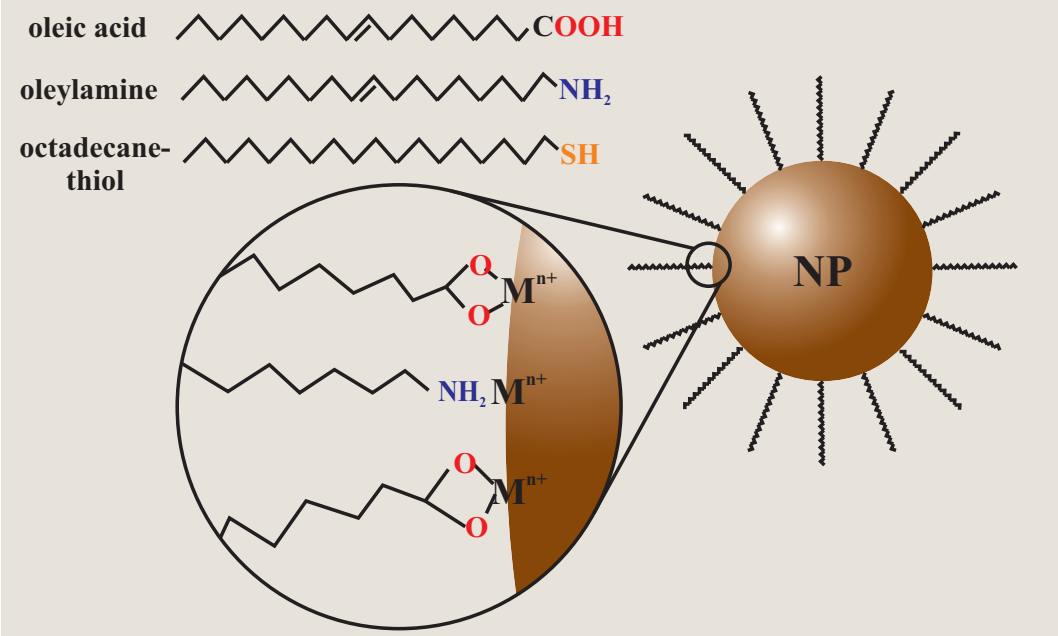

Figure 5.1: Illustration of an as-prepared hydrophobic surfactant capped magnetic NP. Typical surfactants comprise hydrocarbons with functional endgroups, such as carboxylic acids, amines or thiols.

cle surface. Therefore, as-prepared nanoparticles are insoluble in water and a direct application of these unmodified particles into aqueous solutions would inevitably lead to particle aggregation and precipitation. All the worse, if applied directly to a living organism, these nanoparticle aggregates would pose an immediate threat to health, since they would clog up small blood vessels and obstruct an unhampered blood circulation. Furthermore, even if particle agglomeration could be prevented, unprotected inorganic nanoparticles are prone to opsonozation, a defense process initiated by the innate immune system, in which certain serum proteins attach to the particle surface and initiate phagocytosis. Therefore, it is necessary to exchange the hydrophobic protection shell by hydrophilic ligands, that guarantee, not only a high colloidal stability in aqueous environment, but also prevent opsonization by serum proteins under physiological conditions.[1] The latter is often referred to as "stealth effect".[2–4]

This section will focus on some of most common strategies for the protection and

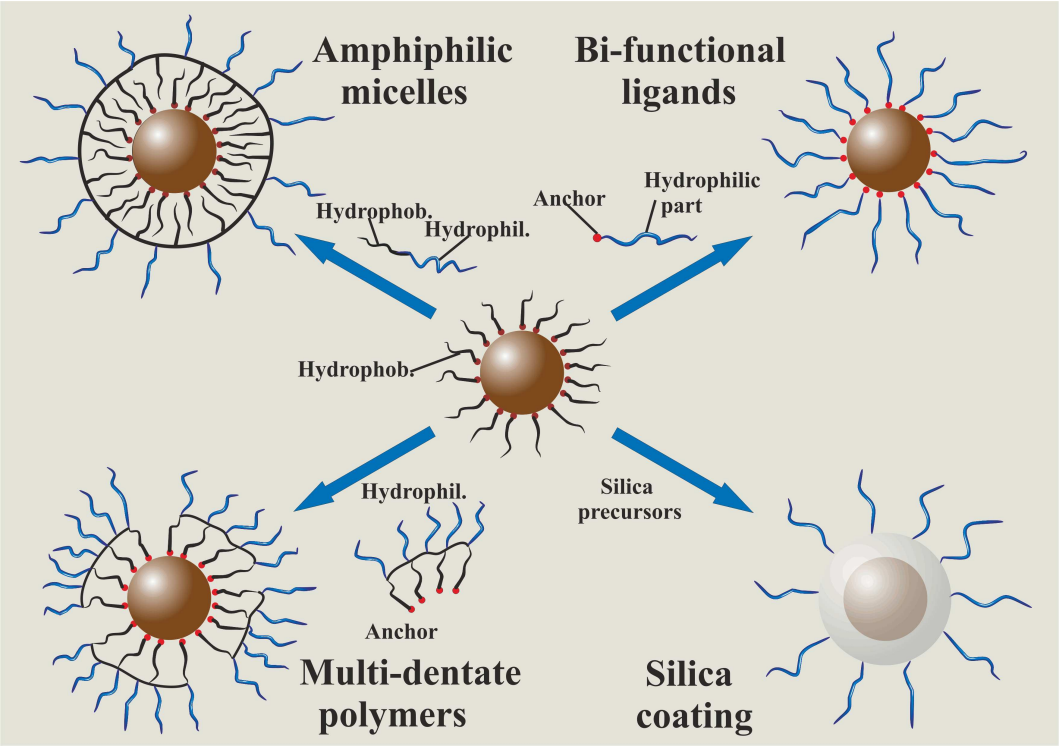

Figure 5.2: Different strategies for the surface modification of magnetic NPs.

stabilization of magnetic nanoparticles (see Figure 5.2). Interestingly, all known surface modification approaches result in a core-shell-like structure, with the magnetic NPs being the core and some kind of inert organic or inorganic material being the protecting/stabilizing shell. Apart from surface passivation, precious-metal or carbon coating (which will not be discussed here), surface modification with surfactant micelles, bi-functional- or polymeric ligands or silica are the most prevailing methods.

5.1 Amphiphilic Micelles

As explained in section 3.5, as-prepared magnetic NPs are covered with a shell of hydrophobic surfactant molecules, such as oleic acid or oleylamine.[5, 6] The functional group of these stabilizing agents are strongly attached to the particle sur-

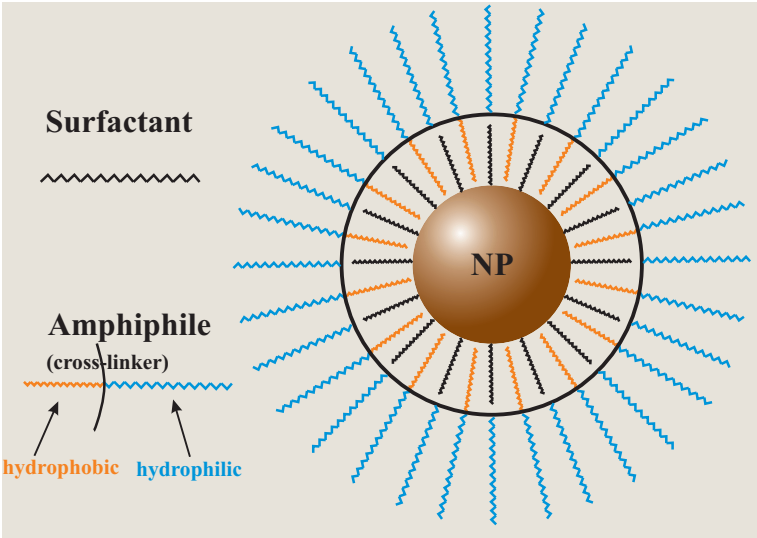

Figure 5.3: Surface coating using amphiphilic molecules. The amphiphilic surfactant molecules can intercalate between the hydrophobic capping molecules on the NP surface due to van-der-Waals interactions. Cross-linking of the surfactant ligands can lead to more rigid structures and higher stability.

face by a coordinative bond (see section 7.3 for more details), whereas the long alkyl chains point into the periphery, creating an inert layer, which offers, not only colloidal stability, but also protection from oxidation and aggregation. Consequently, one of the simplest approaches to enhance the solubility of hydrophobic NPs in aqueous solution, uses the molecular structure of the hydrophobic layer for the incorporation of additional surfactant molecules, like CTAB or oleic acid (see Figure 5.3). This surfactant addition strategy was first developed for the preparation of water-soluble quantum dots and was later also successfully applied for dispersing magnetic NPs in aqueous media.[7–9] During this procedure, the long alkyl chains of the CTAB molecules are integrated in between the C-chains of the oleate/oleylamine molecules due to attractive van-der-Waals interactions, and on the other hand, the cationic trimethylammonium moieties point to the outside, creating repulsive forces and stabilizing the particles in suspension. Unfortunately, NPs prepared in this way exhibit only moderate long-term stabilities and tend to agglomerate at higher salt concentrations.[10]

Many of the existing strategies for NP phase transfer, that were developed in

the following years, use amphiphilic polymers as surface coating ligands.[7, 11] The structure of these polymers usually consists of individual lipophilic and hydrophilic polar components, such as poly(maleic anhydride-*alt*-1-octadecene)-PEG block copolymer, or amphiphilic PEG-phospholipids.[4, 12–15] Here, the lipids act as the nonpolar constituent of larger amphiphiles. Their hydrophobic tails interact with the nonpolar surface ligand of the nanoparticles (see Figure 5.4), which leads to a complete encapsulation of the core and its original coating. The hydrophilic end

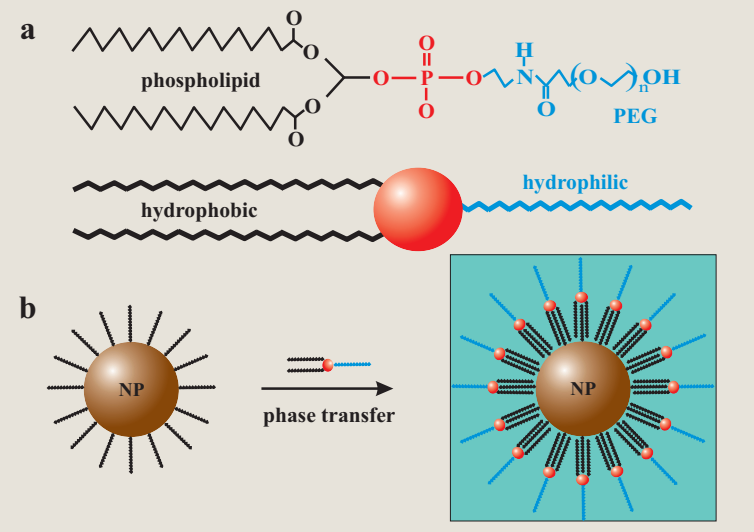

Figure 5.4: (a) Chemical structure of a PEG-phospholipid. (b) Coating procedure: the hydrophobic lipid tails are incorporated between the capping molecules on NP surface, whereas the hydrophilic PEG chains point to the outside creating a hydrophilic shell.

group of the amphiphile makes the material polar and fully dispersible in water. The nanoparticles are assumed to remain encapsulated by the original protecting ligand shell that is never broken up, and particle aggregation is suppressed by steric repulsion. Dai and coworkers recently developed a similar PEG-modified phospholipid surface coating for graphite-protected FeCo NPs with high magnetic moment.[16] Again, the non-polar hydrocarbon chains are bound to the hydrophobic graphite shell to form a stable double layer, while the PEG chain are exposed to the outside. Another example, which uses a similar strategy for monodisperse MnO NPs, was demonstrated by Hyeon et *al.* in 2007 and Lee et *al.* in 2009.[17, 18] Related meth-

ods used a variety of amphiphilic polymers, including polystyrene-poly acrylic acid (PS-PAA) block copolymers, tetradecylphosphonate and PEG-2-tetradecyl ether, to increase the hydrophilicity of various inorganic NPs.[19, 20], Additionally, there are many different amphiphilic polymers commercially available today, which offer different functional groups, like carboxylic acids, thiols, amines, and biotin, for the immobilization of various biomolecules, such as peptides, proteins, or oligonucleotides.
The presence of multiple surface bilayers, however, leads to much larger hydrodynamic sizes than that of the starting material hampering an efficient application in living organisms.[21–23] Furthermore, since the amphiphilic bilayer is only connected to the NP core by considerably weak van-der-Waals interactions, the surfactant molecules are in a dynamic equilibrium with their unbound counterparts, i.e. by shifting the equilibrium they can be removed by washing and diluting, which would result in particle agglomeration and precipitation.

5.2 Polymeric Ligands

One of the most established methods to stabilize magnetic NPs in water or buffered solutions is provided by the use of polymers. PEG, perhaps the most common representative biocompatible polymer, has received great attention due to its non-fouling property, that supports a resistance to protein adsorption and an ability to bypass the RES and natural barriers, such as the nasal mucosa.[24–27] PEGs have been extensively used as stabilizing materials for many NPs used on biomedical applications, particularly in long circulating *in vivo* imaging systems. In principle, chemical attachment to the NP surface can be achieved by using different functional groups (see section 5.3). According to Pearsons concept of hard and soft acids and bases (HSAB), the nature of these groups depends on its affinity toward the metal constituent of the core material.[28] For example, gold nanoparticles show a high affinity towards thiol groups, whereas manganese and iron oxide nanoparticles favor oxygen containing ligands. The use of polymers for this purpose is reasonable, since they have the advantage that numerous functional groups can be applied on a single macromolecule. In this context, "multidentate" polymers, that possess more than one anchoring group, offer much stronger attachment to the nanoparti-

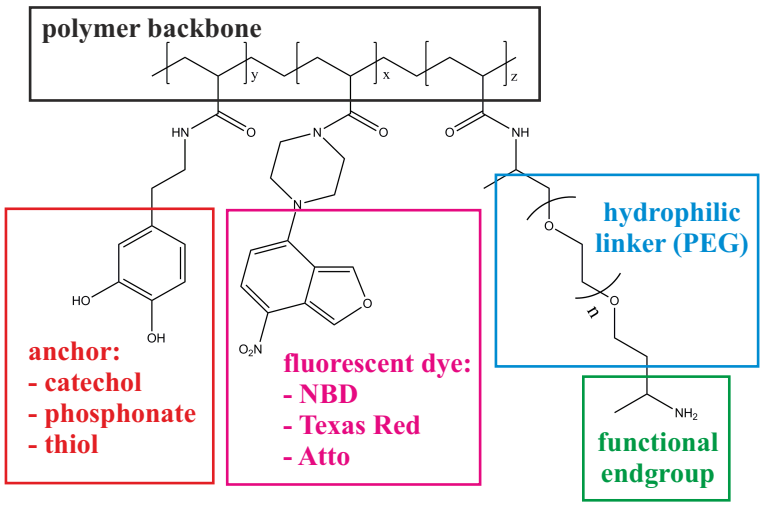

Figure 5.5: Chemical structure of a typical multifunctional polymeric ligand. The copolymer contains 3-hydroxytyramine (dopamine) as an anchor, a fluorescent dye molecule, and functional amino groups for further functionalization.

cle surface. Suitable polymers include poly(analine), poly(methylidene malonate), poly(pyrrole), poly(lactic acid), poly(glycolic acid), poly(ethylene imine) and their copolymers.[29–34] In addition, the possibility of cross-linking between the polymer chains leads to more rigid structures on the NP surface. For example, dextran-coated iron oxide nanoparticles can be cross-linked using epichlorohydrin, and subsequently equipped with free amino groups to allow further modification.[35] Other examples for cross-linked polymer functionalized iron oxide nanoparticles include the use of chitosan and poly(ethylene-glycol)-co-fumarate.[36, 37]

A variety of methods, that use special chelating ligands, have been established in recent years.[38] In fact, there are reports where particle binding of polymeric ligands on Fe_3O_4 nanoparticles was achieved via carboxylic, phosphate, phosphonate and sulphate groups.[39–42] Dopamine is another anchoring group which shows a high affinity towards metal and metal oxide surface (see section 5.3),[43], in fact, it has evolved as a very popular binding ligand.[44, 45] Owing to the multidentate coordination of the chelating moieties, the bonding strength of these polymers is generally very high. Furthermore, the use of reactive ester polymers, such as poly(pentyfluoro phenylacrylate) (PPFA), permits the successive substitution of the pentafluorophenol group by dopamine and other functional groups, including amines, (PEG), or

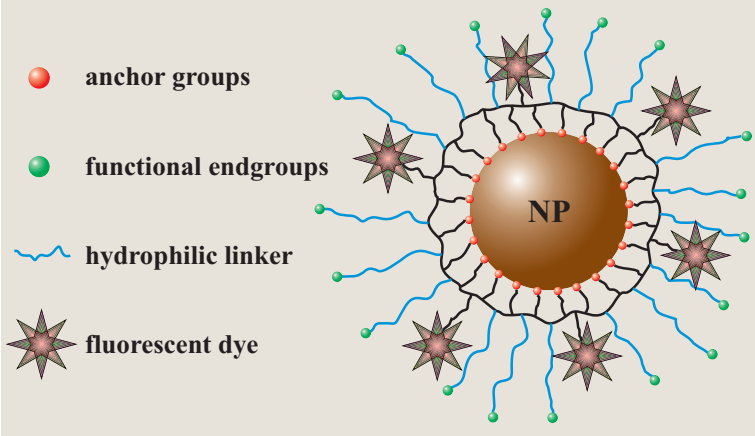

Figure 5.6: Magnetic NP functionalized using a multidentate polymeric ligand. The polymer consists of several anchor groups, hydrophilic linkers, and functional endgroups, which permit further attachment of different ligand molecules. Additionally, fluorescent dyes can be conjugated to the polymer.

fluorescent dyes (see Figures 5.5 and 5.6). Metal oxide nanoparticles functionalized with such polymers containing several dopamine moieties were used in different applications ranging from proteine separation, cell targeting and multimodal imaging.[46–52]

A different approach to functionalize magnetic nanoparticles with polymers is enabled by atom transfer radical polymerisation (ATRP).[53, 54] With this method, polymers are grown on the surface of nanoparticles after previous treatment with an initiator.[55] As an example, Lattuada and coworkers used this method to design water-soluble Fe_3O_4 nanoparticles. The NPs were coated with poly(lactic acid), followed by esterification through acylation, which enabled the addition of halide moieties to transform the nanoparticle surfaces into macroinitiators.[21] In that way, different ligands could be used to grow polymer coatings with, either cationic, anionic or neutral endgroups.

A major drawback for the use of polymers for the surface modification of magnetic nanoparticles is the fact that the presence of multiple anchoring groups facilitates the bonding to more than one nanoparticle at a time. Since the binding of the surface ligands is an equilibrium process with continuous attachment/detachment of the chelating groups, there is a non-neglectable possibility that one polymer chain

simultaneously covers several particles. As a consequence, the presence of large agglomerates cannot be excluded, which impedes a suitable application for biomedical purposes.

5.3 Bifunctional Ligands

A key factor for *in vivo* tracking and targeting applications is a high stability of the bonding between functional molecules and the nanoparticle surface. An early release or uptake of the nanoparticle/molecule system due to other surface reactions, could be detrimental to the application or possibly to the patient.
One of the most often used methods for surface modification of magnetic nanoparticles is the exchange of the hydrophobic stabilizing ligands by hydrophilic bi-functional molecules (see Figure 5.7). As the name implies, bi-functional molecules are generally composed of two parts: an anchor group, which efficiently binds to the surface of the nanoparticle and a hydrophilic part which allows stability in aque-

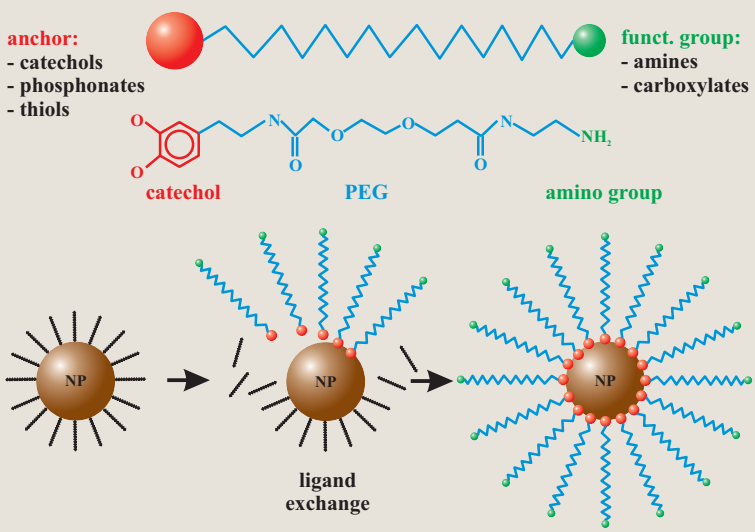

Figure 5.7: Surface modification of magnetic NPs using bi-functional ligands. The ligands consist of an anchor group conjugated to a hydrophilic linker carrying a functional endgroup. A key requirement for a successful exchange of the hydrophobic capping agents is the complete solubilization of NPs and ligands in the same solvent.

ous media. Compared to the amphphilic micelle coating, the bi-functional ligand exchange strategy principally provides much better colloidal stability of the magnetic NPs under physiological conditions, due to stronger (mostly ionic) interactions between the bidentate (or, in some cases, multidentate) functional group and the metal-/ metal oxide surface. Typical anchor groups for metal oxide nanoparticles include carboxylates,[56, 56, 57] phophonates,[58, 59] and catechols,[44] whereas thiols[60] are preferred for metallic and intermetallic NPs. However, the key requirement for an efficient attachment on the surface, is a stronger binding strength of the anchor group, than that of the former hydrophobic stabilizing agent. Although initial attempts to modify hydrophobic nanoparticles were carried out with simple bi-functional molecules, like 2,5 dihydroxybenzoic acid,[56] or tetramethylammonium hydroxide,[61] PEG has evolved as the most often used hydrophilic linker, owing to its outstanding solubility, stability, and excellent biocompatibility.
Among the above mentioned anchor groups, special focus has been addressed to catechols. Especially, dopamine is one of the most considered high affinity binding groups to stabilize metal oxide NPs in water and physiological environment.[62–65] It is a derivative of L-3,4-dihydroxyphenylalanine (L-DOPA), an amino acid, that occurs naturally in the adhesive protein of some marine mussels.[43, 66–68] Indeed, the binding interaction of dopamine with the surface of iron oxide NPs has been thoroughly investigated in the past, and it was confirmed, that the strong attachment was due to an improved orbital overlap of the five-membered ring and a reduced steric effect on the iron complex which can be obtained in a bidentate coordination (see Figure 5.8).[62, 69, 70] Since the dopamine anchor groups were conjugated with a PEG linker, the functionalized iron oxide NPs were readily soluble in aqueous solution and stable over long periods of time.

An example, where two different anchor groups were used for the attachment of bi-functional ligands was provided by Hong et *al.* for intermetallic FePt NPs. Here, the surface of the magnetic particles was functionalized with a dopamine- and a thiol-containing PEG ligand.[71] The use of two different binding groups is reasonable, giving the fact, that both molecules on their own would only ensure poor binding strength on FePt. Based on Pearsons' hard and soft acids and bases (HSAB) concept, the reason for this behavior is simply the circumstance, that catechols, as well as other 1,2-diols, indeed show a high affinity toward the iron sites,[72, 73]

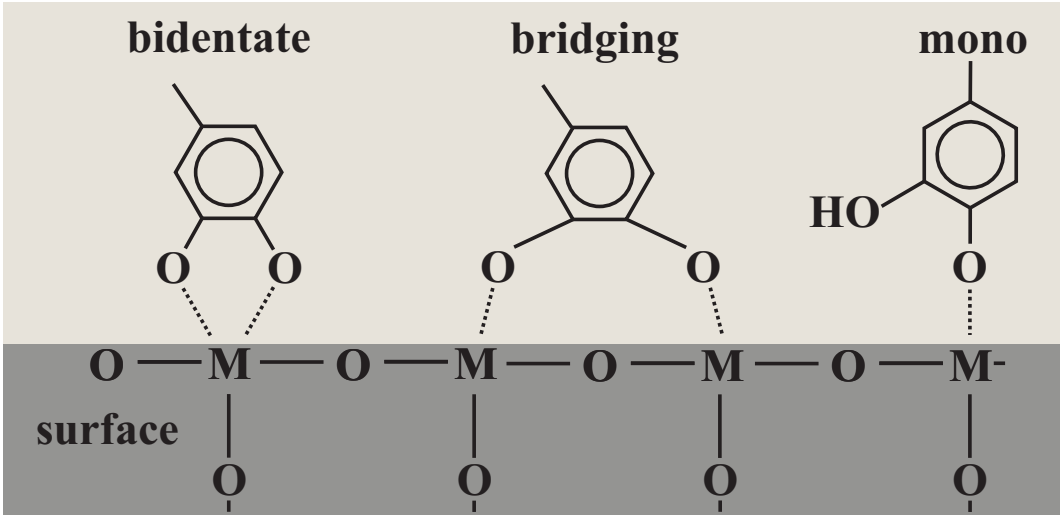

Figure 5.8: Different possible binding coordinations of catechols on metal oxide surfaces. In the bidentate case the metal and the oxygen atoms of the catechol are arranged in a five-membered ring which leads to an improved orbital overlap and, therefore, higher binding strength. Adapted from ref. [70]

but only a weak attraction toward platinum, whereas the opposite is the case for the thiol group. Consequently, the application of both ligands showed much better results compared to studies, where only one of them was used. The NPs were stable in various aqueous media, including water, ionic solutions, and cell culture medium.[71] In a similar way, FePt NPs coated with a protective iron oxide shell were stabilized with a dopamine-PEG ligand.[74, 75] The resulting particles exhibited high cytoxicity due to the presence of the FePt core and strong T_2 MR contrast enhancement due to the presence of an iron oxide shell. Sun et *al.* also reported the modification of monodisperse iron/iron oxide core/shell NPs with a dopamine-PEG (DOPA-PEG) ligand. The ligand was synthesized by a simple EDC/NHS coupling reaction of dopamine with a PEG-dicarboxylic acid. The modified Fe/Fe_3O_4 core/shell NPs were stable in water and phosphate buffer solutions.[76] The same group investigated the influence of the PEG-chain length (HOOC-$PEG_{(n)}$-COOH, M_w(PEG) = 600, 3,000, 6,000, 20,000 g mol^{-1}) on uptake in macrophage cells.[65] The authors revealed, that macrophage uptake decreased with increasing PEG chain length (M_w(PEG)). Additionally, the free carboxylic acid groups of the ligands per-

mitted further conjugation of biomolecules. In a similar way, Wang et *al.* coupled chromones, a group of naturally occurring compounds that show antifungal, antiviral, antihypertensive, and anticancer properties, to PEGylated Fe_3O_4 NPs. In this report the PEG chains were terminated with free amino groups, to which the drug molecules could easily be attached. Furthermore, the authors demonstrated that the drug could be released by variation of the pH value.[77] However, the use of dopamine-PEG ligands can also be applied for more complex nanostructures. Cheng et *al.* reported a new approach for the targeted delivery and controlled release of the anticancer drug cisplatin using PEGylated porous and hollow Fe_3O_4 NPs. The particles themselves were prepared by controlled oxidation of Fe NPs,

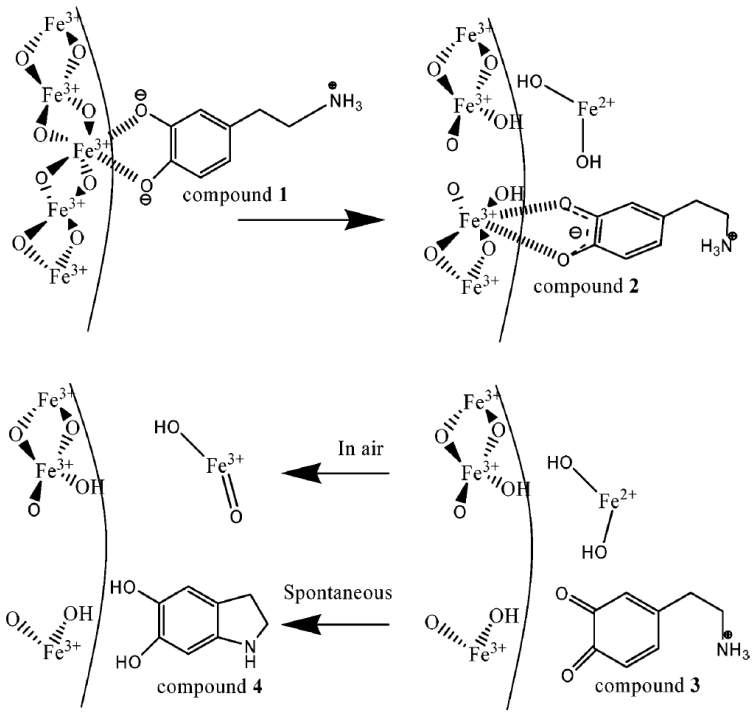

Figure 5.9: Proposed mechanism for the degradation of iron oxide NPs by dopamine (compound 1) in an aqueous solution. First a semiquinone (compound 2)complex is formed via electron transfer from dopamine to the Fe(III) forming $Fe(II)_{aq}$. A second electron transfer leads to the formation of a quinone (compound 3) and further fragmentation. Finally, Michael addition can yield an indole derivative (compound 4) and the oxidation of $Fe(OH)_2$ to FeOOH. From ref.[70]

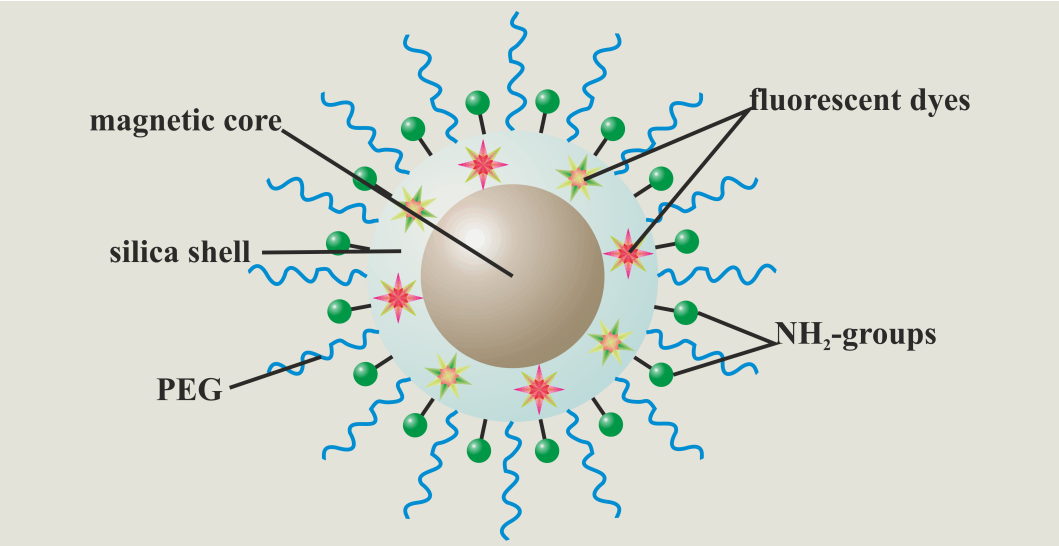

Figure 5.10: Illustration of a multifunctional silica coated magnetic NP.

followed by acid etching to create porous Fe_3O_4 nanocrystals with spherical cavities in the middle. The presence of pores on the surface permitted the slow diffusion of cisplatin inside the hollow structures, as well as the slow release of the drug under physiological conditions. Once coupled to the humanized IgG1 monoclonal antibody Herceptin, the cisplatin-loaded hollow NPs were able to target SK-BR-3 breast cancer cells.[78]

However, there have also been critical remarks concerning the application of dopamine as anchor group for metal oxide NPs. Especially, some authors reported on rather rapid degradation of dopamine due to a surface reaction, once it is attached to the surface of iron oxide NPs (see Figure 5.9).[70, 79] Additionally, catechols are known to be liable to oxidation under aerobic conditions, forming dark and insoluble polymers.[80] Apart from dopamine, other catechol anchor groups were also extensively investigated and found to be more reliable for biomedical applications.[79, 81] Careful selection of the different functionalities allowed close control of the hydrodynamic diameter and the interfacial chemistry of iron oxide nanoparticles.

5.4 Silica Coating

The surface modification strategies presented in the previous sections relied on the coordinative attachment, of organic ligands carrying functional groups, to the metal atoms on the particle surface. However, it has to be assumed that this protecting organic ligand shell around the nanoparticle is not densely packed, and therefore, permits diffusion of water molecules to the surface, which leads to dissolution of metal ions and, eventually, to the degradation of the nanoparticle itself (see chapter 10). The advantage of using silica as a coating material is based on its exceptional stability, especially in aqueous media.

From a technical point of view the easy regulation of the coating process, processability combined with chemical inertness, controlled porosity, and optical transparency are the most important factors.[82, 83] In addition, cations and positively charged molecules can be linked covalently to the polymeric silica layer at silica-water interfaces under basic conditions, i.e. the silica layer provides steric and electrostatic protection for the cores, while acting simultaneously as a dispersing agent for electrostatic colloids. These advantages make silica an ideal, low-cost material to tailor the surface properties of various nanomaterials. Furthermore, silica coatings can equip magnetic NPs with many additionally benefits, such as

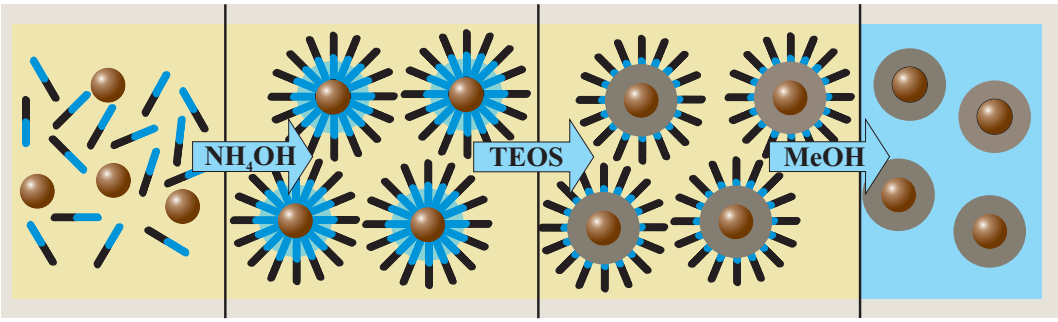

Figure 5.11: Silica functionalization of magnetic NPs in a water-in-oil microemulsion. The hydrophobic NPs and surfactant molecules are dispersed in cyclohexane. Upon addition of aqueous NH_4OH micelles are formed in which the NPs are entrapped. Subsequently, the condensation of tetraethoxysilane (TEOS) leads to the formation of SiO_2 on the NP surface. After complete reaction, the SiO_2 encapsulated magnetic NPs are retrieved by addition of methanol.

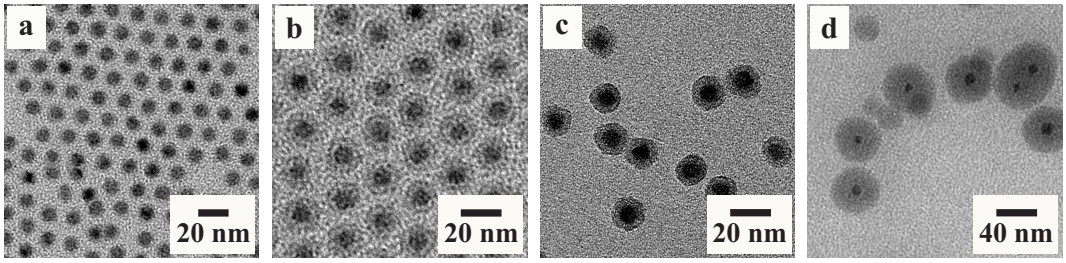

Figure 5.12: TEM images of silica coated MnO NPs synthesized in a water-in-oil microemulsion. The shell thickness is easily controllable by adjustment of the synthetic parameters: (a) 1 nm, (b) 2 nm, (c) 4 nm and (d) 10 nm.

high biocompatibility and the possibility of subsequent functionalization (see Figure 5.10).[84, 85] Thus, the potential applicability increases significantly, and, as an example, allows the use of these core@silica nanomaterials for diagnostic and therapeutic purposes (e.g. MRI).[86, 87]
Over the years, various approaches have been exploited to fabricate silica coatings for colloidal nanoparticles, e.g. the classical Stöber synthesis,[88–90] the formation of biosilica coatings,[50, 91] or the use of silane coupling agents.[92] Although, these strategies have shown good results with various nanomaterials, the downside, however, is the limitation of these processes to aqueous solutions, and therefore, the need to start from water-soluble NPs.

As already stated in chapter 3, high-quality monodisperse NPs are protected by a hydrophobic surfactant layer, and thus, are only soluble in non-polar solvents. Hence, the above mentioned strategies are not applicable on these NPs. An alternative method, which has become quite popular recently, is based on microemulsion synthesis (see also section 3.4), where micelles or inverse micelles are used to confine and control the coating of silica on the core of the inner nanoparticle (see Figure 5.11).[93–96] Microscopically they consist of small heterogeneous domains of water in a surrounding hydrophobic phase (oil) separated by a surfactant monolayer. The great advantage of this approach is the possibility to dissolve as-prepared hydrophobic nanocrystals in the oil phase before entrapping them inside the micelles (see Figure 5.11). By optimizing the synthetic conditions it is even possible to capture only one NP per micelle. Furthermore, the thickness of the silica shell can

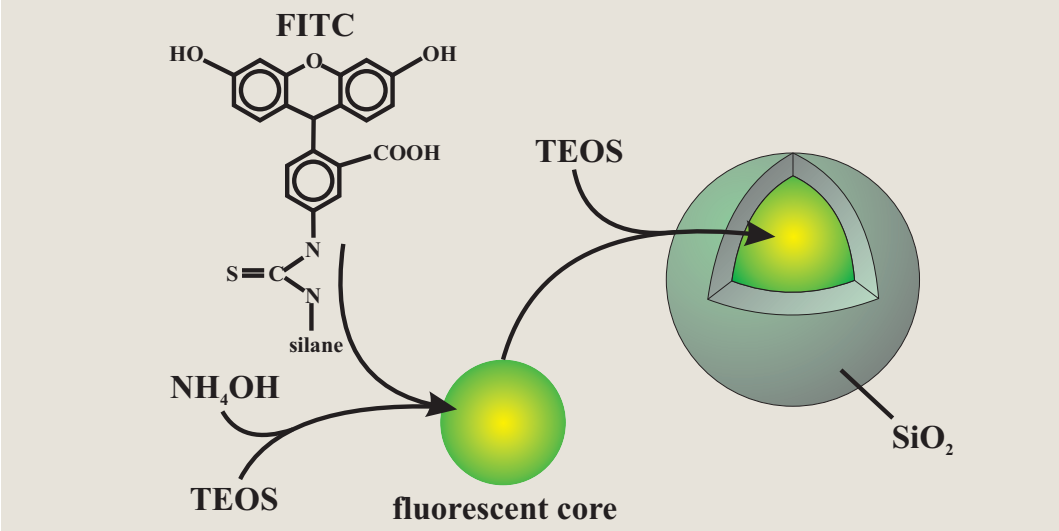

Figure 5.13: Illustration of the synthetic procedure to prepare fluorescent core-silica shell NPs. The fluorescent dye (in this case fluoresceine isothiocyanate (FITC)) is previously conjugated to a reactive silane. Simultaneous condensation of the dye-silane conjugate with TEOS results in a complete incorporation of the dye inside the SiO_2 matrix. Subsequently, further TEOS is added to grow a protecting SiO_2 shell around the core. (Adapted from ref.[102])

easily be controlled, as can be seen in Figure 5.12. The silica coating procedure is then initiated by adding the desired silanes as precursors.[97] As microemulsions are thermodynamically stable systems (as opposed to emulsions), both the content of the droplets and the surfactant molecules at the interfaces, are constantly and rapidly exchanged between different droplets, thereby facilitating chemical reactions involved in particle synthesis.[98]

An interesting feature of silica coating is the possibility to incorporate fluorescent dyes into the SiO_2 matrix (see Figure 5.13). The advantage of this practice is a prolonged stability and higher efficiency of the dye inside the shell compared to simple attachment on the outside of the nanocomposite. The reason for this is an extremely effective protection of the dye molecules towards oxidation and photobleaching, as well as a reduction of quenching effects.[99–105]

Another advantage of silica coating magnetic NPs is the opportunity to create a mesoporous shell. In fact, core-shell magnetic mesoporous silica microspheres with

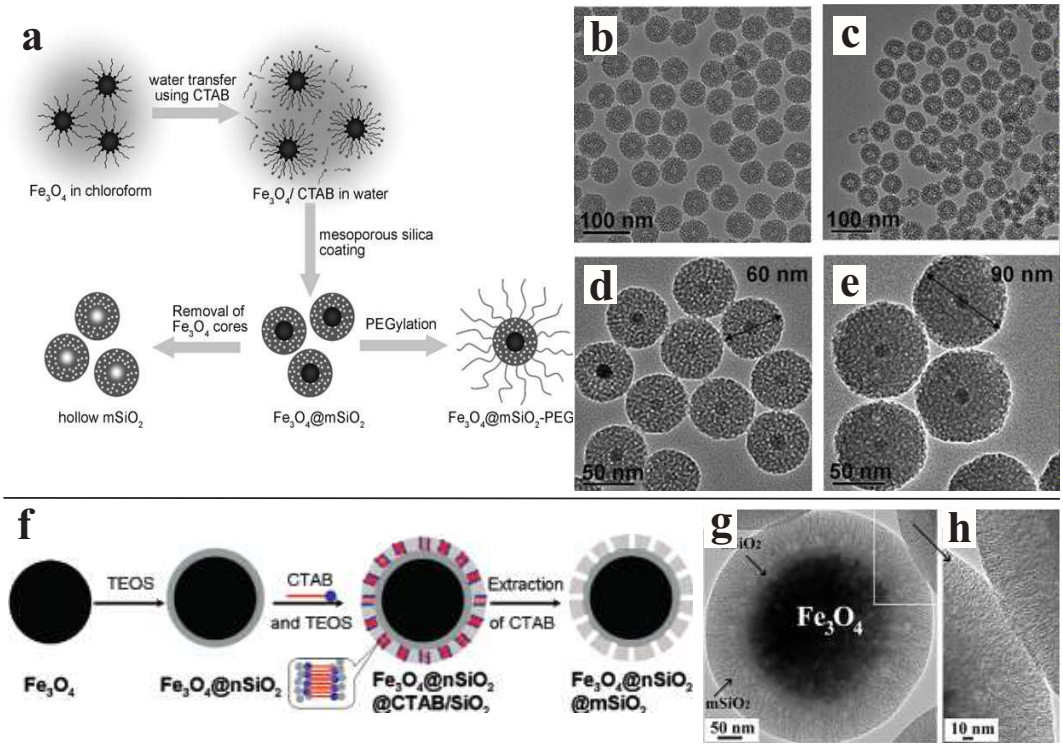

Figure 5.14: Encapsulation of magnetic NPs with mesoporous silica. (a) Scheme illustrating the synthetic procedure to create mesoporous silica coated Fe_3O_4 NPs, or hollow mesoporous silica partilces. (b,c) TEM images of hollow mesoporous silica NPs. (d,e) TEM images of mesoporous silica coated magnetite NPs. (from ref[9]) (f) Scheme depicting the experimental process to create Fe_3O_4@nSiO_2@mSiO_2 microspheres. (g) TEM image showing the thin nSiO_2 layer between Fe_3O_4 and mSiO_2, (h) the porosity in the mSiO_2 shell. (From ref.[106])

strong magnetic responsivity, orientated, accessible mesopores and high colloidal stability are highly valuable for biomedical applications.[107–111] Hyeon and coworkers designed magnetically separable high-performance biocatalysts by cross-linking enzyme molecules on the surface of the Fe_3O_4@SiO_2 nanoparticles.[112] In a similar fashion, discrete and monodisperse mesoporous silica nanoparticles consisting of a single Fe_3O_4 nanocrystal core and a mesoporous silica shell were prepared (see Figure 5.14a-e).[9] The integrated capability of the core-mesoporous-shell structured NPs as MR and fluorescence imaging agents, along with their potential use as a drug delivery vehicles, makes them promising candidates for fu-

ture cancer diagnosis and therapy. However, the highly porous structure of the silica shell permits an easy diffusion of water molecules to the core particle, leading to a possible degradation through metal ion leaching. An improvement of the core-mesoporous-shell approach was reported by Deng et *al.*, who incorporated a thin non-porous silica layer between the magnetic core and the mesoporous shell (Fe_3O_4@nSiO_2@mSiO_2) to provide additional protection.[106] The approach is shown in Figure 5.14f-h. The nonporous silica interface layer (n) is thought to protect the magnetite from leaching, whereas the outer mesoporous (m) silica shell not only offers a high surface area for the derivation of numerous functional groups, but also provides a large accessible pore volume for the adsorption and encapsulation of various agents, like drugs, biomacromolecules or even functional nanoparticles. Additionally, the authors demonstrated, that the Fe_3O_4@nSiO_2@mSiO_2 microspheres still showed superparamagnetic behavior.
Unfortunately, most synthetic routes for the preparation of mesoporous silica coated NPs, are based on templating procedures in aqueous solution.[113] In most approaches, CTAB is used as templating agent to form long tubular structures, around which the silica shell is polymerized. Subsequently, the template is removed either thermally or by chemical treatment yielding highly ordered mesoporous matrices. Since microemulsion techniques are not applicable in this case, Stöber-type methods have to be used, which limits the size of the nanocomposites to diameters larger than 50 nm. This hampers a potential *in vivo* application of these particles.

5.5 References

[1] Cedervall, T.; Lynch, I.; Lindman, S.; Berggard, T.; Thulin, E.; Nilsson, H.; Dawson, K. A.; Linse, S. *Proceedings of the National Academy of Sciences* **2007**, *104*, 2050–2055.

[2] Bruchez, M., JR.; Moronne, M.; Gin, P.; Weiss, S.; Alivisatos, A. *Science* **1998**, *281*, 2013–2016.

[3] Chan, W. C. n.; W.,; Nie, S. *Science* **1998**, *281*, 2016–2018.

[4] Michalet, X.; Pinaud, F. F.; Bentolila, L. A.; Tsay, J. M.; Doose, S.; Li, J. J.; Sundaresan, G.; Wu, A. M.; Gambhir, S. S.; Weiss, S. *Science* **2005**, *307*, 538–544.

[5] Qin, J.; Laurent, S.; Jo, Y.; Roch, A.; Mikhaylova, M.; Bhujwalla, Z.; Muller, R.; Muhammed, M. *Advanced Materials* **2007**, *19*, 1874–1878.

[6] de Palma, R.; Peeters, S.; van Bael, M. J.; van den Rul, H.; Bonroy, K.; Laureyn, W.; Mullens, J.; Borghs, G.; Maes, G. *Chemistry of Materials* **2007**, *19*, 1821–1831.

[7] Shen, L.; Laibinis, P. E.; Hatton, T. A. *Langmuir* **1999**, *15*, 447–453.

[8] Sousa, M. H.; Tourinho, F. A.; Depeyrot, J. A. A.; da Silva, G. J. A.; Lara, M. C. F. L. *Journal of Physical Chemistry B* **2001**, *105*, 1168–1175.

[9] Kim, J.; Kim, H. S.; Lee, N.; Kim, T.; Kim, H.; Yu, T.; Song, I. C.; Moon, W. K.; Hyeon, T. *Angewandte Chemie International Edition* **2008**, *47*, 8438–8441.

[10] Jun, Y.-w.; Lee, J.-H.; Cheon, J. *Angewandte Chemie International Edition* **2008**, *47*, 5122–5135.

[11] Wooding, A.; Kilner, M.; Lambrick, D. B. *Journal of Colloid and Interface Science* **1991**, *144*, 236–242.

[12] Dubertret, B.; Skourides, P.; Norris, D. J.; Noireaux, V.; Brivanlou, A. H.; Libchaber, A. *Science* **2002**, *298*, 1759–1762.

[13] Nitin, N.; LaConte, L.; Zurkiya, O.; Hu, X.; Bao, G. *Journal of Biological Inorganic Chemistry* **2004**, *9*, 706–712.

[14] Medintz, I. L.; Uyeda, H.; Goldman, E. R.; Mattoussi, H. *Nature Materials* **2005**, *4*, 435–446.

[15] Qin, J.; Jo, Y.; Muhammed, M. *Angewandte Chemie International Edition* **2009**, *48*, 7845–7849.

[16] Seo, W. S.; Lee, J. H.; Sun, X.; Suzuki, Y.; Mann, D.; Liu, Z.; Terashima, M.; Yang, P. C.; McConnell, M. V.; Nishimura, D. G.; Dai, H. *Nature Materials* **2006**, *5*, 971–976.

[17] Na, H. B.; Lee, J. H.; An, K.; Park, Y. I.; Park, M.; Lee, S.; Nam, D. H.; Kim, S. T.; Kim, S. H.; Kim, S. W.; Lim, K. H.; Kim, K. S.; Kim, S. O.; Hyeon, T. *Angewandte Chemie International Edition* **2007**, *46*, 5397–5401.

[18] Shin, J.; Anisur, R.; Ko, M.; Im, G.; Lee, J.; Lee, I. *Angewandte Chemie International Edition* **2009**, *48*, 321–324.

[19] Robinson, D. B.; Persson, H. H.; Zeng, H.; Li, G.; Pourmand, N.; Sun, S.; Wang, S. X. *Langmuir* **2005**, *21*, 3096–3103.

[20] Kim, S.-W.; Kim, S.; Tracy, J. B.; Jasanoff, A.; Bawendi, M. G. *Journal of the American Chemical Society* **2005**, *127*, 4556–4557.

[21] Lattuada, M.; Hatton, T. A. *Langmuir* **2007**, *23*, 2158–2168.

[22] Yu, W. W.; Chang, E.; Sayes, C. M.; Drezek, R.; Colvin, V. L. *Nanotechnology* **2006**, *17*, 4483–4487.

[23] Yu, W. W.; Chang, E.; Falkner, J. C.; Zhang, J.; Al-Somali, A. M.; Sayes, C. M.; Johns, J.; Drezek, R.; Colvin, V. L. *Journal of the American Chemical Society* **2007**, *129*, 2871–2879.

[24] Harris, J. M. *Poly(ethylene glycol) chemistry: Biotechnical and biomedical applications*; Topics in applied chemistry; Plenum Press: New York, 1992.

[25] Gref, R.; Minamitake, Y.; Peracchia, M. T.; Trubetskoy, V.; Torchilin, V.; Langer, R. *Science* **1994**, *263*, 1600–1603.

[26] Bazile, D.; Prud'homme, C.; Bassoullet, M. T.; Marlard, M.; Spenlehauer, G.; Veillard, M. *Journal of Pharmaceutical Sciences* **1995**, *84*, 493–498.

[27] Knop, K.; Hoogenboom, R.; Fischer, D.; Schubert, U. *Angewandte Chemie International Edition* **2010**, *49*, 6288–6308.

[28] Pearson, R. G. *Journal of the American Chemical Society* **1963**, *85*, 3533–3539.

[29] Wan, M.; Li, J. *Journal of Polymer Science A: Polymer Chemistry* **1998**, *36*, 2799–2805.

[30] Butterworth, M. D.; Bell, S. A.; Armes, S. P.; Simpson, A. W. *Journal of Colloid and Interface Science* **1996**, *183*, 91–99.

[31] Tartaj, P.; Morales, M. P.; González-Carreño, T.; Veintemillas-Verdaguer, S.; Serna, C. J. *Journal of Magnetism and Magnetic Materials* **2005**, *290-291*, 28–34.

[32] Barratt, G. *Cellular and Molecular Life Sciences* **2003**, *60*, 21–37.

[33] Xia, T.; Kovochich, M.; Liong, M.; Meng, H.; Kabehie, S.; George, S.; Zink, J. I.; Nel, A. E. *ACS Nano* **2009**, *3*, 3273–3286.

[34] Radu, D. R.; Lai, C.-Y.; Jeftinija, K.; Rowe, E. W.; Jeftinija, S.; Lin, V. S. Y. *Journal of the American Chemical Society* **2004**, *126*, 13216–13217.

[35] Josephson, L.; Tung, C. H.; Moore, A.; Weissleder, R. *Bioconjugate Chemistry* **1999**, *10*, 186–191.

[36] Zhao, D.-L.; Wang, X.-X.; Zeng, X.-W.; Xia, Q.-S.; Tang, J.-T. *Journal of Alloys and Compounds* **2009**, *477*, 739–743.

[37] Mahmoudi, M.; Simchi, A.; Imani, M.; Häfeli, U. O. *Journal of Physical Chemistry C* **2009**, *113*, 8124–8131.

[38] Uyeda, H.; Medintz, I. L.; Jaiswal, J. K.; Simon, S. M.; Mattoussi, H. *Journal of the American Chemical Society* **2005**, *127*, 3870–3878.

[39] Kim, S.-W.; Kim, S.; Tracy, J. B.; Jasanoff, A.; Bawendi, M. G. *Journal of the American Chemical Society* **2005**, *127*, 4556–4557.

[40] Nikolic, M. S.; Krack, M.; Aleksandrovic, V.; Kornowski, A.; Förster, S.; Weller, H. *Angewandte Chemie* **2006**, *118*, 6727–6731.

[41] Tromsdorf, U. I.; Bigall, N. C.; Kaul, M. G.; Bruns, O. T.; Nikolic, M. S.; Mollwitz, B.; Sperling, R. A.; Reimer, R.; Hohenberg, H.; Parak, W. J.; Forster, S.; Beisiegel, U.; Adam, G.; Weller, H. *Nano Letters* **2007**, *7*, 2422–2427.

[42] Frey, N. A.; Peng, S.; Cheng, K.; Sun, S. *Chemical Society Reviews* **2009**, *38*, 2532–2542.

[43] Waite, J. H.; Tanzer, M. L. *Science* **1981**, *212*, 1038–1040.

[44] Xu, C.; Xu, K.; Gu, H.; Zheng, R.; Liu, H.; Zhang, X.; Guo, Z.; Xu, B. *Journal of the American Chemical Society* **2004**, *126*, 9938–9939.

[45] Song, H. M.; Kim, Y. J.; Park, J. H. *Journal of Physical Chemistry C* **2008**, *112*, 5397–5404.

[46] Shukoor, M. I.; Natalio, F.; Tahir, M. N.; Ksenofontov, V.; Therese, H. A.; Theato, P.; Schroder, H. C.; Muller, W. E. G.; Tremel, W. *Chemical Communications* **2007**, *43*, 4677–4679.

[47] Shukoor, M.; Natalio, F.; Ksenofontov, V.; Tahir, M.; Eberhardt, M.; Theato, P.; Schröder, H.; Müller, W.; Tremel, W. *Small* **2007**, *3*, 1374–1378.

[48] Schröder, H. C.; Natalio, F.; Wiens, M.; Tahir, M. N.; Shukoor, M. I.; Tremel, W.; Belikov, S. I.; Krasko, A.; Müller, W. E. G. *Molecular Immunology* **2008**, *45*, 945–953.

[49] Shukoor, M.; Natalio, F.; Metz, N.; Glube, N.; Tahir, M.; Therese, H.; Ksenofontov, V.; Theato, P.; Langguth, P.; Boissel, J. P.; Schröder, H. C.; Müller, W. E. G.; Tremel, W. *Angewandte Chemie International Edition* **2008**, *47*, 4748–4752.

[50] Shukoor, M. I.; Natalio, F.; Therese, H. A.; Tahir, M. N.; Ksenofontov, V.; Panthöfer, M.; Eberhardt, M.; Theato, P.; Schröder, H. C.; Müller, W. E. G.; Tremel, W. *Chemistry of Materials* **2008**, *20*, 3567–3573.

[51] Shukoor, M. I.; Natalio, F.; Tahir, M. N.; Divekar, M.; Metz, N.; Therese, H. A.; Theato, P.; Ksenofontov, V.; Schröder, H. C.; Müller, W. E. G.; Tremel, W. *Journal of Magnetism and Magnetic Materials* **2008**, *320*, 2339–2344.

[52] Schladt, T. D. et al. *Angewandte Chemie International Edition* **2010**, *49*, 3976–3980.

[53] Vestal, C. R.; Zhang, Z. *Journal of the American Chemical Society* **2002**, *124*, 14312–14313.

[54] Wang, Y.; Teng, X.; Wang, J.-S.; Yang, H. *Nano Letters* **2003**, *3*, 789–793.

[55] Edmondson, S.; Osborne, V. L.; Huck, W. T. S. *Chemical Society Reviews* **2004**, *33*, 14–22.

[56] Bourlinos, A.; Bakandritsos, A.; Georgakilas, V.; Petridis, D. *Chemistry of Materials* **2002**, *14*, 3226–3228.

[57] Vo, D. Q.; Kim, E.-J.; Kim, S. *Journal of Colloid and Interface Science* **2009**, *337*, 75–80.

[58] Gawalt, E. S.; Avaltroni, M. J.; Danahy, M. P.; Silverman, B. M.; Hanson, E. L.; Midwood, K. S.; Schwarzbauer, J. E.; Schwartz, J. *Langmuir* **2003**, *19*, 7147–7147.

[59] Traina, C. A.; Schwartz, J. *Langmuir* **2007**, *23*, 9158–9161.

[60] Warner, M. G.; Reed, S. M.; Hutchison, J. E. *Chemistry of Materials* **2000**, *12*, 3316–3320.

[61] Salgueirino-Maceira, V.; Liz-Marz\ÂŽ{a}n, L. M.; Farle, M. *Langmuir* **2004**, *20*, 6946–6950.

[62] Xu, C.; Xu, K.; Gu, H.; Zheng, R.; Liu, H.; Zhang, X.; Guo, Z.; Xu, B. *Journal of the American Chemical Society* **2004**, *126*, 9938–9939.

[63] Xie, J.; Xu, C.; Xu, Z.; Hou, Y.; Young, K. L.; Wang, S. X.; Pourmand, N.; Sun, S. *Chemistry of Materials* **2006**, *18*, 5401–5403.

[64] Gu, H.; Yang, Z.; Gao, J.; Chang, C.; Xu, B. *Journal of the American Chemical Society* **2005**, *127*, 34–35.

[65] Xie, J.; Xu, C.; Kohler, N.; Hou, Y.; Sun, S. *Advanced Materials* **2007**, *19*, 3163–3166.

[66] Vaccaro, E.; Waite, J. H. *Biomacromolecules* **2001**, *2*, 906–911.

[67] Holten-Andersen, N.; Mates, T. E.; Toprak, M. S.; Stucky, G. D.; Zok, F. W.; Waite, J. H. *Langmuir* **2009**, *25*, 3323–3326.

[68] Harrington, M. J.; Masic, A.; Holten-Andersen, N.; Waite, J. H.; Fratzl, P. *Science* **2010**, *328*, 216–220.

[69] Xu, C.; Xu, K.; Gu, H.; Zhong, X.; Guo, Z.; Zheng, R.; Zhang, X.; Xu, B. *Journal of the American Chemical Society* **2004**, *126*, 3392–3393.

[70] Shultz, M. D.; Reveles, J.; Khanna, S. N.; Carpenter, E. E. *Journal of the American Chemical Society* **2007**, *129*, 2482–2487.

[71] Hong, R.; Fischer, N. O.; Emrick, T.; Rotello, V. M. *Chemistry of Materials* **2005**, *17*, 4617–4621.

[72] Chen, L. X.; Liu, T.; Thurnauer, M. C.; Csencsits, R.; Rajh, T. *Journal of Physical Chemistry B* **2002**, *106*, 8539–8546.

[73] Boal, A. K.; Das, K.; Gray, M.; Rotello, V. M. *Chemistry of Materials* **2002**, *14*, 2628–2636.

[74] Somaskandan, K.; Veres, T.; Niewczas, M.; Simard, B. *New Journal of Chemistry* **2008**, *32*, 201–209.

[75] Gao, J.; Liang, G.; Cheung, J. S.; Pan, Y.; Kuang, Y.; Zhao, F.; Zhang, B.; Zhang, X.; Wu, E. X.; Xu, B. *Journal of the American Chemical Society* **2008**, *130*, 11828–11833.

[76] Peng, S.; Wang, C.; Xi, J.; Sun, S. *Journal of the American Chemical Society* **2006**, *128*, 10676–10677.

[77] Wang, B.; Xu, C.; Xie, J.; Yang, Z.; Sun, S. *Journal of the American Chemical Society* **2008**, *130*, 14436–14437.

[78] Cheng, K.; Peng, S.; Xu, C.; Sun, S. *Journal of the American Chemical Society* **2009**, *131*, 10637–10644.

[79] Amstad, E.; Gillich, T.; Bilecka, I.; Textor, M.; Reimhult, E. *Nano Letters* **2009**, *9*, 4042–4048.

[80] Zürcher, S.; Wäckerlin, D.; Bethuel, Y.; Malisova, B.; Textor, M.; Tosatti, S.; Gademann, K. *Journal of the American Chemical Society* **2006**, *128*, 1064–1065.

[81] Amstad, E.; Zurcher, S.; Mashaghi, A.; Wong, J. Y.; Textor, M.; Reimhult, E. *Small* **2009**, *5*, 1334–1342.

[82] Nalwa, H. S. *Handbook of surfaces and interfaces of materials*; Academic Press: San Diego, Calif., 2001.

[83] Guerrero-Martínez, A.; Pérez-Juste, J.; Liz-Marzán, L. M. *Advanced Materials* **2010**, *22*, 1182–1195.

[84] Knopp, D.; Tang, D.; Niessner, R. *Analytica Chimica Acta* **2009**, *647*, 14–30.

[85] Herrmann, I. K.; Grass, R. N.; Mazunin, D.; Stark, W. J. *Chemistry of Materials* **2009**, *21*, 3275–3281.

[86] Piao, Y.; Burns, A.; Kim, J.; Wiesner, U.; Hyeon, T. *Advanced Functional Materials* **2008**, *18*, 3745–3758.

[87] Selvan, S. T.; Tan, T. T. Y.; Yi, D. K.; Jana, N. R. *Langmuir* **2010**, *26*, 11631–11641.

[88] Stöber, W.; Fink, A.; Bohn, E. *Journal of Colloid and Interface Science* **1968**, *26*, 62–69.

[89] Ohmori, M.; Matijevic, E. *Journal of Colloid and Interface Science* **1993**, *160*, 288–292.

[90] Liz-Marzán, L. M.; Philipse, A. P. *Journal of Colloid and Interface Science* **1995**, *176*, 459–466.

[91] Schroder, H. C.; Wang, X.; Tremel, W.; Ushijima, H.; Muller, W. E. G. *Natural Product Reports* **2008**, *25*, 455–474.

[92] Plueddemann, E. P. *Silane coupling agents*, 2nd ed.; Plenum Press: New York, 1991.

[93] Chang, S.-Y.; Liu, L.; Asher, S. A. *Journal of the American Chemical Society* **1994**, *116*, 6745–6747.

[94] Santra, S.; Tapec, R.; Theodoropoulou, N.; Dobson, J.; Hebard, A.; Tan, W. *Langmuir* **2001**, *17*, 2900–2906.

[95] Santra, S.; Yang, H.; Dutta, D.; Stanley, J. T.; Holloway, P. H.; Tan, W.; Moudgil, B. M.; Mericle, R. A. *Chemical Communications* **2004**, *40*, 2810–2811.

[96] Yi, D. K.; Selvan, S.; Lee, S. S.; Papaefthymiou, G. C.; Kundaliya, D.; Ying, J. Y. *Journal of the American Chemical Society* **2005**, *127*, 4990–4991.

[97] Li, M.; Schnablegger, H.; Mann, S. *Nature* **1999**, *402*, 393–395.

[98] Cushing, B. L.; Kolesnichenko, V. L.; O'Connor, C. J. *Chemical Reviews* **2004**, *104*, 3893–3946.

[99] van Blaaderen, A.; Vrij, A. *Langmuir* **1992**, *8*, 2921–2931.

[100] Imhof, A.; Megens, M.; Engelberts, J.; de Lang, D.; Sprik, R.; Vos, W. *Journal of Physical Chemistry B* **1999**, *103*, 1408–1415.

[101] Li, Z.; Ruckenstein, E. *Nano Letters* **2004**, *4*, 1463–1467.

[102] Burns, A.; Ow, H.; Wiesner, U. *Chemical Society Reviews* **2006**, *35*, 1028–1042.

[103] Wang, L.; Wang, K.; Santra, S.; Zhao, X.; Hilliard, L. R.; Smith, J. E.; Wu, Y.; Tan, W. *Analytical Chemistry* **2006**, *78*, 646–654.

[104] Fuller, J. E.; Zugates, G. T.; Ferreira, L. S.; Ow, H. S.; Nguyen, N. N.; Wiesner, U. B.; Langer, R. S. *Biomaterials* **2008**, *29*, 1526–1532.

[105] Burns, A. A.; Vider, J.; Ow, H.; Herz, E.; Penate-Medina, O.; Baumgart, M.; Larson, S. M.; Wiesner, U.; Bradbury, M. *Nano Letters* **2009**, *9*, 442–448.

[106] Deng, Y.; Qi, D.; Deng, C.; Zhang, X.; Zhao, D. *Journal of the American Chemical Society* **2008**, *130*, 28–29.

[107] Sen, T.; Sebastianelli, A.; Bruce, I. J. *Journal of the American Chemical Society* **2006**, *128*, 7130–7131.

[108] He, Q.; Zhang, Z.; Gao, Y.; Shi, J.; Li, Y. *Small* **2009**, *5*, 2722–2729.

[109] Coti, K. K.; Belowich, M. E.; Liong, M.; Ambrogio, M. W.; Lau, Y. A.; Khatib, H. A.; Zink, J. I.; Khashab, N. M.; Stoddart, J. F. *Nanoscale* **2009**, *1*, 16–39.

[110] Zhu, Y.; Ikoma, T.; Hanagata, N.; Kaskel, S. *Small* **2010**, *6*, 471–478.

[111] Suteewong, T.; Sai, H.; Lee, J.; Bradbury, M.; Hyeon, T.; Gruner, S. M.; Wiesner, U. *Journal of Materials Chemistry* **2010**, *46*, DOI:10.1039/C0JM01002B.

[112] Lee, J.; Lee, Y.; Youn, J. K.; Na, H. B.; Yu, T.; Kim, H.; Lee, S. M.; Koo, Y. M.; Kwak, J. H.; Park, H. G.; Chang, H. N.; Hwang, M.; Park, J. G.; Kim, J.; Hyeon, T. *Small* **2008**, *4*, 143–152.

[113] Gao, C.; Che, S. *Advanced Functional Materials* **2010**, *20*, 2750–2768.

CHAPTER 6

Biomedical Applications of Magnetic NPs

The use of nanotechnology in biology and medicine has led to tremendous breakthroughs in the past decades, and yet, since research activities in this scientific area are proceeding with great speed, nano-biotechnology and nanomedicine are offering numerous exciting possibilities for the future. Already in the 1960's, artificial liposomes were suggested as carriers of proteins and drugs for the treatment of various diseases,[1] and since then nanotechnology has had a major impact on the development of drug delivery systems. But the application of nanotechnology is not only limited to drug delivery, various organic/inorganic nanostructures are currently being applied or show promising potential in many different biomedical areas including *in vitro* diagnostics, *in vivo* imaging, therapy of various diseases (like cancer, cardiovascular and neurological diseases), biomaterials, and tissue engineering.[2–8] Up to now, there are over 40 FDA approved nanomedicine products on the market and even more are currently in clinical trials,[2, 3] most of them being used for drug delivery applications (see Figure 6.1). In fact, early clinical results suggest that nanoparticle therapeutics can show enhanced efficiency compared to conventional drugs, while at the same time, negative side effects can be reduced significantly.[9, 10] This is due to a more targeted localization inside the desired area of the body (e.g. tumor tissue), either by passive or active cell tar-

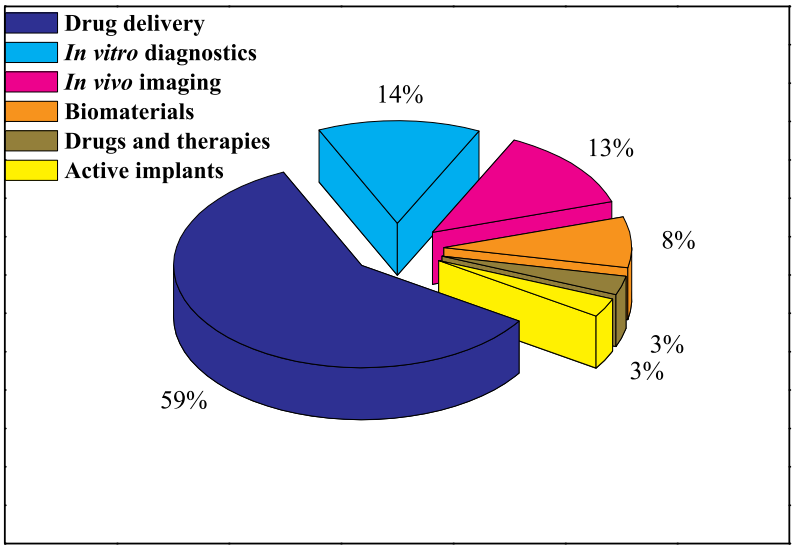

Figure 6.1: Fractions of nanomedicine patents worldwide from 1993-2003. Taken from ref. [2]

geting, followed by active cellular uptake of the nanoparticle probe. Moreover, the utilization of magnetic nanoparticles for simultaneous real-time *in vivo* monitoring of drug delivery is also an area of intense interest, owing to their MR enhancing properties (see section 2.4).

One of the greatest challenges associated with the use of magnetic NPs *in vivo* is the ability to circumvent or overcome the different biological barriers. As an example, the targeting efficiency of nanoparticulate probes is often limited by the precocious recognition and elimination by the reticuloendothelial system (RES). In this respect, the overall NP size, morphology, charge and surface chemistry are crucial properties that determine, not only the circulation time inside the blood vessels, but also the final distribution within in the body.[11–13] In the following, the basic principles of nanoparticle design for biomedical applications, the fundamental interactions with biological systems, as well as the biodistribution and clearance of magnetic NPs from living organisms will be discussed briefly.

6.1 Design Considerations

As mentioned in chapters 3, 4 and 5, there have been remarkable advances in nanomaterial synthesis and functionalization, which today allow a precise engineering of the composition, size, size distribution, morphology, and surface chemistry of magnetic NPs. Both, magnetic properties and surface features, can be tailored individually to meet the particular challenges of *in vitro* and *in vivo* biomedical applications.
Before magnetic NPs can be used for biomedical applications, they require thorough consideration concerning the assembly of different components (see Figure 6.2).

1. First, of course, the NPs themselves act as the active part of the nanocomposite probe, since they represent the platform, on which all other constituents will be assembled, and, depending on their physical properties (magnetic, optical), they are the key factor that ensures the detection of diseases inside the body.

2. The NPs need an inert and hydrophilic shell, that protects them and offers both, stability in biological systems and long circulation times in the cardiovascular system. However, this attribute was already thoroughly discussed in chapter 5.

3. Certain fluorophores, that permit a later detection by optical methods may also be included.

4. Additionally, specific targeting ligands, which recognize certain kinds of cells inside the body, can be attached to the surface of the nanocomposite to ensure a selective delivery to the target tissue.

5. Moreover, responsive moieties can also be included that will react to external excitation, e.g. photosensitizers to produce reactive oxygen species (ROS) upon optical excitation, or gold NPs which produce heat upon NIR-illumination.

6. Lastly, certain drugs may also be attached to the composite to allow a specific treatment in a spatially confined area. In this respect, special responsive

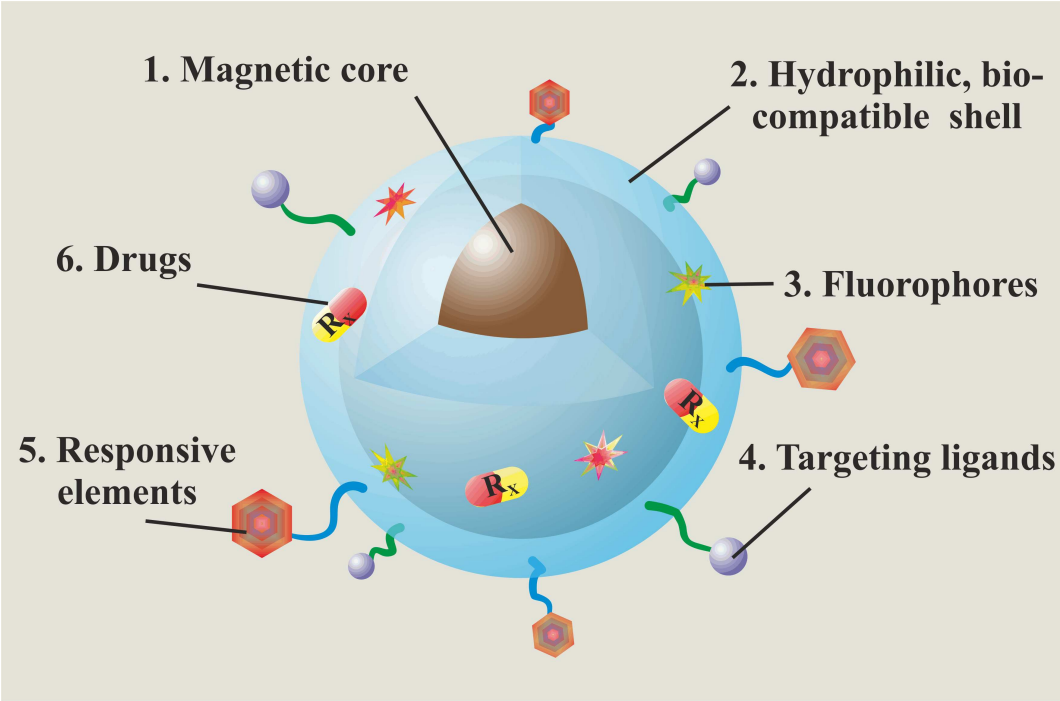

Figure 6.2: Illustration of a multifunctional magnetic nanoparticle. Adapted from ref. [14]

linker molecules, which will cleave under an external stimulus (e.g. heat, pH, enzymatic cleavage), could guarantee a safe delivery of the payload to the desired region.

Additionally, the overall size of the multifunctional magnetic NPs must also be considered. Their hydrodynamic size, which is defined as the overall size of the particle including the solvent shell, is strongly correlated to the ability of the nanoparticle to overcome the initial biological defense system and penetrate through the vascular barriers. On the one hand, the size of the NPs must be sufficiently small to avoid rapid splenic filtration, on the other hand, they should be large enough to circumvent renal clearance.[14, 15] It has been shown, that particles with sizes larger than 200 nm are quickly attacked by phagocytotic cells of the spleen, whereas particles with an average diameter below 5.5 nm are rapidly removed through the kidneys (see Figure 6.3).[16–18] However, particles of the appropriate size range are subject to opsonization, resulting in recognition and elimination by Kupffer cells and

other tissue macrophages, unless they are not protected by an inert hydrophilic shell (see chapter 5).[14, 19] For these NPs, immediate opsonization and/or phagocytosis is reduced.
Furthermore, the surface charge of the magnetic NPs also plays a crucial role in cellular uptake and blood half-life.[13, 20–22] In fact, it has been shown, that positively charged polymers and small particles tend to non-specifically stick to the surface of cells.[23] How great the impact of this non-specific interaction actually is, regarding the blood circulation time, was demonstrated by Papisov et *al.*[24] On the other hand, strong negative charges on the particle surface are also unfavorable, since they lead to increased liver uptake.[11] Therefore, it has to be estimated that NPs with a near neutral surface charge exhibit prolonged blood circulation times.

6.2 Passive Cell-Targeting

After multifunctional NPs are intravenously injected, they travel along the blood stream through the cardiovascular system. At this point, the surface chemistry can change significantly by the adsorption of proteins, demonstrating the importance of an efficient shielding of the NPs ("stealth effect", see chapter 5).[25] During blood circulation, there is a constant exchange of blood substances through the capillary microcirculation, which is regulated by concentration gradients. Since after injection the local NP concentration in the blood is very high, compared to th extravascular space, the NPs will slowly travel outside the blood vessels into the surrounding extracellular matrix (ECM), as long as the gradient persists. Once in the extravascular space, some NPs are taken up by the cells of the tissue and others are retained in the interstitial fluid, eventually entering the lymphatic system.[26–28] However, these processes are comparatively slow.
On the other hand, a faster diffusion of macromolecules and NPs into the ECM is observed in tumor tissue, a feature commonly referred to as enhanced permeability and retention (EPR) effect (see Figure 6.3).[29] This effect originates from the intrinsic vascular characteristics of tumor tissue and the lack of an efficient lymphatic recovery system in solid tumors. In contrast to the vasculature in healthy tissue, the blood vessels, that sustain a tumor, are leaky, with large fenestrations and without an effective clearance by the lymphatic system. This leads to a preferred accumula-

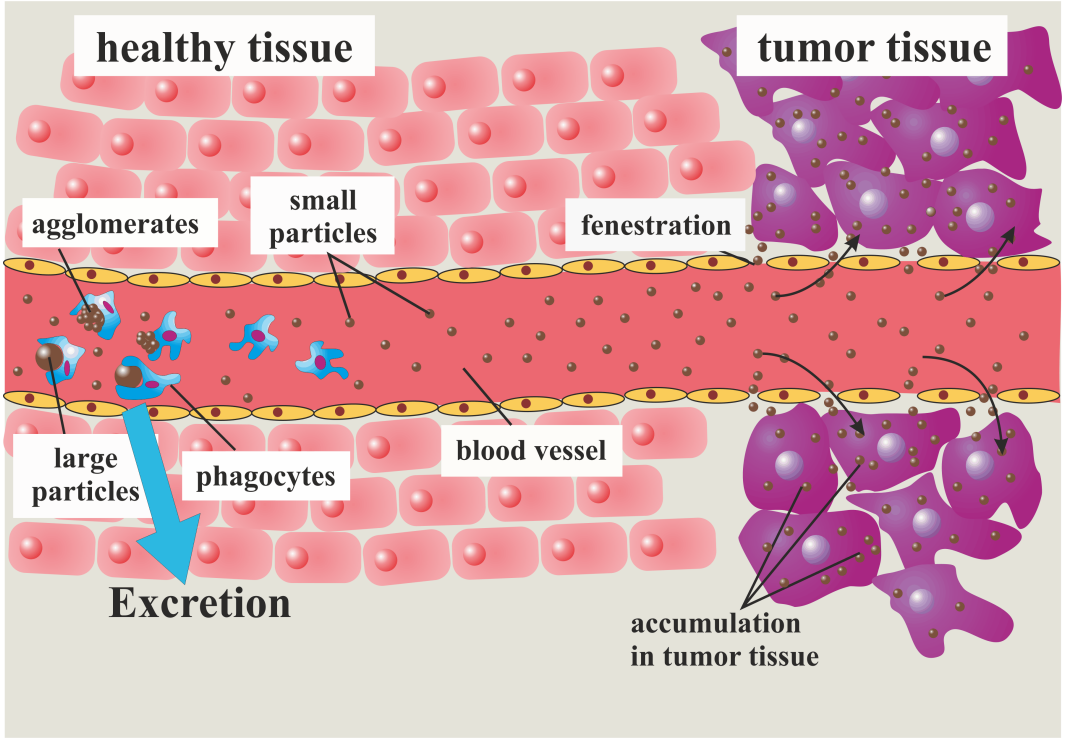

Figure 6.3: Illustration of passive tumor targeting with magnetic NPs: large particles and agglomerates are rapidly attacked by phagocytes, smaller particles can ravel longer through the blood vessels to reach their target site. Once at the tumor site, the magnetic NPs are accumulated inside the tumor tissue due to the EPR effect.

tion of the NPs in the interstitial space inside the tumor, and eventually, the uptake of the nanocomposites into the tumor cells.[30, 31]

Passive targeting can also be exploited through the clearance of NPs by the reticuloendothelial system (RES) (i.e. liver, spleen, lymph nodes and bone marrow). Indeed, the first clinically approved T_2 contrast agents for MRI, based on magnetic iron oxide NPs, benefited from the rapid uptake of the NPs by Kupffer cells of healthy hepatic parenchyma. Thus, healthy tissue appeared darker than diseased tissue in the MR image, due to enhanced T_2 contrast, leading to an improved diagnostic differentiation.[32–34]

However, a successful passive targeting of tumor tissue can only be achieved, if the blood circulation time of the NPs is reasonably long. This is another reason, why

efficient surface functionalization strategies are of supreme importance.

6.3 Active Cell-Targeting

There is no doubt about the fact, that the passive accumulation of magnetic NPs in tumor tissue due to the EPR effect is a great benefit for the application of these NPs in the diagnosis and treatment of cancer. Nevertheless, a longer residence time and a more site-specific accumulation of the NP probes is desired in most cases. For this reason, active targeting strategies have been developed, in which magnetic NPs were further functionalized with specific targeting molecules that possess a high affinity toward unique molecular signatures found on malignant cells (see Figure 6.4).[14, 34] The key issue in this case is the fact that cancer cells overexpress certain kinds of receptors compared to healthy cells. Therefore, NPs carrying ligands which will specifically bind to these receptors will preferably accumulate in tumor tissue and , eventually, will be taken up by the cancer cells. Several targeting ligands, including proteins, peptides, aptamers and small molecules, have been examined for this purpose.[35–42]

The first targeting agents, that were used for the specific delivery of magnetic NPs, comprised monoclonal antibodies (mAbs).[43, 44] Up to the present day, mAbs have evolved as one of the most popular targeting ligands, which is mainly due to their extremely high specificity.[45, 46] During the last decade, the development of Herceptin^{TM}(trastuzumab), an FDA-approved mAb that binds to the HER2 /*neu* receptor on the surface of certain cancer cells (overexpressed in breast, ovarian, stomach cancer), has lead to various applications of magnetic NPs for selective targeting of cancer cells.[47–49] However, a major drawback of mAbs is their comparatively large size and inherent immunogenicity, which impedes a sufficient circulation and diffusion through biological barriers.[50]

Another popular technique for the targeted delivery of magnetic NPs to tumor cells, is the use of short peptides or small molecules conjugated to the NP surface. The advantage, in these cases, is the possibility to attach several (hundreds, or even thousands of) targeting ligands on each NP. As a result, more cell receptors can be addressed simultaneously, leading to the formation of more bonding sites, and therefore, an increased binding affinity.[37] The most investigated ligand in this respect

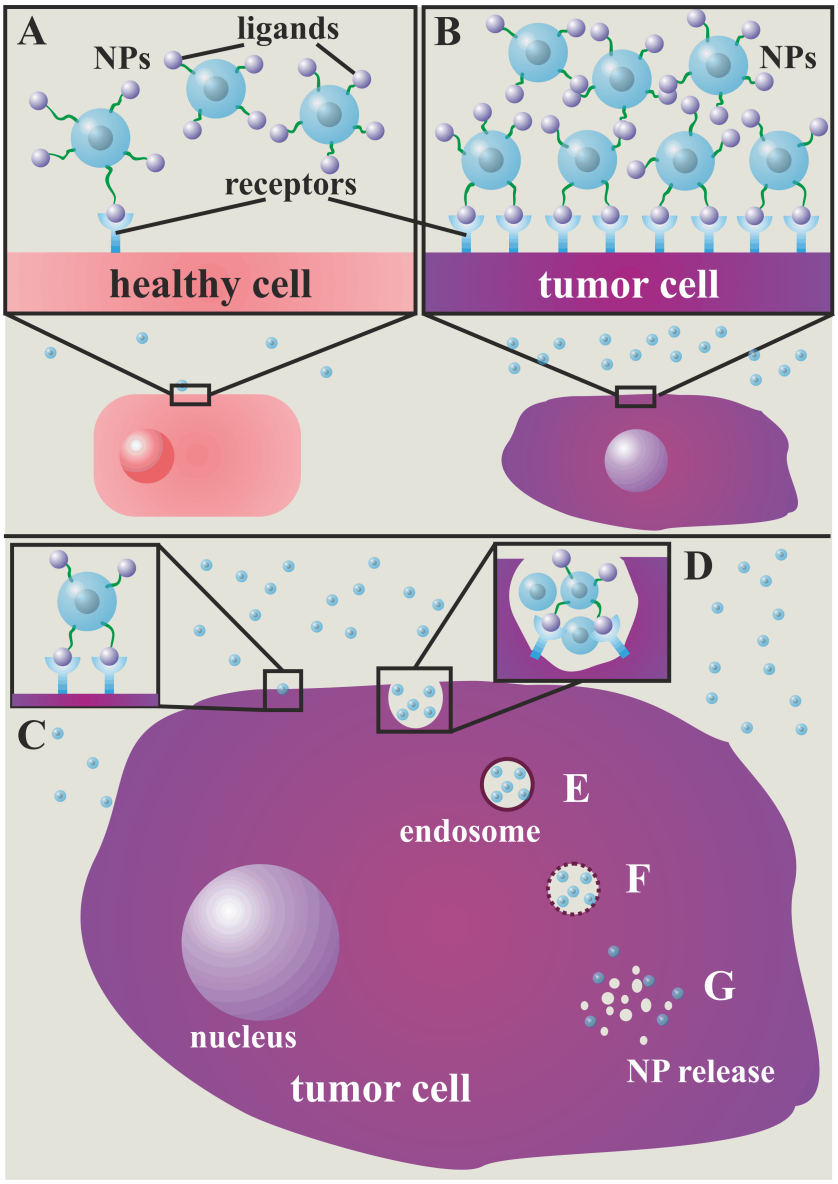

Figure 6.4: Illustration of active tumor trageting using magnetic NPs with cell-specific ligands: (A) healthy cells carry a certain number of specific cell receptors, which can be used for active targeting, (B) in cancer cells these receptors are overexpressed, which leads to accumulation of the magnetic NPs on the surface of malignant cells. (C) Receptor-mediated endocythosis of the NPs, (D) formation of an endosome carrying the NPs, (E) the endosome is internalized into the cell, (F) endosomal acidification by proton pumps leads to elevated osmotic pressure and swelling, (G) finally, the endosome ruptures, releasing the magnetic NPs.

is folic acid, since the receptors of this vitamin can be found on the surface of many human cancer cells, including breast, ovarian, lung, renal, and colon cancer.[51] Indeed, folic acid modified magnetic NPs have been used in the past, not only to improve the MRI detectability of various tumors *in vivo*[52–54] but also to destroy cancer cells via hyperthermia treatment.[55] A great advantage of short peptides and other small molecules is their high bonding strength once they are conjugated to the NP surface. Compared to large peptides or proteins, there is a reduced risk of bond breaking and loss of functionality after administration of the NPs into the body.

Another important issue associated with the targeted delivery of magnetic NPs to tumor cells is the internalization of the particles into the malignant cell. In principle, there are several possible mechanisms for the cellular uptake of NPs. For example, it has been shown, that small PEGylated NPs can easily diffuse through the cell membrane,[52, 56], on the other hand, permeation enhancers, such as TAT peptides, can significantly increase the degree of NP uptake.[57–60]. The typical pathway for a receptor-mediated cellular uptake of NPs is shown in Figure 6.4. After attachment on the cell surface, the NPs are internalized by formation of an endosome.

Figure 6.4 also illustrates another common challenge of targeted (drug) delivery that needs to be addressed for NP design, i.e. the controlled release of the NPs, and especially the loaded therapeutic agents, once the NPs have entered the interior of the cell. Various strategies have been developed to accomplish this task. The release mechanisms of most delivery systems depend on processes such as diffusion, dissolution, chemical and enzymatic reactions, or changes in various environmental factors, including temperature, pH, solvent effects, and ionic concentrations.[61–65] As an example, an efficient release can be achieved by providing a positive surface charge to the NP probe. The incorporation of cationic polymers on NP surfaces has proved to be an appropriate method to induce osmotic swelling of the endosome caused by the "proton sponge" effect.[14, 66, 67] As a result the endosomal membrane is disrupted and the NPs are released into the cytosol. The downside of this approach, however, is the possibility of uncontrolled release due to different release mechanisms depending on the location in and the character of the respective cell. For this reason various methods have been developed that rely on physical triggers, such as heat or radiation, to initiate payload release.[68–71] For these pur-

poses specific stimuli responsive chemical linkers can be tailored and subsequently inserted between the NP and the drug. These strategies can involve bond breaking by radiative excitation, slow diffusion mediated processes from hollow or mesoporous NP structures, or by cleavage of the linker bond by pH reduction inside the lysosome.[72–80]

6.4 MR Imaging Using Magnetic NPs

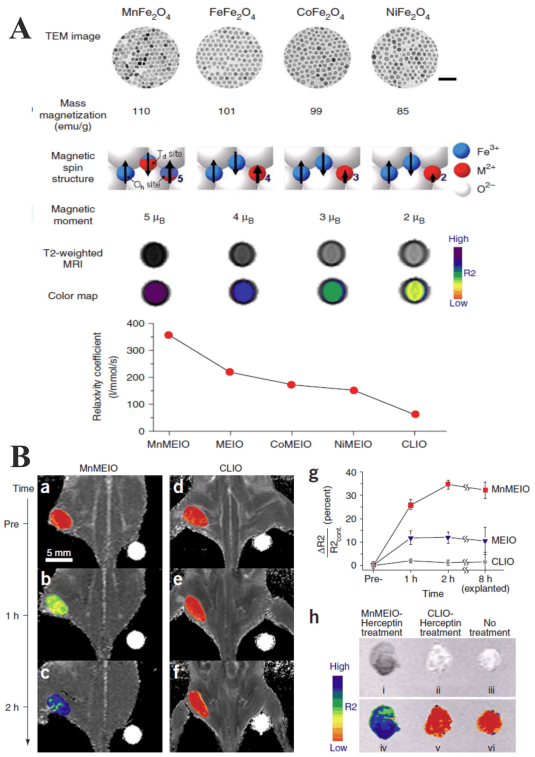

Figure 6.5: Specifically engineered $M\mathrm{Fe_2O_4}$ NPs as MRI contrast agents. (A) The magnetic properties can be tuned by varying the composition of the NPs. A higher magnetic moment leads to an increase in magnetic relaxivity and, therefore, an enhanced T_2 contrast effect. (B) In vivo MR detection of cancer cells using Herceptin conjugated $\mathrm{MnFe_2O_4}$ NPs (left) and bare cross-linked iron oxide NPs (CLIOs) (right), over time an increase in contrast enhancement due to preferable accumulation of Herceptin-conjugates $\mathrm{MnFe_2O_4}$ NPs in the tumor tissue is observed. From ref. [86]

Superparamagnetic iron oxide NPs (SPIONs) have been used as T_2 contrast agents for over two decades.[33, 43, 81] Although enormous progress has been achieved in the technological development of MRI, especially sophisticated pulse sequences for image generation, there has hardly been any improvement in the development of the contrast agents which are in clinical use today.[82] Typical T_2 contrast agents consist of polydisperse and aggregated iron oxide NPs, which show a comparably weak performance. However, as mentioned in chapters 3 and 5, there have been tremendous advances in the synthesis and functionalization of magnetic NPs leading to new possibilities in the future design of MRI contrast enhancing probes.[83–85]

The basic physical phenomena leading to an enhancement in MR contrast were presented in section 2.4. As already mentioned, the nanoparticles must be monodisperse, highly crystalline, and watersoluble to provide reproducible quality, high magnetization values and good biocompatibility under biological conditions. In this respect, magnetic NPs have been studied thoroughly during the past years as MRI contrast agents for applications, such as cancer imaging, cell migration, gene expression, angiogenesis, apoptosis, cardiovascular disease imaging, or molecular imaging.[14, 87–94] Specially designed NPs with tailored properties and cell-specific surface ligands have a great potential to pinpoint biological targets, such as cancer, already in the early stages of the disease.

Concerning cancer imaging, the development of multifunctional magnetic NPs has led to many improvements in the detection, diagnosis and treatment of solid tumors. Weissleder et *al.* demonstrated the transgene expression in gliosarcoma cells *in vivo* using dextran coated iron oxide NPs.[88] As example for magnetic NPs being used as molecular sensors, Perez et *al.* developed biocompatible magnetic nanosensors that act as magnetic relaxation switches to detect molecular interactions (e.g. DNA-DNA, or protein-protein interactions) by the reversible self-assembly of SPIONs.[95] The changes in the magnetic relaxation which are associated with the particle self-assembly could then be detected by MRI. On the other hand, Hu et *al.* showed that PEGylated Fe_3O_4 NPs conjugated to the monoclonal antibody rch 24, effectively targeted human colon carcinoma xenograft tumors implanted in nude mice.[96] Another example, in which magnetic NPs were used to detect cancer markers by MRI *in vivo*, was given by Cheon and coworkers (see Fig-

ure 6.5).[86] The authors developed novel magnetic nanoprobes by systematically tuning the spin, size and composition of metal ferrite NPs, followed by conjugation of different cancer specific antibodies, such as Herceptin. These NPs showed enhanced MRI sensitivity for the detection of cancer and enabled the visualization of small implanted tumors in mice. Hultman et *al.*, on the other hand, created immunotargeted SPIONs to investigate the MHC Class II expression in renal medulla.[97] For this purpose, monodisperse Fe_3O_4 NPs were encapsulated in a phospholipid shell and further conjugated to RT1 anti-MHC Class II antibodies that are capable of targeting normal cells expressing specific target antigens. Enhanced binding of the RT1 functionalized SPIONs indicated a definitive specificity for the renal medulla and thus potential for disease detection. Recently, nanocomposite particles consisting of silica spheres decorated with Fe_3O_4 NPs were synthesized by Lee et *al.* (see Figure 6.6).[98] Additionally, a fluorescent dye was incorporated into the silica domain to permit both MRI and optical detection. The use of mesoporous silica furthermore offered the possibility to load, and slowly release, an anti-cancer drug into the pores of the silica sphere.

Although the use of manganese oxide NP as T_1 contrast agents is not as common yet, there is a number of reports dealing with the design of different manganese oxide NPs and their application for MR contrast enhancement. Hyeon and coworkers were the first to prepare a T_1 contrast agent based on monodisperse MnO NPs and investigate its performance *in vivo* (see Figure 6.7).[99] The particles were coated with an amphiphilic phospholipid, functionalized with Herceptin and showed no severe toxicity even after several weeks. The authors showed that the Herceptin-functionalized NPs accumulated in breast cancer tissue, whereas un-functionalized control NPs also illuminated the surrounding tissue. In a similar way, Shapiro et *al.* showed that un-functionalized Mn_3O_4 and $MnCO_3$ NPs can be internalized within phagocytotic cells and subsequently shuttled to endosomes and/or lysosomes.[100] The following decomposition of the NPs inside the lysosome leads to the release of Mn^{2+} ions which act as T_1 agent. It was also shown that a combination of SPIONs and MnO NPs can be used to track transplanted cells.[91] While the SPIONs produced a negative contrast, the MnO NPs generated a positive contrast and by combination of both imaging techniques, simultaneous imaging with opposite contrast offers the possibility for MR "double labeling" of different cell populations.

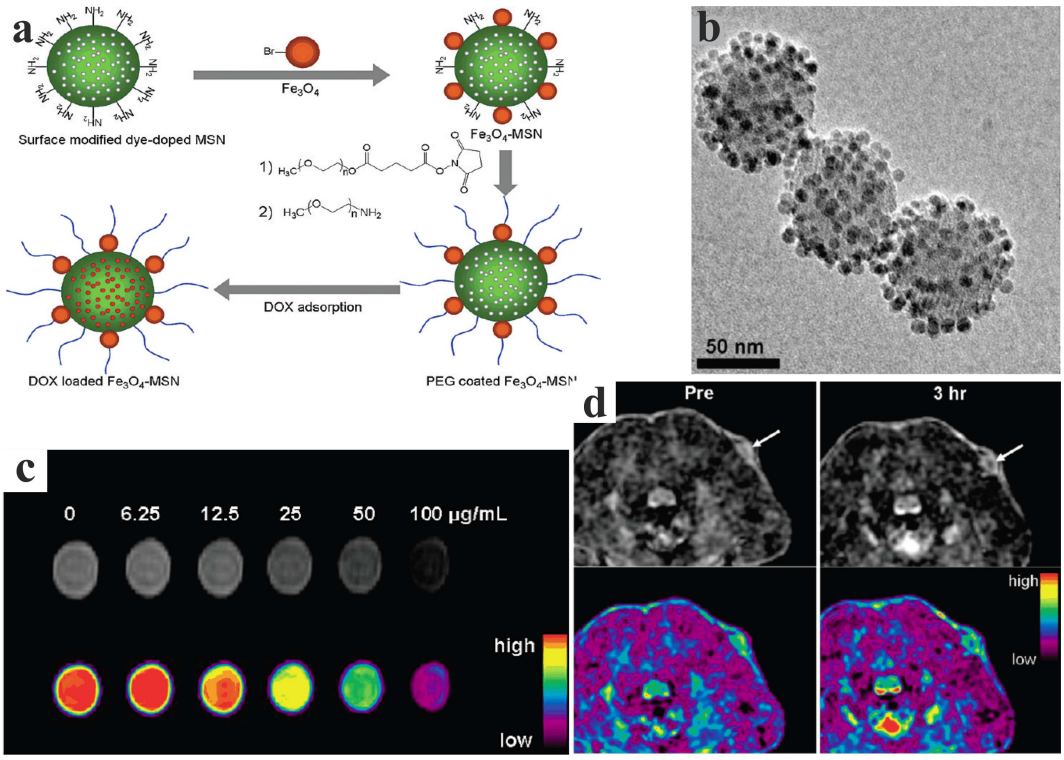

Figure 6.6: Fe_3O_4-decorated mesoporous SiO_2 spheres as MRI imaging agents. (a) Schematic illustration of the synthetic procedure for the preparation of of SiO_2-Fe_3O_4 NPs. (b) TEM image of SiO_2-Fe_3O_4 NPs. (c) MR images of different concentrations of SiO_2-Fe_3O_4 NPs. (d) *In vivo* accumulation of SiO_2-Fe_3O_4 NPs at tumor site. From ref. [98]

Additionally, Yang et *al.* developed silica coated Mn_3O_4 NPs functionalized with folic acid and contained Rhodamine B isothiocyanate (RBITC) as fluorescent dye for optical detection.[101] These particles accumulated selectively in cancer cells overexpressing folic acid receptors and could be traced by MRI. Very recently, our group reported on the development of highly watersolule MnO NPs conjugated with protoporphyrin IX as multifunctional agents for MRI and photodynamic therapy (see chapter 9).[102] Protoporphyrin IX, as a photosensitizer initiates the production of reactive oxygen species when irradiated with visible light. We were able to show, that the NPs not only showed excelellent T_1 contrast, but also induced apoptosis in Caki-1 cells once illuminated with visible light.

Apart from sole MRI contrast enhancement, magnetic NPs may also serve as

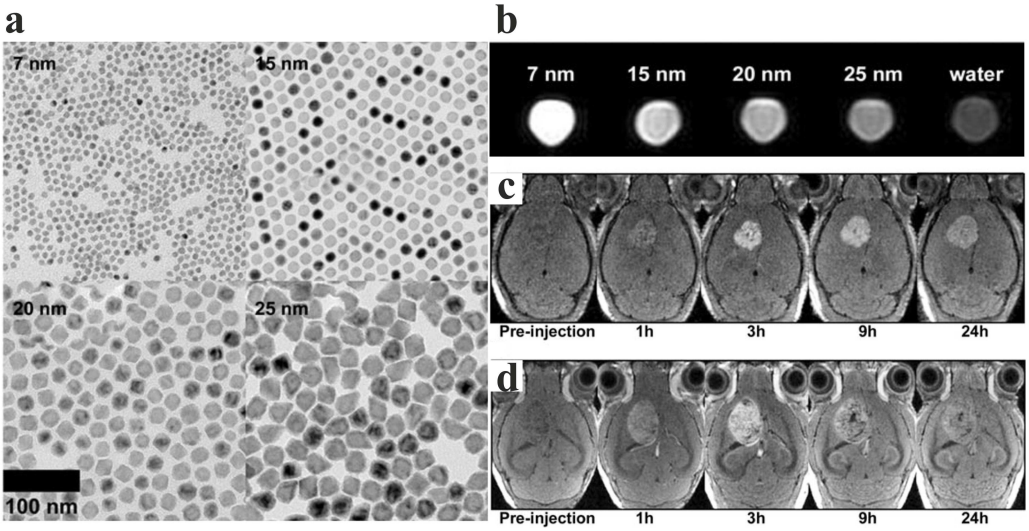

Figure 6.7: MnO NPs as T1 contrast agents. (a) TEM images of monodisperse MnO NPs of different sizes. (b) T_1 weighted images of aqueous MnO NP solutions. (c) Herceptin conjugated MnO NPs increased the contrast inside the tumor tissue, whereas bare MnO NPs (d) also led to an enhanced contrast in the surrounding tissue. From ref. [99]

probes for multimodal imaging. As described in chapter 4, the combination of different materials enables the selective utilization of the individual properties. For example, Choi et *al.* reported that the incorporation of ^{124}I into the biocompatible shell of manganese ferrite NPs, permitted the use of these hybrid NPs as dual imaging agents for MRI and positron emission tomography (PET) and, therefore, combining the benefits of MRI together with the high sensitivity of PET (see Figure6.8).[103] A similar approach was recently reported where the authors used MnO NPs coated with human serum albumin (HSA) and which were further conjugated with a ^{64}Cu containing complex.[104] With this method it was possible to visualize xenografted U87MG glioblastoma cells *in vivo*, both by MRI and PET. Another example for multimodal imaging was demonstrated by watersoluble FePt NPs that were used for *in vitro* and *in vivo* imaging by MRI and computer tomography (CT).[105] Different sized FePt NPs were functionalized with cysteamine to ensure hydrophilicity and the possibility for further bio-functionalization. Upon conjugation with the antibody Anti-Her2, the NPs preferably accumulated in Her2-overexpressing cancer

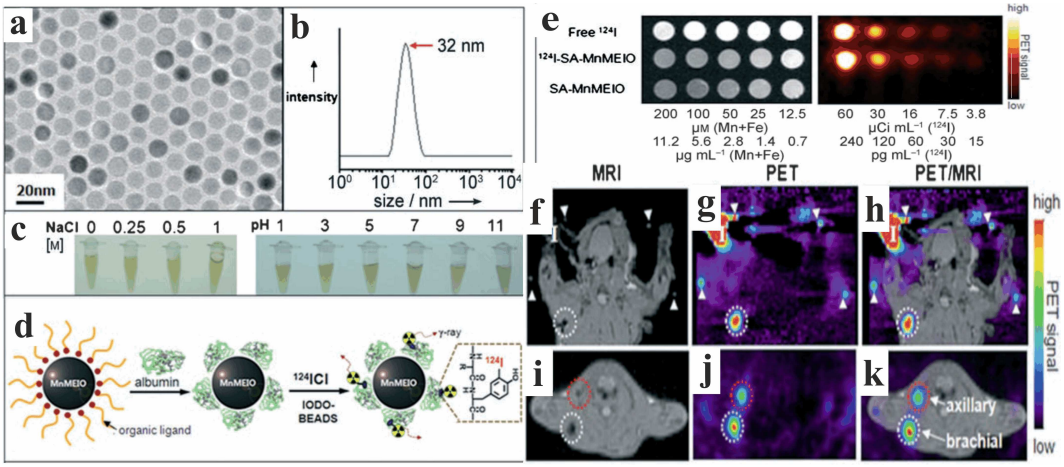

Figure 6.8: Bimodal imaging using ^{124}I conjugated $MnFe_2O_3$ NPs. (a) TEM image of monodisperse $MnFe_2O_3$ NPs. (b) Hydrodynamic size of $MnFe_2O_3$ NPs. (c) Aqueous solutions with different NaCl concentration and varying pH. (d) Preparation scheme for the conjugation of ^{124}I onto $MnFe_2O_3$ NPs. (e) MRI and PET images of free ^{124}I, $MnFe_2O_3$ NPs, and ^{124}I-conjugated $MnFe_2O_3$ NPs. (f-k) *In vivo* MRI/PET images of a tumor bearing rat after injection of ^{124}I-conjugated $MnFe_2O_3$ NPs. From ref. [103]

cells, as confirmed by MRI and CT. On the other hand, we were able to combine the properties of MnO NPs and Au NPs for simultaneous MRI and optical detection by creating biocompatible Au@MnO "nanoflowers" (see chapter 8).[106, 107]

6.5 Toxicity of Magnetic Nanoparticles

The need to evaluate the possible risk of human exposure to different kinds of nanomaterials has become a central issue in modern materials and biomedical science. Especially, as the number of different nanomaterials increases with an unprecedented speed, there is the predominant opinion among both, proponents and skeptics, that the vast potential of nanotechnology requires immediate attention to safety issues. Particularly, in the field of nano-biotechnology, direct exposure to the human body is definitely intended, and therefore, understanding the behavior and properties of magnetic NPs on the organism after administration, is essential before considering clinical use. Since these NPs are intentionally designed to inter-

act with cells, it is crucial to investigate the cellular responses upon NP exposure, to counteract any possible harmful effects, already during NP development. However, since most research on the toxicology of nanomaterials has focused on the effects of nanoparticles that enter the body accidentally, reliable methodologies to estimate the toxicological impact upon intended administration are still lacking, although there are already numerous studies on cytotoxic effects of different kinds of nanoparticles.[108] Despite the fact that an *in vivo* application of any nanomaterial requires a thorough comprehension of the kinetic processes and the toxicological impact this material exerts inside a living organism, the most frequently used screening studies are based on *in vitro* cytotoxicity experiments, since they are simpler, faster and less expensive compared to *in vivo* studies.[109–112]

An often examined parameter to assess possible harmful effects of nanomaterials inside living organisms is an inflammatory response.[113] For instance, recent studies revealed that TiO_2 NPs, which are a common component in many commercially available products, such as cosmetics or sun screen lotions, can cause inflammatory responses and generation of reactive oxygen species (ROS) leading to DNA damage.[114] Moreover, it was also shown that *in vitro* incubation of single-walled carbon nanotubes (SWNTs) with keratinocytes and bronchial epithelial cells, led to lipid peroxidation, oxidative stress, mitochondrial dysfunction, and changes in cell morphology.[115, 116] Additionally, a size-dependent toxicity was reported for silver and gold NPs exposed to alveolar macrophages, connective tissue fibroblasts, epithelial cells, macrophages, and melanoma cells.[117–119]. On the other hand, quantum dots can also initiate an inflammatory response and the production of ROS.[120]

Concerning magnetic metal oxide NPs (above all, Fe_3O_4, γ-Fe_2O_3 and MnO), most *in vitro* cytotoxicity studies revealed rather negligible toxic effects. However, it was stated by several authors that "naked" iron oxide NPs show a higher toxic potential compared to those that were modified with an inert biocompatible coating. For example, Gupta et *al.* reported that PEGylated iron oxide NPs had almost no toxic effect on fibroblast cells, even at concentrations as high as 2 mg mL^{-1}, whereas uncoated NPs caused a 50% decrease in cell viability already at comparatively low concentrations (250 μg mL^{-1}).[121] The low cytotoxicity of PEGylated Fe_3O_4 NPs was further confirmed by other authors using different kinds of PEG.[122, 123] Be-

sides PEG, iron oxide NPs with other surface coatings, including various polymers or silica, also showed hardly any toxic effect.[124–126] The reason for the higher cytotoxicity of "naked" iron oxide NPs was attributed to both, cellular uptake of the NPs and the production of ROS, caused by Fe-ion leaching.[127] For instance, Brunner et *al.* reported a significant reduction in cell viability in human mesothelioma cells upon addition of only 3.75 ppm iron oxide.[128] The authors proposed that this high toxicity was due to iron-induced free radical production (e.g. hydroxyl radicals) by Fenton or Haber-Weiss reactions. However, these results further substantiate the importance of effective surface coating techniques for magnetic NPs in biomedical applications.

On the other hand, the toxic properties of MnO NPs have hardly been investigated so far. However, most reports on the biomedical application of MnO NPs suggest that the toxicity of this material is comparatively low.[91, 101] For instance, Choi et *al.* investigated the toxic potential of Fe_3O_4 and MnO NPs coated with a hydrophilic micellar phospholipid shell and revealed that, although the MnO NPs showed a slightly higher toxicity than the Fe_3O_4 NPs, the overall toxic potential is acceptable.[129] Furthermore, our group demonstrated recently that both, Au@MnO nanoflowers and PEGylated MnO NPs carrying protoporphyrin IX as a photosensitizer, exhibited no cytoxic effect in CaKi-1 cells in concentrations as high as 140 μg mL^{-1}.[102, 107] Concerning free manganese ions, literature data suggest that, although minor concentrations of these ions are not considered to be harmful to the human body, thermodynamically stable Mn compounds which are not prone to Mn ion-leaching should be preferred as NP platforms for *in vivo* applications.[130]

6.6 Biodistribution and Clearance

An essential topic, that is often neglected in literature, is the long-term fate of magnetic NPs after they have fulfilled their duty inside the body. For this purpose it is not only important to understand the behavior and interaction of magnetic NPs with living organisms, it is also crucial to determine where nanoparticulate probes will eventually end up and how they are finally excreted from the body. However, to the present day, no reliable experimental technique nor a universal set of criteria have been developed to address this critical aspect.[108]

6.7 References

[1] Bangham, A. D.; Horne, R. W. *Journal of Molecular Biology* **1964**, *8*, 660–668, IN2–IN10.

[2] Wagner, V.; Dullaart, A.; Bock, A.-K.; Zweck, A. *Nature Biotechnology* **2006**, *24*, 1211–1217.

[3] Davis, M. E.; Chen, Z.; Shin, D. M. *Nature Reviews on Drug Discovery* **2008**, *7*, 771–782.

[4] Pankhurst, Q. A.; Thanh, N. T.; Jones, S. K.; Dobson, J. *Journal of Physics D: Applied Physics* **2009**, *42*, 224001.

[5] Shi, J.; Votruba, A. R.; Farokhzad, O. C.; Langer, R. *Nano Letters* **2010**, *10*, 3223–3230.

[6] Ferrari, M. *Nature Reviews: Cancer* **2005**, *5*, 161–171.

[7] Wickline, S. A.; Neubauer, A. M.; Winter, P. M.; Caruthers, S. D.; Lanza, G. M. *Journal of Magnetic Resonance Imaging* **2007**, *25*, 667–680.

[8] Corot, C.; Petry, K. G.; Trivedi, R.; Saleh, A.; Jonkmanns, C.; Le Bas, J.-F.; Blezer, E.; Rausch, M.; Brochet, B.; Foster-Gareau, P.; Balériaux, D.; Gaillard, S.; Dousset, V. *Investigative Radiology* **2004**, *39*, 619–625.

[9] Lübbe, A. S. et al. *Cancer Research* **1996**, *56*, 4686–4693.

[10] Lübbe, A. S.; Alexiou, C.; Bergemann, C. *Journal of Surgical Research* **2001**, *95*, 200–206.

[11] Chouly, C.; Pouliquen, D.; Lucet, I.; Jeune, J.; Jallet, P. *Journal of Microencapsulation: Micro and Nano Carriers* **1996**, *13*, 245–255.

[12] Choi, H. S.; Ipe, B. I.; Misra, P.; Lee, J. H.; Bawendi, M. G.; Frangioni, J. V. *Nano Letters* **2009**, *9*, 2354–2359.

[13] Verma, A.; Stellacci, F. *Small* **2010**, *6*, 12–21.

[14] Sun, C.; Lee, J. S. H.; Zhang, M. *Advanced Drug Delivery Reviews* **2008**, *60*, 1252–1265.

[15] Larsen, E. K.; Nielsen, T.; Wittenborn, T.; Birkedal, H.; Vorup-Jensen, T.; Jakobsen, M. H.; Astergaard, L.; Horsman, M. R.; Besenbacher, F.; Howard, K. A.; Kjems, J. *ACS Nano* **2009**, *3*, 1947–1951.

[16] Tanimoto, A.; Kuribayashi, S. *European Journal of Radiology* **2006**, *58*, 200–216.

[17] Soo Choi, H.; Liu, W.; Misra, P.; Tanaka, E.; Zimmer, J. P.; Itty Ipe, B.; Bawendi, M. G.; Frangioni, J. V. *Nat Biotech* **2007**, *25*, 1165–1170.

[18] Owens III, D. E.; Peppas, N. A. *International Journal of Pharmaceutics* **2006**, *307*, 93–102.

[19] Moghimi, S. M.; Hunter, A. C.; Murray, J. C. *Pharmacological Reviews* **2001**, *53*, 283–318.

[20] Massignani, M.; LoPresti, C.; Blanazs, A.; Madsen, J.; Armes, S. P.; Lewis, A. L.; Battaglia, G. *Small* **2009**, *5*, 2424–2432.

[21] Zhang, Y.; Yang, M.; Park, J.-H.; Singelyn, J.; Ma, H.; Sailor, M. J.; Ruoslahti, E.; Ozkan, M.; Ozkan, C. *Small* **2009**, *5*, 1990–1996.

[22] Arvizo, R. R.; Miranda, O. R.; Thompson, M. A.; Pabelick, C. M.; Bhattacharya, R.; Robertson, J.; Rotello, V. M.; Prakash, Y.; Mukherjee, P. *Nano Letters* **2010**, *10*, 2543–2548.

[23] Fujita, T.; Nishikawa, M.; Ohtsubo, Y.; Ohno, J.; Takakura, Y.; Sezaki, H.; Hashida, M. *Journal of Drug Targeting* **1994**, *2*, 157–165.

[24] Papisov, M. I.; Bogdanov, A., JR.; Schaffer, B.; Nossiff, N.; Shen, T.; Weissleder, R.; Brady, T. J. *Journal of Magnetism and Magnetic Materials* **1993**, *122*, 383–386.

[25] Cedervall, T.; Lynch, I.; Lindman, S.; Berggard, T.; Thulin, E.; Nilsson, H.; Dawson, K. A.; Linse, S. *Proceedings of the National Academy of Sciences* **2007**, *104*, 2050–2055.

[26] Ballou, B.; Lagerholm, B.; Ernst, L. A.; Bruchez, M. P.; Waggoner, A. S. *Bioconjugate Chemistry* **2004**, *15*, 79–86.

[27] Bhang, S. H.; Won, N.; Lee, T.-J.; Jin, H.; Nam, J.; Park, J.; Chung, H.; Park, H.-S.; Sung, Y.-E.; Hahn, S. K.; Kim, B.-S.; Kim, S. *ACS Nano* **2009**, *3*, 1389–1398.

[28] Pons, T.; Pic, E.; Lequeux, N.; Cassette, E.; Bezdetnaya, L.; Guillemin, F.; Marchal, F.; Dubertret, B. *ACS Nano* **2010**, *4*, 2531–2538.

[29] Maeda, H.; Wu, J.; Sawa, T.; Matsumura, Y.; Hori, K. *Journal of Controlled Release* **2000**, *65*, 271–284.

[30] Matsumura, Y.; Maeda, H. *Cancer Research* **1986**, *46*, 6387–6392.

[31] Maeda, H. *Advances in Enzyme Regulation* **2001**, *41*, 189–207.

[32] Clément, O.; Siauve, N.; Lewin, M.; de Kerviler, E.; Cuénod, C.-A.; Frija, G. *Biomedecine & Pharmacotherapy* **1998**, *52*, 51–58.

[33] Stark, D. D.; Weissleder, R.; Elizondo, G.; Hahn, P. F.; Saini, S.; Todd, L. E.; Wittenberg, J.; Ferrucci, J. T. *Radiology* **1988**, *168*, 297–301.

[34] Corot, C.; Robert, P.; Idée, J.-M.; Port, M. *Advanced Drug Delivery Reviews* **2006**, *58*, 1471–1504.

[35] Gao, X.; Cui, Y.; Levenson, R. M.; Chung, L. W. K.; Nie, S. *Nature Biotechnology* **2004**, *22*, 969–976.

[36] Cai, W.; Shin, D.-W.; Chen, K.; Gheysens, O.; Cao, Q.; Wang, S. X.; Gambhir, S. S.; Chen, X. *Nano Letters* **2006**, *6*, 669–676.

[37] Weissleder, R.; Kelly, K.; Sun, E. Y.; Shtatland, T.; Josephson, L. *Nature Biotechnology* **2005**, *23*, 1418–1423.

[38] Smith, A. M.; Duan, H.; Mohs, A. M.; Nie, S. *Advanced Drug Delivery Reviews* **2008**, *60*, 1226–1240.

[39] Liong, M.; Lu, J.; Kovochich, M.; Xia, T.; Ruehm, S. G.; Nel, A. E.; Tamanoi, F.; Zink, J. I. *ACS Nano* **2008**, *2*, 889–896.

[40] Kim, J.; Kim, H. S.; Lee, N.; Kim, T.; Kim, H.; Yu, T.; Song, I. C.; Moon, W. K.; Hyeon, T. *Angewandte Chemie International Edition* **2008**, *47*, 8438–8441.

[41] Choi, H. S.; Liu, W.; Liu, F.; Nasr, K.; Misra, P.; Bawendi, M. G.; Frangioni, J. V. *Nature Nanotechnology* **2010**, *5*, 42–47.

[42] Rosenholm, J.; Sahlgren, C.; Linden, M. *Journal of Materials Chemistry* **2010**, *20*, 2707–2713.

[43] Cerdan, S.; Lötscher, H.; Künnecke, B.; Seelig, J. *Magnetic Resonance in Medicine* **1989**, *12*, 151–163.

[44] Tiefenauer, L. X.; Kuehne, G.; Andres, R. Y. *Bioconjugate Chemistry* **1993**, *4*, 347–352.

[45] Gu, F. X.; Karnik, R.; Wang, A. Z.; Alexis, F.; Levy-Nissenbaum, E.; Hong, S.; Langer, R. S.; Farokhzad, O. C. *Nano Today* **2007**, *2*, 14–21.

[46] Lee, J.; Choi, Y.; Kim, K.; Hong, S.; Park, H.-Y.; Lee, T.; Cheon, G. J.; Song, R. *Bioconjugate Chemistry* **2010**, *21*, 940–946.

[47] Artemov, D.; Mori, N.; Ravi, R.; Bhujwalla, Z. M. *Cancer Research* **2003**, *63*, 2723–2727.

[48] Artemov, D.; Mori, N.; Okollie, B.; Bhujwalla, Z. *Magnetic Resonance in Medicine* **2003**, *49*, 403–408.

[49] Huh, Y.-M.; Jun, Y.-w.; Song, H.-T.; Kim, S.; Choi, J.-s.; Lee, J.-H.; Yoon, S.; Kim, K.-S.; Shin, J.-S.; Suh, J.-S.; Cheon, J. *Journal of the American Chemical Society* **2005**, *127*, 12387–12391.

[50] Nie, S.; Xing, Y.; Kim, G. J.; Simons, J. W. *Annual Review of Biomedical Engineering* **2007**, *9*, 257–288.

[51] Ross, J.; Chaudhuri, P.; Ratnam, M. *Cancer* **1994**, *73*, 2432–2443.

[52] Zhang, Y.; Kohler, N.; Zhang, M. *Biomaterials* **2002**, *23*, 1553–1561.

[53] Kohler, N.; Fryxell, G. E.; Zhang, M. *Journal of the American Chemical Society* **2004**, *126*, 7206–7211.

[54] Wang, S.; Shi, X.; VanAntwerp, M.; Cao, Z.; Swanson, S.; Bi, X.; Baker, J. *Advanced Functional Materials* **2007**, *17*, 3043–3050.

[55] Sonvico, F.; Mornet, S.; Vasseur, S.; Dubernet, C.; Jaillard, D.; Degrouard, J.; Hoebeke, J.; Duguet, E.; Colombo, P.; Couvreur, P. *Bioconjugate Chemistry* **2005**, *16*, 1181–1188.

[56] Amiji, M. M. *Nanotechnology for cancer therapy*; CRC Press Taylor & Francis: Boca Raton, Fla., 2007.

[57] Wunderbaldinger, P.; Josephson, L.; Weissleder, R. *Bioconjugate Chemistry* **2002**, *13*, 264–268.

[58] Lewin, M.; Carlesso, N.; Tung, C. H.; Tang, X. W.; Cory, D.; Scadden, D. T.; Weissleder, R. *Nature Biotechnology* **2000**, *18*, 410–414.

[59] Santra, S.; Yang, H.; Dutta, D.; Stanley, J. T.; Holloway, P. H.; Tan, W.; Moudgil, B. M.; Mericle, R. A. *Chemical Communications* **2004**, *40*, 2810–2811.

[60] Wadia, J. S.; Dowdy, S. F. *Advanced Drug Delivery Reviews* **2005**, *57*, 579–596.

[61] Panyam, J.; Labhasetwar, V. *Advanced Drug Delivery Reviews* **2003**, *55*, 329–347.

[62] Kim, C. K.; Ghosh, P.; Pagliuca, C.; Zhu, Z.-J.; Menichetti, S.; Rotello, V. M. *Journal of the American Chemical Society* **2009**, *131*, 1360–1361.

[63] LaVan, D. A.; McGuire, T.; Langer, R. *Nature Biotechnology* **2003**, *21*, 1184–1191.

[64] Kim, S. Y.; Shin, I. G.; Lee, Y. M.; Cho, C. S.; Sung, Y. K. *Journal of Controlled Release* **1998**, *51*, 13–22.

[65] Chilkoti, A.; Dreher, M. R.; Meyer, D. E.; Raucher, D. *Advanced Drug Delivery Reviews* **2002**, *54*, 613–630.

[66] Boussif, O.; Lezoualc'h, F.; Zanta, M. A.; Mergny, M. D.; Scherman, D.; Demeneix, B.; Behr, J. P. *Proceedings of the National Academy of Sciences* **1995**, *92*, 7297–7301.

[67] Asati, A.; Santra, S.; Kaittanis, C.; Perez, J. M. *ACS Nano* **2010**, *5*, DOI:10.1021/nn100816s.

[68] Kay, M. A.; Glorioso, J. C.; Naldini, L. *Nature Medicine* **2001**, *7*, 33–40.

[69] Sokolova, V.; Epple, M. *Angewandte Chemie International Edition* **2008**, *47*, 1382–1395.

[70] Whitehead, K. A.; Langer, R.; Anderson, D. G. *Nature Reviews on Drug Discovery* **2009**, *8*, 129–138.

[71] Shalek, A. K.; Robinson, J. T.; Karp, E. S.; Lee, J. S.; Ahn, D.-R.; Yoon, M.-H.; Sutton, A.; Jorgolli, M.; Gertner, R. S.; Gujral, T. S.; MacBeath, G.; Yang, E. G.; Park, H. *Proceedings of the National Academy of Sciences* **2010**, *107*, 1870–1875.

[72] Yavuz, M. S.; Cheng, Y.; Chen, J.; Cobley, C. M.; Zhang, Q.; Rycenga, M.; Xie, J.; Kim, C.; Song, K. H.; Schwartz, A. G.; Wang, L. V.; Xia, Y. *Nature Materials* **2009**, *8*, 935–939.

[73] Nappini, S.; Bombelli, F. B.; Bonini, M.; Norden, B.; Baglioni, P. *Soft Matter* **2010**, *6*, 154–162.

[74] Zelikin, A. N. *ACS Nano* **2010**, *4*, 2494–2509.

[75] Weissleder, R.; Tung, C.-H.; Mahmood, U.; Bogdanov, A. *Nature Biotechnology* **1999**, *17*, 375–378.

[76] Bareford, L. M.; Swaan, P. W. *Advanced Drug Delivery Reviews* **2007**, *59*, 748–758.

[77] Tung, C.-H.; Mahmood, U.; Bredow, S.; Weissleder, R. *Cancer Research* **2000**, *60*, 4953–4958.

[78] You, J.; Zhang, G.; Li, C. *ACS Nano* **2010**, *4*, 1033–1041.

[79] Gordijo, C. R.; Shuhendler, A. J.; Wu, X. Y. *Advanced Functional Materials* **2010**, *20*, 1404–1412.

[80] Timko, B. P.; Dvir, T.; Kohane, D. S. *Advanced Materials* **2010**, DOI:10.1002/adma.201002072.

[81] Weissleder, R.; Bogdanov, A.; Neuwelt, E. A.; Papisov, M. *Advanced Drug Delivery Reviews* **1995**, *16*, 321–334.

[82] Weishaupt, D.; Köchli, V. D.; Marincek, B. *Wie funktioniert MRI? Eine Einführung in Physik und Funktionsweise der Magnetresonanzbildgebung*, 6th ed.; Springer Berlin Heidelberg: Berlin, Heidelberg, 2009.

[83] Frullano, L.; Meade, T. *Journal of Biological Inorganic Chemistry* **2007**, *12*, 939–949.

[84] Jun, Y.-w.; Lee, J.-H.; Cheon, J. *Angewandte Chemie International Edition* **2008**, *47*, 5122–5135.

[85] Na, H. B.; Song, I. C.; Hyeon, T. *Advanced Materials* **2009**, *21*, 2133–2148.

[86] Lee, J.-H.; Huh, Y.-M.; Jun, Y.-w.; Seo, J.-w.; Jang, J.-T.; Song, H.-T.; Kim, S.; Cho, E.-J.; Yoon, H.-G.; Suh, J.-S.; Cheon, J. *Nature Medicine* **2007**, *13*, 95–99.

[87] Josephson, L.; Tung, C. H.; Moore, A.; Weissleder, R. *Bioconjugate Chemistry* **1999**, *10*, 186–191.

[88] Weissleder, R.; Moore, A.; Mahmood, U.; Bhorade, R.; Benveniste, H.; Chiocca, E.; Basilion, J. P. *Nature Medicine* **2000**, *6*, 351–354.

[89] Bulte, J. W. M.; Douglas, T.; Witwer, B.; Zhang, S.-C.; Strable, E.; Lewis, B. K.; Zywicke, H.; Miller, B.; van Gelderen, P.; Moskowitz, B. M.; Duncan, I. D.; Frank, J. A. *Nature Biotechnology* **2001**, *19*, 1141–1147.

[90] Weissleder, R. *Science* **2006**, *312*, 1168–1171.

[91] Gilad, A. A.; Walczak, P.; McMahon, M. T.; Bin Na, H.; Lee, J. H.; An, K.; Hyeon, T.; van Zijl, P. C. M.; Bulte, J. W. M. *Magnetic Resonance in Medicine* **2008**, *60*, 1–7.

[92] Kang, H. W.; Josephson, L.; Petrovsky, A.; Weissleder, R.; Bogdanov, A. *Bioconjugate Chemistry* **2002**, *13*, 122–127.

[93] Zhao, M.; Beauregard, D. A.; Loizou, L.; Davletov, B.; Brindle, K. M. *Nature Medicine* **2001**, *7*, 1241–1244.

[94] Jun, Y. W.; Huh, Y. M.; Choi, J. S.; Lee, J. H.; Song, H. T.; Kim, S.; Yoon, S.; Kim, K. S.; Shin, J. S.; Suh, J. S.; Cheon, J. *Journal of the American Chemical Society* **2005**, *127*, 5732–5733.

[95] Perez, J.; Josephson, L.; O'Loughlin, T.; Hogemann, D.; Weissleder, R. *Nature Biotechnology* **2002**, *20*, 816–820.

[96] Hu, F. Q.; Wei, L.; Zhou, Z.; Ran, Y. L.; Li, Z.; Gao, M. Y. *Advanced Materials* **2006**, *18*, 2553–2556.

[97] Hultman, K. L.; Raffo, A. J.; Grzenda, A. L.; Harris, P. E.; Brown, T. R.; OBrien, S. *ACS Nano* **2008**, *2*, 477–484.

[98] Lee, J. E.; Lee, N.; Kim, H.; Kim, J.; Choi, S. H.; Kim, J. H.; Kim, T.; in Song, C.; Park, S. P.; Moon, W. K.; Hyeon, T. *Journal of the American Chemical Society* **2010**, *132*, 552–557.

[99] Na, H. B.; Lee, J. H.; An, K.; Park, Y. I.; Park, M.; Lee, S.; Nam, D. H.; Kim, S. T.; Kim, S. H.; Kim, S. W.; Lim, K. H.; Kim, K. S.; Kim, S. O.; Hyeon, T. *Angewandte Chemie International Edition* **2007**, *46*, 5397–5401.

[100] Shapiro, E. M.; Koretsky, A. P. *Magnetic Resonance in Medicine* **2008**, *60*, 265–269.

[101] Yang, H.; Zhuang, Y.; Hu, H.; Du, X.; Zhang, C.; Shi, X.; Wu, H.; Yang, S. *Advanced Functional Materials* **2010**, *20*, 1733–1741.

[102] Schladt, T. D.; Schneider, K.; Shukoor, M. I.; Natalio, F.; Bauer, H.; Tahir, M. N.; Weber, S.; Schreiber, L. M.; Schröder, H. C.; Müller, W. E. G.; Tremel, W. *Journal of Materials Chemistry* **2010**, *20*, 8297–8304.

[103] Choi, J.-s.; Park, J. C.; Nah, H.; Woo, S.; Oh, J.; Kim, K. M.; Cheon, G. J.; Chang, Y.; Yoo, J.; Cheon, J. *Angewandte Chemie International Edition* **2008**, *47*, 6259–6262.

[104] Huang, J.; Xie, J.; Chen, K.; Bu, L.; Lee, S.; Cheng, Z.; Li, X.; Chen, X. *Chemical Communications* **2010**, *46*, 6684–6686.

[105] Chou, S.-W.; Shau, Y.-H.; Wu, P.-C.; Yang, Y.-S.; Shieh, D.-B.; Chen, C.-C. *Journal of the American Chemical Society* **2010**, doi:10.1021/ja1035013.

[106] Schladt, T. et al. *Angewandte Chemie* **2010**, *122*, 4068–4072.

[107] Schladt, T. D. et al. *Angewandte Chemie International Edition* **2010**, *49*, 3976–3980.

[108] Garnett, M.; Kallinteri, P. *Occupational Medicine (London)* **2006**, *56*, 307–311.

[109] Kagan, V. E.; Bayir, H.; Shvedova, A. A. *Nanomedicine* **2005**, *1*, 313–316.

[110] Fischer, H. C.; Chan, W. C. W. *Current Opinion in Biotechnology* **2007**, *18*, 565–571.

[111] Linkov, I.; Satterstrom, F. K.; Corey, L. M. *Nanomedicine* **2008**, *4*, 167–171.

[112] Lewinski, N.; Colvin, V.; Drezek, R. *Small* **2008**, *4*, 26–49.

[113] Nel, A. E.; Mädler, L.; Velegol, D.; Xia, T.; Hoek, E. M.; Somasundaran, P.; Klaessig, F.; Castranova, V.; Thompson, M. *Nature Materials* **2009**, *8*, 543–557.

[114] Schanen, B. C.; Karakoti, A. S.; Seal, S.; Drake, D. R.; Warren, W. L.; Self, W. T. *ACS Nano* **2009**, *3*, 2523–2532.

[115] Shvedova, A.; Castranova, V.; Kisin, E.; Schwegler-Berry, D.; Murray, A.; Gandelsman, V.; Maynard, A.; Baron, P. *Journal of Toxicology and Environmental Health, Part A: Current Issues* **2003**, *66*, 1909–1926.

[116] Lam, C.-W.; James, J. T.; McCluskey, R.; Hunter, R. L. *Toxicological Sciences* **2004**, *77*, 126–134.

[117] Carlson, C.; Hussain, S. M.; Schrand, A. M.; Braydich-Stolle, L. K.; Hess, K. L.; Jones, R. L.; Schlager, J. J. *Journal of Physical Chemistry B* **2008**, *112*, 13608–13619.

[118] Male, K. B.; Lachance, B.; Hrapovic, S.; Sunahara, G.; Luong, J. H. T. *Analytical Chemistry* **2008**, *80*, 5487–5493.

[119] Pan, Y.; Neuss, S.; Leifert, A.; Fischler, M.; Wen, F.; Simon, U.; Schmid, G.; Brandau, W.; Jahnen-Dechent, W. *Small* **2007**, *3*, 1941–1949.

[120] Nel, A.; Xia, T.; Mädler, L.; Li, N. *Science* **2006**, *311*, 622–627.

[121] Gupta, A. K.; Gupta, M. *Biomaterials* **2005**, *26*, 3995–4021.

[122] Cheng, F. Y.; Su, C. H.; Yang, Y. S.; Yeh, C. S.; Tsai, C. Y.; Wu, C. L.; Wu, M. T.; Shieh, D. B. *Biomaterials* **2005**, *26*, 729–738.

[123] Yu, W. W.; Chang, E.; Sayes, C. M.; Drezek, R.; Colvin, V. L. *Nanotechnology* **2006**, *17*, 4483–4487.

[124] Petri-Fink, A.; Chastellain, M.; Juillerat-Jeanneret, L.; Ferrari, A.; Hofmann, H. *Biomaterials* **2005**, *26*, 2685–2694.

[125] Cengelli, F.; Maysinger, D.; Tschudi-Monnet, F.; Montet, X.; Corot, C.; Petri-Fink, A.; Hofmann, H.; Juillerat-Jeanneret, L. *Journal of Pharmacology and Experimental Therapeutics* **2006**, *318*, 108–116.

[126] Tan, H.; Xue, J. M.; Shuter, B.; Li, X.; Wang, J. *Advanced Functional Materials* **2010**, *20*, 722–731.

[127] Hu, F.; Neoh, K. G.; Cen, L.; Kang, E. T. *Biomacromolecules* **2006**, *7*, 809–816.

[128] Brunner, T. J.; Wick, P.; Manser, P.; Spohn, P.; Grass, R. N.; Limbach, L. K.; Bruinink, A.; Stark, W. J. *Environmental Science & Technology* **2006**, *40*, 4374–4381.

[129] Choi, J.; Lee, S.; Na, H.; An, K.; Hyeon, T.; Seo, T. *Bioprocess and Biosystems Engineering* **2010**, *33*, 21–30.

[130] Misselwitz, B.; Mühler, A.; Weinmann, H.-J. *Investigative Radiology* **1995**, *30*, 611–620.

Part II

CHAPTER 7

Synthesis of Monodisperse MnO Nanoparticles: Evaluation of the Nucleation and Growth Mechanism

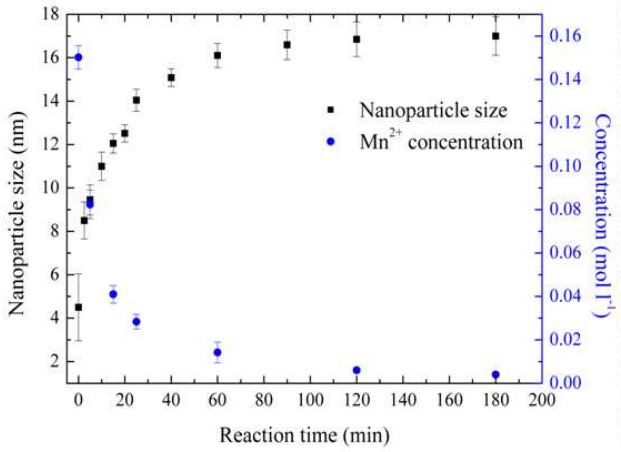

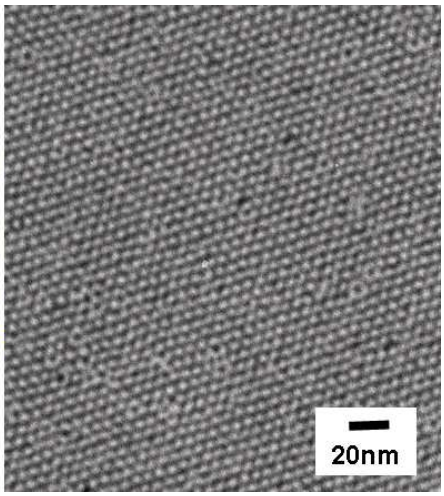

7.1 Abstract

Magnetic nanoparticles of 3d transition metal oxides have gained enormous interest for applications in various fields, such as data storage devices, catalysis, drug-delivery, and biomedical imaging. One major requirement for these applications is a narrow size distribution of the particles. We have studied the nucleation and growth mechanism for the formation of MnO NPs synthesized by decomposition of a manganese oleate complex in high boiling nonpolar solvents using TEM, FT-IR, and AAS analysis. The exceptionally narrow size distribution indicates that nucleation and growth are clearly separated. This leads to a uniform growth with a very narrow size distribution on the existing nuclei. The particle size can be controlled by adjusting the reaction time, reaction temperature, solvent, and heating rate. The particle size increases with temperature, reaction time, and the chain length (boiling point) of the solvent. FT-IR and NMR spectra revealed that the oleate capping agent binds to the surface in a bidentate manner. In addition, XPS measurements indicate that MnO nanocrystals are air-stable, since no significant oxidation of Mn^{2+} to Mn^{3+} occurred even after several days.

7.2 Introduction

Magnetic nanoparticles of the 3d transition metal oxides have gained enormous interest for applications in various fields such as data storage devices, catalysis, drug delivery, and biomedical imaging.[1–5] Especially nanocrystals of simple binary metal oxides like MnO, NiO, or CoO have served as model systems for the detailed description of magnetic properties in the nanometer regime.[6–8] Different from the antiferromagnetic bulk material, MnO exhibits ferromagnetic behavior when the crystallite size is decreased to a few nanometers. Multiple attempts have been made to explain this behavior. The common opinion today is based on the presence of uncompensated spins on the crystal surface.[9] Over the past years, several different synthesis methods have been developed to produce magnetic NPs in various sizes and shapes. However, a major requirement concerning later application in the above-mentioned areas is a narrow size distribution of the particles, usually with $\sigma < 10\%$. On the basis of the LaMer model,[10] a separation of nucleation

and growth is necessary to achieve such a narrow size distribution. Therefore, a detailed knowledge of the nucleation and growth process is essential. A commonly used approach is the "hot-injection" method, in which a cold precursor is injected into a hot solvent leading to a fast increase in monomer concentration and a short nucleation event. Both concentration and temperature rapidly decrease, followed by a simultaneous growth of all NPs as the precursor concentration is depleted (see chapter 3).

During the last years many "one-pot" methods have been developed for the synthesis of monodisperse NPs in which all components are heated at the same time. MnO NPs have been synthesized starting from $Mn_2(CO)_8$,[11] manganese acetylacetonate,[12] acetate,[13] or formate[14] in trioctylamine, with oleic acid as a stabilizing agent and manganese cupferronate[8] complexes or fatty acid salts in high boiling solvents.[15] Most of these methods use oleic acid as a surfactant to control nucleation and growth and it must be expected that a metal oleate complex is generated *in situ* in the early stages of the reaction. Therefore, a metal oleate complex seems to be an ideal precursor for the synthesis of monodisperse nanocrystals.[16] Detailed studies on the formation mechanism of MnO NPs by heating a manganese stearate complex in high boiling solvents have been accomplished by Chen et al.[17]

Here we report the synthesis of MnO NPs by a related method[16, 18] using the decomposition of a manganese oleate complex at high temperatures in high-boiling point solvents. We were able to produce MnO nanocrystals with high crystallinity and exceptionally narrow size distribution (in some cases with σ < 3%). In addition, we observed that the heating rate has a major influence on the dispersity of the final product.

7.3 Results and Discussion

X-ray diffraction (XRD) data were acquired to characterize phase purity of the final product (see Figure 7.1). Particle sizes were estimated by deconvolution of the peak-broadening within the framework of the fundamental parameter approach; they are in good agreement with the values obtained from TEM analysis (average values from approximately 200 individual particles). The observed intensities match well with the cubic rock-salt structure of MnO($cF8$, $Fm\bar{3}m$); no secondary phases were

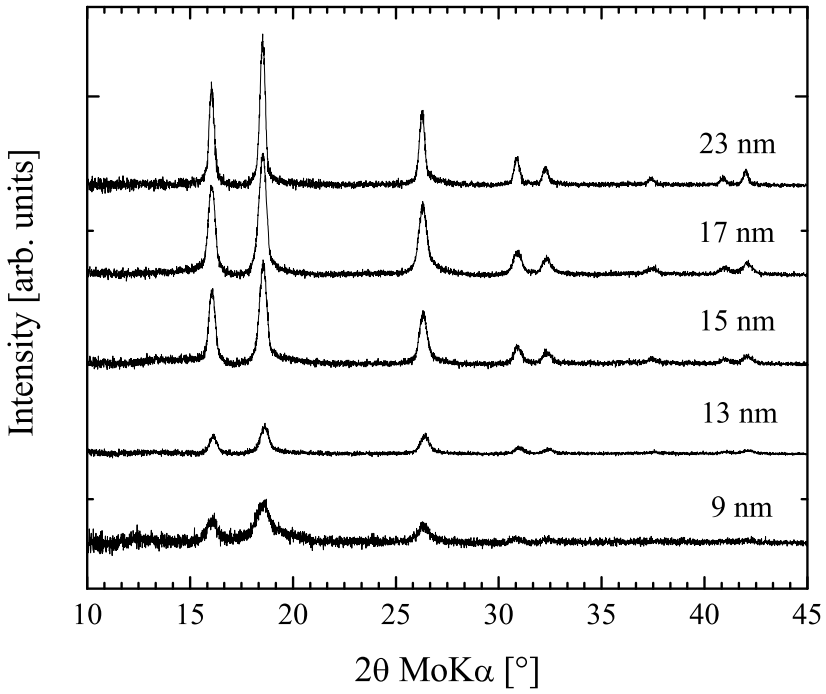

Figure 7.1: Size-dependent powder XRD patterns of MnO nanoparticle samples.

detected.

Thermal Decomposition of Manganese Oleate. As the MnO particles are formed by thermal decomposition of the manganese oleate precursor, thermogravimetric analysis was performed to examine its decomposition behavior. Usually, metal carboxylates decompose at temperatures around 300 °C, and it is known that this process is accompanied by the formation of free radicals.[19] These radicals can undergo various reactions such as recombination, decay into smaller fragments, or, as desired here, propagate the decomposition by reacting with other carboxylate complexes. As a result, a variety of compounds are formed, including CO, CO_2, free acids, ketones, hydrocarbons, and of course, metal oxide target compounds. However, a detailed and stoichiometric description of this process has not yet been established.

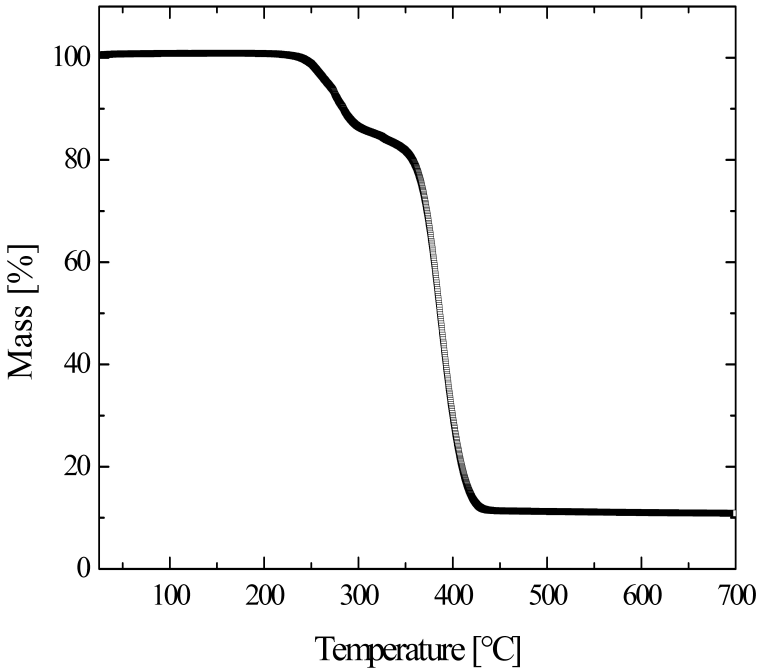

Figure 7.2: TGA-curve of Mn-oleate.

Figure 7.2 shows the thermogravimetric traces (in Ar) of manganese oleate. The first step in the diagram can be associated with a mass loss that we ascribe to two molecules of CO_2 (Δm_{rel} = 14.5% (0.5% loss, corresponding to a molar mass of 89.5 g mol^{-1} (3.1 g mol^{-1}). This decomposition is initiated between 220 and 230 °C. Around 400 °C, there is a sharper fall in mass, that corresponds to the remaining organic residues being stripped off (Δm_{rel} = 74.2% (0.5% mass loss). The remaining solid material (Δm_{rel} = 11.4% (0.5% of the starting material) with a mass of 70.4 g mol^{-1} (3.1 g mol^{-1} corresponds in good approximation to MnO (molar mass 70.94 g mol^{-1}).

Nucleation and Growth. A detailed understanding of the nucleation and growth process is essential for the controlled synthesis of monodisperse MnO NPs. Unfortunately, an observation of the nucleation event by common techniques is very difficult. We have used FT-IR spectroscopy, TEM, and AAS analysis to study the decomposition of the precursor and to evaluate the mechanism of the MnO particle formation.

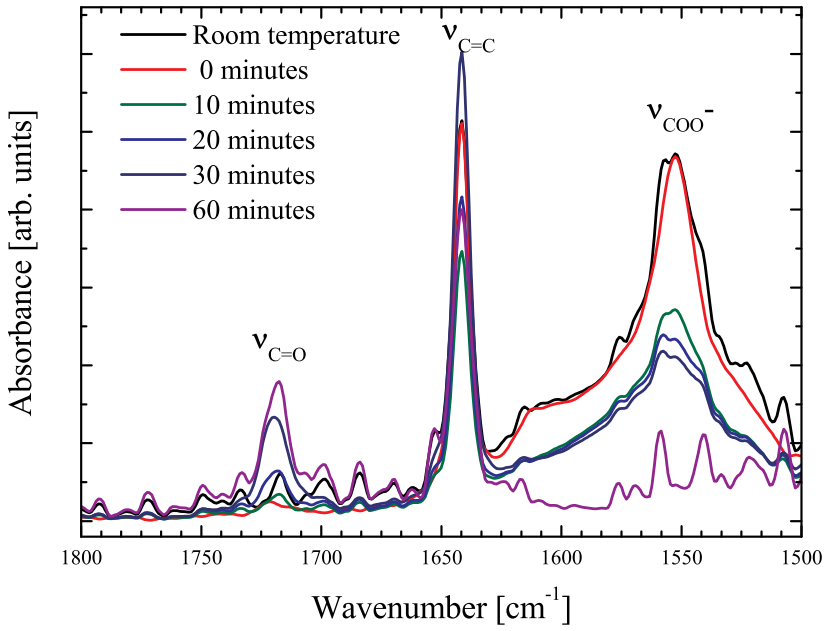

Figure 7.3: FT-IR spectra of aliquots taken at different stages of the reaction after the reaction solution had reached 200 °C (the variation of intensity of the C=C band at 1645 cm^{-1} is due to varying amounts of solvent in the samples).

After having reached 200 °C, the reaction mixture was heated with a constant heating rate of 1.5 °C/min and aliquots of the solution were taken at different times and temperatures. Figure 7.3 shows FT-IR spectra of these samples. Typical TEM images of the resulting NPs at different stages of the synthesis are presented in Figure 7.4. At room temperature, the antisymmetric stretching vibration of the oleate group is clearly detectable at 1555 cm^{-1}. At temperatures above 200 °C, the color of the solution changed from light red to brown. Nevertheless, neither a significant depletion of precursor nor nanocrystals were detectable. As the temperature increases, the oleate complex starts decomposing, as concluded from the reduced intensities of the $RCOO^{-}$ bands of the samples heated at 215 °C (10 min in Figure 7.4) and 230 °C (20 min in Figure 7.3). In accordance with earlier observations,[17] we assume that during this decomposition process, free oleic acid and small MnO clus-

ters are formed. This assumption is confirmed by the fact that an absorption band appears at 1719 cm^{-1} in the spectra, which can be assigned to the carbonyl stretching mode of free oleic acid (see Figure 7.3). We expect that in the further course of the reaction, the concentration of these MnO clusters increases until a critical value of supersaturation is reached upon which spontaneous nucleation is initiated. Consequently, the MnO cluster concentration decreases rapidly below a level where the net nucleation rate is zero; this is in agreement with the concept proposed by LaMer.[10]

Figure 7.4a shows NPs isolated in these early stages of the reaction. They are poorly crystalline with an average diameter of 4.5 nm and a relatively broad size distribution. Growth is very fast during this phase of the reaction, because in samples taken shortly afterward (Figure 7.4b, $\approx$ 2.5 min after taking the first sample (230 °C)) the particles have not only grown to a diameter of 8.5 nm but also appear more uniform in size. Subsequently the nanocrystals grow further by consuming precursor molecules from solution without any new nuclei being formed.

Because all particles emerge virtually at the same time, their growth histories are nearly identical and remain independent from the nucleation event. Therefore, their size distribution is exceptionally narrow with standard deviation values below 5%. This concept has often been used to describe the formation of monodisperse NPs in the past and is generally referred to as "separation of nucleation and growth" mechanism.[19–21] In contrast to the results presented by Chen et *al.*[17] for the manganese stearate method, the oleate precursor was still detectable in the reaction solution by FT-IR spectroscopy and AAS even at higher temperatures and after prolonged reaction times (see Figures 7.3 and 7.5). This fact indicates that the growth of the nanocrystals occurs by consumption of the dissolved precursor.

Above 250 °C, a light greenish precipitate appears that turns dark green at higher temperatures and redissolves again at approximately 300 °C, forming a clear green solution. After 60 min of reaction, the carboxylate band at 1555 cm^{-1} (Figure 7.3) has almost disappeared completely. The remaining intensity can be attributed to the carboxylate band of the oleate molecules which cover the surfaces of the NPs. The carbonyl band at 1719 cm^{-1}, on the other hand, shows strong absorbance, which suggests a nearly complete conversion of the precursor. This is in agreement with the depletion of the concentration of free Mn^{2+} as obtained from AAS measure-

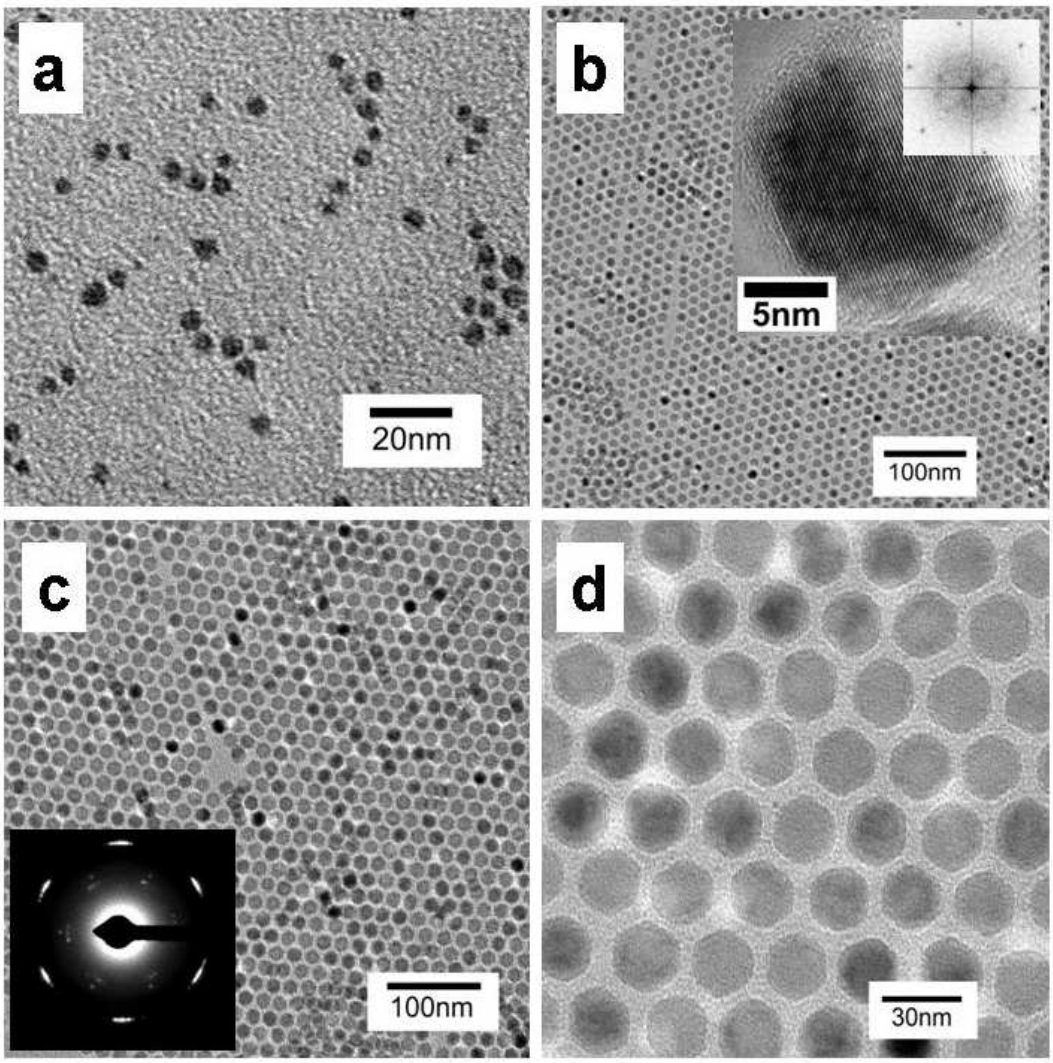

Figure 7.4: TEM images of MnO NPs at different stages of the reaction. NPs isolated (a) immediately after initiated precursor decomposition, (b) after $\approx$ 2.5 min, (c) after 60 min of reflux in 1-hexadecene, (d) after 60 min of reflux in 1-octadecene. Inset (b) HRTEM and FFT image of a single particle. Inset (c) SAED image corresponding to image (c).

ments (Figure 7.5). As a consequence, no further growth of the NPs under consumption of dissolved manganese oleate is possible. Images c and d in Figure 7.4 show particles isolated after 60 min of reflux from reaction solutions containing 1-hexadecene and 1-octadecene, respectively. They have average diameters of 17 and

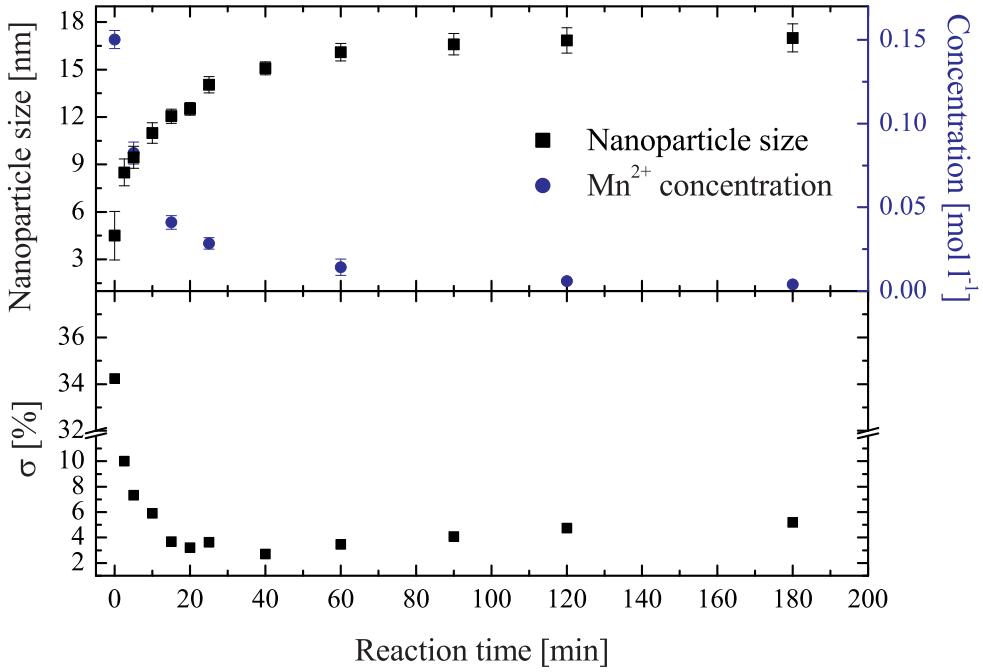

Figure 7.5: Evolution of particle size and concentration of free Mn^{2+} with reaction time in 1-hexadecene (top), evolution of the standard deviation of the mean particle diameter with time (bottom).

22.5 nm, respectively.

The evolution of particle size with time was studied to derive the kinetics of the MnO nanoparticle formation (see Figure 7.5). As mentioned above the size of the nanocrystals increases rapidly within the first minutes of reaction. After 30 min their growth slows down and eventually stagnates in the further course of the experiment.

The AAS results confirm a rapid conversion of the precursor in the initial phase of the experiment. However, manganese oleate is still detectable as free Mn in the solution even after 60 min and longer, suggesting once more that particle growth is driven by a consumption of dissolved precursor molecules. The observed depletion of the manganese precursor matches well with the growth of the particles with time. Figure 7.5 (bottom) shows the evolution of the relative standard deviation of the par-

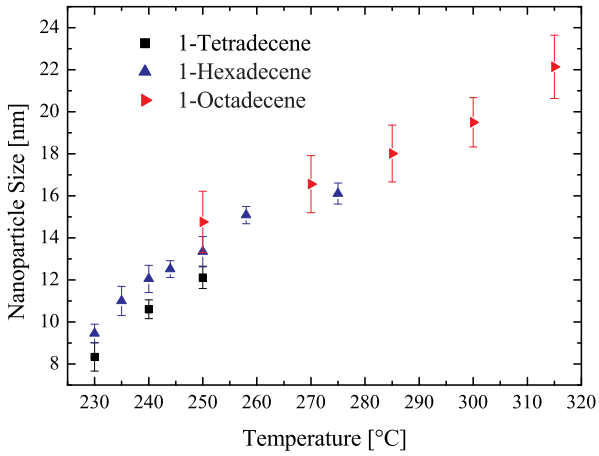

Figure 7.6: MnO nanoparticle size as a function of temperature and solvent.

ticles size as a function of time. A decrease of σ from 34.2% to 7.3% within 5 min indicates a fast focusing of the size distribution. The standard deviation reaches a minimum value of 2.7% after 40 min. Surprisingly, neither a significant broadening of the size distribution, nor changes in size or shape of the particles occurred even after the reaction was continued for 180 min. This behavior is atypical for a classical Ostwald ripening process.

Figure 7.6 shows the evolution of particle size as a function of reaction temperature. The crystal size increases almost linearly with temperature for all solvents used. However, a correlation between size and solvent becomes apparent when the particle sizes at a fixed reaction temperature of 250 °C are compared. When the reaction is heated to 250 °C in 1-octadecene (C18, bp. 318 °C), the NPs grow to a mean diameter of 14.6 nm (σ = 9.7%), whereas in 1-hexadecene (C16, bp. 275 °C) and 1-tetradecene (C14, bp. 254 °C), they grow up only to 13.3 nm (σ = 5.4%) and 12.1 nm (σ = 4.4%), respectively, at this temperature. It also seems that the narrowest size distributions are achieved in the lower boiling solvents 1-hexadecene and 1-tetradecene.

When trioctylamine (TOA) was used as a solvent, however, the results are significantly different. Figure 7.7 shows TEM micrographs of particles synthesized in

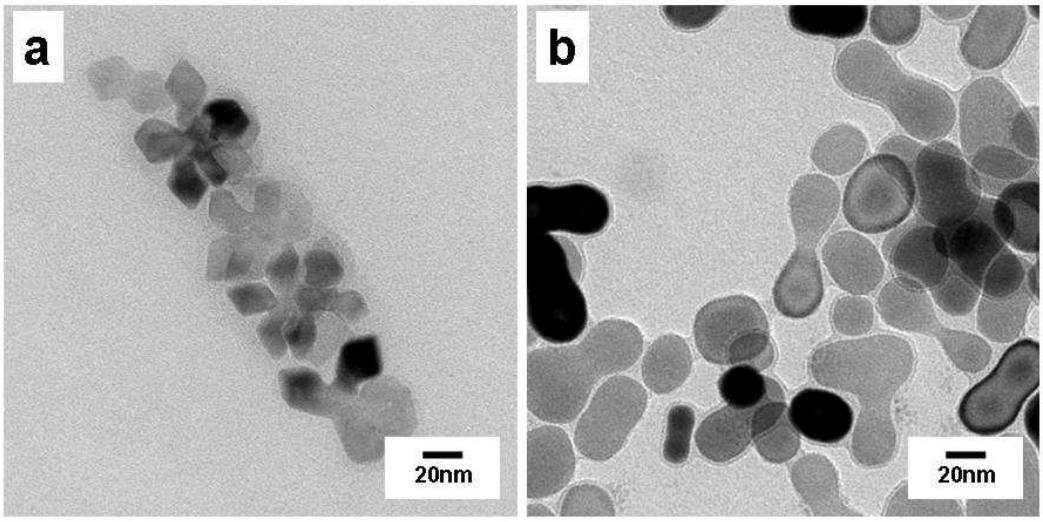

Figure 7.7: TEM images of MnO NPs prepared in trioctylamine after (a) 5 and (b) 60 min.

TOA. The particles appear randomly shaped, forming multipods and rods. At the beginning of the reaction, the crystals are well-faceted with sharp edges. As the reaction proceeds, the edges are smoothed out and the particles lose their shape. This result is consistent with observations reported by Ould-Ely et *al.*[22, 23] who synthesized MnO nanocrystals by decomposition of manganese formate in a mixture of oleic acid and trioctylamine. The reason for this behavior is presumably that TOA itself, different from long-chained alkenes, has a strong affinity to the surface of metal oxides.[24] In fact, it has often been used as stabilizing agent in the synthesis of NPs.[13] Therefore, a competition reaction on the nanocrystal surface between the surface ligands oleate and TOA seems likely that results in an additional growth on partly uncovered surfaces of the crystals.

An interesting feature of the present system emerges when the solution is cooled to room temperature after the reaction was complete. Below 250 °C, the initially clear green mixture turns brown, and below 200 °C, it turns dark brown while remaining clear. However, the color changes to green again when the mixture is reheated above 280 °C. This thermochromic effect can be repeated several times.

Surface Ligands of the NPs. A key aspect in the synthesis of NPs is to over-

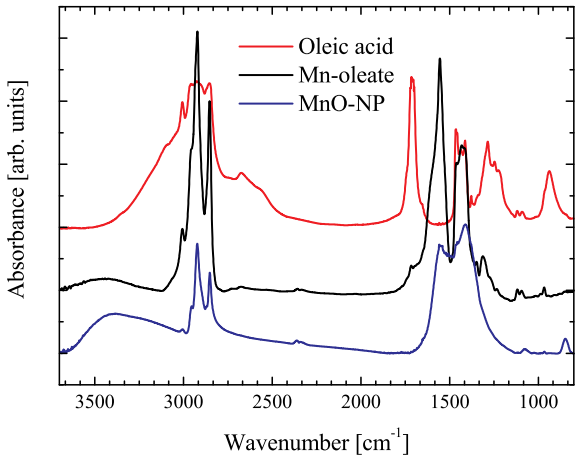

Figure 7.8: FT-IR spectra of oleic acid, manganese oleate, and washed MnO NPs.

come the high surface energy and to stabilize their thermodynamically unfavorable state. In most synthetic methods, this task is accomplished by adding certain organic molecules, that are able to bind onto the surface of the crystals and stabilize them against aggregation and oxidation. These stabilizing agents also control nucleation and growth and often comprise long-chain phosphines such as trioctylphosphine, long-chain thiols, or fatty acids like stearic acid or oleic acid.

We used different techniques to determine the coordination of the surfactant molecules (oleic acid) on the surface of the NPs. Figure 7.8 shows the FT-IR spectra of oleic acid, manganese oleate, and washed MnO nanocrystals. The characteristic bands of the oleyl group are present in all spectra. The weak absorption band at 2956 cm^{-1} results from the asymmetric CH_3- stretching mode, whereas two bands at 2922 and 2852 cm^{-1} can be assigned to the symmetric and asymmetric -CH_2- stretching modes, respectively. Additionally, a small maximum at 3005 cm^{-1}, due to asymmetric stretching of the vinyl C–H bond, is also characteristic for the oleyl group. The free carbonyl stretching mode of the acid is visible at 1711 cm^{-1}. In comparison, the intensity of this band is reduced in the other samples, and strong absorption bands that can be assigned to the asymmetric and symmetric stretching bands of the $RCOO^-$ group, respectively, appear at 1555 and 1410 cm^{-1}. Further-

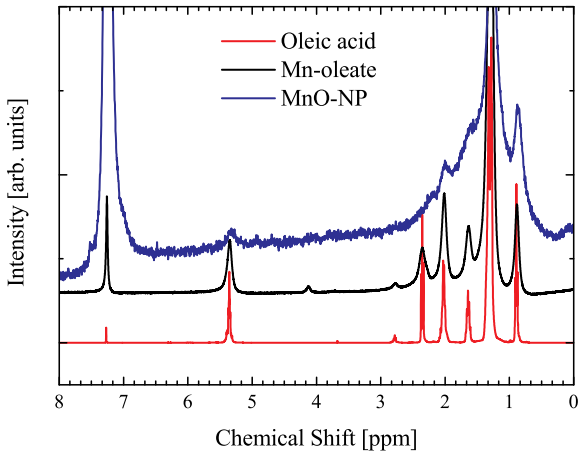

Figure 7.9: ^{1}HNMR spectra of oleic acid,manganese oleate, and washed MnO NPs.

more, the difference of 145 cm^{-1} between both stretching modes is characteristic for a bidentate coordination of the carboxylate to a metal atom, as has been observed in zinc oleate complexes.[25–27] Maxima at 1462, 1410, 1379, and 1286 cm^{-1} in the oleic acid spectrum can be assigned to deformation vibrations of CH_2- and CH_3-groups of the alkyl chain, whereas the broad absorption band at 930 cm^{-1} can be ascribed to the O–H $\cdots$ O bending vibration of the carboxylic acid group.

In a simplistic view, spherical MnO NPs are terminated by facets whose structure contains fragments of the polar $\{111\}$ surface. In contrast to nonpolar $\{100\}$ surfaces of rocksalt structured metal oxides, which are thermodynamically stable, $\{111\}$ polar surfaces of bulk single crystal oxides are unstable if they remain in the bulk terminated structure because of the diverging surface potential.[28] From a theoretical point of view, it has been shown for crystalline surfaces that the compensation of polarity occurs through an interplay of different mechanisms, such as changes in the surface electronic structure, structural reconstructions accompanied by changes in the surface stoichiometry, and interaction with the residual atmosphere adsorption, hydroxylation, etc.[29–32] Thus, the stabilization of spherical NPs by the charged carboxylate ligands is compatible with a binding of the ligands to the polar $\{111\}$ surface. On the other hand, the uncharged amine ligand can-

not stabilize the MnO $\{111\}$ surface sufficiently, and particles terminated by the MnO $\{100\}$ surface are formed. The presence of the very weak carbonyl peak at 1710 cm^{-1} suggests the presence of trace amounts of free oleic acid in the manganese oleate complex. However, in the MnO NP sample, no free oleic acid is detectable.

Nuclear magnetic resonance (NMR) spectroscopy is typically used to determine the coordination and interactions of ligands on the surface of diamagnetic NPs.[33, 34] NMR spectroscopy of paramagnetic nanocrystals is only rarely reported due to large broadening effects caused by the large magnetic moment of paramagnetic materials.[35, 36] Figure 7.9 compares the ^{1}HNMR spectra of free oleic acid, the manganese oleate complex and washed MnO NPs. The signal broadening is clearly visible in the MnO NP sample, which complicates a spectral assignment. Willis et *al.*[35] reported a reduction of the double bond of oleic acid at high reaction temperatures (350 °C) during the synthesis of iron oxide NPs. Nevertheless, the vinyl and allyl proton resonances appear at 5.34 and 2.01 ppm in all three samples, suggesting that no loss of unsaturation (hydration of the double bond) occurs during the synthesis. This is presumably due to the relatively low reaction temperatures used in our synthesis.

Further characterization of the ligand-coated MnO nanocrystals was performed using high-resolution XPS. Renaud and Barbier[37, 38] reported that the MnO $\{111\}$ single-crystal surface is nonstoichiometric, containing a mixture of the MnO $\{111\}$ and Mn_3O_4 $\{111\}$ phases; the latter was suggested to play a stabilizing role in compensating the polarity. Figure 7.10 shows a high-resolution XPS spectrum of the Mn 2p region acquired on a MnO nanoparticle sample that was washed and stored in air for several days. The Mn $2p_{1/2}$ and $2p_{3/2}$ signals are located at 653.4 and 641.4 eV, respectively. These values are in good agreement with literature values of Mn^{2+} in bulk MnO.[39, 40] These results confirm, within the limit of detection, that no significant oxidation of Mn^{2+} to Mn^{3+} on the surface of the NPs occurred during the reaction and the subsequent purification and indicates the importance of surface coverage with the oleate ligand. However, it should be stated that a high-resolution electron energy loss (HREEL) spectrum is more sensitive than XPS in detecting cation surface defects leading to the formation of overlayers from higher oxides such as Mn_2O_3 or Mn_3O_4.[41]

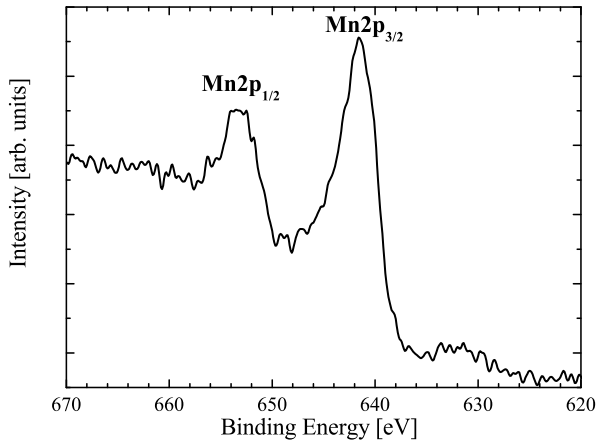

Figure 7.10: High-resolution XPS scans of the Mn 2p region.

Finally, the amount of oleate on the nanoparticle surface was determined by thermogravimetric analysis. A typical TGA trace for MnO NPs with 8.5 nm diameter is presented in Figure 7.11. The first step can again be associated to loss of CO_2. The second step in the diagram is due to decomposition of the remaining organic residues. The oleate on the surface sums up to a fraction Δm_{rel} = 34% ($\pm$ 0.5%) of the total mass.

Influence of the Heating Rate. It was found that the heating rate had a major influence not only on the size, but also on the dispersity of the NPs. Images of nanocrystals synthesized with different heating rates are displayed in Figure 7.12. All images show particles formed in reaction mixtures heated to 300 °C in 1-octadecene solvent after 1 h of aging. It appears that the particle size is inversely dependent on the heating rate, whereas the size distribution is narrowest when the reaction solution is heated slowly. In Figure 7.12a (90 °C min^{-1}), the particles have an average diameter of 6.5 nm (σ = 12.5%), in Figure 7.12b (50 °C min^{-1}) the particle size is 8.5 nm (σ = 19.3%). When slow heating rates are used, the nanocrystals appear more uniform in size and shape, as can be seen in Figure 7.12c (3.3 °C min^{-1}) with d = 12.5 nm (σ = 5.3%) and Figure 7.12d (1.5 °C min^{-1}) with d = 18.9 nm (σ = 5.5%).

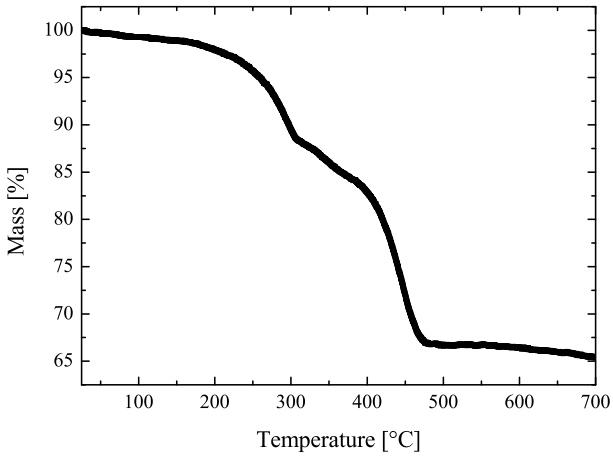

Figure 7.11: TGA curve of washed MnO nanocrystals (⌀ = 8.5 nm).

Magnetic Properties. It has been reported that MnO NPs show weak ferromagnetic behavior at low temperatures although bulk MnO is antiferromagnetic with T_N = 122 K.[42] The observed weak ferromagnetism was explained by the existence of noncompensated surface spins of the antiferromagnetic core of the MnO nanoparticle. These disordered spins originate from a change in the metal coordination at the surface.[11] Figure 7.13 shows the field-cooled (FC) and zero-field cooled (ZFC) magnetizations measured in an applied field of 100 Oe, yielding magnetic blocking temperatures (T_B) of 18.0, 12.7, and 11.6 K for the 6, 16, and 25 nm particles, respectively. The inverse proportionality of T_B on the size is illustrated in inset (i) in Figure 7.13. Smaller MnO particles exhibit a higher surface-to-volume ratio and thus the higher number of noncompensated surface spins. This leads to a higher blocking temperature and to higher magnetization values compared to larger particles. This result is in good agreement with a results reported by Seo et al.[43] The 16 nm MnO NPs show a weak feature at approximately 122 K, the Néel temperature of bulk MnO(inset (ii) in Figure 7.14). However, the susceptibility of a MnO antiferromagnetic powder is expected to decrease below T_N. But in the case of the 16 nm particles, a further increase in the susceptibility is observed. The expected behavior is found for the 25 nm particles for which the magnetic transition

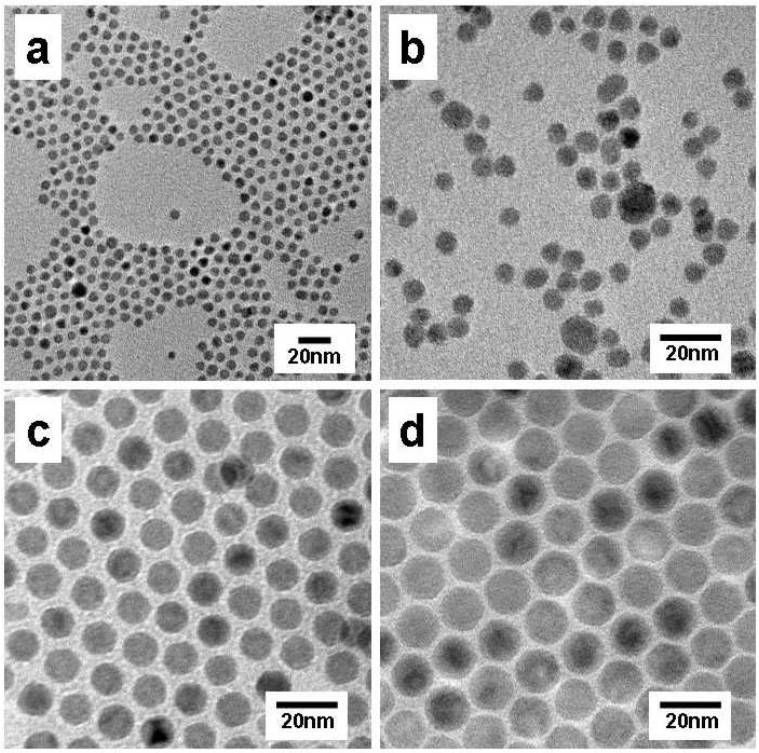

Figure 7.12: TEM images of MnO NPs synthesized at different heating rates: (a) 90 , (b) 50, (c) 3.3, and (d) 1.5 °C min^{-1}.

at T_N is considerably enhanced.

Hysteresis loops at 5 K of different sized NPs are shown in Figure 7.14. An increase in the magnetization and the width of the hysteresis loop with decreasing size is observed. Inset (ii) displays the hysteresis loops of 12 nm MnO NPs measured in a ZFC and a FC state with an applied field of 2 T. The exchange coupling between the antiferromagnetic core of the particle and the surface spins leads to a magnetic behavior corresponding to two magnetic systems.[44] This causes a loop shift along the field axis in the FC state. Furthermore, H_C and H_{ex} increase in the field-cooled hysteresis loop. These results demonstrate that the magnetic properties of MnO NPs strongly depend on the size of the particles.

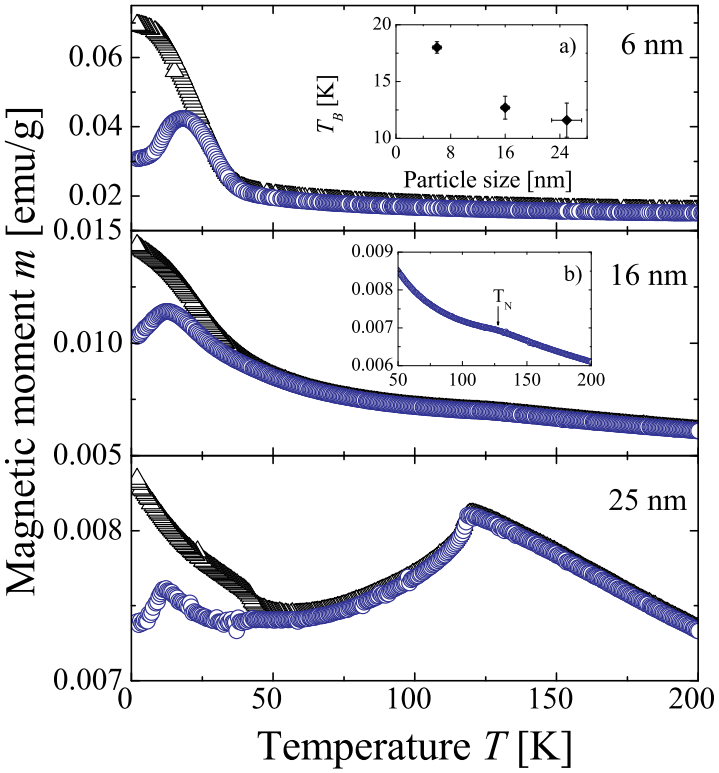

Figure 7.13: Size-dependent ZFC (blue circles) and FC (black triangles) magnetization measurements of MnO NPs in an applied field of 100 Oe. Inset (i) displays the size dependency of T_B, inset (ii) shows the temperature range from 50 to 200 K of the 16 nm particles on an enlarged scale.

7.4 Conclusion

In summary, we have shown that MnO NPs can easily be produced by a simple one-pot heating-up method. The nucleation and growth procedure of the particles was studied by TEM, FT-IR, and AAS analysis. Our results suggest a single nucleation event followed by a growth on the existing nuclei. Because nucleation and growth are clearly separated, the crystals grow uniformly, leading to a narrow size distribution. The particle size can be controlled by adjusting the reaction time and temperature, the solvent and the heating rate. The particle size increases with temperature, reaction time, and chain length (boiling point) of the solvent. We investigated the surface of the MnO nanocrystals by FT-IR and NMR and demonstrated

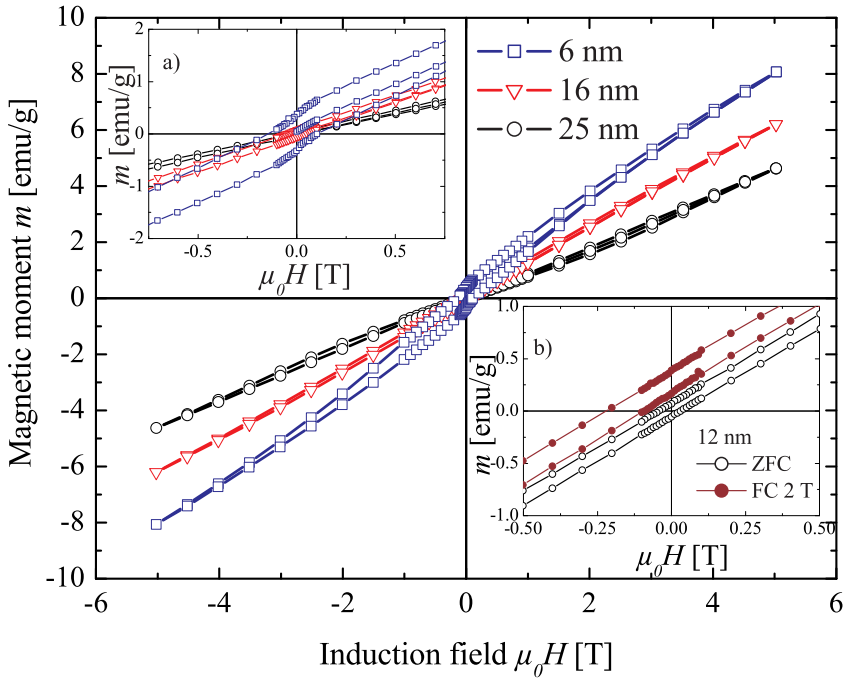

Figure 7.14: Hysteresis loops of different-sized MnO NPs measured at 5 K. Inset (i) shows enlarged view of the hysteresis loops. Inset (ii) shows hysteresis loops of 12 nm particles measured in a ZFC and a FC(2 T) state.

that oleate binds to the surface in a bidentate manner. In addition, XPS measurements indicate that no significant oxidation of Mn^{2+} to Mn^{3+} occurred even after several days. Magnetic measurements showed that the magnetic properties strongly depend upon the size of the NPs. Both magnetic moment and blocking temperature increase when the particle size is decreased.

7.5 Experimental Section

All reactions were carried out using standard Schlenk conditions. All syntheses were carried out in a home-built metal bath heater equipped with a temperature controller and monitoring unit. The heater was made out of brass and equipped with two 180 W heating elements operating at 220 V and a Pt100 temperature sen-

sor. It was filled with 1.2 kg of Wood metal (Roth, T_M = 70 °C).

Materials. All syntheses were carried out under argon and using commercially available reagents: 1-tetradecene (technical grade, 92%, Aldrich), 1-hexadecene (technical grade, 92%, Aldrich), 1-octadecene (technical grade, 90%, ACROS), tri-n-octylamine (98%, Fluka), oleic acid (technical grade, Fisher), methanol, hexane, acetone, ethanol, and manganese chloride tetrahydrate ($MnCl_2 \times 4H_2O$, 99%, Aldrich) were used as received.

Synthesis of the Manganese Oleate Precursor. Manganese oleate was prepared according to a reported procedure[15, 16, 18] with some modifications: 7.94 g (40 mmol) of manganese chloride tetrahydrate and 22.60 g (80 mmol) oleic acid were dissolved in 200 mL of methanol. A solution of 3.2 g (80 mmol) of sodium hydroxide in 200 mL of methanol was added dropwise to the stirred Mn-/oleic acid solution over a period of 1 h. The initially clear colorless mixture turned pink, and a deep red oily substance precipitated. After being stirred for another hour, the solvent was discarded and the product washed with water, ethanol, and acetone. The oily residue was dissolved in hexane and dried over $MgSO_4$. After evaporating the solvent the product was dried *in vacuo* (1×10^{-2} mbar) at 100–150 °C for 2 h to produce a deep red waxy solid.

Synthesis of MnO NPs. In a typical reaction, 1.24 g (2 mmol) of the manganese oleate were dissolved in 10 g of solvent and degassed at 70 °C *in vacuo* (1×10^{-2} mbar) for 2 h and intermittently backfilled with argon to remove any moisture and oxygen. The reaction mixture was subsequently treated with a definitive temperature program. First of all the solution was rapidly heated to 200 °C with approximately 5 °C/min. For the further course of the reaction the heating rate was fixed to 1.5 °C/min and the temperature was held at reflux (318 °C) for 1 h. The as-prepared nanocrystals were easily soluble in nonpolar solvents such as hexane or toluene. The NPs were washed three times according to the following procedure: They were first dissolved in hexane, precipitated with acetone or ethanol, and subsequently collected by centrifugation. The washed NPs were thereupon redissolved in hexane or toluene for storage. Depending on solvent, reaction time, temperature, and heating, rate different particle sizes and shapes were obtained.

Nanoparticle Characterization. The particles were characterized by means of powder X-ray diffraction (XRD), transmission electron microscopy (TEM), Fourier

transformed infrared spectroscopy (FT-IR), atomic absorption spectroscopy (AAS), nuclear magnetic resonance spectroscopy (NMR), thermogravimetric analysis (TGA), and X-ray photoelectron spectroscopy (XPS). The magnetic properties of the MnO NPs were investigated with a superconducting quantum interference device (SQUID). XRD measurements were performed on a Bruker D8 Advance diffractometer equipped with a Sol-X energydispersive detector and operating with Mo Kα radiation. Full pattern profile fits were performed with TOPAS Academic V1.0 applying the fundamental parameter approach.[45] Samples for transmission electron microscopy were prepared by placing a drop of dilute nanoparticle solution in hexane on a carbon coated copper grid. Low-resolution TEM images and ED patterns were recorded on a Philips EM420 microscope operating at an acceleration voltage of 120 kV. High-resolution TEM data was obtained on a FEI Tecnai F30 S-TWIN with a 300 kV field emission gun. FT-IR spectra were acquired on a Nicolet 5DXC spectrometer. For AAS measurements ethanol was added to each sample to precipitate any NPs. After centrifugation the supernatant was treated with conc. HNO_3 to oxidize all organic components. Magnetic measurements were carried out using a Quantum Design MPMS-XL SQUID magnetometer. XPS data were acquired on a VG ECA-LAB MK2. AAS experiments were performed on a Perkin-Elmer 5100 ZL.

7.6 References

[1] Raj, K.; Moskowitz, R. *Journal of Magnetism and Magnetic Materials* **1990**, *85*, 233–245.

[2] Sun, S.; Murray, C. B.; Weller, D.; Folks, L.; Moser, A. *Science* **2000**, *287*, 1989–1992.

[3] Hyeon, T. *Chemical Communications* **2003**, 927–934.

[4] Sun, S. *Advanced Materials* **2006**, *18*, 393–403.

[5] Jun, Y.-w.; Lee, J.-H.; Cheon, J. *Angewandte Chemie International Edition* **2008**, *47*, 5122–5135.

[6] Kodama, R. H. *Journal of Magnetism and Magnetic Materials* **1999**, *200*, 359–372.

[7] Makhlouf, S. A.; Parker, F. T.; Spada, F. E.; Berkowitz, A. E. *Journal of Applied Physics* **1997**, *81*, 5561–5563.

[8] Ghosh, M.; Biswas, K.; Sundaresan, A.; Rao, C. N. *Journal of Materials Chemistry* **2006**, *16*, 106–111.

[9] Kodama, R. H.; Makhlouf, S. A.; Berkowitz, A. E. *Physical Review Letters* **1997**, *79*, 1393–1396.

[10] LaMer, V. K.; Dinegar, R. H. *Journal of the American Chemical Society* **1950**, *72*, 4847–4854.

[11] Lee, G. H.; Huh, S. H.; Jeong, J. W.; Choi, B. J.; Kim, S. H.; Ri, H.-C. *Journal of the American Chemical Society* **2002**, *124*, 12094–12095.

[12] Seo, W. S.; Jo, H. H.; Lee, K.; Kim, B.; Oh, S. J.; Park, J. T. *Angewandte Chemie* **2004**, *116*, 1135–1137.

[13] Yin, M.; O'Brien, S. *Journal of the American Chemical Society* **2003**, *125*, 10180–10181.

[14] Zhong, X.; Xie, R.; Sun, L.; Lieberwirth, I.; Knoll, W. *Journal of Physical Chemistry B* **2006**, *110*, 2–4.

[15] Park, J.; An, K.; Hwang, Y.; Park, J. G.; Noh, H. J.; Kim, J. Y.; Park, J. H.; Hwang, N. M.; Hyeon, T. *Nature Materials* **2004**, *3*, 891–895.

[16] Park, J.; Joo, J.; Kwon, S. G.; Jang, Y.; Hyeon, T. *Angewandte Chemie International Edition* **2007**, *46*, 4630–4660.

[17] Chen, Y.; Johnson, E.; Peng, X. *Journal of the American Chemical Society* **2007**, *129*, 10937–10947.

[18] Jana, N. R.; Chen, Y.; Peng, X. *Chemistry of Materials* **2004**, *16*, 3931–3935.

[19] Kwon, G. S.; Piao, Y.; Park, J.; Angappane, S.; Jo, Y.; Hwang, N. M.; Park, J. G.; Hyeon, T. *Journal of the American Chemical Society* **2007**, *129*, 12571–12584.

[20] Peng, X.; Wickham, J.; Alivisatos, A. P. *Journal of the American Chemical Society* **1998**, *120*, 5343–5344.

[21] Peng, Z.; Peng, X. *Journal of the American Chemical Society* **2002**, *124*, 3343–3353.

[22] Ould-Ely, T.; Prieto-Centurion, D.; Kumar, A.; Guo, W.; Knowles, W. V.; Asokan, S.; Wong, M. S.; Rusakova, I.; Lüttge, A.; Whitmire, K. H. *Chemistry of Materials* **2006**, *18*, 1821–1829.

[23] Rusakova, I.; Ould-Ely, T.; Hofmann, C.; Prieto-Centurión, D.; Levin, C. S.; Halas, N. J.; Lüttge, A.; Whitmire, K. H. *Chemistry of Materials* **2007**, *19*, 1369–1375.

[24] Ritchie, J. E.; Murray, W. R.; Kershan, K.; Diaz, V.; Tran, L.; McDevitt, J. T. *Journal of the American Chemical Society* **1999**, *121*, 7447–7448.

[25] Barman, S.; Vasudevan, S. *Journal of Physical Chemistry B* **2006**, *110*, 651–654.

[26] Barman, S.; Vasudevan, S. *Journal of Physical Chemistry B* **2007**, *111*, 5212–5217.

[27] Alcock, N. W.; Tracy, V. M.; Waddington, T. C. *Dalton Transactions* **1976**, 2243–2246.

[28] Wolf, D. *Physical Review Letters* **1992**, *68*, 3315.

[29] Langell, M. A.; Berrie, C. L.; Nassir, M. H.; Wulser, K. W. *Surface Science* **1994**, *320*, 25–38.

[30] Dulub, O.; Diebold, U.; Kresse, G. *Physical Review Letters* **2003**, *90*, 016102.

[31] Kresse, G.; Dulub, O.; Diebold, U. *Physical Reviews B* **2003**, *68*, 245409.

[32] Lazarov, V. K.; Plass, R.; Poon, H. C.; Saldin, D. K.; Weinert, M.; Chambers, S. A.; Gajdardziska-Josifovska, M. *Physical Reviews B* **2005**, *71*, 115434.

[33] Sachleben, J. R.; Colvin, V.; Emsley, L.; Wooten, E. W.; Alivisatos, A. P. *Journal of Physical Chemistry B* **1998**, *102*, 10117–10128.

[34] Ladizhansky, V.; Hodes, G.; Vega, S. *Journal of Physical Chemistry B* **1998**, *102*, 8505–8509.

[35] Willis, A. L.; Turro, N. J.; O'Brien, S. *Chemistry of Materials* **2005**, *17*, 5970–5975.

[36] Benn, R.; Rufinska, A. *Angewandte Chemie International Edition* **1986**, *25*, 861–881.

[37] Woodruff, D. P. *Oxide surfaces: The Chemical Physics of Solid Surfaces*, 1st ed.; Elsevier: Amsterdam, 2001; Vol. 9.

[38] Henrich, V. E.; Cox, P. A. *The surface science of metal oxides*; Cambridge University Press: Cambridge, 1994.

[39] Tan, B. J.; Klabunde, K. J.; Sherwood, P. M. *Journal of the American Chemical Society* **1991**, *113*, 855–861.

[40] Strohmeier, B. R.; Hercules, D. M. *Journal of Physical Chemistry B* **1984**, *88*, 4922–4929.

[41] Langell, M. A.; Hutchings, C. W.; Carson, G. A.; Nassir, M. H. *Journal of Vacuum Science and Technology A* **1996**, *14*, 1656–1661.

[42] Hill, R. J.; Howard, C. J. *Journal of Applied Crystallography* **1987**, *20*, 467–474.

[43] Seo, W. S.; Jo, H. H.; Lee, K.; Kim, B.; Oh, S. J.; Park, J. T. *Angewandte Chemie International Edition* **2004**, *43*, 1115–1118.

[44] Kodama, R. H.; Berkowitz, A. E.; McNiff, E. J., JR.; Foner, S. *Journal of Applied Physics* **1997**, *81*, 5552–5557.

[45] Cheary, R. W.; Coelho, A. *Journal of Applied Crystallography* **1992**, *25*, 109–121.

CHAPTER 8

Au@MnO Nanoflowers: Hybrid Nanocomposites for Selective Dual Functionalization and Imaging

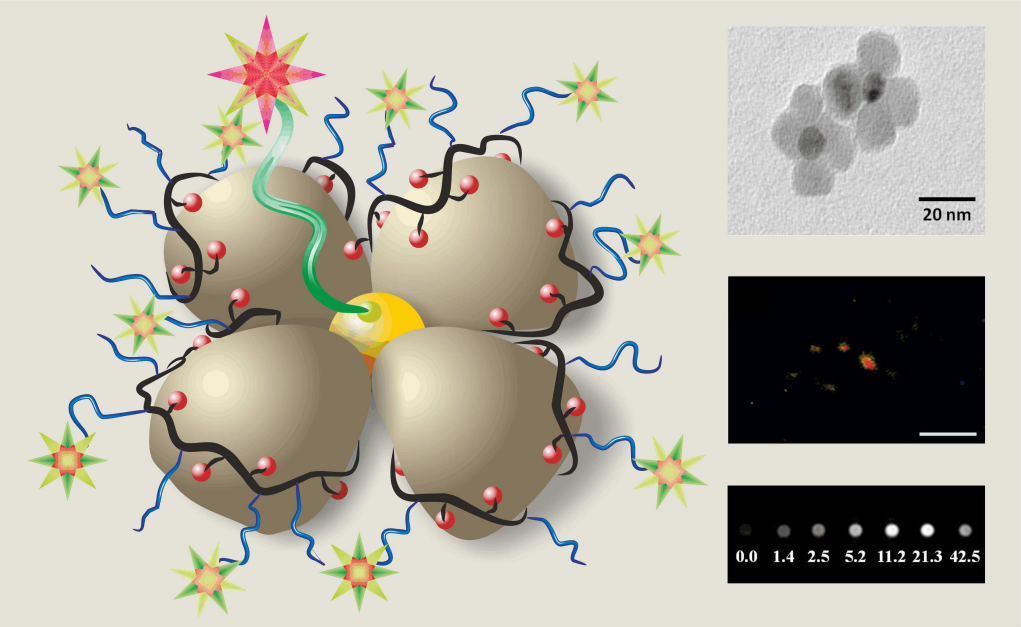

8.1 Abstract

A convenient strategy for preparing core-tunable multicomponent Au@MnO nanocrystals has been developed. The magnetic nanoflowers are not only efficient as cargo-specific carriers but also have excellent fluorescent properties resulting from fluorophors bound to the Au and MnO domains.

8.2 Introduction

Recently, the development of hybrid nanostructures consisting of various materials has attracted considerable interest. The assembly of different nanomaterials with specific optical, magnetic, or electronic properties to multicomponent composites can change and even enhance the properties of the individual constituents (see chapter 4).[1, 2, 4–12] Specifically tuning the structure and interface interactions within the nanocomposites has resulted in novel platforms of materials that may lead the way to various future technologies, such as synchronous biolabeling, protein separation and detection,[13–15] heterogeneous catalysis,[16–18] and multimodal imaging in biomedicine.[20–22, 24–26]

Of the various kinds of nanomaterials, gold nanorods show an unusually high polarizability at optical frequencies arising from the excitation of localized surface-plasmon resonances (LSPRs).[27, 28] Furthermore, gold nanorods have promising therapeutic properties as hyperthermal agents because the local temperature around the gold nanorods can be increased by laser illumination through the tunable surface plasmon bands in the near infrared (NIR) region.[29–31] Using NIR radiation for hyperthermal therapy is beneficial because of the low absorption and low scattering by blood and tissue in this spectral range.[32, 33]

Magnetic nanoparticles constitute another major class of nanomaterials that have attracted much research effort over the past decades.[34–38] In particular, exchange-coupled magnetic nanocomposites, such as antiferromagnetic/ferromagnetic core-shell nanoparticles, such as MnO/Mn_3O_4, have magnetic properties that are quite different from those of the individual components.[2, 39–43] Concerning biomedical applications, superparamagnetic nanoparticles are attractive as contrast agents for magnetic resonance imaging (MRI). The majority of nanoparticles that

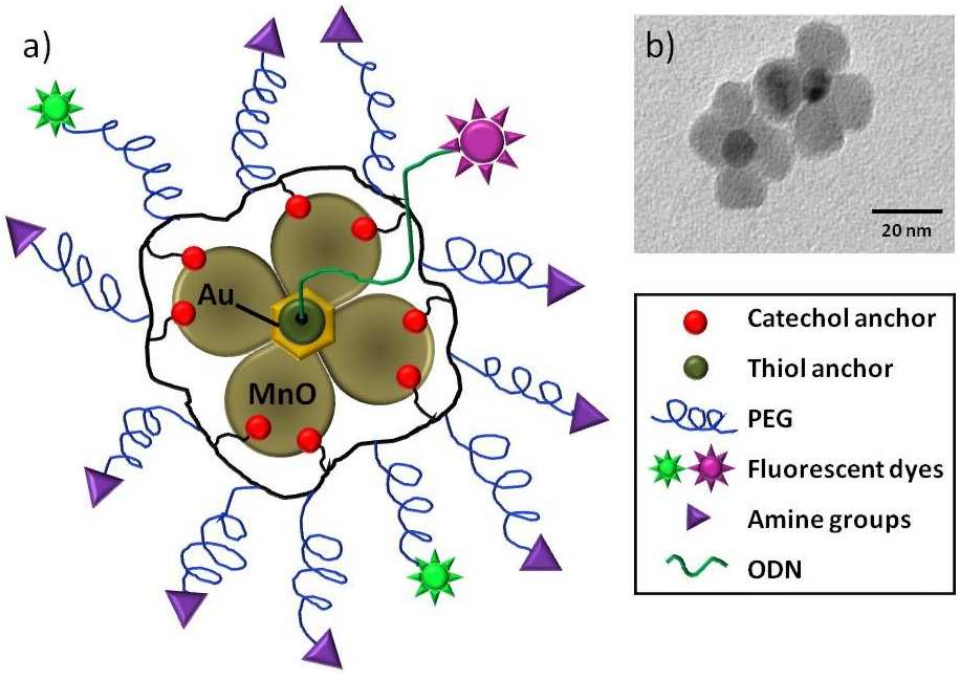

Figure 8.1: (a) Au@MnO nanoflowers separately functionalized using a multifunctional polymeric ligand carrying catechol anchor groups and a fluorescent dye (NBD) tagged to PEG(800) side groups. The gold core is functionalized with a Texas-Red-tagged thiolated oligonucleotide. (b) TEM image of polymer-coated Au@MnO nanoflowers

have been investigated in this field comprise iron oxides (Fe_3O_4, γ–Fe_2O_3), which are known to shorten the transverse (or spin-spin) relaxation time T_2.[44, 45] Recently, manganese oxide nanoparticles (MnO NPs) have been shown to be interesting candidates as contrast agents for shortening of the longitudinal (or spin-lattice) relaxation time T_1.[47, 48] Consequently, a nanoparticulate system containing both an optically active plasmonic gold unit and a magnetically active MnO component would be advantageous for simultaneous optical and MRI detection.

Although considerable research efforts have been put into the chemical design of suitable surface ligands,[49, 50, 52] one of the major obstacles for biocompatible applications remains the lack of surface addressability. Therefore, a nanocomposite made up of individually addressable Au and MnO domains offers two functional

surfaces for the attachment of different kinds of molecules, thus increasing both diagnostic and therapeutic potential.[21] Furthermore, the size of either of the two components can be varied to optimize the magnetic and optical properties. Herein we present the successful synthesis of Au@MnO nanocomposites consisting of both paramagnetic MnO NPs and Au crystallites followed by separate surface functionalization of both domains with fluorescent ligands.

8.3 Results and Discussion

Nanoparticle synthesis and characterization. Figure 8.1 depicts a functionalized Au@MnO nanoflower with selective attachment of catechol anchors to the metal oxide petals and thiol anchors to the gold core. The nanoflowers were synthesized by decomposition of manganese acetylacetonate [$Mn(acac)_2$] in diphenyl ether in the presence of preformed Au NPs ("seeds"), with oleic acid and oleylamine as surfactants, following a similar procedure for the preparation of $Au@Fe_3O_4$ heteroparticles by Sun et *al.*[53] The gold "seeds" were generated in situ by decomposition of gold acetate [$Au(OAc)_3$] at low temperature, which could be traced by a color change to deep red. At higher temperatures, MnO petals form by epitaxial growth on the surface of the Au NPs. The size and morphology of the nanoflowers can be varied by changing the molar ratio of the precursors (Figure 8.2). The number

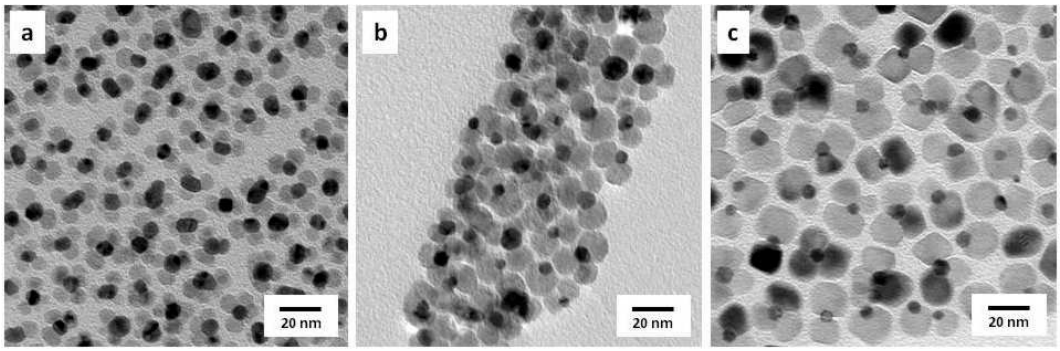

Figure 8.2: Au@MnO nanoflowers synthesized with different [$Mn(acac)_2$]/[$Au(OAc)_3$] molar ratios: (a) 5:1, (b) 10:1, and (c) 20:1.

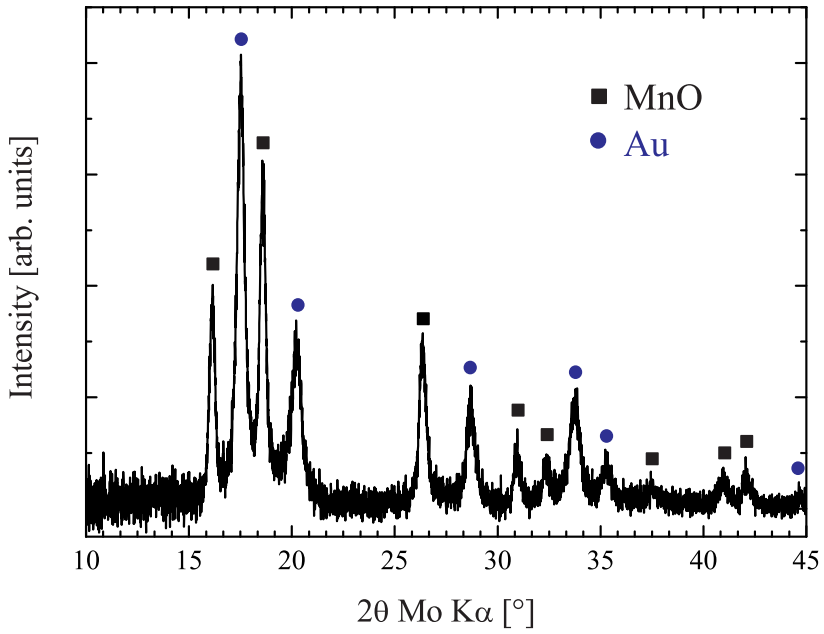

Figure 8.3: Powder XRD pattern of 7@18 nm Au@MnO nanoparticles. The positions and relative intensities of the reflections match well with those of standard MnO and Au powder diffraction data, indicating that the synthesis yielded a hetero-nanocomposite consisting of rock-salt MnO (*cF*8, $Fm\bar{3}m$) and *fcc* Au.

and size of the MnO petals increases with increasing $[Mn(acac)_2]/[Au(OAc)_3]$ ratio. Furthermore, the variation in size and morphology is accompanied by a change in the optical and magnetic properties.

Figure 8.2 shows Au@MnO nanoflowers prepared with different precursor ratios. Increasing the amount of manganese precursor leads to larger MnO petals. In all cases the MnO particles nucleate heterogeneously on the gold seeds, and no unattached MnO NPs were observed. Phase purity was confirmed by powder X-ray diffraction (see Figure 8.3).

Magnetic properties. The magnetic properties of the nanocomposites were investigated to evaluate the influence of the diamagnetic Au cores on the MnO domains. Figure 8.4 shows magnetic hysteresis loops recorded at 5 K of Au@MnO nanoflowers with Au cores of 7 nm and MnO petals of approximately 10 nm and 18 nm,

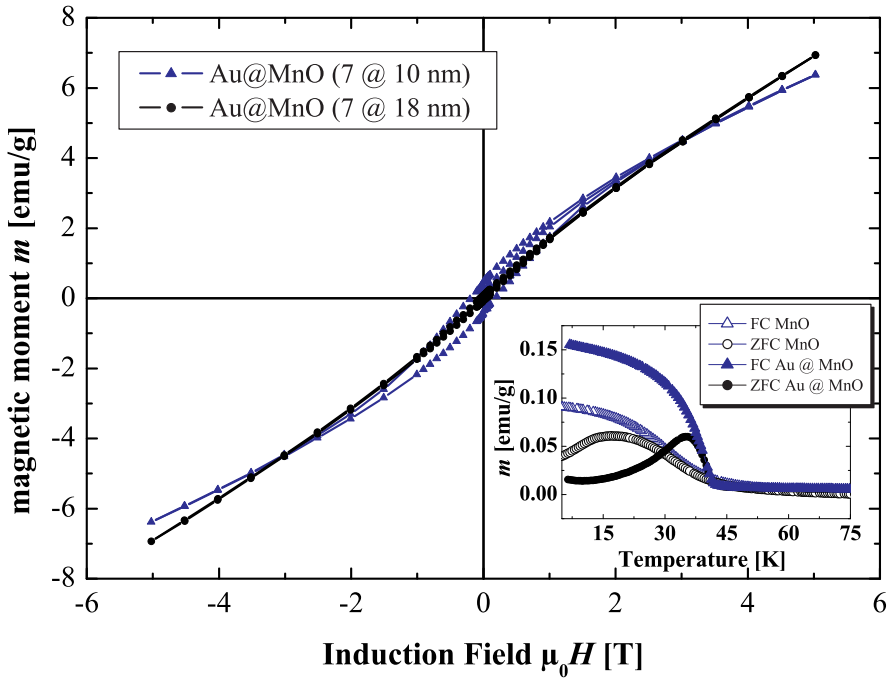

Figure 8.4: Magnetic hysteresis loops recorded at 5 K for Au@MnO nanoflowers with different petal sizes. The inset shows temperature dependent magnetization curves (FC–ZFC) of pure MnO nanoparticles and Au@MnO nanoflowers.

respectively. The nanocomposites are superparamagnetic; however, the saturation magnetization increases with MnO particle size, whereas the coercivity decreases. A more dramatic change can be seen in the field-cooled/zero-field-cooled (FC/ZFC) curves (inset in Figure 8.4), in which the magnetic blocking temperature increases to 35 K compared to pure MnO NPs.[54, 55] A change in the magnetic behavior of the Au@Fe_3O_4 dumbbells depending on the size of the Fe_3O_4 domain was also reported by Sun et *al.*; the authors explained this behavior with thermal agitation of the nanoparticles and canting of the surface spins.[53]

Optical properties. The interaction of MnO and Au NPs leads to a red-shift of the gold plasmon resonance (Figure 8.5). Pure Au NPs in the size range of 5-20 nm have a characteristic collective oscillation frequency (the plasmon resonance) at 520-525 nm,[56–60] the exact position varying with particle morphology and parti-

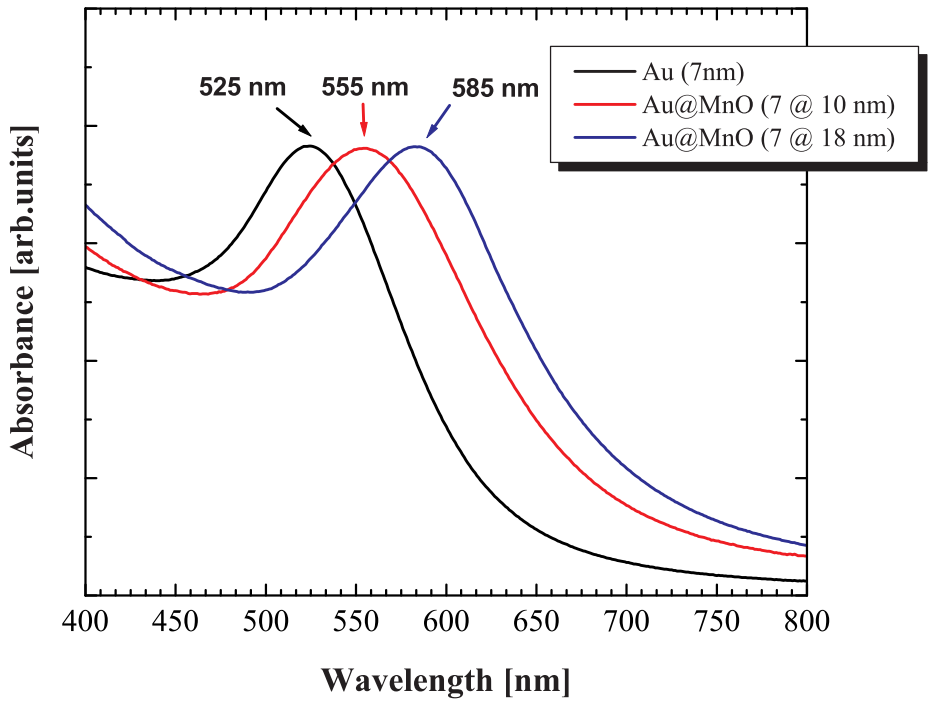

Figure 8.5: UV/Vis spectra of Au NPs and of Au@MnO NPs of different sizes.

cle surface coating.[61, 62] Attachment of the Au crystallites to MnO NPs leads to a significant shift of the extinction maximum to 555/585 nm (in the case of 7@10 nm and 7@18 nm Au@MnO particles, respectively, see Figure 8.5). The red-shift is due to the MnO petals, which increase the effective local dielectric function around the gold cores; this effect may be evaluated quantitatively using the classical Mie theory,[55, 63–68] using literature values for the optical constants for Au NPs,[69] and by approximating the local dielectric environment around these particles as a linear combination of the dielectric functions of the toluene solvent and the MnO domains.[70] Both experimental results confirm the assumption that the Au@MnO nanoflowers are both magnetically and optically active making them ideal candidates for multimodal biomedical imaging.

Selective surface functionalization. In the further course of our experiments,

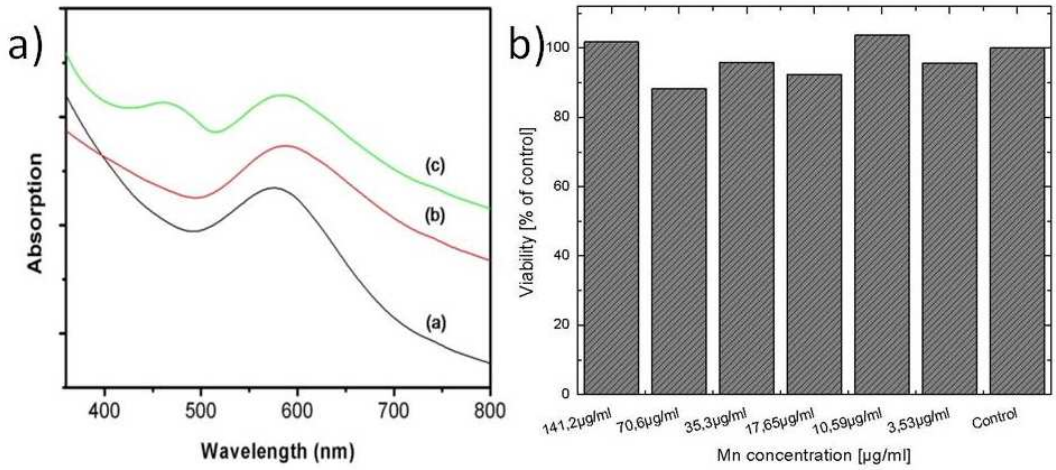

Figure 8.6: a) UV-vis spectra of the (a) as synthesized, (b) polymer functionalized and (c) NBD conjugated polymer functionalized Au@MnO NPs. b) Vitality assay of Caki 1 cells incubated with Au@MnO NPs. The density of Caki 1 cells were 105 cells/well. Cells were grown for 24 h before they were exposed to different concentrations of Au@MnO nanoparticle solutions for 24 h. The concentration of the NPs is referred to the concentration of Mn as measured by AAS.

we investigated the addressability of both individual surfaces. First, the surfactant molecules on the MnO surface were replaced by a multidentate copolymer carrying catechol anchor groups and poly(ethylene glycol) linkers (PEG; $M_r \approx 800$) with free amino groups for further surface conjugation (Figure 8.1).[71, 73] To visualize the polymer functionalization, the fluorescent dye 4-chloro-7-nitrobenzofurazan (NBD) was conjugated to the amine groups of the polymer (see Figure 8.6a).

Selective functionalization of the gold domain was achieved by incubating an aqueous solution of NBD-polymer- modified Au@MnO NPs with thiol-modified 24-mers customized oligonucleotide tagged with Texas red.[74] Excess reagents were removed by centrifugation. The functionalization approach is shown in Figure 8.7. The polymer-functionalized **NP stability and cytotoxicity.** The Au@MnO NPs were stable against aggregation and precipitation in various aqueous media, including deionized water and PBS buffer solution for several days. Viability assays of nanocomposite solutions with the renal cell carcinoma line Caki-1 showed negligible toxicity of the NPs even for concentrations as high as 140 μgmL^{-1} (see

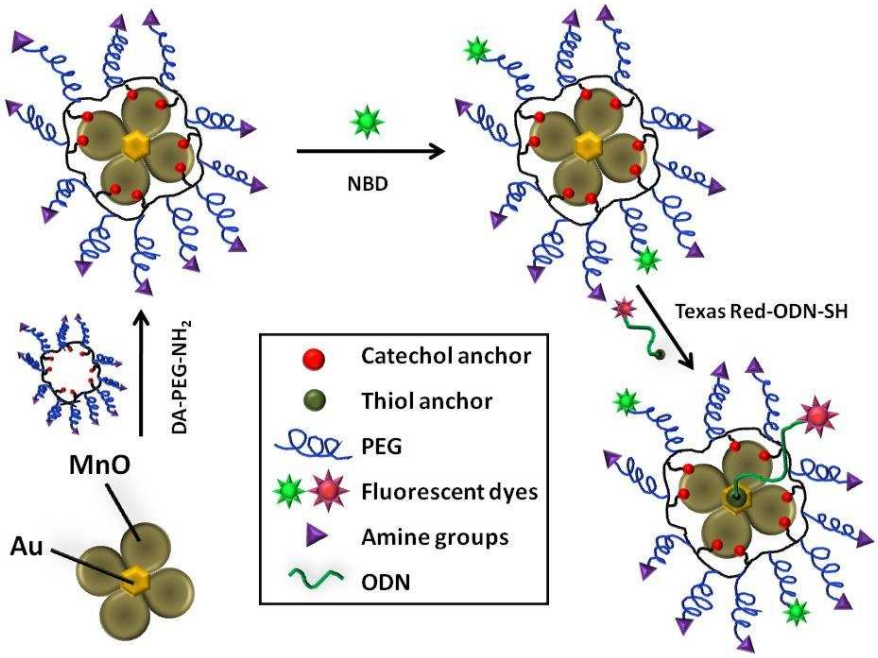

Figure 8.7: Surface functionalization of Au@MnO nanoflowers with a multidentate copolymer and subsequent conjugation with NBD. The gold domain was selectively functionalized with a Texas-Red-tagged thiolated oligonucleotide.

Figure 8.6b).

Optical imaging. The NPs were analyzed under an epifluorescent microscope at different emission wavelengths to visualize polymer-functionalized MnO domains (green fluorescence) and Texas-Red-tagged Au domains (red fluorescence). The co-localization of the green/red fluorescence signals in Figure 8.8a - c supports the idea that the nanoflowers are not only efficient as cargo-specific carriers but can simultaneously be used as optical probes for multimodal targeted delivery and imaging.

The optical properties of Au@MnO NPs were further explored with an optical transmission microscope in darkfield mode using a high-numerical aperture condenser and a 40 $\times$ air objective.[75] The particles were immobilized in a flat glass capillary with hexane as embedding medium (Figure 8.8d, seen as separated bright colored spots, each corresponding to one single nanoparticle). Most of the spots appear green- yellow to the eye, with minor variances in color and intensity demonstrating a relatively low polydispersity. A few brighter red spots indicate a negligible

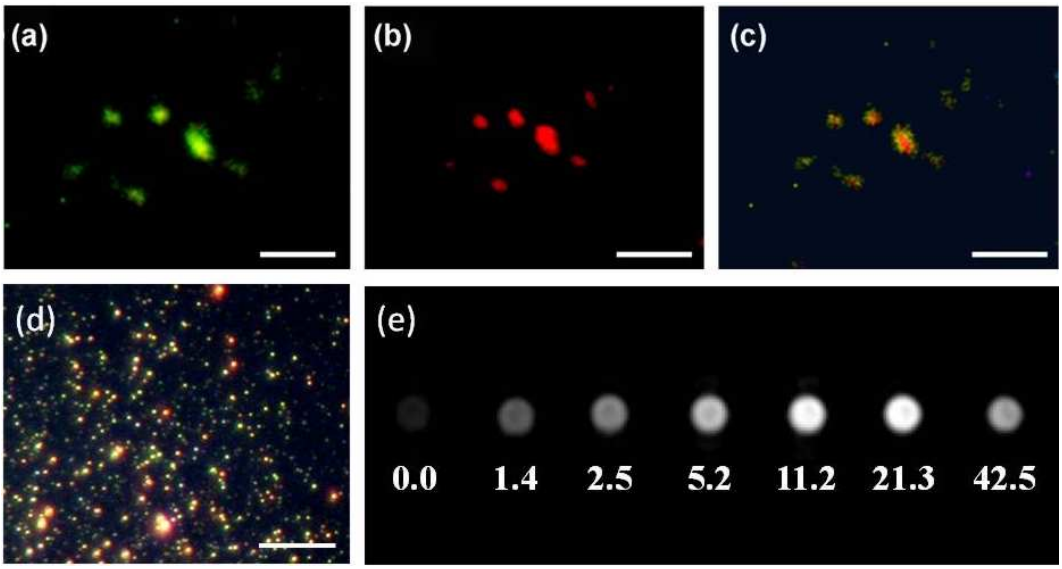

Figure 8.8: (a) Fluorescence microscope images of NBD−polymer-functionalized 7@18 nm Au@MnO nanoflowers (green fluorescence), (b) conjugated with Texas-Red-tagged thiolated oligonucleotide (red fluorescence), and (c) a co-localized image. (d) Real color picture of immobilized Au@MnO nanoflowers under dark-field illumination (all scale bars: 10 μm). (e) T_1-weighted MRI images of aqueous solutions containing 7@18 nm Au@MnO nanoflowers (concentrations in mM Mn).

number of aggregated particles with direct contact of the gold cores.
Investigation of a few dozen single particles shows a mean resonance wavelength λ_{res} = 584 $\pm$ 9 nm and a mean spectral linewidth Γ = 302 $\pm$ 51 meV (see Figure 8.9). These data agree well with the ensemble extinction spectrum of the sample (Figure 8.5). Pure gold spheres of comparable size to the gold core (ca. 10 nm) would be hardly detectable with this experimental setup; therefore, surrounding MnO panels enlarge the total particle volume and significantly increase the amplitude of the scattered light. Calculations within the quasi-static approximation[76] show an increase of the scattering cross-sections for a 10 nm MnO layer (n = 2.16) by a factor of 23 together with a red-shift of the resonance of 76 nm (see Figure 8.10).

Magnetic resonance imaging. For magnetic resonance imaging, T_1 relaxivity measurements were performed on a clinical 3.0 Tesla scanner (Magnetom Trio, Siemens Medical Solutions, Erlangen, Germany) by means of a T_1 measurement

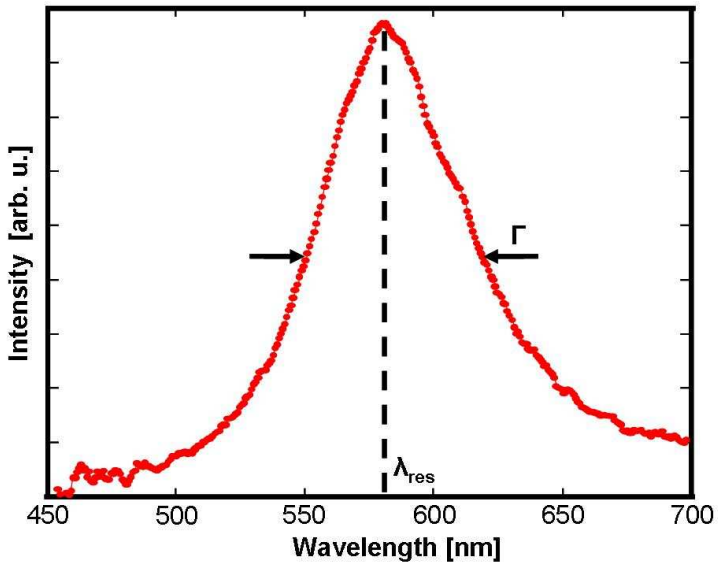

Figure 8.9: Typical scattering spectrum of a single Au@MnO nanoflower, revealing a resonance wavelength of approximately $\lambda_{res} \approx 580$ nm and a spectral linewidth of about $\Gamma \approx 300$ meV.

using a centric reordered saturation recovery (SR) prepared snapshot fast low angle shot (SR-TurboFLASH) pulse sequence with different preparation times (TI) ranging from 20 ms up to 8000 ms (other pulse sequence parameters: repetition time TR = 3.4 ms, echo time TE = 1.5 ms, flip angle = 208°). Figure 8.8e shows a T_1-weighted MR image of seven different MnO@Au nanocomposite concentrations dissolved in water ranging from 0 to 42.5 mM. T_1 measurement revealed a T_1 relaxivity of 0.224 $ms^{-1}mM^{-1}$ for the Au@MnO nanocomposites.

8.4 Conclusion

In summary, we have described the synthesis and characterization of a group of flowerlike Au@MnO NPs. By taking advantage of their constituent properties, different functional molecules were loaded onto each component of the heterostructure. The NPs are magnetically and optically active, and they are therefore useful for simultaneous magnetic and optical detection. The fact that the nanoflowers are

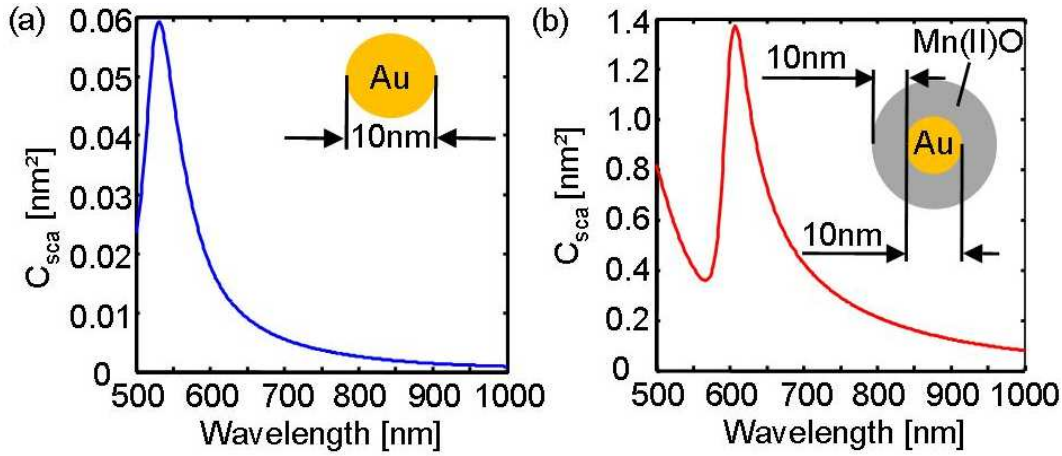

Figure 8.10: Theoretical scattering spectra based on the quasi-static approximation for gold spheres (a) and MnO coated gold spheres (b). While bare gold spheres of 10 nm size show a resonance wavelength of 531 nm, the same particle coated with a 10 nm MnO layer (n = 2.16) shows a resonance of 607 nm. Furthermore the scattering cross-section C_{sca} increases about 23 times due to the shell.

capable of imaging the same tissue area with both MRI and an optical source without the fast signal loss observed in the common fluorescent labeling implies, that they can be used to achieve high sensitivity in diagnostic imaging applications. It would be interesting to extend this synthetic method to nanoflowers made of different materials, such as Cu@MnO, Ag@MnO, or Pt@MnO, and to use these multidomain particles as building blocks of higher-order structures, the symmetries of which would derive from "directional" interactions between NP petals (for example, linear particle chains from nanoflowers having two leaves). Work on attaching therapeutic molecules to these dumbbell NPs for target-specific imaging and delivery is currently underway.

8.5 Experimental Section

Materials. Manganese (II) acetylacetonate (97%, ABCR), gold(III) acetate ($\geq$99.9%, Alfa Aesar), oleic acid (90%, Aldrich), oleylamine (80-90%, ACROS), phenyl ether ($\geq$99%, Sigma Aldrich), di-*tert*-butyl dicarbonate ($(Boc)_2O$) ($\geq$99%, Aldrich), dioxane (p.A., Fisher), H_2N-PEG(800)-NH_2 ($M_w \approx 800$ g mol^{-1}, Ald-

rich), triethylamine (≥99%, Aldrich), 3-hydroxy tyramine hydrochloride (dopamine·HCl) (98%, Aldrich), 4-chloro-7-nitrobenzofurazan (NBD) (98%, Aldrich) trifluoroacetic acid (TFA) (99%, Sigma-Aldrich), ethanol (99.8%, Roth), toluene (≥99%, Sigma-Aldrich), hexane (p.A., Fisher), DCM (p.A., Fisher), DMF (extra dry, ≥99.8%, Acros), diethyl ether (p.A. Fisher) were used as received without further purification.

Synthesis of Au@MnO Nanoflowers. All reactions were carried out using standard Schlenk techniques. 1 mmol of manganese (II) acetylacetonate and 0.05 mmol of gold (III) acetate were added to a mixture of phenylether (12 mL), oleic acid (1 mL) and oleylamine (2 mL) under argon. The mixture was degassed at 50 °C (10^{-2} mbar) for 1 hour and repeatedly backfilled with argon to remove any traces of air and moisture. The resulting solution was rapidly heated to reflux (259-261 °C) with approx. 20-25 °Cmin^{-1} and kept at this temperature for 60 minutes before cooling to room temperature. The product was precipitated by addition of excess ethanol and collected by centrifugation. The NPs were repeatedly washed by dissolving them in toluene, precipitating them with ethanol and centrifugation. Finally, the product was dissolved in toluene, flushed with argon and stored in a fridge.

Nanoparticle Characterization. The particles were characterized by means of powder X-ray diffraction (XRD), and transmission electron microscopy (TEM). The magnetic properties of the Au@MnO NPs were investigated with a superconducting quantum interference device (SQUID). XRD measurements were performed on a Bruker D8 Advance diffractometer equipped with a Sol-X energy-dispersive detector and operating with Mo Kα radiation. Samples for transmission electron microscopy were prepared by placing a drop of dilute nanoparticle solution in hexane on a carbon coated copper grid. Low-resolution TEM images and ED patterns were recorded on a Philips EM420 microscope operating at an acceleration voltage of 120 kV. Magnetic measurements were carried out using a Quantum Design MPMS-XL SQUID magnetometer.

Morphology of the Au@MnO NPs. In order to quantitatively investigate the morphology we determined the ratio *r* of the average diameter of MnO petals to Au cores. In all samples the gold cores retained almost the same average diameter (5-10 nm), whereas the size and number of the MnO petals changed. For a $Mn(acac)_2$: $Au(ac)_3$ ratio of $R = 5 : 1$ (Figure 8.2a), *r* is 1.2 with the MnO domains hav-

ing an average diameter of 10 nm and the composite particles mainly consisting of dimers, trimers and only few "nanopansies". For *R* = 10 : 1, *r* is 1.5 and more and larger petals are visible on the Au cores (Figure 8.2b). Finally, for *R* = 20 : 1, r is 2.1 and "nanopansies" with 3 or more petals are the predominant morphology (Figure 8.2c).

Synthesis of Boc protected Bis-Amine-PEG (NBoc-PEG-NH_2). A solution of $(Boc)_2O$ (0.02 mol) in 30 mL of anhydrous dioxane was added drop wise to a solution of NH_2-PEG-NH_2 (0.1 mol) in 50 mL anhydrous dioxane. The resulting solution was stirred overnight at room temperature. The solvent was evaporated, and the oily product obtained was dissolved in 50 mL of water and extracted using 50 mL of CH_2Cl_2 (three times). The combined organic phases were washed with a conc. solution of NaCl and dried over anhydrous Na_2SO_4. The resulting organic phase was concentrated by rotary evaporation to produce a viscous, colourless oil. Further purification was achieved by flash chromatography on silica using a CH_2Cl_2 / ethanol mixture (2:1) as eluent.

Preparation of the polymer. The poly (active ester) poly(pentafluorophenylacrylate) (PFA) was prepared as reported earlier.[71, 72, 77] GPC analysis of the obtained polymer (THF, light scattering detection) gave: M_n = 16,390 gmol^{-1}, PDI = 1.39, with an average of 70 repeating units.

For the synthesis of the multifunctional poly(acrylamides), poly(active ester) poly(pentafluorophenylacrylate) (700 mg, 2.94 mmol repeating units) was dissolved in a mixture of 9 mL dry DMF and 0.7 mL triethylamine. After that, 3-hydroxytyramine hydrochloride (24 mg) dissolved in 3 mL DMF and 0.4 mL triethylamine was added and the reaction mixture was stirred for 3 hours at 50 °C. In the final step the remaining active ester groups were substituted using an excess of NBoc-PEG-NH_2 (dissolved in 3 mL dry DMF) and stirring for 5 h at 50 °C. The solution was concentrated to about 2 mL and the polymeric ligand was precipitated by addition of cold ethyl ether. The precipitated polymer was centrifuged and the solvent was decanted. Upon drying, 286 mg of a colorless oil was obtained.

Cleavage of the Boc group. The polymer obtained above was dissolved in CH_2Cl_2 (30 mL). After that, trifluoroacetic acid (2.0 mL) was added and the mixture was stirred at room temperature for 2 h. After that the reaction solution was treated with mixture of water and hexane (30 mL/50 mL) and vigorously stirred for 30 minutes.

The aqueous phase containing the polymer was separated and concentrated to 2 mL and dialysed against deionized water for 2 days (cellulose bag, MWCO = 3,500). Finally, the water was evaporated and the product was redissolved in chloroform to make a stock solution which was kept in a fridge.

Selective functionalization of MnO domains in Au@MnO nanoflowers. 10 mg of Au@MnO nanoflowers dispersed in 15 mL of chloroform were slowly added over 1 h into the above synthesized polymer solution (20 mg/ 10 mL, chloroform). The reaction was continuously stirred at 50 °C, overnight under inert condition. The functionalized NPs were precipitated by addition of hexane und separated from unbound polymer and surfactants by centrifugation. The Au@MnO NPs were washed twice by dissolving them in acetone and precipitating them with hexane. Finally, the particles were stored in acetone or DMF in a fridge.

Conjugation of NBD dye to free NH_2 groups of polymer functionalized Au@MnO nanoflowers. 8 mg of 4-chloro-7-nitrobenzofurazan (NBD) dissolved in 1 mL acetone along with 0.1 mL of triethylamine was added to a solution of polymer functionalized Au@MnO NPs in acetone (10 mg in 10 mL). The resulting solution was stirred for 3 hours at 50 °C in the dark under argon protection. After that, the dye modified NPs were precipitated and washed with hexane/acetone.

Transfer of Au@MnO-polymer-NBD into the aqueous phase. To transfer the polymer-NBD functionalized nanoflowers into an aqueous solution same amounts of water and hexane were added dropwise to a nanoflower solution in chloroform. After complete addition, the solution was stirred for further 30 min. at room temperature. Separation of the aqueous and the organic phase was achieved with a separatory funnel. The Au@MnO NPs were almost exclusively found in the aqueous phase. The concentration was determined using atomic absorption spectroscopy (AAS, Perkin-Elmer 5100 ZL).

Selective modification of the Au cores in Au@MnO-polymer-NBD composites using Texas Red-ODN-SH. For modification of the Au core a 24-mers customized oligonucleotide with the following composition: TTTTTTTTTTTTTTTTTTTTTT-TTT-SH containing Texas red at the 5' end and a thiol group on the 3' end (Texas Red-ODN-SH, Sigma Aldrich) was used. A stock solution with a concentration of 75 mM was prepared in Tris-EDTA buffer (pH 7.5) and aliquots were kept at -20 °C. For oligonucleotide functionalization, NBD-polymer modified Au@MnO

nanoflowers (2 mg mL^{-1}) were incubated with a 10 mM solution of Texas Red-ODN-SH as described elsewhere.[30] After shaking for 24 h at 20 °C, the sample was treated with phosphate buffer (10 mM, pH 7.0) containing NaCl (0.1 M) followed by a centrifugation step (15 min at 10000 rpm, room temperature) to remove unbound oligonucleotides. Following removal of the supernatant, the NPs were washed twice with phosphate buffer (10 mM, pH 7.0) + NaCl (0.1 M), re-centrifuged (15 min, 10000 rpm, room temperature) and re-dispersed in the same phosphate buffer solution. The fluorescence analysis of the multi-fluorescent labeled NPs was performed with an Olympus AHBT3 light microscope, together with an AH3-RFC reflected light fluorescence attachment at the emission wavelength of 456 nm (filter U) and 565 nm (filter G) to visualize both, NBD on the MnO domains and Texas Red labelled ODN-SH on the Au cores. The images were co-localized using the software Analysis (Olympus, USA).

Cell culture and cytotoxicity-assay. The human renal cell carcinoma line (Caki 1) was kindly provided by the group of Prof. Dr. P Langguth, Institute for pharmacy and biochemistry, Johannes Gutenberg-University, Mainz. Cells were grown in McCoys 5A media (Sigma-Aldrich, Germany) supplemented with 10% fetal bovine serum (FBS, Sigma-Aldrich, Germany), 1% Penicillin-Streptomycin (PEST, 10000 U mL^{-1} Penicillin and 10 mg mL^{-1} Streptomycin, Sigma-Aldrich) 2 mM L-glutamine (Sigma-Aldrich, Germany), 1x Mycokill (PAA, Germany) and 1x MEM non essential amino acids (Sigma-Aldrich, Germany). Cell cultures were routinely grown in 75 cm^2 sterile cell culture flask until and were contained at 37 °C, 95% relative humidity and 5% CO_2 until reaching the confluence of $2{,}1 \cdot 10^6$ cells mL^{-1}. The cytotoxicity assay was performed according to the supplier. Cells were grown in 96 well plates under standard conditions in 90 μL McCoys 5A. The density was 105 cells/well. In 6 wells only media was added to allow background subtraction. After 24 h of cell growth, different concentrations of Au@MnO NPs functionalized with polymer and NBD in McCoys 5A were added. NPs were sterile filtered using a mixed ester 0,22 μm filter (Sigma-Aldrich) prior to use. Incubation time was set at 24 h. After this period of time, the media was replaced by 100 μL RPMI 1640 media without phenol red (Sigma-Aldrich, Germany) supplemented with 10% FBS, 1% PEST, 2 mM L-gluthamine and mycokill. 10 μL MTT labelling reagent (WST 8, Sigma-Aldrich, Germany) was added. Cells were incubated at 37 °C, 5% CO_2

and 95% relative humidity for 1.5 h, followed by incubation at room temperature on a shaker in the dark for further 2 h. The absorption of formazan which was formed due to cellular activity was measured at 450 nm. Wells without cells were used to allow background substraction. All results were normalized to wells that did contain cells, but where media was added instead of NPs.

8.6 References

[1] Hines, M. A.; Guyot-Sionnest, P. *J. Phys. Chem. (Journal of Physical Chemistry)* **1996**, *100*, 468–471.

[2] Peng, X.; Schlamp, M. C.; Kadavanich, A. V.; Alivisatos, A. *Journal of the American Chemical Society* **1997**, *119*, 7019–7029.

[3] Cao, Y. W.; Banin, U. *Angewandte Chemie* **1999**, *111*, 3913–3916.

[4] Cao, Y. W.; Banin, U. *Angewandte Chemie International Edition* **1999**, *38*, 3692–3694.

[5] Cozzoli, P. D.; Pellegrino, T.; Manna, L. *Chemical Society Reviews* **2006**, *35*, 1195–1208.

[6] Hu, M.; Chen, J.; Li, Z.-Y.; Au, L.; Hartland, G. V.; Li, X.; Marquez, M.; Xia, Y. *Chemical Society Reviews* **2006**, *35*, 1084–1094.

[7] Zeng, H.; Sun, S. *Advanced Functional Materials* **2008**, *18*, 391–400.

[8] McGuire, J. A.; Joo, J.; Pietryga, J. M.; Schaller, R. D.; Klimov, V. I. *Accounts of Chemical Research* **2008**, *41*, 1810–1819.

[9] Gao, J.; Gu, H.; Xu, B. *Accounts of Chemical Research* **2009**, *42*, 1097–1107.

[10] Wang, C.; Daimon, H.; Sun, S. *Nano Letters* **2009**, *9*, 1493–1496.

[11] Wang, C.; Irudayaraj, J. *Small* **2010**, *6*, 283–289.

[12] Choi, S.-H.; Na, H. B.; Park, Y. I.; An, K.; Kwon, S. G.; Jang, Y.; Park, M.-h.; Moon, J.; Son, J. S.; in Song, C.; Moon, W. K.; Hyeon, T. *Journal of the American Chemical Society* **2008**, *130*, 15573–15580.

[13] Gu, H.; Xu, K.; Xu, C.; Xu, B. *Chemical Communications* **2006**, 941–949.

[14] Schröder, H. C.; Natalio, F.; Wiens, M.; Tahir, M. N.; Shukoor, M. I.; Tremel, W.; Belikov, S. I.; Krasko, A.; Müller, W. E. G. *Molecular Immunology* **2008**, *45*, 945–953.

[15] Shukoor, M. I.; Natalio, F.; Tahir, M. N.; Ksenofontov, V.; Therese, H. A.; Theato, P.; Schroder, H. C.; Muller, W. E. G.; Tremel, W. *Chemical Communications* **2007**, 4677–4679.

[16] Yang, S.; Peng, Z.; Yang, H. *Advanced Functional Materials* **2008**, *18*, 2745–2753.

[17] Liu, Q.; Yan, Z.; Henderson, N. L.; Bauer, J. C.; Goodman, D. W.; Batteas, J. D.; Schaak, R. E. *Journal of the American Chemical Society* **2009**, *131*, 5720–5721.

[18] Lim, B.; Jiang, M.; Camargo, P. H. C.; Cho, E. C.; Tao, J.; Lu, X.; Zhu, Y.; Xia, Y. *Science* **2009**, *324*, 1302–1305.

[19] Kim, J.; Park, S.; Lee, J. E.; Jin, S. M.; Lee, J. H.; Lee, I. S.; Yang, I.; Kim, J. S.; Kim, S. K.; Cho, M. H.; Hyeon, T. *Angewandte Chemie* **2006**, *118*, 7918–7922.

[20] Kim, J.; Park, S.; Lee, J. E.; Jin, S. M.; Lee, J. H.; Lee, I. S.; Yang, I.; Kim, J. S.; Kim, S. K.; Cho, M. H.; Hyeon, T. *Angewandte Chemie International Edition* **2006**, *45*, 7754–7758.

[21] Xu, C.; Xie, J.; Ho, D.; Wang, C.; Kohler, N.; Walsh, E.; Morgan, J.; Chin, Y.; Sun, S. *Angewandte Chemie International Edition* **2008**, *47*, 173–176.

[22] Liong, M.; Lu, J.; Kovochich, M.; Xia, T.; Ruehm, S. G.; Nel, A. E.; Tamanoi, F.; Zink, J. I. *ACS Nano* **2008**, *2*, 889–896.

[23] Wang, L.; Bai, J.; Li, Y.; Huang, Y. *Angewandte Chemie* **2008**, *120*, 2473–2476.

[24] Wang, L.; Bai, J.; Li, Y.; Huang, Y. *Angewandte Chemie* **2008**, *47*, 2439–2442.

[25] Park, H.; Yang, J.; Seo, S.; Kim, K.; Suh, J.; Kim, D.; Haam, S.; Yoo, K. H. *Small* **2008**, *4*, 192–196.

[26] Kim, C.-k.; Ghosh, P.; Rotello, V. M. *Nanoscale* **2009**, *1*, 61–67.

[27] Becker, J.; Zins, I.; Jakab, A.; Khalavka, Y.; Schubert, O.; Sönnichsen, C. *Nano Letters* **2008**, *8*, 1719–1723.

[28] Pérez-Juste, J.; Pastoriza-Santos, I.; Liz-Marzán, L. M.; Mulvaney, P. *Coordination Chemistry Reviews* **2005**, *249*, 1870–1901.

[29] Huang, X.; El-Sayed, I. H.; Qian, W.; El-Sayed, M. A. *Journal of the American Chemical Society* **2006**, *128*, 2115–2120.

[30] Norman, R. S.; Stone, J. W.; Gole, A.; Murphy, C. J.; Sabo-Attwood, T. L. *Nano Letters* **2008**, *8*, 302–306.

[31] Dickerson, E. B.; Dreaden, E. C.; Huang, X.; El-Sayed, I. H.; Chu, H.; Pushpanketh, S.; McDonald, J. F.; El-Sayed, M. A. *Cancer Letters* **2008**, *269*, 57–66.

[32] Weissleder, R.; Tung, C.-H.; Mahmood, U.; Bogdanov, A. *Nature Biotechnology* **1999**, *17*, 375–378.

[33] Becker, A.; Hessenius, C.; Licha, K.; Ebert, B.; Sukowski, U.; Semmler, W.; Wiedenmann, B.; Grotzinger, C. *Nature Biotechnology* **2001**, *19*, 327–331.

[34] Salgueirino-Maceira, V.; Correa-Duarte, M. A.; Farle, M. *Small* **2005**, *1*, 1073–1076.

[35] Jun, C.-H.; Park, Y. J.; Yeon, Y.-R.; Choi, J.-r.; Lee, W.-r.; Ko, S.-j.; Cheon, J. *Chemical Communications* **2006**, 1619–1621.

[36] Kang, S.; Miao, G.; Shi, S.; Jia, Z.; Nikles, D. E.; Harrell, J. *Journal of the American Chemical Society* **2006**, *128*, 1042–1043.

[37] Jun, Y.-w.; Seo, J.-w.; Cheon, J. *Accounts of Chemical Research* **2008**, *41*, 179–189.

[38] Bodnarchuk, M. I.; Kovalenko, M. V.; Groiss, H.; Resel, R.; Reissner, M.; Hesser, G.; Lechner, R. T.; Steiner, W.; Schäffler, F.; Heiss, W. *Small* **2009**, *5*, 2247–2252.

[39] Zeng, H.; Li, J.; Liu, J.; Wang, Z. L.; Sun, S. *Nature* **2002**, *420*, 395–398.

[40] Zeng, H.; Li, J.; Wang, Z.; Liu, J.; Sun, S. *Nano Letters* **2004**, *4*, 187–190.

[41] Berkowitz, A. E.; Rodriguez, G. F.; Hong, J. I.; An, K.; Hyeon, T.; Agarwal, N.; Smith, D. J.; Fullerton, E. E. *Journal of Physics D: Applied Physics* **2008**, *41*, 5.

[42] Malik, M. A.; O'Brien, P.; Revaprasadu, N. *Chemistry of Materials* **2002**, *14*, 2004–2010.

[43] Decker, S.; Klabunde, K. J. *Journal of the American Chemical Society* **1996**, *118*, 12465–12466.

[44] Merbach, A. E.; Tóth, E. *The chemistry of contrast agents in medical magnetic resonance imaging*; Wiley: Chichester, 2001.

[45] Jun, Y.-w.; Lee, J.-H.; Cheon, J. *Angewandte Chemie International Edition* **2008**, *47*, 5122–5135.

[46] Jun, Y. w.; Lee, J. H.; Cheon, J. *Angewandte Chemie* **2008**, *120*, 5200–5213.

[47] Na, H. B.; Lee, J. H.; An, K.; Park, Y. I.; Park, M.; Lee, S.; Nam, D. H.; Kim, S. T.; Kim, S. H.; Kim, S. W.; Lim, K. H.; Kim, K. S.; Kim, S. O.; Hyeon, T. *Angewandte Chemie International Edition* **2007**, *46*, 5397–5401.

[48] Na, H.; Lee, J.; An, K.; Park, Y.; Park, M.; Lee, I.; Nam, D. H.; Kim, S.; Kim, S. H.; Kim, S. W.; Lim, K. H.; Kim, K. S.; Kim, S. O.; Hyeon, T. *Angewandte Chemie* **2007**, *119*, 5341–5341.

[49] Shukoor, M.; Natalio, F.; Ksenofontov, V.; Tahir, M.; Eberhardt, M.; Theato, P.; Schröder, H.; Müller, W.; Tremel, W. *Small* **2007**, *3*, 1374–1378.

[50] Shukoor, M.; Natalio, F.; Metz, N.; Glube, N.; Tahir, M.; Therese, H.; Ksenofontov, V.; Theato, P.; Langguth, P.; Boissel, J. P.; Schröder, H. C.; Müller, W. E. G.; Tremel, W. *Angewandte Chemie International Edition* **2008**, *47*, 4748–4752.

[51] Shukoor, M.; Natalio, F.; Metz, N.; Glube, N.; Tahir, M.; Therese, H.; Ksenofontov, V.; Theato, P.; Langguth, P.; Boissel, J. P.; Schröder, H. C.; Müller, W. E. G.; Tremel, W. *Angewandte Chemie* **2008**, *120*, 4826–4830.

[52] Shukoor, M. I. et al. *Advanced Functional Materials* **2009**, *19*, 3717–3725.

[53] Yu, H.; Chen, M.; Rice, P. M.; Wang, S. X.; White, R.; Sun, S. *Nano Letters* **2005**, *5*, 379–382.

[54] Seo, W. S.; Jo, H. H.; Lee, K.; Kim, B.; Oh, S. J.; Park, J. T. *Angewandte Chemie International Edition* **2004**, *43*, 1115–1118.

[55] Schladt, T. D.; Graf, T.; Tremel, W. *Chemistry of Materials* **2009**, *21*, 3183–3190.

[56] Faraday, M. *Philosphical Transactions of the Royal Society, London* **1857**, *147*, 1145–1181.

[57] Kreibig, U.; Vollmer, M. *Optical properties of metal clusters*; Springer: Berlin, 1995; Vol. 25.

[58] Raschke, G.; Kowarik, S.; Franzl, T.; Sönnichsen, C.; Klar, T. A.; Feldmann, J.; Nichtl, A.; Kürzinger, K. *Nano Letters* **2003**, *3*, 935–938.

[59] Kelly, K. L.; Coronado, E.; Zhao, L. L.; Schatz, G. C. *Journal of Physical Chemistry B* **2003**, *107*, 668–677.

[60] Daniel, M.-C.; Astruc, D. *Chemical Reviews* **2004**, *104*, 293–346.

[61] Rothenhäusler, B.; Knoll, W. *Optics Communications* **1987**, *63*, 301–304.

[62] Nelles, G.; Schönherr, H.; Jaschke, M.; Wolf, H.; Schaub, M.; Küther, J.; Tremel, W.; Bamberg, E.; Ringsdorf, H.; Butt, H.-J. *Langmuir* **1998**, *14*, 808–815.

[63] Seo, W. S.; Jo, H. H.; Lee, K.; Kim, B.; Oh, S. J.; Park, J. T. *Angewandte Chemie* **2004**, *116*, 1135–1137.

[64] Mie, G. *Annalen der Physik* **1908**, *330*, 377–445.

[65] Pinchuk, A.; Kreibig, U. *New Journal of Physics* **2003**, *5*, 151–166.

[66] Pinchuk, A. O.; Kalsin, A. M.; Kowalczyk, B.; Schatz, G. C.; Grzybowski, B. A. *Journal of Physical Chemistry C* **2007**, *111*, 11816–11822.

[67] Wei, Y.; Klajn, R.; Pinchuk, A. O.; Grzybowski, B. A. *Small* **2008**, *4*, 1635–1639.

[68] Hens, Z.; Vanmaekelbergh, D.; Stoffels, E. J. A. J.; van Kempen, H. *Physical Review Letters* **2002**, *88*, 236803.

[69] Johnson, P. B.; Christy, R. W. *Physical Reviews B* **1972**, *6*, 4370.

[70] Kim, K. J.; Young Ran Park, *Journal of Crystal Growth* **2004**, *270*, 162–167.

[71] Eberhardt, M.; Mruk, R.; Zentel, R.; Théato, P. *European Polymer Journal* **2005**, *41*, 1569–1575.

[72] Tahir, M. N.; Eberhardt, M.; Theato, P.; Faiss, S.; Janshoff, A.; Gorelik, T.; Kolb, U.; Tremel, W. *Angewandte Chemie* **2006**, *118*, 922–926.

[73] Tahir, M. N.; Eberhardt, M.; Theato, P.; Faiss, S.; Janshoff, A.; Gorelik, T.; Kolb, U.; Tremel, W. *Angewandte Chemie International Edition* **2006**, *45*, 908–912.

[74] Storhoff, J. J.; Elghanian, R.; Mucic, R. C.; Mirkin, C. A.; Letsinger, R. L. *Journal of the American Chemical Society* **1998**, *120*, 1959–1964.

[75] Becker, J.; Schubert, O.; Sönnichsen, C. *Nano Letters* **2007**, *7*, 1664–1669.

[76] Liu,; Guyot-Sionnest, P. *Journal of Physical Chemistry B* **2004**, *108*, 5882–5888.

[77] Theato, P. *Journal of Polymer Science Part A: Polymer Chemistry* **2008**, *46*, 6677–6687.

CHAPTER 9

Highly Soluble Multifunctional MnO Nanoparticles for Simultaneous Optical and MRI Imaging and Cancer Treatment using Photodynamic Therapy

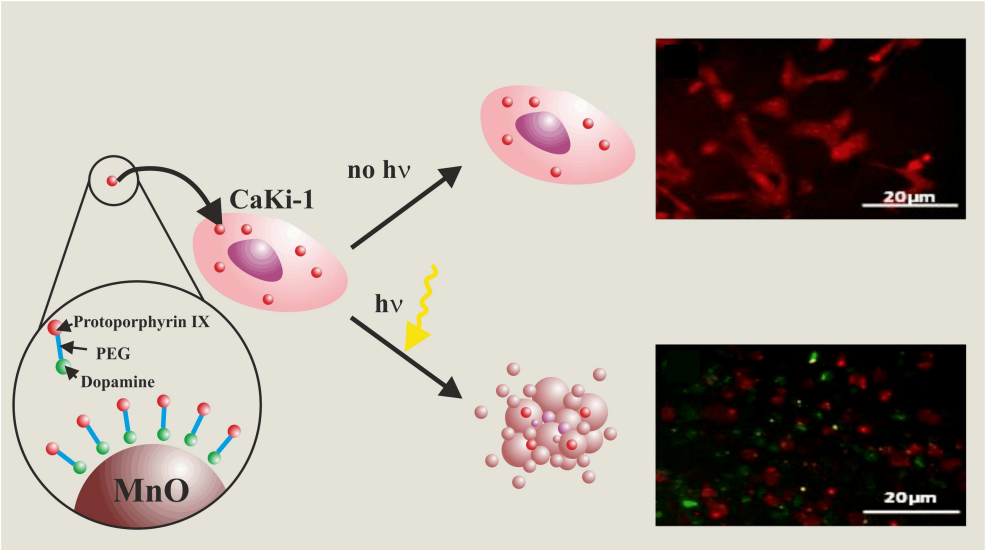

9.1 Abstract

Superparamagnetic MnO nanoparticles were functionalized using a hydrophilic ligand containing protoporphyrin IX as photosensitizer. By virtue of their magnetic properties these NPs may serve as contrast enhancing agents for magnetic resonance imaging (MRI), while the fluorescent target ligand protoporphyrin IX allows simultaneous tumor detection and treatment by photodynamic therapy (PDT). Caki-1 cells were incubated with these NPs. Subsequent exposure to visible light lead to cell apoptosis due to photoactivation of the photosensitizer conjugated to the NPs. This method offers great diagnostic potential for highly proliferative tissues, including tumors. In addition, it is an efficient platform that combines the advantages of a biocompatible photosensitizer with the possibility for MRI monitoring due to the magnetic properties of the highly soluble functionalized manganese oxide NPs.

9.2 Introduction

Cancer "theragnostics", the ability to simultaneous diagnose and treat cancer, has become one of the major driving forces in nano-biotechnology. In this context, NPs of 3d transition metal oxides have gained enormous attention in recent years due to their unique magnetic properties which make them promising candidates for various applications ranging from protein separation,[1–3] specific cell targeting, drug delivery,[4, 5] and magnetic resonance imaging (MRI).[6–9] To date, most interest in the clinical use of magnetic NPs (NPs) has focused on magnetite (Fe_3O_4) and maghemite (γ-Fe_2O_3) NPs, which are known to shorten the transverse (or spin-spin) relaxation time T_2.[9–11] Additionally, manganese oxide (MnO) NPs have recently proved to be interesting candidates as contrast agents for shortening of the longitudinal (or spin-lattice) relaxation time T_1.[12–15] However, a major requirement for the successful application of magnetic NPs in biomedicine is in addition to solubility and colloidal stability in physiological environment a low toxicity. Efficient strategies for surface modification have lead to a tremendous improvement of both, biocompatibility and stability, in biological media.[16–20] Most of these strategies employ poly(ethylene glycol) (PEG) as hydrophilic linker because it not only guarantees prolonged blood half-life and circulation, but also reduced opsonization and

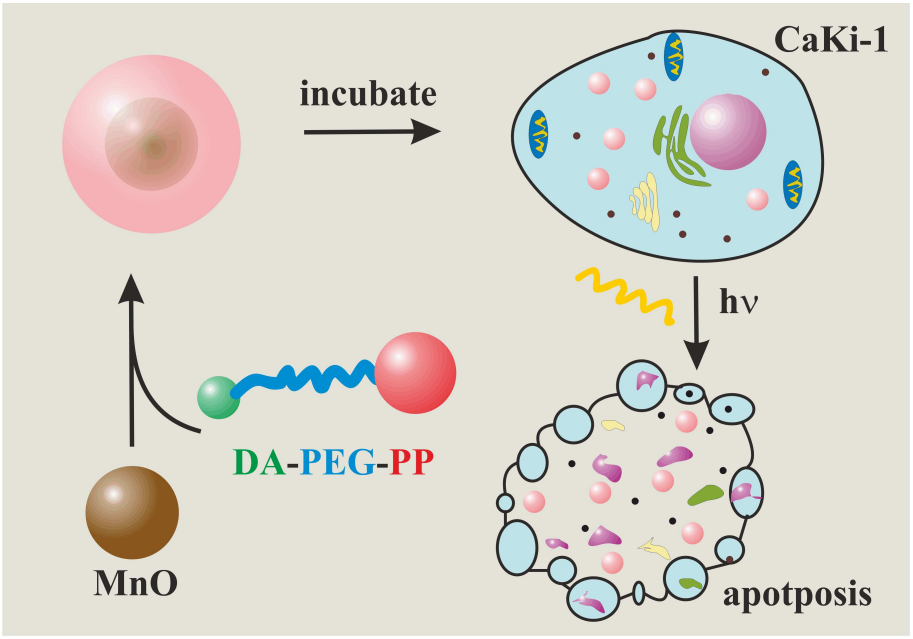

Figure 9.1: Experimental scheme: MnO NPs were first functionalized using a bifunctional catechol-PEG-protoporphyrin IX (DA-PEG-PP) ligand. These MnO-DA-PEG-PP NPs were then incubated in CaKi-1 cells. Subsequent irradiation with visible light led to the photoactivation of protoporphyrin IX and, thus, production of reactive singlet oxygen ($^1O_2$), which induced cell death by apoptosis.

non-specific uptake by macrophage cells.[21–27] In order to achieve sufficient surface coverage of the magnetic NPs highly effective anchor molecules are necessary. 3-Hydroxytyramine (dopamine), a derivative of the amino acid L-DOPA, a key component in many marine adhesive proteins,[28–34] has proven to be a powerful chelating ligand which strongly binds to metal and metal oxide surfaces.[35, 36] Consequently, the conjugation of dopamine and PEG has evolved as a popular method among the scientific community to functionalize magnetic NPs.[17, 37–40] However, extensive studies on the surface modification and biomedical application of manganese oxide NPs have only rarely been reported so far.

Photosensitizers, active compounds used for photodynamic therapy (PDT), have the intrinsic advantage of distributing primarily in highly regenerative tissues after intravenous or oral administration.[41] Their therapeutic effect is activated by photoexcitation of the localized photosensitizer to generate cytotoxic species, e.g., sin-

glet oxygen ($^1O_2$), free radicals, or peroxides. This leads to selective and irreversible destruction of diseased tissues, without damaging adjacent healthy cells.[42–45] Compared to other current cancer therapies such as surgery, radiotherapy or chemotherapy, PDT is an effective and selective means of suppressing cancer tissues growth without affecting the surrounding healthy tissue. Since 1993, government regulatory approval for photodynamic therapy involves the use of a partially purified, commercially available hematoporphyrin derivative compound (Photofrin) for patients suffering of early and advanced stages of cancer of the lung, digestive tract, and genitourinary tract.[46] The application of PDT is now considered an alternative solution for the treatment of tumors that eludes conventional chemo- and radiotherapy methods.

In recent years increased research effort has been devoted to NPs as novel platforms to enhance the drug delivery efficiency to cancer cells.[47] This leads to applications not only as therapeutic drugs in non-invasive cancer treatment,[48, 49] but also in clinical diagnostics,[50, 51] e.g. in the diagnosis of tumors and cardiovascular diseases.[52]

In this contribution we describe the synthesis of a novel highly water-soluble multifunctional MnO nanoparticle system carrying protoporphyrin IX as photosensitizer (see Figure 9.1). Monodisperse MnO nanocrystals were synthesized by the oleate route and subsequently functionalized with a dopamine-PEG-protoporphyrin IX (DA-PEG-PP) ligand. As fluorescent molecules are amenable to photodetection, these protoporphyrin IX-functionalized magnetic NPs also offer unique opportunities to simultaneously detect and treat tumor tissues by a combination of analytical (MRI, optical) and therapeutic (PDT) methods.

9.3 Results and Discussion

MnO NPs: Synthesis and Properties. Monodisperse spherical MnO NPs were synthesized by decomposition of a manganese oleate precursor in 1-octadecene at 300 °C. Figure 9.2a shows a representative transmission electron microscopy (TEM) image of as prepared oleate capped MnO NPs with an average diameter of 14 nm. The particles have spherical shape; due to their narrow size distribution they self-assemble into two dimensional superlattices. Phase purity of the product

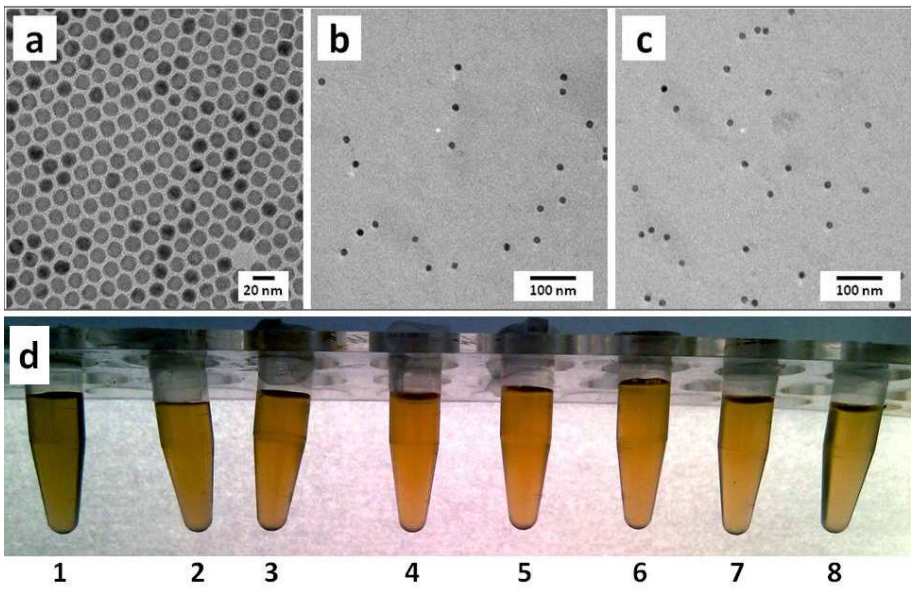

Figure 9.2: (a-c) Transmission electron microscopic (TEM) images of spherical manganese oxide NPs: (a) as prepared, (b) functionalized with DA-PEG-NH_2, (c) functionalized with DA-PEG-PP ((b) and (c) in water). (d) Aqueous solutions of DA-PEG-NH_2 (odd numbers) and DA-PEG-PP (even numbers) functionalized MnO NPs after more than two weeks: 1 & 2 in human blood serum (stored at 4 °C), 3 & 4 in human blood serum (at 37 °C), 5 & 6 in deionized water (at 4 °C), 7 & 8 in deionized water (at 37 °C).

was confirmed by powder X-ray diffraction (XRD, see Figure 9.3a). All reflections can be indexed to the cubic rock-salt structure of MnO (*cF*8, $Fm\bar{3}m$) with (111), (200), (220), (311), (222) and (400) as strongest reflections in the powder pattern. No traces of other manganese oxide phases could be detected.

Size dependent magnetic properties of MnO NPs were reported previously.[53, 54, 56–58] Due to super-exchange interactions between neighboring Mn^{2+} cations bulk MnO is a classical antiferromagnet.[59] MnO NPs, on the other hand, exhibit superparamagnetic behavior, a phenomenon which is generally explained by the presence of uncompensated moments on the particle surface.[53, 54, 60, 61] Magnetic hysteresis loops of the MnO NPs used in this study were recorded at 5 K and 300 K (Figure 9.3b). The NPs were superparamagnetic at room temperature but showed weakly ferromagnetic behavior at 5 K. Temperature dependent zero-field-

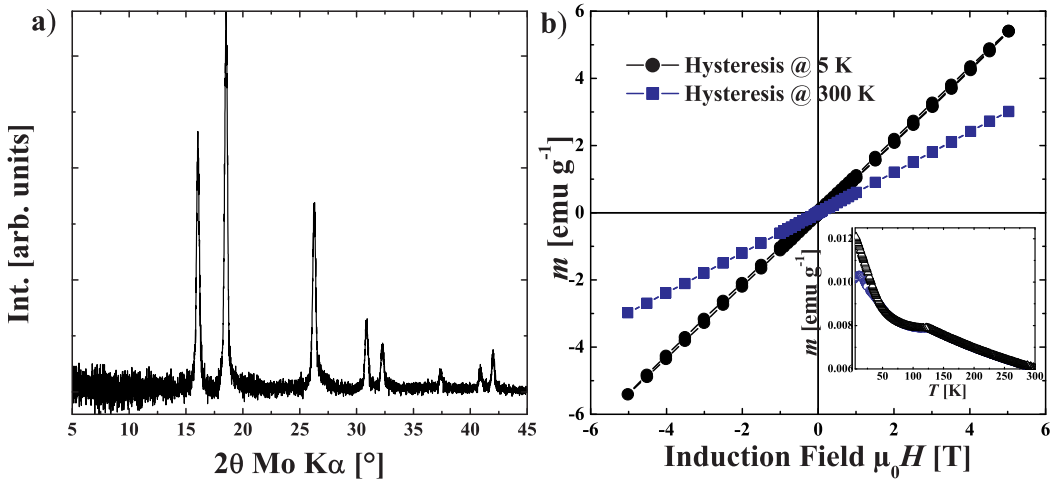

Figure 9.3: (a) Powder XRD-pattern of as-prepared MnO NPs. (b) Magnetic hysteresis loops of MnO NPs recorded at 300 K and 5 K (the inset shows temperature dependent magnetization curves (ZFC-FC) of MnO NPs recorded with an applied induction field of 100 Oe).

cooled/field-cooled (ZFC/FC) measurements at an applied field of 100 Oe revealed a magnetic blocking temperature T_B of 13 K, a value similar to those reported before.[53, 54, 56–58]

Nanoparticle Functionalization. Ligand exchange of the hydrophobic oleate layer by a hydrophilic DA-PEG-PP ligand yielded highly water soluble NPs. The ligand contained a bisamine poly(ethylene glycol) (H_2N-PEG-NH_2) with an average molecular weight of 800 g mol^{-1} (PEG_{800}) as a hydrophilic linker. PEG is used in numerous *in vivo* applications to allow better body distribution and prolonged blood half-life of drugs.[62–65] However, sufficient surface coverage of magnetic NPs can only be accomplished by the introduction of strong anchor groups into the ligand molecules. Catechols, like L-DOPA or dopamine, have recently evolved as preferred components to efficiently bind onto the surface of metal oxides.[66–69] In order to ensure strong attachment to the MnO surface, a catechol derivative 3,4-dihydroxyhydrocinnamic acid (DA) was conjugated to the NBoc-PEG-NH_2 linker by a common DCC coupling technique. Deprotection of the DA-PEG-NBoc conjugate with TFA resulted in DA-PEG-NH_2. The presence of a terminal primary

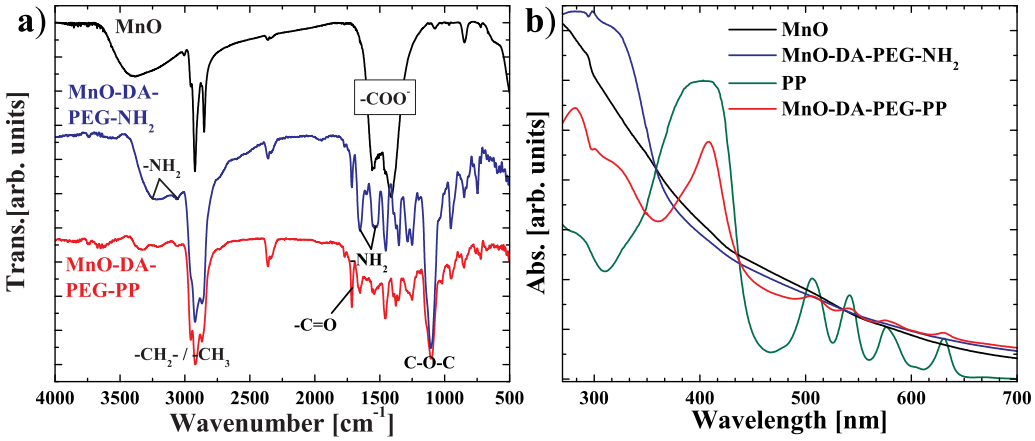

Figure 9.4: (a) FT-IR spectra of oleate capped (black line), DA-PEG-NH_2 functionalized (blue line) and DA-PEG-PP functionalized MnO NPs (red line). (b) UV-Vis spectra of naked MnO NPs, MnO-DA-PEG-NH_2 (blue), protoporphyrin IX (PP) unbound (green) and MnO-DA-PEG-PP NPs (red).

amino group in DA-PEG-NH_2 permitted the covalent attachment of protoporphyrin IX (PP) to form DA-PEG-PP. One crucial criterion for the *in vivo* applicability is the solubility of the NPs in body fluids. After surface functionalization in chloroform, transfer into deionized water was possible and did not result in particle agglomeration as confirmed by TEM (see Figure 9.2b,c). Figure 9.2b displays NPs functionalized with DA-PEG-NH_2, whereas Figure 9.2c shows MnO NPs functionalized with DA-PEG-PP. In both cases well separated NPs were obtained. This is an important attribute for photosensitizers, because particle aggregation tends to exhibit poor PDT efficacy due to the deactivation of the excited state energy.[70] The surface charges were determined to be -4.15 and -6.32 mV for the DA-PEG-NH_2 and DA-PEG-PP functionalized MnO NPs, respectively. They were stable against aggregation in various aqueous solutions for several weeks. Figure 9.2d shows a photograph of aqueous solutions containing DA-PEG-NH_2 and DA-PEG-PP functionalized MnO NPs. The particles were dispersed in water and in human blood serum and stored at 4 °C and 37 °C for more than two weeks. No particle agglomeration or precipitation was observed during this time period.

FT-IR analysis. Ligand exchange of the oleate group by DA-PEG-NH_2 and DA-

PEG-PP was confirmed by FT-IR measurements. The corresponding FT-IR spectra are displayed in Figure 9.4a. As prepared MnO NPs (black line in Figure 9.4a) exhibit characteristic vibrational bands of the oleate group. Most notably, the asymmetric and symmetric stretching bands of the $RCOO^-$ group appear at 1555 and 1410 cm^{-1}, respectively. It has been reported that the spectral difference of 145 cm^{-1} is typical for a bidentate coordination of the carboxylate group to the metal ions on the surface.[53, 71–73] However, these bands are absent in the spectra of DA-PEG-NH_2 and DA-PEG-PP functionalized MnO NPs, respectively, indicating a complete replacement of the oleate layer by the hydrophilic ligands. Furthermore, the appearance of vibrational bands at 1290, 1251 and 1107 cm^{-1} in the MnO-DA-PEG-NH_2 and MnO-DA-PEG-PP spectra, which can be assigned to the stretching modes of C–O–C ether groups in PEG, confirms this assumption. In addition, the partial disappearance of the stretching modes of the free amine groups at 3219, 3064, 1653 and 1528 cm^{-1} in the protoporphyrin IX modified sample confirms the successful functionalization of the MnO-DA-PEG-NH_2 NPs with the photosensitizer molecules.

UV-Vis analysis. The absorption properties of protoporphyrin IX were still intact after binding to MnO as confirmed by UV/Vis spectroscopy for the DA-PEG-PP sample (see Figure 9.4b). For comparison, the UV/Vis spectra of protoporphyrin IX, as-synthesized MnO NPs, DA-PEG-NH_2 and DA-PEG-PP functionalized MnO NPs are presented in Figure 9.4b. The spectrum of as-prepared MnO NPs (black line in Figure 9.4b) shows an increase in absorption for smaller wavelengths. DA-PEG-NH_2 shows an absorption maximum at 280 nm due to the presence of the phenyl ring in the catechol moiety (Figure 9.4b, blue line). For the protoporphyrin IX (green line in Figure 9.4b), the well-known "stairs" formed by the absorption maxima in the 500-630 nm region (Q band of protoporphyrin IX) and an absorption maximum at 400 nm also appear for the DA-PEG-PP functionalized MnO NPs (red line in Figure 9.4b). Hence, UV/Vis spectroscopy confirms successful binding of DA-PEG-PP onto the MnO NPs.

Cell Studies: Cytotoxicity. For *in vivo* applications it is of utter importance, that the toxicity of the NPs themselves is rather low. For this purpose, a cytotoxicity assay was performed based on the capacity of living cells to metabolically reduce water soluble formazan to give an insoluble (typically purple) formazan

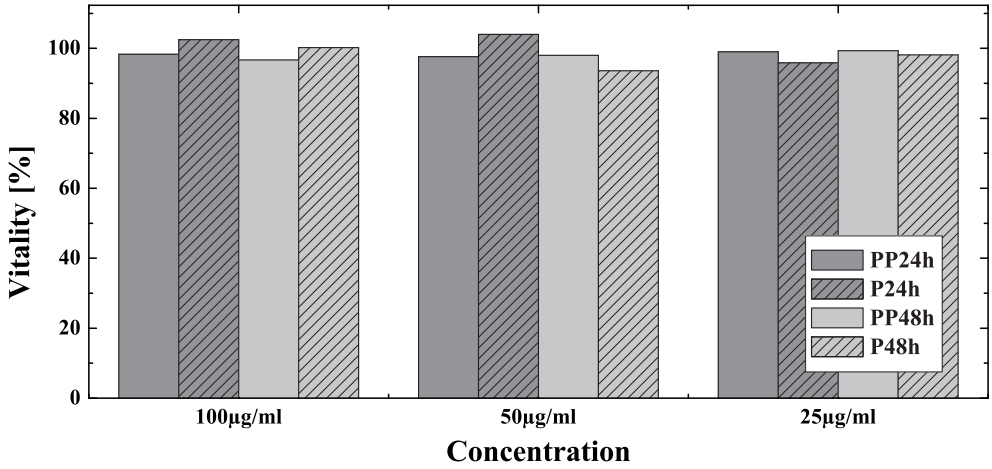

Figure 9.5: Vitality test of Caki 1 cells incubated with different concentration of DA-PEG-NH_2 functionalized MnO NPs (P, dashed columns) for 24 h (dark gray) and 48 h (light gray) as well as DA-PEG-PP modified MnO NPs (PP) incubated for 24 h (dark gray) and 48 h (light gray). To estimate cell viability WST-8 (Sigma-Aldrich) was applied. The resulting absorbance was normalized to the corresponding control sample (medium was added).

product that can be quantified spectrophometrically. For this assay, Caki-1 cells (105 cells/well) were grown on a 96 well plate for 24 h under standard conditions. After this time, they were incubated with different concentrations of sterile filtered DA-PEG-NH_2 and DA-PEG-PP functionalized MnO NPs (resuspended in a corresponding medium) for 24 h and 48 h, respectively. To test for cell viability, the cells were washed, as well as the excess of non internalized NPs and the medium replaced by RPMI 1640 medium without phenol red supplemented with 10% FBS, 1% PEST, 2 mM L-glutamine and mycokill in order to avoid misleading values obtained upon reading. Then, WST-8 was added to the cell culture and incubated for an overall period of 3.5 h. However, when WST-8 is converted metabolically by the dehydrogenases, it forms a water soluble orange compound contrary to the classical MTT assay where insoluble purple formazan crystals are formed (M5655; Sigma-Aldrich Chemie GmbH).[74] The presence of orange coloration and an intense absorption in the corresponding wavelength region (450 nm) is an indication

for cell viability and can be referred to a control sample (see Figure 9.5).
In general the toxicity was low, in respect to a maximum loss in cell viability of 6.4% (48 h incubation, 50 μg/ml MnO particles functionalized with DA-PEG-NH_2). Neither MnO-DA-PEG-PP, nor MnO-DA-PEG-NH_2 showed a significant difference, when the incubation times were compared. For NPs that carried PP a slight decrease in cell viability of 2% was observed when incubated at a concentration of 100 μg/mL. Cells that were incubated with MnO-DA-PEG-NH_2 exhibited a decrease of 2% (100 μg/mL) and 10% (50 μg/mL) as well as an increase of 25% (25 μg/mL). In comparison, MnO-DA-PEG-PP shows slightly lower cell viability (3-6%) after 24 h and 48 h than MnO-DA-PEG-NH_2. However, for both cases the toxicity is low confirming the findings for other MnO NPs.[75, 76]
Cell Studies: Photodynamic Activity. The internalization and photodynamic activity of DA-PEG-PP functionalized MnO NPs were demonstrated with Caki-1 cells. These cells were incubated with NPs for 48 h in the dark and at 37 °C, 95% relative humidity and 5% CO_2 as described in the experimental section. After the incubation period, non-internalized NPs were washed off with PBS-buffer solution (pH 7.4) and the cells were kept in RPMI 1640 medium until the blast experiments were carried out. The internalization of DA-PEG-PP functionalized MnO NPs into the Caki-1 cells was investigated via fluorescence microscopy.
Figure 9.6a shows an overlay of two different filters where DA-PEG-PP functionalized MnO NPs show the typical red fluorescence emission signal and the cell nuclei, stained with DAPI, display a bright blue fluorescence thus indicating that DA-PEG-PP functionalized NPs were internalized by the cells. Additionally, no modification of cell morphology was observed. Simultaneously, cells were tested for a potential cellular damage induced by the DA-PEG-PP functionalized MnO NPs using FITC-labeled Annexin-V. This assay is based on the fact that during the early stages of apoptosis phosphatidylserine (PS), an important component of cytoplasmic membranes, is redistributed to the external surface of plasma membranes, where it is accessible for Annexin-V, a phospholipid binding protein that targets phosphatidylserine.[77, 78] Figure 9.6c shows no green fluorescent signal indicating that the NPs do not induce apoptosis confirming earlier observations on cell-nanoparticle toxicity assays. The fact that the cells were kept in the dark elicits an inactivation of the photodynamic activity of bonded protoporphyrins.

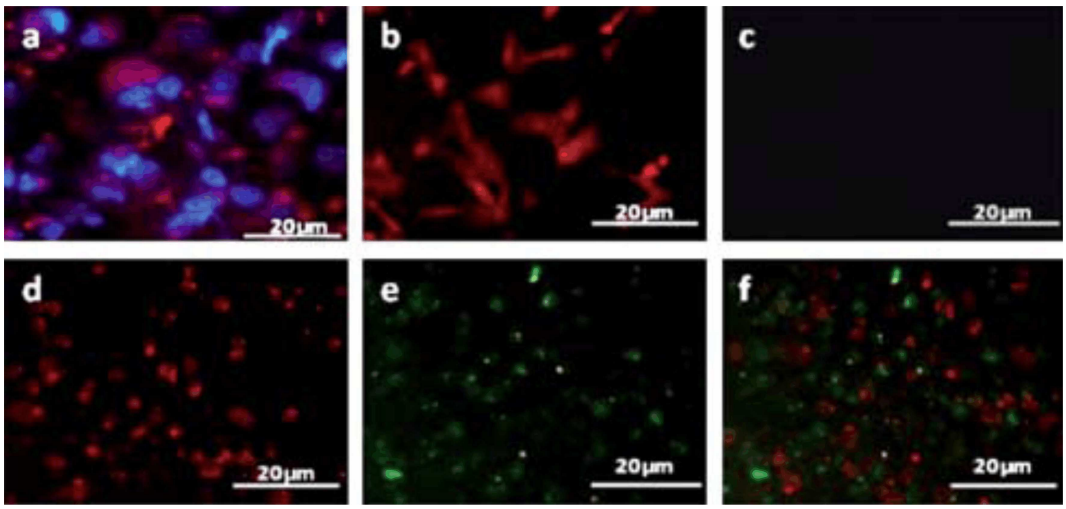

Figure 9.6: Light microscopic images of human kidney cancer cells (Caki-1). (a) MnO-DA-PEG-PP NPs exhibit red fluorescence under a fluorescence microscope that can be co-localized to cell cores stained with DAPI. (b) Caki-1 incubated with MnO-PP, (c) labeling of Caki-1 incubated with MnO-DA-PEG-PP and Annexin-V. These cells were not irradiated and, therefore, show no signs of apoptosis. (d-f) Caki-1 cells incubated with MnO-DA-PEG-PP and irradiated with light of a wavelength of 630 nm. (d) Fluorescence of the NPs within the cells, (e) Annexin-V fluorescence of apoptotic cells, (f) overlay of (d) and (e).

However, when Caki-1 cells were incubated with DA-PEG-PP functionalized MnO nanoparticle for 48 h and subsequently irradiated with a He-Ne laser source at 630 nm wavelength with an adjusted intensity of 40 mWcm^{-2}, corresponding to an incidental dose of 72 Jcm^{-2}, protoporphyrin IX was photoactivated, leading to formation of reactive oxygen species (singlet oxygen ($^1O_2$) randomly dispersed inside cells, targeting proteins, nucleic acids, and membrane components and ultimately inducing cell death. The use of laser light for PDT brings several advantages such as monochromaticity which provides maximum irradiance to minimize the therapeutic exposure time, and finally, the application of fiberglass optics coupling, enabling light delivery to any organ.

In Figure 9.6d, the fluorescent microscope image shows severe modifications in the cell morphology as distinct indicators of induced apoptosis. Thus, the characteristic features of apoptotic cells can easily be visualized, including cytoplasmic

blebbing and condensation, cell shrinkage, and formation of apoptotic bodies. The presence of protoporphyrin functionalized MnO NPs in the cytoplasm (Figure 9.6d, red fluorescent signal) confirms that the cellular demise is directly associated with the photoactivation of protoporphyrin functionalized MnO NPs.
In order to further confirm apoptosis induction, Caki-1 cells incubated with MnO-DA-PEG-PP and exposed to a light source were incubated with FITC-labeled Annexin-V. Since Annexin-V was FITC-labeled, cell membrane bound protein elicits a strong green fluorescence signal (Figure 9.6e and the overlay in Figure 9.6f). In addition, cells treated in the same fashion (containing MnO-DA-PEG-PP NPs and exposed to laser irradiation) were stained with propidium iodine but no signal

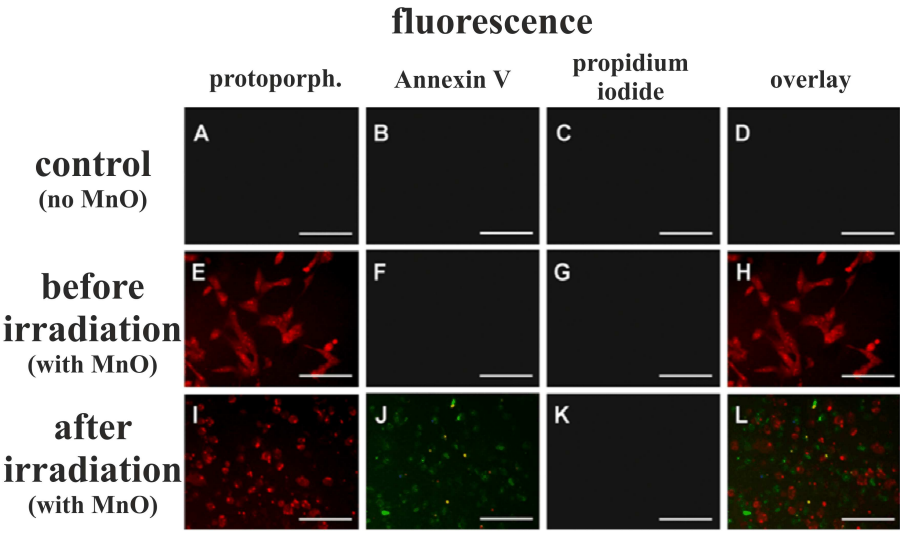

Figure 9.7: Light microscopic images of human kidney cancer cells. (A-D) MnO NPs functionalized with PEG as control. (A, E, I) Protoporphyrin-functionalized MnO NPs (red fluorescence signal) and control sample respectively inside of the Caki-1 cells. (E) Caki-1 cells analyzed by the Nomarski light system before irradiation, (I) subjected to fluorescence light microscopy analysis at an excitation wavelength of 410 nm, respectively. After photoactivation of the protoporphyrin-functionalized NPs (I, L) the Nomarsky light system shows cytoplasmic blebbing and condensation, cell shrinkage, and formation of apoptotic bodies (J). The presence of Annexin-V-FITC labeled (green fluorescence, (J)) confirms cell apoptosis. (Scale bar: 20 μm). Absence of propidium iodine fluorescence (K) confirms cell apoptosis in favor of cell necrosis.

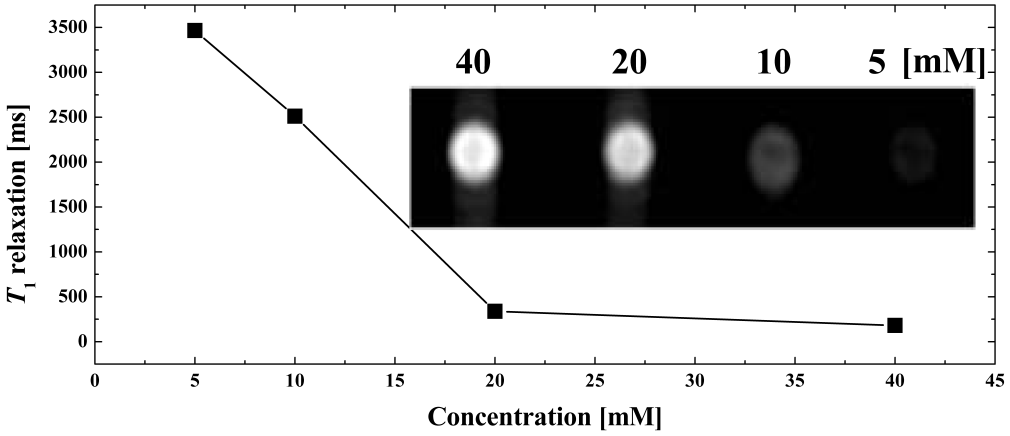

Figure 9.8: MRI data for MnO-DA-PEG-PP NPs. Concentration dependent evolution of longitudinal relaxation time T_1. Inset: T_1 weighted MRI images of aqueous solutions containing DA-PEG-PP functionalized MnO NPs.

was observed (Figure 9.7), thereby supporting the fact, that cells undergo apoptosis rather than necrosis during photodynamic therapy (PDT).

As controls, untreated Caki-1 cells and cells treated with DA-PEG-NH_2 functionalized MnO NPs (48 h) were exposed to same laser source for 30 min showing no signs of modified morphology or induced cell death (see Figure 9.7.

Magnetic Resonance Imaging. To investigate the MR signal enhancement effects, the aqueous solutions of functionalized MnO NPs at different Mn concentrations were measured on a clinical 3.0 T MRI scanner. MnO NPs shorten the longitudinal relaxation (T_1), leading to a brightening in the MR image when compared to samples without contrast agent. This effect was shown for the PEGylated particles as can be seen in Figure 9.8. DA-PEG-PP functionalized MnO NPs where diluted in water to give concentrations of 40 mM to 5 mM. The intensity was directly propotional to the concentration of the NPs. This was not only shown by imaging but was also confirmed by calculating the relaxation time (see plot in Figure 9.8). The higher the Mn concentration, the shorter was T_1. The step between 20 mM and 40 mM might be due to saturation effects.

9.4 Conclusion

In summary, hydrophobic superparamagnetic MnO NPs were functionalized using hydrophilic DA-PEG-NH_2 and DA-PEG-PP ligands respectively. Efficient surface binding of the ligand molecules was confirmed by FT-IR and UV-Vis analysis. We showed that the optical properties of protoporphyrin IX are not significantly changed by binding to the MnO surface. Internalization of well dispersed protoporphyrin functionalized MnO NPs by human renal cell carcinoma (Caki-1) cells was demonstrated by fluorescence microscopy. We further demonstrated that laser light radiation (PDT) irradiation (635 nm, incident dose of 72 Jcm^{-2}) of Caki-1 cells incubated with protoporphyrin IX-functionalized MnO NPs leads to cell death by apoptosis due to formation of reactive singlet oxygen ($^1O_2$) initiated by photoactivation of protoporphyrin IX. Furthermore, the presence of protoporphyrin IX on the MnO NPs permits detection of the particles by fluorescence microscopy due to its intrinsic fluorescence. Finally, we demonstrated that by virtue of their magnetic properties functionalized MnO NPs exhibit a strong T_1 contrast enhancement effect for MRI. Hence, hydrophilic protoporphyrin IX functionalized MnO NPs show potential for application not only as imaging agents for MRI and fluorescence microscopy but also as target systems for photodynamic therapy.

9.5 Experimental Section

Materials. Manganese (II) chloride tetrahydrate (99%), oleic acid (techn. 90%), sodium hydroxide (p.A.), 1-octadecene (techn. 90%), *O,O'*-bis(2-aminopropyl) polypropylene glycol-block-polyethylene glycol-block-polypropylene glycol 800 (H_2N-PEG-NH_2, $M_w \approx 800$ g mol^{-1}), di-*tert*-butyl-dicarbonate ($(Boc)_2O$, 97%), 3,4 dihydroxyhydrocinamic acid (DA, 98%), 1-hydroxyhydro-benzotriazol-hydrate (HOBt, 98%), N,N‘-diiso-propylethyl-amine (DIPEA, 99%), dicyclohexylcarbodiimide (DCC, 99%), and protoporphyrin IX (PP, 95%) were purchased from Sigma-Aldrich (Germany). N-hydroxy-succinimide (NHS, 97%) was from Fluka. Ethanol, hexane, chloroform, and dichloromethane were of analytical grade and purchased from Fisher. DMF (99.5%+, extra dry) was purchased from ACROS. All chemicals were used as received without further purification. In addition 4,6-diamino-2-

phenylindole (DAPI, Invitrogen GmbH - Molecular Probes, Karlsruhe, Germany), and Annexin-V (Annexin-V-FLUOS kit, Roche Applied Science) were used for staining of cell compartments. McCoys 5A cell culture medium with phenol red, RPMI 1640 cell culture medium without phenol red, non-essential amino acids (NEA), penicillin-streptomycin (PEST), L-gluthamine, fetal bovine serum (FBS), phosphate buffer saline (PBS, 1x) and cell counting kit 8 (WST-8) were purchased from Sigma-Aldrich (Germany). Mycokill was provided by PAA, Germany.

Synthesis of MnO NPs. The synthesis of the manganese (II) oleate precursor and the synthesis of MnO NPs have been described elsewhere.[53] Briefly, manganese oxide NPs were synthesized by thermal decomposition of manganese (II) oleate in 1-octadecene at elevated temperatures. Size and morphology of the naked and surface functionalized manganese oxide NPs were investigated using transmission electron microscopy (TEM, Philips EM 420 instrument with an acceleration voltage of 120 kV). X-ray powder diffraction measurements were performed on a Bruker D8 Advance powder diffractometer, operating with Mo-Kα radiation equipped with a Sol-X energy-dispersive detector. The magnetic properties of powder samples were measured with a superconductive quantum interference device (SQUID, Quantum Design MPMS XL).

Synthesis of Dopa-PEG-Protoporphyrin (DA-PEG-PP).

NBoc-PEG-NH_2. In a typical reaction, 10 mmol of *O,O'*-bis(2-aminopropyl) polypropylene glycol-block-polyethylene glycol-block-polypropylene glycol 800 (H_2N-PEG-NH_2) was dissolved in 100 mL of 1,4 dioxan under standard Schlenk conditions. 10 mmol of triethylamine was added and the solution was allowed to stir vigorously for 30 min at room temperature. 10 mmol di-tert-butyl-dicarbonat ($(Boc)_2O$) were dissolved in 50 mL of 1,4-dioxan and added dropwise to the H_2N-PEG-NH_2 solution (at a constant speed of one drop per second). The reaction was allowed to proceed overnight at room temperature under an inert atmosphere. After removal of the solvent the crude product was transferred into dichloromethane. The organic phase was washed three times with aqueous saturated NaCl solution and subsequently dried over $MgSO_4$. Further purification was achieved by flash chromatography using a silica column and a mixture of dichloromethane and ethanol (ratio 2:1) as eluent. Evaporation of the solvent produced a viscous colorless oil.

DA-PEG-NH_2. Conjugation of NBoc-PEG-NH_2 to 3,4-dihydroxyhydrocinnamic

acid (DA) was performed by a common DCC coupling reaction under inert conditions. First, 3,4-dihydroxyhydrocinnamic acid (5 mmol) and HOBt (5.1 mmol) were dissolved in 10 mL of dry DMF and stirred at room temperature. After 10 minutes DCC (5.1 mmol in 10 mL of dry DMF) were added, and the solution was stirred for another 10 minutes before NHS (5.1 mmol in 10 mL of dry DMF) was added dropwise over a period of 30 minutes. The reaction was continued for 2 hours. The resulting DA-NHS ester was subsequently added to a stirred solution of NBoc-PEG-NH_2 (5 mmol) in 15 mL of dry DMF over a period of 45 minutes. The solution was stirred overnight at room temperature. After removal of the urea side product by filtration, the crude product was transferred to chloroform. The organic solution was extracted several times with a saturated NaCl solution and washed with deionized water. The solvent was evaporated and the oily residue redissolved in dichloromethane. Cleavage of the BOC protection group was accomplished by addition of trifluoroacetic acid and stirring at room temperature for two hours. After removal of DCM the product was dissolved in 40 mL of chloroform and washed with a saturated aqueous $NaHCO_3$ solution and deionized water. The organic phase was dried over $MgSO_4$ and the solvent removed *in vacuo* to produce a light brown oil.

DA-PEG-PP. Protoporphyrin IX was bound to DA-PEG-NH_2 as NHS-ester. Protoporphyrin IX (0.1 mmol) was dissolved in 10 mL of dry DMF under an argon atmosphere in the dark. HOBt (0.24 mmol) was added and the solution was stirred for 5 minutes before addition of DCC (0.3 mmol in 1 mL dry DMF). After 30 minutes NHS (0.3 mmol in 1 mL dry DMF) was added and the solution was stirred at room temperature overnight in the dark. The solid urea side product was removed by centrifugation, and the product was kept as DMF stock solution in the dark at -40 °C.

DA-PEG-NH_2 (0.1 mmol) was mixed with PP-NHS (0.05 mmol from the stock solution) in 5 mL of chloroform, and the reaction was allowed to proceed for 24 hours in the dark under argon. The final product was precipitated by addition of hexane and collected by centrifugation (9000 rpm for 10 minutes). The supernatant was discarded and the residue redissolved in 5 mL chloroform. The washing cycle was repeated twice and DA-PEG-PP was finally stored as chloroform solution in the dark at -40 °C.

Functionalization of the MnO NPs. The surface of the hydrophobic oleate capped MnO NPs was modified by a ligand exchange reaction in chloroform. In a typical reaction 10 mg MnO NPs were dissolved in 40 mL of chloroform and added drop wise to a solution of 30 mg DA-PEG-NH_2 or DA-PEG-PP in 40 mL of chloroform under argon. The solution was stirred overnight at room temperature and subsequently concentrated to 10 mL by rotary evaporation. Phase transfer of the functionalized hydrophilic particles into deionized water was achieved by adding a mixture of 30 mL of hexane and 40 mL milli Q water under vigorous stirring. The aqueous phase containing the MnO NPs was separated and the final Mn concentration was estimated by atomic absorption spectroscopy (AAS, Perkin-Elmer 5100 ZL).

The functionalized MnO NPs were characterized by TEM and Fourier–transformed-Infrared (FT–IR) spectroscopy (Mattson Instruments 2030 Galaxy− FT−IR spectrometer). Surface charges (Zeta potential) were determined with a Malvern Zetasizer Nano ZS. Unless mentioned differently, all nanoparticle concentrations are referred to the Mn concentration measured with AAS.

Cell culture and cytotoxicity-assay. The human renal cell carcinoma line (Caki-1) was kindly provided by the group of Prof. Dr. Langguth, Institute for Pharmacy and Biochemistry, Johannes Gutenberg-University, Mainz. Cells were grown in McCoys 5A medium (Sigma-Aldrich) supplemented with 10% fetal bovine serum (FBS, Sigma-Aldrich), 1% Penicillin-Streptomycin (PEST, 10000 U/mL Penicillin and 10 mg/mL Streptomycin, Sigma-Aldrich) 2mM L-glutamine (Sigma-Aldrich), 1x Mycokill (PAA) and 1x MEM non essential amino acids (Sigma-Aldrich). Cell cultures were routinely grown in 75 cm^2 sterile cell culture flask and were contained at 37 °C, 95% relative humidity and 5% CO_2 until reaching the confluence of 2,1 x 10^6 cells/mL. To assay the nanoparticle cytotoxicity, Caki-1 cells were grown in 96 well plates in McCoys 5A medium with a cell density of 105 cells/well under standard conditions. In 6 wells only medium was added to allow background subtraction. After 24 h of cell growth, 10 μl of sterile filtered [0.22 μm filter (Sigma-Aldrich)] MnO-DA-PEG-NH_2 and MnO-DA-PEG-PP-NPs (concentrations ranging from 25 - 100 μg/mL) resuspended in McCoys 5A medium were co-incubated for 24 and 48 h. After this incubation time, excess NPs were washed off with sterile PBS buffer (pH 7.4) and the medium was replaced by RPMI 1640 medium without

phenol red (Sigma-Aldrich, Germany), supplemented with 10% FBS, 1% PEST, 2 mM L-glutamine and mycokill and finally MTT labeling reagent (WST 8, Sigma-Aldrich) was added according to the supplier. The cells were incubated at 37 °C, 5% CO_2 and 95% relative humidity for 1.5 h, followed by incubation at room temperature on a shaker in the dark for a further 2 h. The absorption of soluble orange formazan which was formed due to cellular activity was measured at 450 nm using an ELISA reader Titertek Plus MS 212 (ICN, Eschwege, Germany). For background subtraction, blank wells without cells but treated in parallel were used. The measurements were performed in triplicate and data analyzed by using Origin. All results were normalized to wells that did contain cells, but where media was added instead of NPs.

Incubation of MnO-DA-PEG-PP NPs with CaKi-1 cells and laser exposure. Sterile DA-PEG-PP functionalized MnO NPs (100 μg mL^{-1} per well) were incubated with confluent Caki-1 cells for 48 h at 37 °C, 5% CO_2 and 95% relative humidity, in the dark. In order to initiate photochemical reactions, the cells were irradiated at 630 nm, and the intensity adjusted to 40 mW cm^{-2} for a period of 30 min, corresponding to an incidental dose of 72 J cm^{-2}, using an excitation light source He-Ne laser (635 nm). This wavelength range was chosen to match the long wavelength part of the protoporphyrin IX absorption spectrum. Afterwards, the cell culture was washed twice with sterile PBS buffer-solution (pH 7.4) and RPMI medium supplemented with 10% FBS, mycokill, L-glutamine and PEST. As controls, DA-PEG-NH_2 functionalized MnO NPs (100 μg mL^{-1}) (e.g. without bound protoporphyrin) were incubated in parallel under the same experimental conditions and the untreated Caki-1 cells were exposed to the same light source for 30 min. The cells nuclei were stained with DAPI and in order to assess cellular integrity FITC-labeled Annexin-V (Annexin-V-FLUOS kit, Cat. No. 11 858 777 001 Roche Diagnostics GmbH, Penzberg, Germany). The fluorescence analysis was performed with a light microscope, together with an AH3-RFC reflected light fluorescence attachment. The images were co-localized using the software AnalySIS (Olympus, USA). To exclude necrosis of the cells, staining with propidium iodine was performed in parallel. The corresponding image is provided in the supporting information (Figure 9.7).

Magnetic Resonance Imaging. MR signal enhancement effects were measured for

the aqueous solutions of functionalized MnO NPs at different Mn concentrations (measured with AAS) on a clinical 3.0 T MRI scanner (Magnetom Trio, Siemens Medical Solutions, Erlangen, Germany). Signal reception and radio frequency (RF) excitation was performed using 8-channel knee coil. For T_1-measurement, a saturation prepared (SR) snapshot fast low angle shot (SR-TurboFLASH) pulse sequence with repetition time (TR) / echo time / flip angle of 3.0 ms / 1.5 ms / 20 ° was used with varying saturation times starting from 20 ms up to 8000 ms. For measuring the T_2 relaxation time, a multi-echo spin-echo pulse sequence (CPMG, Carr-Purcell-Meiboom-Gill) with a total of 32 echos and TR = 5000 ms was used, the echo time was varied from 7 ms to 224 ms. In a second T_2 measurement T_E was varied from 15 ms up to 480 ms.

9.6 References

[1] Gu, H.; Xu, K.; Xu, C.; Xu, B. *Chemical Communications* **2006**, 941–949.

[2] Shukoor, M. I.; Natalio, F.; Tahir, M. N.; Ksenofontov, V.; Therese, H. A.; Theato, P.; Schroder, H. C.; Muller, W. E. G.; Tremel, W. *Chemical Communications* **2007**, 4677–4679.

[3] Schröder, H. C.; Natalio, F.; Wiens, M.; Tahir, M. N.; Shukoor, M. I.; Tremel, W.; Belikov, S. I.; Krasko, A.; Müller, W. E. G. *Molecular Immunology* **2008**, *45*, 945–953.

[4] Liong, M.; Lu, J.; Kovochich, M.; Xia, T.; Ruehm, S. G.; Nel, A. E.; Tamanoi, F.; Zink, J. I. *ACS Nano* **2008**, *2*, 889–896.

[5] Park, H.; Yang, J.; Seo, S.; Kim, K.; Suh, J.; Kim, D.; Haam, S.; Yoo, K. H. *Small* **2008**, *4*, 192–196.

[6] Kim, J.; Park, S.; Lee, J. E.; Jin, S. M.; Lee, J. H.; Lee, I. S.; Yang, I.; Kim, J. S.; Kim, S. K.; Cho, M. H.; Hyeon, T. *Angewandte Chemie International Edition* **2006**, *45*, 7754–7758.

[7] Hu, F. Q.; Wei, L.; Zhou, Z.; Ran, Y. L.; Li, Z.; Gao, M. Y. *Advanced Materials* **2006**, *18*, 2553–2556.

[8] Xu, C.; Xie, J.; Ho, D.; Wang, C.; Kohler, N.; Walsh, E.; Morgan, J.; Chin, Y.; Sun, S. *Angewandte Chemie International Edition* **2008**, *47*, 173–176.

[9] Jun, Y.-w.; Lee, J.-H.; Cheon, J. *Angewandte Chemie International Edition* **2008**, *47*, 5122–5135.

[10] Merbach, A. E.; Tóth, E. *The chemistry of contrast agents in medical magnetic resonance imaging*; Wiley: Chichester, 2001.

[11] Sun, C.; Lee, J. S. H.; Zhang, M. *Advanced Drug Delivery Reviews* **2008**, *60*, 1252–1265.

[12] Na, H. B.; Lee, J. H.; An, K.; Park, Y. I.; Park, M.; Lee, S.; Nam, D. H.; Kim, S. T.; Kim, S. H.; Kim, S. W.; Lim, K. H.; Kim, K. S.; Kim, S. O.; Hyeon, T. *Angewandte Chemie International Edition* **2007**, *46*, 5397–5401.

[13] Gilad, A. A.; Walczak, P.; McMahon, M. T.; Bin Na, H.; Lee, J. H.; An, K.; Hyeon, T.; van Zijl, P. C. M.; Bulte, J. W. M. *Magnetic Resonance in Medicine* **2008**, *60*, 1–7.

[14] Na, H. B.; Hyeon, T. *Journal of Materials Chemistry* **2009**, *19*, 6267–6273.

[15] Na, H. B.; Song, I. C.; Hyeon, T. *Advanced Materials* **2009**, *21*, 2133–2148.

[16] Berry, C. C.; Curtis, A. S. G. *Journal of Physics D: Applied Physics* **2003**, *36*, R198.

[17] Xie, J.; Xu, C.; Kohler, N.; Hou, Y.; Sun, S. *Advanced Materials* **2007**, *19*, 3163–3166.

[18] Tahir, M. N.; Eberhardt, M.; Theato, P.; Faiss, S.; Janshoff, A.; Gorelik, T.; Kolb, U.; Tremel, W. *Angewandte Chemie* **2006**, *118*, 922–926.

[19] Berry, C. C. *Journal of Physics D: Applied Physics* **2009**, *42*, 224003.

[20] Frey, N. A.; Peng, S.; Cheng, K.; Sun, S. *Chemical Society Reviews* **2009**, *38*, 2532–2542.

[21] Gref, R.; Minamitake, Y.; Peracchia, M. T.; Trubetskoy, V.; Torchilin, V.; Langer, R. *Science* **1994**, *263*, 1600–1603.

[22] Gref, R.; Domb, A.; Quellec, P.; Blunk, T.; Müller, R. H.; Verbavatz, J. M.; Langer, R. *Advanced Drug Delivery Reviews* **1995**, *16*, 215–233.

[23] Moghimi, S. M.; Hunter, A. C.; Murray, J. C. *Pharmacological Reviews* **2001**, *53*, 283–318.

[24] Owens, D. E.; Peppas, N. A. *International Journal of Pharmaceutics* **2006**, *307*, 93–102.

[25] Torchilin, V. P. *Advanced Drug Delivery Reviews* **2006**, *58*, 1532–1555.

[26] Prencipe, G.; Tabakman, S. M.; Welsher, K.; Liu, Z.; Goodwin, A. P.; Zhang, L.; Henry, J.; Dai, H. *Journal of the American Chemical Society* **2009**, *131*, 4783–4787.

[27] Knop, K.; Hoogenboom, R.; Fischer, D.; Schubert, U. *Angewandte Chemie International Edition* **2010**, *49*, 6288–6308.

[28] Waite, J. H.; Tanzer, M. L. *Science* **1981**, *212*, 1038–1040.

[29] Bryan, G. W.; Gibbs, P. E. *Journal of the Marine Biological Association of the UK* **1980**, *60*, 641–654.

[30] Vaccaro, E.; Waite, J. H. *Biomacromolecules* **2001**, *2*, 906–911.

[31] Holten-Andersen, N.; Fantner, G. E.; Hohlbauch, S.; Waite, J. H.; Zok, F. W. *Nature Materials* **2007**, *6*, 669–672.

[32] Holten-Andersen, N.; Mates, T. E.; Toprak, M. S.; Stucky, G. D.; Zok, F. W.; Waite, J. H. *Langmuir* **2009**, *25*, 3323–3326.

[33] Harrington, M. J.; Masic, A.; Holten-Andersen, N.; Waite, J. H.; Fratzl, P. *Science* **2010**, *328*, 216–220.

[34] Wilker, J. J. *Angewandte Chemie* **2010**.

[35] Lee, H.; Dellatore, S. M.; Miller, W. M.; Messersmith, P. B. *Science* **2007**, *318*, 426–430.

[36] Latham, A. H.; Williams, M. E. *Accounts of Chemical Research* **2008**, *41*, 411–420.

[37] Xu, C.; Xu, K.; Gu, H.; Zheng, R.; Liu, H.; Zhang, X.; Guo, Z.; Xu, B. *Journal of the American Chemical Society* **2004**, *126*, 9938–9939.

[38] Hong, R.; Fischer, N. O.; Emrick, T.; Rotello, V. M. *Chemistry of Materials* **2005**, *17*, 4617–4621.

[39] Amstad, E.; Gillich, T.; Bilecka, I.; Textor, M.; Reimhult, E. *Nano Letters* **2009**, *9*, 4042–4048.

[40] Amstad, E.; Zurcher, S.; Mashaghi, A.; Wong, J. Y.; Textor, M.; Reimhult, E. *Small* **2009**, *5*, 1334–1342.

[41] Konan, Y. N.; Gurny, R.; Allémann, E. *Journal of Photochemistry and Photobiology B: Biology* **2002**, *66*, 89–106.

[42] Dougherty, T. J.; Kaufman, J. E.; Goldfarb, A.; Weishaupt, K. R.; Boyle, D.; Mittleman, A. *Cancer Research* **1978**, *38*, 2628–2635.

[43] Allémann, E.; Rousseau, J.; Brasseur, N.; Kudrevich, S. V.; Lewis, K.; van Lier, J. E. *International Journal of Cancer* **1996**, *66*, 821–824.

[44] Wieder, M. E.; Hone, D. C.; Cook, M. J.; Handsley, M. M.; Gavrilovic, J.; Russell, D. A. *Photochemical and Photobiological Sciences* **2006**, *5*, 727–734.

[45] Roy, I.; Ohulchanskyy, T. Y.; Pudavar, H. E.; Bergey, E. J.; Oseroff, A. R.; Morgan, J.; Dougherty, T. J.; Prasad, P. N. *Journal of the American Chemical Society* **2003**, *125*, 7860–7865.

[46] Dougherty, T. J.; Henderson, B. W.; Gomer, C. J.; Jori, G.; Kessel, D.; Korbelik, M.; Moan, J.; Peng, Q. *Journal of the National Cancer Institute* **1998**, *90*, 889–905.

[47] Alexiou, C.; Arnold, W.; Klein, R. J.; Parak, F. G.; Hulin, P.; Bergemann, C.; Erhardt, W.; Wagenpfeil, S.; Lübbe, A. S. *Cancer Research* **2000**, *60*, 6641–6648.

[48] Jordan, A.; Scholz, R.; Wust, P.; Fähling, H.; Felix, R. *Journal of Magnetism and Magnetic Materials* **1999**, *201*, 413–419.

[49] Neuberger, T.; Schöpf, B.; Hofmann, H.; Hofmann, M.; von Rechenberg, B. *Journal of Magnetism and Magnetic Materials* **2005**, *293*, 483–496.

[50] Gu, H.; Ho, P.-L.; Tsang, K. W. T.; Wang, L.; Xu, B. *Journal of the American Chemical Society* **2003**, *125*, 15702–15703.

[51] Sun, E. Y.; Josephson, L.; Kelly, K. A.; Weissleder, R. *Bioconjugate Chemistry* **2006**, *17*, 109–113.

[52] Jaffer, F. A.; Weissleder, R. *Circulation Research* **2004**, *94*, 433–445.

[53] Schladt, T. D.; Graf, T.; Tremel, W. *Chemistry of Materials* **2009**, *21*, 3183–3190.

[54] Schladt, T. D. et al. *Angewandte Chemie International Edition* **2010**, *49*, 3976–3980.

[55] Schladt, T. et al. *Angewandte Chemie* **2010**, *122*, 4068–4072.

[56] Seo, W. S.; Jo, H. H.; Lee, K.; Kim, B.; Oh, S. J.; Park, J. T. *Angewandte Chemie International Edition* **2004**, *43*, 1115–1118.

[57] Park, J.; Kang, E.; Bae, C. J.; Park, J.-G.; Noh, H.-J.; Kim, J. Y.; Park, J. H.; Park, H. M.; Hyeon, T. *Journal of Physical Chemistry B* **2004**, *108*, 13594–13598.

[58] Ghosh, M.; Biswas, K.; Sundaresan, A.; Rao, C. N. *Journal of Materials Chemistry* **2006**, *16*, 106–111.

[59] Rao, C. N. R.; Raveau, B. *Transition metal oxides*; VCH: New York, NY, 1995.

[60] Lee, G. H.; Huh, S. H.; Jeong, J. W.; Choi, B. J.; Kim, S. H.; Ri, H.-C. *Journal of the American Chemical Society* **2002**, *124*, 12094–12095.

[61] Han, M. J.; Ozaki, T.; Yu, J. *Journal of Chemical Physics* **2005**, *123*, 034306–5.

[62] Zalipsky, S. *Advanced Drug Delivery Reviews* **1995**, *16*, 157–182.

[63] Veronese, F. M. *Biomaterials* **2001**, *22*, 405–417.

[64] Caliceti, P.; Veronese, F. M. *Advanced Drug Delivery Reviews* **2003**, *55*, 1261–1277.

[65] Veronese, F. M.; Pasut, G. *Drug Discovery Today* **2005**, *10*, 1451–1458.

[66] Jander, G.; Blasius, E.; Strähle, J.; Schweda, E. *Einführung in das anorganisch-chemische Praktikum: (einschließlich der quantitativen Analyse) ; mit 61 Tabellen /*, 14th ed.; Hirzel: Stuttgart, 1995.

[67] McBride, M. B.; Wesselink, L. G. *Environmental Science & Technology* **1988**, *22*, 703–708.

[68] Dalsin, J. L.; Hu, B.-H.; Lee, B. P.; Messersmith, P. B. *Journal of the American Chemical Society* **2003**, *125*, 4253–4258.

[69] Tahir, M. N.; Eberhardt, M.; Theato, P.; Faiss, S.; Janshoff, A.; Gorelik, T.; Kolb, U.; Tremel, W. *Angewandte Chemie International Edition* **2006**, *45*, 908–912.

[70] Sun, Y.; Chen, Z. I.; Yang, X. X.; Huang, P.; Zhou, X. P.; Du, X. X. *Nanotechnology* **2009**, *20*, 135102/1–135102/8.

[71] Alcock, N. W.; Tracy, V. M.; Waddington, T. C. *Dalton Transactions* **1976**, 2243–2246.

[72] Barman, S.; Vasudevan, S. *Journal of Physical Chemistry B* **2006**, *110*, 651–654.

[73] Barman, S.; Vasudevan, S. *Journal of Physical Chemistry B* **2007**, *111*, 5212–5217.

[74] Ishiyama, M.; Tominaga, H.; Shiga, M.; Sasamoto, K.; Ohkura, Y.; Ueno, K. *Biological and Pharmaceutical Bulletin* **1996**, *19*, 1518–1520.

[75] Shukoor, M. I. et al. *Advanced Functional Materials* **2009**, *19*, 3717–3725.

[76] Choi, J.; Lee, S.; Na, H.; An, K.; Hyeon, T.; Seo, T. *Bioprocess and Biosystems Engineering* **2010**, *33*, 21–30.

[77] van den Eijnde, S. M.; Boshart, L.; Baehrecke, E. H.; de Zeeuw, C. I.; Reutelingsperger, C. P.; Vermeij-Keers, C. *Apoptosis* **1998**, *3*, 9–16.

[78] Konduru, N. V. et al. *PLoS ONE* **2009**, *4*, e4398/1–e4398/15.

CHAPTER 10

Multifunctional Superparamagnetic $MnO@SiO_2$ Core/Shell Nanoparticles and their Application for Optical and Magnetic Resonance Imaging

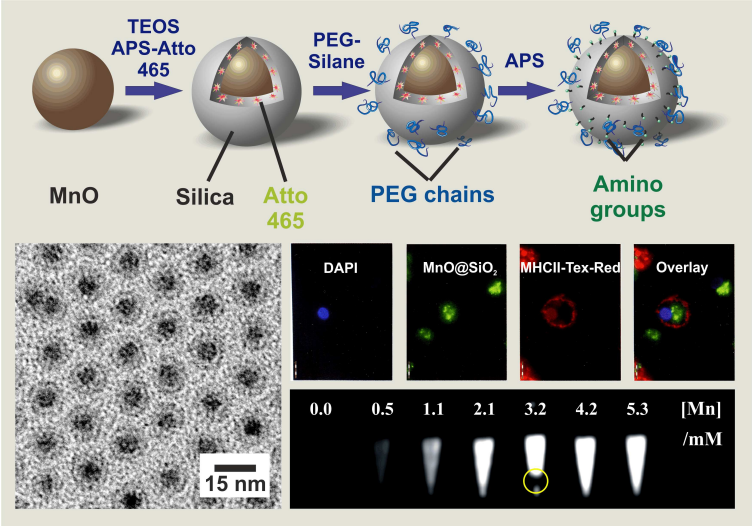

10.1 Abstract

Highly biocompatible multifunctional nanocomposites consisting of monodisperse manganese oxide nanoparticles with luminescent silica shells were synthesized by a novel approach, involving a combination of w/o-microemulsion techniques and common sol-gel procedures. The NPs were characterized by TEM analysis, powder XRD, SQUID magnetometry, FT-IR-, UV/Vis- and fluorescence spectroscopy and dynamic light scattering. Due to the presence of hydrophilic poly(ethylene glycol) (PEG) chains on the SiO_2 surface, the nanocomposites are highly soluble and stable in various aqueous solutions, including physiological saline, buffer solutions and human blood serum. As the quantification of the particle bound target molecules is crucial for their drug loading capacity the number of surface amino groups available for ligand binding on each particle were determined using a colorometric assay with fluorescein isothiocyanate (FITC). MnO@SiO_2 NPs were less prone to Mn-leaching compared to NPs coated with a conventional bi-functional dopamine-PEG ligand. Interestingly, the presence of a silica shell did not change the magnetic properties significantly, and therefore, the MnO@SiO_2 nanocomposite particles showed a T_1 contrast with relaxivity values comparable to those of PEGylated MnO NPs.

10.2 Introduction

The design of new multifunctional nanomaterials that combine different physical and chemical properties has become a distinct driving force in modern-day materials science. Especially the integration of magnetic nanomaterials with molecular biology and biomedicine has evolved into a new research area, which is now widely called nano-biotechnology.[1] So far, magnetic NPs have been used in various biomedical applications ranging from protein separation, targeted drug delivery, magnetic hyperthermia, and magnetic resonance imaging (MRI).[2–8] MRI is one of the most powerful non-invasive diagnostic techniques, since it provides unsurpassed 3D soft tissue detail, without using ionizing radiation, deep tissue penetration and high resolution, and therefore, has been applied for the diagnosis of various diseases. The method is based on the relaxation of protons in an external static magnetic field after transmission of an excitation pulse. This process occurs according

to two different mechanisms: either by spin-lattice relaxation (with a relaxation time T_1), or by spin-spin relaxation (with relaxation times T_2 and T_2^*). Like in any other imaging technique, contrast agents are used in MRI to shorten the respective relaxation times, and thus enhance the visibility of pathological aberrations.[9]
The utilization of magnetic NPs for these purposes is quite reasonable, given the fact, that their size, size distribution, and morphology are easily controllable, which enables a precise tuning of their magnetic properties. Superparamagnetic iron oxide NPs (SPIONs) (i.e. magnetite (Fe_3O_4) and maghemite (γ-Fe_2O_3)) are, by far, the most intensively studied materials in this field, owing to their high saturation magnetization and low coercivity. They accelerate the spin-spin relaxation, and therefore, are used as negative (T_2) contrast agents. In fact, some iron oxide nanoparticle probes have been approved for clinical use by the Food and Drug Administration (FDA) of the United States.[9–11] However, T_2 (or MR negative) contrast agents lead to a decrease in signal intensity, and thus to a darkening in the MR image. Positive MR contrast agents, on the other hand, are known to decrease the spin-lattice relaxation time T_1, leading to a brightening in the corresponding MR image. These agents usually comprise paramagnetic gadolinium complexes, such as Gd-DTPA or Gd-DOTA. Unfortunately, these complexes exhibit low relaxivity (r_1) values. Higher, r_1 values have recently been reported for Gd-based NPs, like Gd_2O_3,[12–14] $GdPO_4$, [15, 16] or GdF_3, [17] however, they lack of a precise control over size and morphology, which hampers their possible application.[18] Recently, superparamagnetic MnO NPs have also proven to be potential candidates as T_1 contrast agents.[19–23] In the case of MnO, the magnetic behavior results from the presence of uncompensated magnetic moments on the surface of the NPs.[24]
Most synthetic approaches for size and shape controlled magnetic NPs are based on the decomposition of metal-organic compounds at high temperatures and in the presence of hydrophobic surfactant molecules.[25, 26, 28, 29] In those cases, a narrow size distribution is achieved by precise adjustment of the individual synthetic parameters. However, efficient surface modification strategies are needed to enhance both, hydrophilicity and biocompatibility of the NPs and to prevent both, agglomeration in physiological environment and non-specific uptake by the reticuloendothelial system (RES).[30, 31] Most of these strategies employ poly-(ethylene glycol) (PEG) as hydrophilic linker, since it not only guarantees pro-

longed blood half-life and circulation, but also reduced opsonization by serum proteins.[32–37] Besides ligand exchange, with either bi-functional[38–41] or multifunctional polymers[3, 22, 43, 44] and micellar incorporation with functional amphiphilic polymers,[45–47] silica encapsulation is one of the most often used methods for surface functionalization of inorganic nanomaterials.[48]

Apart from excellent biocompatibility, the presence of a silica shell around metal oxide NPs offers many advantages, such as chemical and physical protection from the surrounding environment, stability in aqueous media and a vast and robust platform for further modification. In fact, the well developed surface chemistry for silica micro- and NPs provides the opportunity to specifically tune the particle properties for later applications.[11, 49–52] Additionally, the possibility to incorporate fluorescent dyes inside the SiO_2 shells has led to a wide extension of applicability, owing to reduced photobleaching, blocked quenching effects and suppression of energy transfer through the silica matrix.[53–57]

In recent years, there has been a tremendous progress in the development of new strategies for silica encapsulation of inorganic NPs.[54, 58–64] However, the most often applied procedures for the coating of hydrophobic NPs are based on the polymerization of silane monomers (usually tetraethyl orthosilicate (TEOS)) inside the micelles of reverse (or water-in-oil (w/o)) microemulsions.[65–73] The micelles comprise of basic aqueous droplets, which are stabilized by a nonionic surfactant in a continuous non-polar phase. Their size can easily be tuned by varying the individual synthetic parameters, including the molar water/surfactant ratio. Since the hydrolysis of silane monomer only occurs inside the micelles or at the water-oil interface, the resulting silica coated NPs are very homogeneous in size and shape, which is favorable compared to particles obtained by a Stöber-type approach.[74]

Inspired by these processes we have developed a novel one-pot encapsulation strategy, which can be applied on various hydrophobic NPs, to create multifunctional nanocomposites. It is based on a combination of w/o microemulsion techniques and common sol-gel methods and involves the successive addition of different functional silanes. We demonstrate that our multifunctional silica coated MnO NPs are stable against aggregation in water, physiological saline, and human blood serum over several weeks. Additionally, the incorporation of the fluorescent dye Atto 465 permits the detection during *in vitro* studies. Besides colloidal stability, the quan-

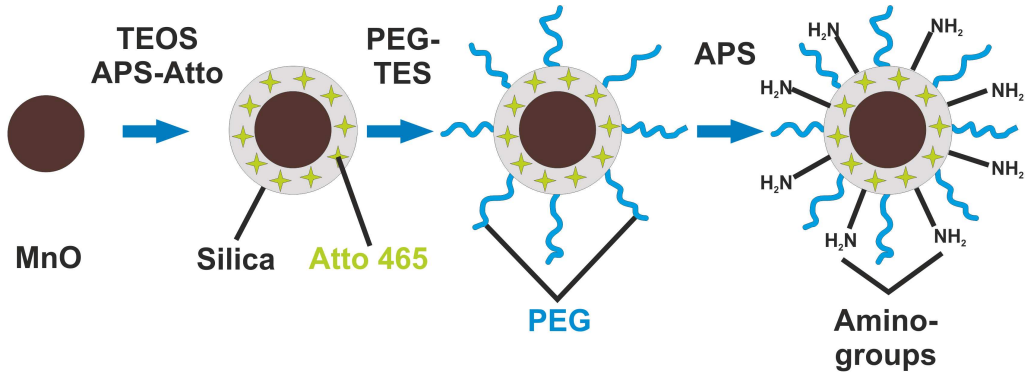

Figure 10.1: Experimental scheme for the preparation of multifunctional silica coated MnO NPs.

tification of the particle bound target molecules is a matter of interest because the drug loading capacity is decisive for the dose rate determination and a successful application of the particles in drug delivery. Quantification of the particle bound molecules is an analytical challenge, because either the lack (or the superposition) of chromophores excludes direct spectrophotometrical detection by excitation of fluorescence. For instance, several colorimetric assays have been developed for quantifying the PEGylation.[75–78] An elegant method for quantifying the PEGylation of nanoparticle drug carrier systems based on asymmetrical flow field-flow fractionation was reported recently.[76–79] We have determined the number of surface amino groups available for ligand binding on each particle using a colorometric assay with fluorescein isothiocyanate (FITC).

Furthermore, we show that the silica shell has only a negligible influence on the magnetic properties, and that therefore, the MnO@SiO_2 NPs still exhibit a considerable T_1 MR contrast enhancement effect. Additonally, the silica encapsulated MnO NPs showed negligible cytotoxicity and are well taken up by bone marrow-derived dendritic cells (BMDCs) making them suitable candidates for *in vivo* applications.

10.3 Results and Discussion

Particle synthesis and silica coating. The synthesis scheme for the preparation of the multifunctional silica coated MnO nanocomposites is illustrated in Scheme 10.1. First, hydrophobic oleate capped MnO NPs are synthesized according to a previously published method.[24, 80] In the second step, the NPs are coated with a thin shell of SiO_2 by hydrolysis of tetraethylorthosilicate (TEOS) in a reverse microemulsion. The shell thickness is easily adjustable by variation of the synthetic parameters, including micelle size, amount of TEOS, or reaction time. During this procedure, a fluorescent dye (Atto 465) is additionally incorporated into the silica shell, to allow optical detection of the NPs by fluorescence microscopy. In the following steps, further functionalization is achieved by condensation of a PEG-silane conjugate (PEG-TES) and 3-aminopropyltriethoxysilane (APS) onto the nanocomposite surface. The attachment of PEG groups not only increases the hydrophilic character, but also ensures biocompatibility of the magnetic NPs in physiological environment, whereas the presence of free amino groups on the particle surface enables for further conjugation. Consequently, the MnO@SiO_2-PEG/NH_2 nanocomposite particles are readily soluble in polar solvents, such as ethanol or acetone, which permits a simple purification procedure by repeated precipitation/centrifugation/resuspension with hexane and ethanol/acetone.

Nanoparticle characterization. The successive silane-functionalization steps of the MnO NPs were monitored by transmission electron microscopy (TEM) and Fourier-transformed infrared (FT-IR) spectroscopy. Representative TEM images of the different synthesis stages are displayed in Figure 10.2. Figure 10.2a shows as-prepared oleate capped MnO NPs before functionalization with SiO_2. The particles are uniform in size and shape with an average diameter of 10 nm ($\sigma \leq 5\%$). After the first modification step the particles are covered by a 3 nm thick silica shell (Figure 10.2b) and retain their narrow size distribution. Due to the higher electron density, MnO appears darker in the TEM images compared to SiO_2. It should be noted, that no multiple MnO NPs per SiO_2 shell are observed. This can be ascribed to an ideal micelle size during the reverse microemulsion step, in which each micelle contains only one MnO nanoparticle. Figure 10.2c and Figure 10.2d show the final MnO@SiO_2-PEG/NH_2 NPs after complete functionalization. There is a slight

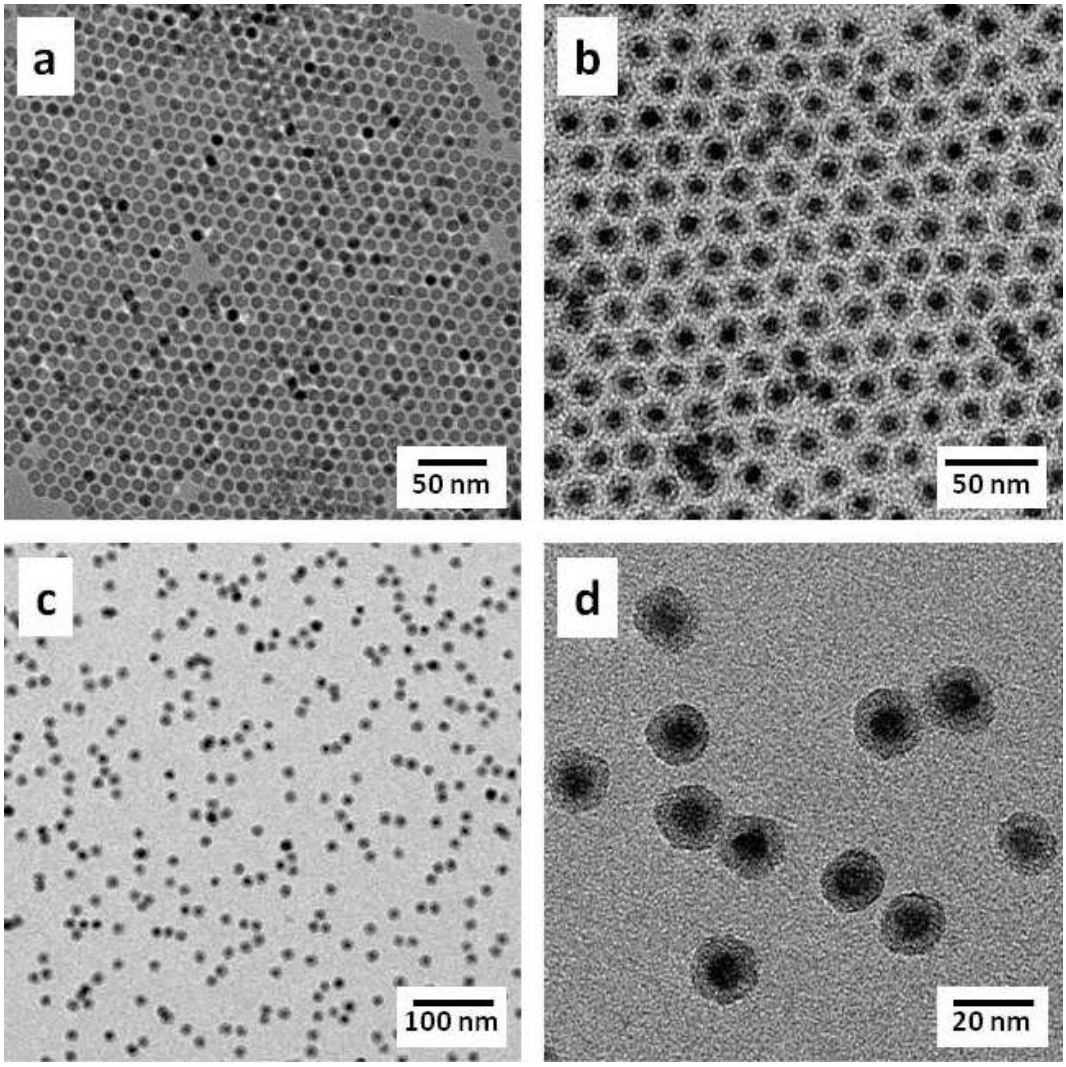

Figure 10.2: TEM images of "naked" and silica functionalized MnO NPs. (a) As synthesized MnO NPs with an average diameter of 10 nm. (b) MnO NPs coated with a uniform shell of silica after hydrolysis of TEOS. (c) MnO@SiO_2 NPs after conjugation with PEG-silane and APS, no significant aggregation is visible. (d) Enlarged view of MnO@SiO_2-PEG/NH_2 NPs in image (c).

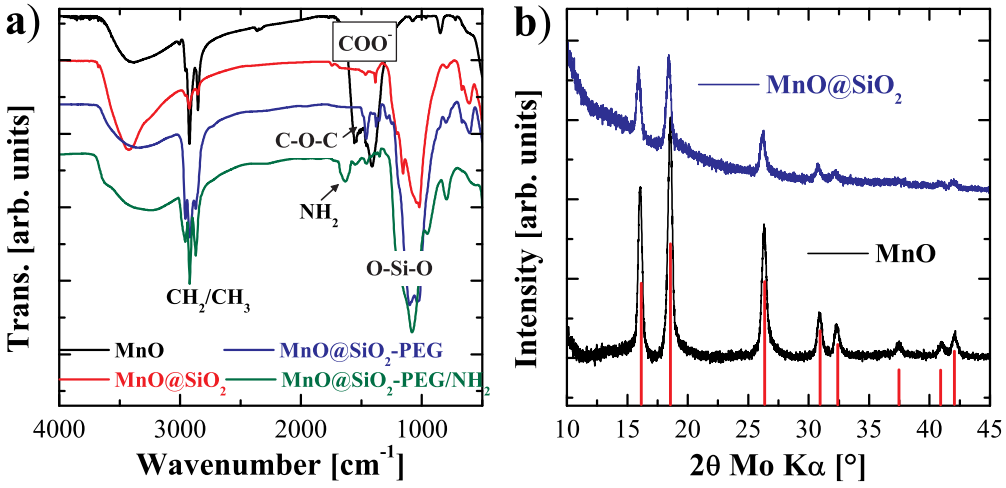

Figure 10.3: (a) FT-IR spectra of MnO NPs recorded after each functionalization step during the synthesis (from top to bottom). (b) powder XRD pattern of "naked" and silica coated MnO NPs. The red bars indicate the expected reflection positions.

increase in shell thickness to 4-5 nm, however, no significant particle aggregation is observable and the NPs appear uniform and well separated.

The presence of the individual functionalities on the MnO nanoparticle surface was confirmed by FT-IR spectroscopy. Figure 10.3a displays FT-IR spectra the MnO@SiO_2 nanocomposites after each functionalization step (top to bottom). The spectrum of as-prepared oleate capped MnO NPs (black line, top) exhibits characteristic vibrational bands at 1555 and 1410 cm^{-1} which can be assigned to the asymmetric and symmetric stretching modes of the carboxylate group of the oleate molecules.[24] The weak absorption band at 2956 cm^{-1} results from the asymmetric CH_3- stretching mode. Two bands at 2922 and 2852 cm^{-1} can be assigned to the symmetric and asymmetric CH_2-stretching modes of the alkyl chain, respectively. After the first step (MnO@SiO_2, red line), the carboxylate bands have almost disappeared completely, however, strong and broad absorption bands appear in the spectral region between 1155 and 1020 cm^{-1}, that can be associated with asymmetric O-Si-O stretching vibrations. This is a clear indication for the successful exchange of the oleate layer by SiO_2. The coupling of PEG molecules on the surface of the MnO@SiO_2 nanocomposites (MnO@SiO_2-PEG, blue line) is accompanied by the

appearance of two new bands at 1463 and 1377 cm^{-1}. They are due to the symmetric stretching vibrations of the C-O-C ether groups inside the PEG moieties. Additionally, the asymmetric and symmetric CH_3- and CH_2- stretching vibrations at 2954, 2918, and 2869 cm^{-1} appear more pronounced, owing to the PEG alkyl structure. Finally, the presence of free amino groups on MnO@SiO_2-PEG/NH_2 (green line) was confirmed by the occurrence of a band at 1636 cm^{-1} which can be assigned to the H-N-H scissoring vibration, and an absorption band at 800 cm^{-1}, that is due to the NH_2- wagging vibration. Unfortunately, the expected asymmetric and symmetric NH_2- stretching vibrations between 3300 and 3400 cm^{-1} are not visible among the broad OH-oscillation in the concerning spectral region. Moreover, the CN-stretching vibration, which is expected around 1080 cm^{-1}, is superimposed by the strong absorption of SiO_2. Phase purity of the silica coated MnO NPs was investigated by powder X-ray diffraction. For comparison, the powder patterns of pure MnO NPs and MnO@SiO_2 NPs are displayed in Figure 10.3b. In both cases the observed intensities match well with the cubic rock salt structure of MnO (*cF*8, $Fm\bar{3}m$). Therefore, it has to be estimated that no significant oxidation to Mn_3O_4 has occurred during the synthesis. However, the presence of the silica shell around the NPs leads to a considerable increase in background intensity which impedes a definite assignment.

Magnetic properties. As mentioned before, the magnetic behavior of MnO nanoparticles result from the presence of uncompensated spins on the particle surface. Hence, it was expected, that the silica shell has a considerable influence on the magnetic behavior of the NPs. The magnetic properties of "naked" and silica coated MnO NPs with shell thicknesses of 2 and 5 nm were studied using a superconducting quantum interference device (SQUID) (see Figure 10.4). Field-dependent magnetization measurement revealed superparamagnetic behavior at 300 K and weak ferromagnetic behavior at 5 K. Interestingly, the effect of the silica coating is by far less pronounced as expected from literature reports on other silica coated magnetic NPs, such as magnetite.[81] In contrast to Tan et al. we observed only a slight decrease in magnetization at 5 T with increasing silica shell thickness. Temperature-dependent magnetization curves of the corresponding samples (see insets in Figure 10.4) further confirm the observed superparamagnetism. The magnetic blocking temperature T_B, which is located at the maximum of the zero-field-cooled curves, is

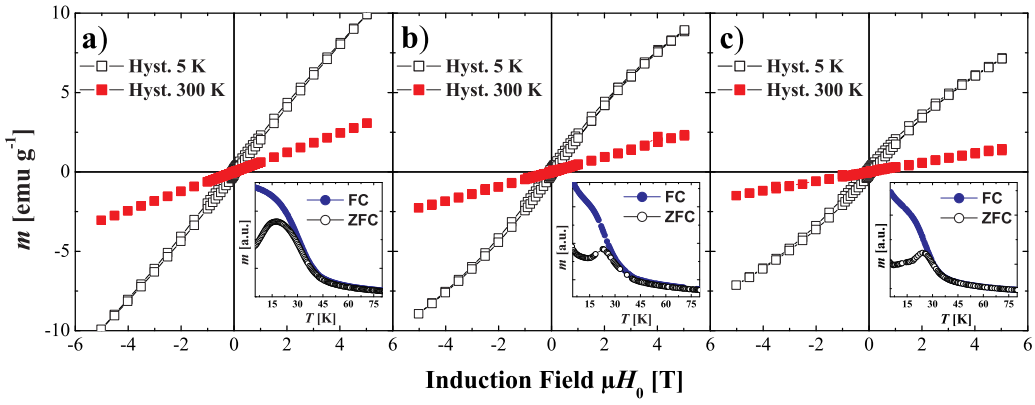

Figure 10.4: Magnetic hysteresis loops recorded at 300 and 5 K of (a) "naked" MnO NPs, (b) MnO@SiO_2 NPs with a silica shell thickness of 2 nm, and (c) MnO@SiO_2 NPs with a silica shell thickness of 5 nm. The insets display the corresponding zero-field-cooled/field-cooled (ZFC/FC) curves recorded with an applied induction field of 100 Oe.

a measure for the transition from the superparamagnetic to the ferromagnetic state. It indicates the temperature below which the thermal energy is insufficient to freely flip the magnetic moments of the NPs, therefore, inducing ferromagnetism. For bare MnO NPs T_B was reported to be in the range between 10 to 20 K.[24, 82, 83] Indeed, the observed T_B of 17 K for the uncoated MnO NPs (inset Figure 10.4) is in good agreement with the literature values. Upon silica encapsulation, the magnetic blocking temperature increases to 23 K for the sample with a 2 nm SiO_2 shell, and to 24 K for the sample containing a 5 nm SiO_2 shell, respectively. This circumstance can be explained by considering the larger effective mass of the MnO@SiO_2 NPs compared to pure MnO NPs. A larger mass leads to a higher thermal energy which is necessary to randomly flip the magnetic moments. A similar behavior has recently been reported for Au@MnO NPs.[22, 44]

UV/Vis and fluorescence spectroscopy. As mentioned above, the incorporation of fluorescent dyes into a silica matrix offers many advantages compared to their attachment on the outside of the nanocomposites. However, a sufficient integration of free dyes into SiO_2 can only be achieved after prior modification of the dye molecules. For this purpose, the NHS-ester of the fluorescent dye Atto 465

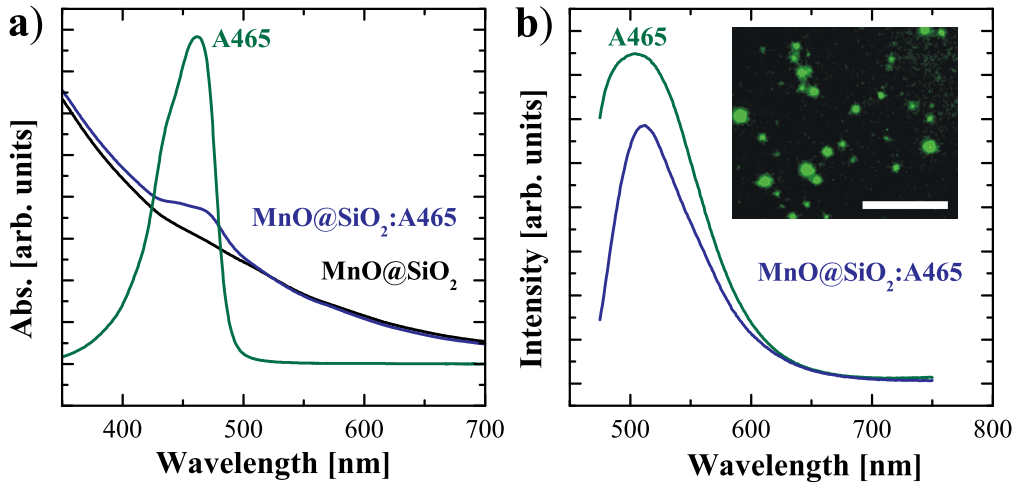

Figure 10.5: (a) UV-vis-spectra of pure MnO@SiO_2 NPs (black line), pure Atto 465 dye (green line), and MnO@SiO_2:Atto 465 NPs (blue line) in water. (b) Photoluminescence spectra of pure Atto 465 dye (green line) and MnO@SiO_2:Atto 465 NPs (blue line) at room temperature in water (inset: fluorescence microscopy image of MnO@SiO_2:A465 NPs, scale bar 0.5 μm).

was reacted with APS in anhydrous DMF, to form a reactive silane-dye conjugate. After that, TEOS and the APS-Atto 465 conjugate were injected into the reverse microemulsion at the same time. Since the hydrolysis of both components occurred simultaneously inside the micelles, the dye was efficiently incorporated into the silica shell, as confirmed by UV-vis and fluorescence spectroscopy (Figure 10.5). The UV-vis absorption spectra of pure MnO@SiO_2, pure Atto 465, and Atto 465 doped MnO@SiO_2 (MnO@SiO_2:A465) are displayed in Figure 10.5a. Pure MnO@SiO_2 nanocomposites containing no dye (black line) exhibit no prominent absorption characteristics, the absorbance increases gradually with decreasing wavelength. On the other hand, Atto 465-doped MnO@SiO_2 NPs (blue line) show a maximum in absorbance at 470 nm, even if the dye concentration is considerably low (molar ratio Atto 465/TEOS = 0.04%). However, the free dye (green line) exhibits a sharp maximum at 460 nm, and therefore, it has to be assumed, that the presence of the silica matrix around the dye molecules leads to a red-shift in the absorbance of approximately 10 nm. This observation is in accordance with previous reports on silica

NPs containing fluorescent dyes.[53, 54] Furthermore, the fluorescence properties of the nanocomposites (Figure 10.5b) revealed a similar behavior. Free Atto 465 fluoresces with a maximum emission intensity at 508 nm (green line), whereas for MnO@SiO_2:A465 (blue line), the maximum is shifted to 512 nm. The inset in Figure 10.5b shows MnO@SiO_2:A465 NPs observed under a fluorescent microscope. The particles are clearly visible as green dots and appear well separated. These results substantiate the potential to utilize these NPs as fluorescent probes for optical imaging.

Colloidal stability and quantification of NH_2 groups. A key requirement for later biomedical application of different nanomaterials is, besides a low toxicity, a sufficient stability in physiological environments. For this purpose, we investigated the colloidal stability of our silica encapsulated MnO NPs in various aqueous solutions, including deionized water, physiological saline and human blood serum. Figure 10.6b shows photographs of the different nanoparticle solutions in water and human blood serum, respectively, after 24h at 22 °C. Zeta-potential (ζ) measurements, conducted on pure MnO@SiO_2, MnO@SiO_2-PEG and MnO@SiO_2-PEG/NH_2 NPs, revealed, that the net surface charges are altered upon additional surface functionalization. For MnO NPs coated with bare silica, the determined surface charge is ζ = -40 mV, whereas for MnO@SiO_2-PEG the value is -45 mV, which both is due to the presence of deprotonated silanol groups (-Si-O^-, pK_a = 7.0). Since, amino groups (pK_a = 9.0) usually occur as protonated ammonium moieties (-NH_3^+) at ambient pH, the introduction of APS onto the silica surface should be accompanied by shift of the zeta-potential into the positive regime.[84] In fact, the expected alteration was observed, with ζ = -4,4 mV. Furthermore, dynamic light scattering (DLS) measurements confirmed the excellent colloidal stability of the NPs (see Figure 10.6a)). The determination of surface bound amino groups by the above mentioned colorimetric method (see Experimental Section) revealed an average NH_2-group concentration of 2,4 μmol per mg NPs.

Another interesting feature of the MnO@SiO_2-PEG/NH_2 NPs is the comparatively fast degradation of the particles at lower pH values. Experiments carried out in citrate buffer solutions with a pH of 5 showed, that the MnO core is rather rapidly dissolved (see Figure 10.6c), which was visible by a decoloration of samples in citrate/KOH buffer in comparison to NPs incubated in water for 24 h at 22 °C.

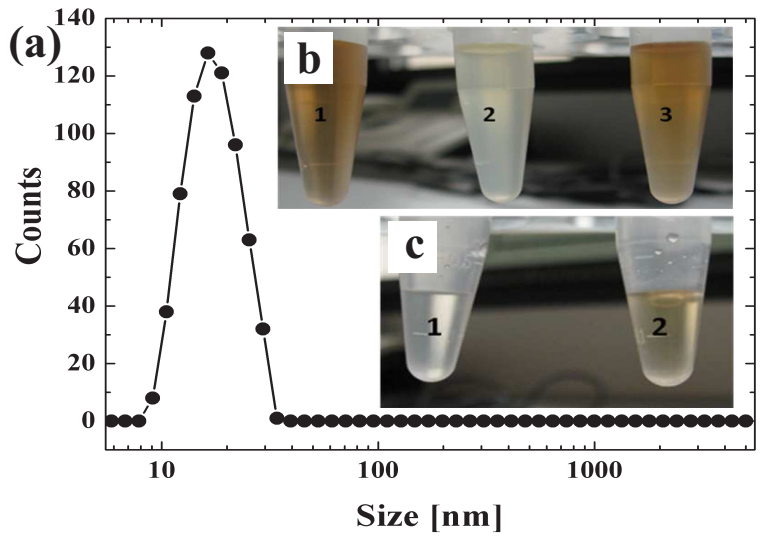

Figure 10.6: (a) DLS size distribution of MnO@SiO_2-PEG NPs with an average size of 12.5 nm. (b) Photograph of these NPs in (1) water in human blood serum before (3) at 22 °C for 24 h (image (2) shows pure human blood serum). (c) MnO@SiO_2-PEG NPs in (1) citrate/KOH buffer at pH 5 and (2) water.

MR imaging. To investigate the MR signal enhancement effects, aqueous solutions of silica functionalized MnO NPs, at different Mn concentrations, were measured on a clinical 3.0 T MRI scanner. As mentioned above, MnO NPs are known to shorten the longitudinal relaxation time (T_1), which leads to a brightening in the corresponding MR image, compared to samples without contrast agent. Prior to the experiment, MnO@SiO_2-PEG/NH_2 NPs were diluted in physiological saline solution yielding concentrations of 0 to 5.3 mM (with respect to manganese, determined by AAS). Figure 10.7 displays T_1-weighted phantom MR images of these solutions. It is clearly evident, that the brightness of the image increases with increasing manganese (and therefore, MnO@SiO_2-PEG/NH_2 nanoparticle) concentration. For an exact quantification of the MR signal enhancing properties, the relaxivities r_1 and r_2 were determined according to the general relation:

$$\frac{1}{T_1} = \frac{1}{T_1^0} + r_1 \cdot c \tag{10.1}$$

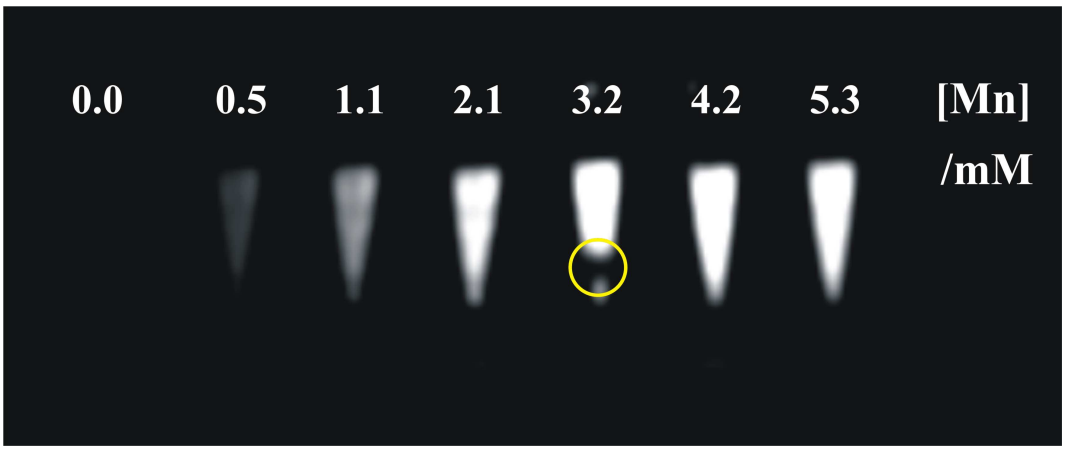

Figure 10.7: T_1 weighted images of physiological saline solutions containing MnO@SiO_2-PEG/NH_2 NPs in different concentrations. The yellow circle indicates an air bubble in the sample tube, which occurred during sample placement into the MRI scanner.

and

$$\frac{1}{T_2} = \frac{1}{T_2^0} + r_2 \cdot c \tag{10.2}$$

in which T_1 and T_2 are the measured longitudinal and transverse relaxation times, respectively, T_1^0 and T_2^0 are the corresponding relaxation times in the pure media, and c is the concentration of the contrast agent. Figure 10.8a shows plots of $1/T_1$ and $1/T_2$ versus the Mn concentration, in which a linear increase is obvious in both cases. The r_1 and r_2 values, derived from the slope of the curve, are 0.47 and 2.85 mM^{-1} s^{-1}, respectively, which is in good agreement with earlier reports on manganese oxide NPs.[19, 21, 73] Additionally, the relaxivity ratio (r_2/r_1 = 6.06) is considerably low, which indeed suggests that the silica encapsulated MnO NPs are potential candidates as T_1 contrast agents.

Leaching experiments. Manganese leaching experiments were carried out to evaluate the liability of the manganese oxide cores inside the silica shells for degradation in aqueous solution. For this purpose, solutions of MnO@SiO_2-PEG NPs in water were transferred into dialysis membranes and dialyzed against deionized water (18 MΩ). The manganese content inside the membranes was monitored by AAS measurements over a period of four weeks. For comparison, an aqueous solution

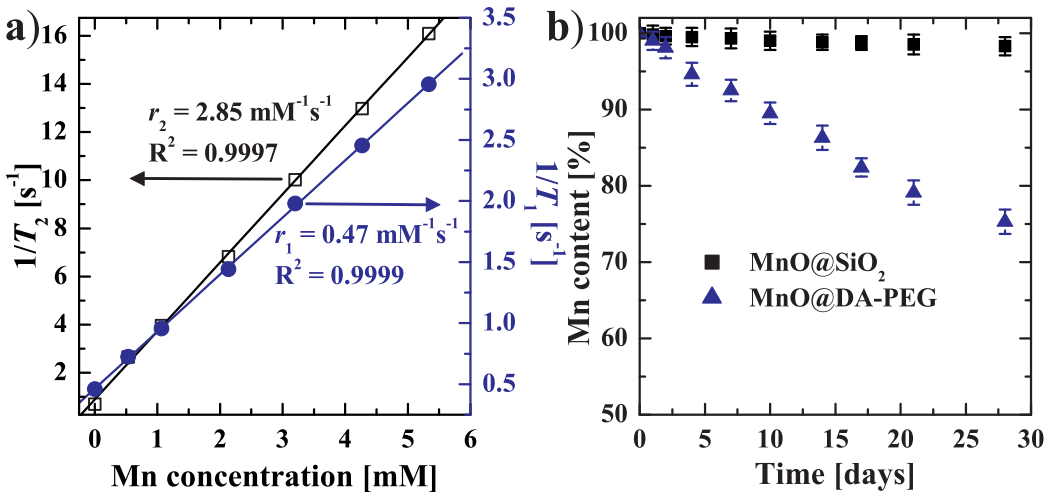

Figure 10.8: (a) T_1 (right) and T_2 (left) relaxation rates as a function of manganese concentration. (b) Evolution of the manganese content during the leaching experiment for silica coated and dopamine-PEG functionalized MnO NPs.

of manganese oxide NPs, which were stabilized by a bi-functional dopamine-PEG ligand (DA-PEG), rather than a robust silica shell, was treated in the same way. The results, presented in Figure 10.8b, show an obvious trend: Without the protection of a SiO_2 shell, the Mn content decreased to almost 75% within 28 days, whereas only a minor depletion of ≈1.5% was observed in the MnO@SiO_2-PEG sample, over the same time period. These results elucidate the advantage of silica encapsulation of MnO NPs for potential biomedical applications. Additionally, TEM measurements confirmed the expected degradation of the DA-PEG functionalized NPs. TEM images of both samples after the leaching experiments are shown in Figure 10.9. The SiO_2 modified NPs retained almost their initial size and shape. The DA-PEG-MnO NPs, on the other hand, although not being dramatically reduced in size, appear rougher and less homogeneous, which is a clear indication that dissolution has taken place on the particle surface.

Cytotoxicity. To evaluate the biocompatibility of silica encapsulated MnO nanoparticles, we assessed the induction of apoptosis in two primary bone marrow-derived phagocytic cell types that are relevant for innate and adaptive immune responses. Firstly, we examined the effects of MnO@SiO_2-PEG/NH_2 NPs on BM-

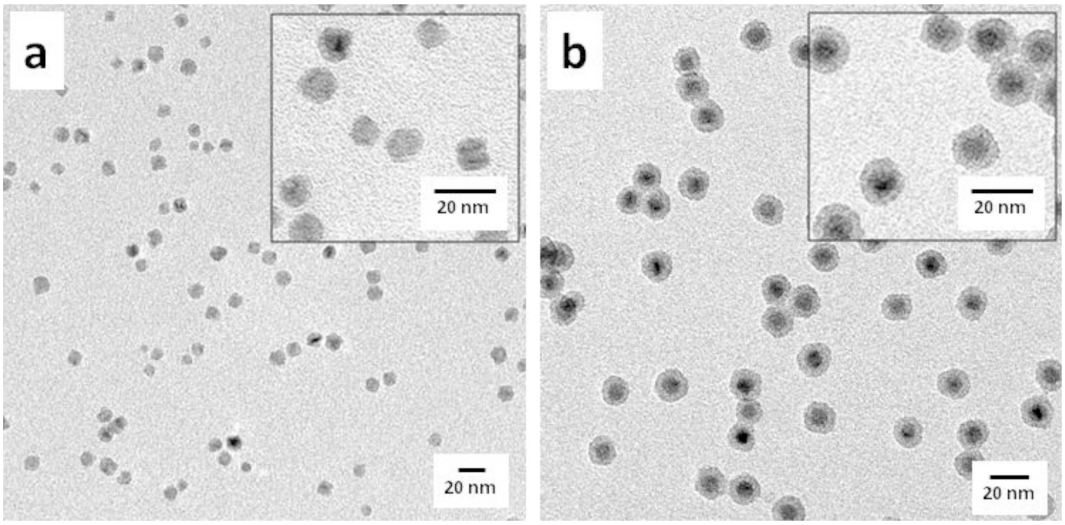

Figure 10.9: TEM images of (a) DA-PEG functionalized and (b) silica coated MnO NPs after the leaching experiments (enlarged images are shown in the insets).

PMN as short lived cells that are highly sensitive to external (i.e. microbial) stimuli and undergo apoptosis rapidly in vitro unless adequately activated. Secondly, we evaluated the rate of apoptosis in BMDCs as master regulators for the initiation of adaptive immune responses. For the assessment of apoptosis, we used two independent assays. The staining with Annexin V and PI identifies early apoptotic events by the detection of externalized phosphatidylserine on the cell membrane, while Nicoletti staining of isolated nuclei detects fragmented DNA as later apoptotic event.

As depicted in Figure 10.10, we were unable to detect a decrease in cell viability for BM-PMN (Figure 10.10a, b) indicating that these NPs do not have any significant toxic effects on this cell type. For BMDC, a decrease in cell viability was only observed at the highest concentration of MnO@SiO_2 NPs (30 μg/mL) suggesting that these NPs exert toxic effects only at high concentrations on primary cells. The results indicate that these MnO@SiO_2 NPs can be expected to have an acceptable toxicity profile and are suitable for the application in vivo.

BM-PMN (Figure 10.10a, b) or BMDC (Figure 10.10c, d) (2×10^5 /well) were incubated in the presence of the indicated concentration of MnO@SiO_2 NPs and assayed for the induction of apoptosis. Cycloheximide (10 μg/mL) as strong inducer of apoptosis[85] served as positive control for BM-PMN and BMDC, while

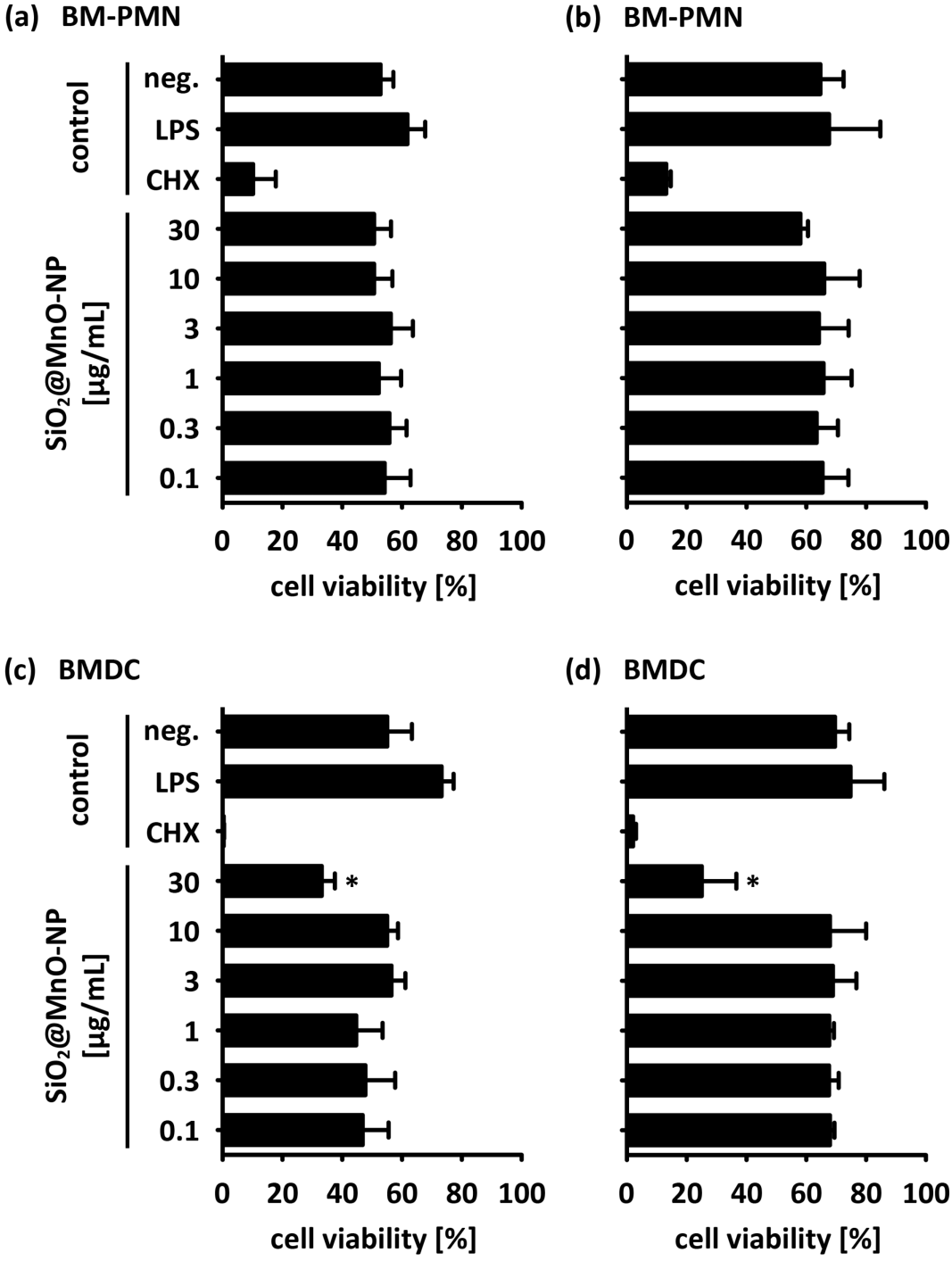

Figure 10.10: Induction of apoptosis by MnO@SiO2 NPs in primary bone marrow derived cells.

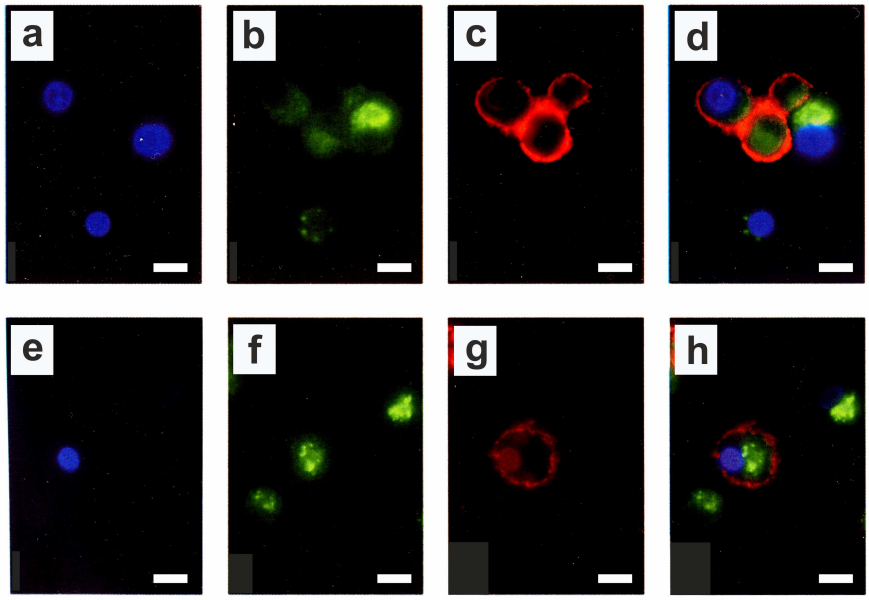

Figure 10.11: Fluorescence microscopic images of BMDCs. BMCDs were incubated with Atto 465 doped MnO@SiO_2-PEG/NH_2 (green fluorescence (f)). Cell nuclei were stained with DAPI (e) and the MHCII was stained using a combination of biotinylated MHCII antibody and streptavidin coupled texas red (g), (h) shows an overlay of the images (e - g). (a - d) show the control. In this case no NPs were added, the cells were treated the same way as samples incubated with NPs.

the TLR4 agonist LPS (100 ng/mL), that is well known to delay the constitutive apoptosis in PMN, was used as an additional control for BM-PMN. (Figure 10.10a, b) BM-PMN were harvested after 24 h of in vitro culture with the indicated stimuli and assayed for apoptosis by staining with Annexin-V/PI (Figure 10.10a) or by Nicoletti staining (Figure 10.10b). BMDC (Figure 10.10c, d) were harvested after 72 h of culture with the indicated stimuli and assayed for apoptosis by staining with Annexin-V/PI (Figure 10.10c) or by Nicoletti staining (Figure 10.10d). The depicted data show the cumulative results of two independent experiments each assayed in duplicate wells (mean $\pm$ SD percentage of cell viability of one representative experiment assayed in duplicate wells). (*) indicates a significant difference ($p \leq 0.05$) compared to the untreated control by student's t test.

Uptake of silica coated NPs by BMDC. Since the silica-coated nanoparticles carry Atto 465 as fluorophore, they could be detected using a fluorescence micro-

scope. To further confirm their uptake the cell nuclei were stained with DAPI and the MHCII was stained with MHCII-bio. Texas-Red functionalized with streptavidin, which was then able to couple with the biotinylated MHCII to result in a red fluorescence, where MCHII was present. A control was performed in which BMDCŽs were incubated without NPs (see Figure 10.11a - d). The green fluorescence is due to the fact, that BMDCs show fluorescence in this channel by themselves. Despite this fact, a difference between the control samples and samples with NPs (Figure 10.11f) can be seen. When NPs were present, they could be detected as small green dots. The majority was found in close proximity to the blue stained cell nuclei (see overlay in figure 10.11h) indicating a successful cellular uptake.

10.4 Conclusion

In summary, we have demonstrated a novel way to prepare biocompatible multifunctional MnO@SiO_2 nanocomposites. The procedure combines a water-in-oil microemulsion, to create an initial silica shell around MnO, and common Stöber-like processes to condense further functionalities, such as PEG or NH_2-groups, on the silica surface. The silica encapsulated MnO NPs showed excellent stability in various aqueous solutions, including physiological saline solution and human blood serum. Furthermore, by virtue of their magnetic properties, MnO@SiO_2-PEG/NH_2 NPs showed a considerable T_1 MR contrast enhancement, and, since a fluorescent dye was also incorporated into the silica shell during the synthesis, our silica coated MnO NPs may serve as multimodal imaging agents for both, optical and MR imaging. We also demonstrated that silica encapsulated MnO NPs are less prone to manganese leaching in aqueous solution, compared to simple PEGylated NPs. Finally, the vast and well-established silane chemistry permits additional modification of the NPs, which leads to numerous further applications which is also confirmed by their low toxicity and their cellular uptake.

10.5 Experimental Section

Materials. Manganese chloride tetrahydrate ($MnCl_2 \times 4H_2O$) (99.9%), oleic acid (90%), sodium hydroxide (99%), 1-octadecene (90%), Igepal CO-520, ammonium hydroxide (25%, aqueous solution), tetraethoxysilane (TEOS) (99.999%), 3-aminopropyltriethoxysilane (APS) ($\geq$99%), fluorescein isothiocyanate (FITC), and DMF ($\geq$99.9%, extra dry) were purchased from Aldrich. Atto 465-NHS-ester was from Fluka, and 2-methoxy(polyethyleneoxy)propyltrimethoxysilane (PEG-silane, n = 6-9) (90%) was from ABCR. Methanol, hexane, cyclohexane, and acetone were of analytical grade (Fisher Scientific). All chemicals were used without further purification.

Synthesis of MnO NPs. Monodisperse MnO NPs were prepared by the decomposition of manganese oleate in high boiling point solvents as described previously.[24, 80] Briefly, 2 mmol of manganese oleate were mixed with 10 g of 1-octadecene, degassed at 70 °C and slowly heated to reflux with a defined temperature program. The particles were washed by repeated precipitation with acetone, centrifugation and dispersion in hexane.

Synthesis of APS-Atto 465. APS-Atto 465 was prepared by reacting 1 mg ($\approx$ 2 μmol) Atto 465-NHS-ester with 23.5 μL (100 μmol) APS in 500 μL of dry DMF for 4 hours in a shaker at 20 °C in the dark. The solution was kept as a stock solution at -20 °C in the dark.

Silica encapsulation of MnO NPs. The hydrophobic MnO NPs were encapsulated with SiO_2 by a w/o microemulsion technique using cyclohexane as the oil phase, aqueous NH_4OH solution as the water-phase and Igepal CO-520 as non-ionic surfactant. For the encapsulation process, Igepal CO-520 (2.0 g) was dissolved in 35 mL of cyclohexane and degassed by bubbling a gentle stream of argon through the solution for 30 minutes. The NPs were added to the solution and the degassing procedure was continued for another 15 minutes. Subsequently, aqueous NH_4OH (150 μL) was added to initiate the micelle formation. This process could be observed as a temporary cloudiness in the solution. After 5 minutes TEOS (112 μL, 0.5 mmol) and APS-Atto 465 were added and the reaction mixture was stirred under argon protection over night. For further functionalization of the silica shell, PEG-silane was added to the solution. The covalent attachment of PEG on the

surface led to complete precipitation of the MnO@SiO_2 NPs within 2 hours. The NPs were collected by centrifugation (5000 rpm for five minutes) and washed thoroughly by repeated dispersion in acetone and precipitation with hexane. The fact that the resulting particles were easily soluble in polar solvents, such as acetone or ethanol, is a clear indication for the successful hydrophilic modification of the initially hydrophobic MnO surface. After complete removal of any unreacted silanes and surfactant molecules, the MnO@SiO_2-PEG NPs were dissolved in 20 mL of acetone. Amino groups were introduced by addition of APS (150 μL, 0.64 mmol) and 150 μL aqueous NH_4OH. The reaction was continued for another two hours followed by concentration of the solution to 2 mL and precipitation of the MnO@SiO_2-PEG/NH_2 NPs with 2 mL of hexane. Again, the resulting particles were thoroughly washed by repeated dissolving and precipitating with acetone and hexane accompanied by centrifugation (5000 rpm for five minutes). The MnO@SiO_2-PEG/NH_2 NPs obtained by this method were very easily soluble and stable in various aqueous media, including deionized water, physiological saline, and different buffer solutions.

Nanoparticle Characterization. The particles were characterized by means of powder X-ray diffraction (XRD), transmission electron microscopy (TEM), Fourier transformed infrared spectroscopy (FT-IR), atomic absorption spectroscopy (AAS), UV-Vis and fluorescence spectroscopy, and dynamic light scattering (DLS). The magnetic properties of the MnO@SiO_2 NPs were investigated with a superconducting quantum interference device (SQUID, Quantum Design MPMS-XL). XRD measurements were performed on a Bruker D8 Advance diffractometer equipped with a Sol-X energy-dispersive detector and operating with Mo Kα radiation. Samples for transmission electron microscopy were prepared by placing a drop of dilute nanoparticle solution in the appropriate solvent (hexane, acetone, water) on a carbon coated copper grid. Low-resolution TEM images and ED patterns were recorded on a Philips EM420 microscope operating at an acceleration voltage of 120 kV. FT-IR spectra were acquired on a Mattson Instruments 2030 Galaxy-FT-IR spectrometer. For AAS measurements (Perkin-Elmer 5100 ZL), aliquots of aqueous nanoparticle solutions were treated with conc. HNO_3 at 90 °C for 30 minutes followed by adjustment of the pH-value to 3 with NH_4OH. UV-Vis spectroscopy was carried out on a Perkin-Elmer Lambda 19 UV-vis/NIR spectrometer. Fluorescence spectra were

acquired on a Spex Fluorolog 1680/81. Determinations of the zeta-potential and dynamic light scattering were performed on a Malvern Zetasizer Nano ZS.

Mn leaching experiments. To evaluate the stability of the MnO NPs encapsulated by SiO_2 in comparison to MnO NPs functionalized by a bi-functional dopamine-PEG ligand, aqueous solutions of both kinds of particles were dyalized, in a cellulose membrane with molecular weight cut-off (MWCO) of 3500 (Spectra/Por 3, SpectrumLabs), against deionized water. The variation of the Mn concentration over a period of four weeks was monitored by atomic absorption spectroscopy (AAS) on aliquots taken after definite time intervals. In a typical experiment, 10 mg of the concerning functionalized NPs were dissolved in 5 mL of deionized water, loaded into the dialysis tube, and placed in a 2000 mL glass cylinder filled with deionized water. The cylinder was sealed to prevent any contamination. The dialysis was carried out for four weeks with the surrounding water being replaced every second day. Aliquots of 50 μL were carefully extracted after fixed time intervals.

Quantification of surface amino groups. To determine the number of amino groups on each particle, the MnO@SiO_2-PEG/NH_2 NPs were treated with fluorescein isothiocyanate (FITC). After complete reaction, the amount of unreacted FITC in the supernatant was determined by UV-Vis spectroscopy. In a typical experiment the prepared MnO@SiO_2-PEG/NH_2 particles were dissolved in 10 mL of acetone. An aliquot of 1 mL of this stock-solution was treated with an equal amount of hexane to completely precipitate the NPs followed by centrifugation (5 min, 9000 rpm). Subsequently, the particles were resuspended and diluted in acetone by a factor of 1:100, before FITC was added according to the maximum possible amount of APS in the dilute sample. After completed reaction (one hour) the particles were precipitated by adding exactly 1 mL of hexane followed by centrifugation (10 min, 13300 rpm). The concentration of unreacted FITC in the supernatant was determined using a calibration curve according to the Lambert-Beer-law. The difference in the amount of FITC before and after the reaction was used to estimate the amount of free amino groups in the sample. With this result, the average number of free amino groups on each particle can be calculated by correlating the total amount of NH2-groups with the average number of NPs in the sample.

Generation of BMDCs. Bone marrow-derived DCs (BMDCs) were generated from C57BL/6 mice as described previously.[86] Briefly, bone marrow from 6-8

week old mice was cultured in medium (IscoveŽs medium supplemented with 5% fetal calve serum (FCS), 1% glutamate, 1% sodium pyruvate) and supplemented with GM-CSF (50 ng/mL). These cells were typically >85% CD11c^{+}H2-A^{b+} as determined by flow cytometry. Furthermore, the cells were CD80^{low} and CD86^{low}. Medium was changed on day 3 and 5. Cells were used for the experiments at day 7 as immature BMDCs.

BM-PMN. Bone marrow-derived polymorphonuclear neutrophils (BM-PMN) were purified by magnetic beads (MACS from Miltenyi, Bergisch Gladbach, Germany) using Ly6G/C specific antibodies (clone Gr-1) according to the manufacturer's protocol. BM-PMN were cultured in medium (described above). Cell purity (Ly6-G^{hi}CD11b^{hi}) was generally greater than 90% assessed by flow cytometry.

Determination of apoptosis. 2×10^5 cells (BMDCs or BM-PMN) were cultured in 96 well plates (Greiner) with the indicated stimuli and kept up to 3 days at 37 °C with 7.5% CO_2 in air. At the indicated time points the cells were harvested and analyzed for apoptosis by Annexin-V (BD Pharmingen) /propidium iodide (PI, Fluka) staining or Nicoletti staining for fragmented nuclear DNA using established protocols described.[85]

Fluorescence-Spectroscopy and immunostaining. In a typical experiment 100 μl cell suspension (2×10^6 cells) were diluted 1:1 with and without solution that contained silica coated NPs, respectively, (final concentration of NPs 30 μg/mL) and were incubated in a μ-Slide 8 well (ibidi; Germany) at 37 °C; 5% CO_2 for 18 h. Before staining, the cells were washed with 150 μL FACS buffer (PBS supplemented with 0.5% BSA (Roth, Germany), 5 mM EDTA (Roth, Germany) and 0.01% NaN_3 (Merck, Germany). 100 μL solution of MHCII-bio in FACS buffer (dilution 1:1000) was added for 20 min at room temp. After washing with FACS buffer streptavidin coupled texas red was added and incubated for 20 min at rt. After an additional washing step, DAPI (4,6-diamidin-2-phenylindol), diluted in PBS was added. After a final incubation of 20 min as well as two final washing steps with PBS, the BM-CDs were characterized using the fluorescence microscope IX81 (Olympus).

Magnetic resonance imaging. MR signal enhancement effects of MnO@SiO_2 nanocomposite particles were measured with different Mn concentrations on a clinical 3.0 T MRI scanner (Magnetom Trio, Siemens Medical Solutions, Erlangen, Germany). Signal reception and radio frequency (RF) excitation was performed

using a 8-channel knee coil. For the T_1-measurement, a saturation prepared (SR) snapshot fast low angle shot (SR-TurboFLASH) pulse sequence with repetition time (TR) / echo time / flip angle = 3.0 ms/1.5 ms/20° was used with varying saturation times starting from 20 ms up to 8000 ms. For measuring the T_2 relaxation time, a multi-echo spin-echo pulse sequence with a total of 32 echos and TR = 5000 ms was used, the echo time was varied from 7 ms to 224 ms. In a second T_2 measurement TE was varied from 15 ms up to 480 ms.

10.6 References

[1] Cheon, J.; Lee, J.-H. *Accounts of Chemical Research* **2008**, *41*, 1630–1640.

[2] Pankhurst, Q. A.; Connolly, J.; Jones, S. K.; Dobson, J. *Journal of Physics D: Applied Physics* **2003**, *36*, R167.

[3] Shukoor, M. I.; Natalio, F.; Tahir, M. N.; Ksenofontov, V.; Therese, H. A.; Theato, P.; Schroder, H. C.; Muller, W. E. G.; Tremel, W. *Chemical Communications* **2007**, *43*, 4677–4679.

[4] Sun, C.; Lee, J. S. H.; Zhang, M. *Advanced Drug Delivery Reviews* **2008**, *60*, 1252–1265.

[5] Schröder, H. C.; Natalio, F.; Wiens, M.; Tahir, M. N.; Shukoor, M. I.; Tremel, W.; Belikov, S. I.; Krasko, A.; Müller, W. E. G. *Molecular Immunology* **2008**, *45*, 945–953.

[6] Arruebo, M.; Fernández-Pacheco, R.; Ibarra, M. R.; Santamaría, J. *Nano Today* **2007**, *2*, 22–32.

[7] Pankhurst, Q. A.; Thanh, N. T.; Jones, S. K.; Dobson, J. *Journal of Physics D: Applied Physics* **2009**, *42*, 224001.

[8] Gao, J.; Gu, H.; Xu, B. *Accounts of Chemical Research* **2009**, *42*, 1097–1107.

[9] Jun, Y.-w.; Lee, J.-H.; Cheon, J. *Angewandte Chemie International Edition* **2008**, *47*, 5122–5135.

[10] Jun, Y.-w.; Seo, J.-w.; Cheon, J. *Accounts of Chemical Research* **2008**, *41*, 179–189.

[11] Lee, J. H.; Jun, Y. W.; Yeon, S. I.; Shin, J. S.; Cheon, J. *Angewandte Chemie International Edition* **2006**, *45*, 8160–8162.

[12] Bridot, J.-L.; Faure, A.-C.; Laurent, S.; Rivière, C.; Billotey, C.; Hiba, B.; Janier, M.; Josserand, V.; Coll, J.-L.; Elst, L. V.; Muller, R.; Roux, S.; Perriat, P.; Tillement, O. *Journal of the American Chemical Society* **2007**, *129*, 5076–5084.

[13] Park, J. Y.; Baek, M. J.; Choi, E. S.; Woo, S.; Kim, J. H.; Kim, T. J.; Jung, J. C.; Chae, K. S.; Chang, Y.; Lee, G. H. *ACS Nano* **2009**, *3*, 3663–3669.

[14] Petoral, R. M.; Söderlind, F.; Klasson, A.; Suska, A.; Fortin, M. A.; Abrikossova, N.; Selegard, L.; Käll, P.-O.; Engström, M.; Uvdal, K. *Journal of Physical Chemistry C* **2009**, *113*, 6913–6920.

[15] Hifumi, H.; Yamaoka, S.; Tanimoto, A.; Citterio, D.; Suzuki, K. *Journal of the American Chemical Society* **2006**, *128*, 15090–15091.

[16] Hifumi, H.; Yamaoka, S.; Tanimoto, A.; Akatsu, T.; Shindo, Y.; Honda, A.; Citterio, D.; Oka, K.; Kuribayashi, S.; Suzuki, K. *Journal of Materials Chemistry* **2009**, *19*, 6393–6399.

[17] Evanics, F.; Diamente, P. R.; van Veggel, F. C. J. M.; Stanisz, G. J.; Prosser, R. S. *Chemistry of Materials* **2006**, *18*, 2499–2505.

[18] Na, H. B.; Song, I. C.; Hyeon, T. *Advanced Materials* **2009**, *21*, 2133–2148.

[19] Na, H.; Lee, J.; An, K.; Park, Y.; Park, M.; Lee, I.; Nam, D. H.; Kim, S.; Kim, S. H.; Kim, S. W.; Lim, K. H.; Kim, K. S.; Kim, S. O.; Hyeon, T. *Angewandte Chemie* **2007**, *119*, 5341–5341.

[20] Gilad, A. A.; Walczak, P.; McMahon, M. T.; Bin Na, H.; Lee, J. H.; An, K.; Hyeon, T.; van Zijl, P. C. M.; Bulte, J. W. M. *Magnetic Resonance in Medicine* **2008**, *60*, 1–7.

[21] Na, H. B.; Hyeon, T. *Journal of Materials Chemistry* **2009**, *19*, 6267–6273.

[22] Schladt, T. D. et al. *Angewandte Chemie International Edition* **2010**, *49*, 3976–3980.

[23] Schladt, T. D.; Schneider, K.; Shukoor, M. I.; Natalio, F.; Bauer, H.; Tahir, M. N.; Weber, S.; Schreiber, L. M.; Schröder, H. C.; Müller, W. E. G.; Tremel, W. *Journal of Materials Chemistry* **2010**, *20*, 8297–8904.

[24] Schladt, T. D.; Graf, T.; Tremel, W. *Chemistry of Materials* **2009**, *21*, 3183–3190.

[25] Park, J.; Joo, J.; Kwon, S. G.; Jang, Y.; Hyeon, T. *Angewandte Chemie International Edition* **2007**, *46*, 4630–4660.

[26] Lu, A.-H.; Salabas, E. L.; Schüth, F. *Angewandte Chemie International Edition* **2007**, *46*, 1222–1244.

[27] Goesmann, H.; Feldmann, C. *Angewandte Chemie* **2010**, *122*, 1402–1437.

[28] Goesmann, H.; Feldmann, C. *Angewandte Chemie International Edition* **2010**, *49*, 1362–1395.

[29] Frey, N. A.; Peng, S.; Cheng, K.; Sun, S. *Chemical Society Reviews* **2009**, *38*, 2532–2542.

[30] Berry, C. C.; Curtis, A. S. G. *Journal of Physics D: Applied Physics* **2003**, *36*, R198.

[31] Berry, C. C. *Journal of Physics D: Applied Physics* **2009**, *42*, 224003.

[32] Moghimi, S. M.; Hunter, A. C.; Murray, J. C. *Pharmacological Reviews* **2001**, *53*, 283–318.

[33] Xu, C.; Xu, K.; Gu, H.; Zheng, R.; Liu, H.; Zhang, X.; Guo, Z.; Xu, B. *Journal of the American Chemical Society* **2004**, *126*, 9938–9939.

[34] Torchilin, V. P. *Advanced Drug Delivery Reviews* **2006**, *58*, 1532–1555.

[35] Prencipe, G.; Tabakman, S. M.; Welsher, K.; Liu, Z.; Goodwin, A. P.; Zhang, L.; Henry, J.; Dai, H. *Journal of the American Chemical Society* **2009**, *131*, 4783–4787.

[36] Owens, D. E.; Peppas, N. A. *International Journal of Pharmaceutics* **2006**, *307*, 93–102.

[37] Dobrovolskaia, M. A.; Aggarwal, P.; Hall, J. B.; McNeil, S. E. *Molecular Pharmaceutics* **2008**.

[38] Amstad, E.; Gillich, T.; Bilecka, I.; Textor, M.; Reimhult, E. *Nano Letters* **2009**, *9*, 4042–4048.

[39] Amstad, E.; Zurcher, S.; Mashaghi, A.; Wong, J. Y.; Textor, M.; Reimhult, E. *Small* **2009**, *5*, 1334–1342.

[40] Xie, J.; Xu, C.; Kohler, N.; Hou, Y.; Sun, S. *Advanced Materials* **2007**, *19*, 3163–3166.

[41] Hong, R.; Fischer, N. O.; Emrick, T.; Rotello, V. M. *Chemistry of Materials* **2005**, *17*, 4617–4621.

[42] Shukoor, M.; Natalio, F.; Metz, N.; Glube, N.; Tahir, M.; Therese, H.; Ksenofontov, V.; Theato, P.; Langguth, P.; Boissel, J. P.; Schröder, H. C.; Müller, W. E. G.; Tremel, W. *Angewandte Chemie* **2008**, *120*, 4826–4830.

[43] Shukoor, M.; Natalio, F.; Metz, N.; Glube, N.; Tahir, M.; Therese, H.; Ksenofontov, V.; Theato, P.; Langguth, P.; Boissel, J. P.; Schröder, H. C.; Müller, W. E. G.; Tremel, W. *Angewandte Chemie International Edition* **2008**, *47*, 4748–4752.

[44] Schladt, T. et al. *Angewandte Chemie* **2010**, *122*, 4068–4072.

[45] Yu, W. W.; Chang, E.; Sayes, C. M.; Drezek, R.; Colvin, V. L. *Nanotechnology* **2006**, *17*, 4483–4487.

[46] Kim, B.-S.; Qiu, J.-M.; Wang, J.-P.; Taton, T. *Nano Letters* **2005**, *5*, 1987–1991.

[47] Park, J.; Yu, M. K.; Jeong, Y. Y.; Kim, J. W.; Lee, K.; Phan, V. N.; Jon, S. *Journal of Materials Chemistry* **2009**, *19*, 6412–6417.

[48] Basiruddin, S. K.; Saha, A.; Pradhan, N.; Jana, N. R. *Journal of Physical Chemistry C* **2010**, *114*, 11009–11017.

[49] Schroedter, A.; Weller, H.; Eritja, R.; Ford, W. E.; Wessels, J. M. *Nano Letters* **2002**, *2*, 1363–1367.

[50] Santra, S.; Yang, H.; Holloway, P. H.; Stanley, J. T.; Mericle, R. A. *Journal of the American Chemical Society* **2005**, *127*, 1656–1657.

[51] Salgueiriño Maceira, V.; Correa-Duarte, M. A.; Spasova, M.; Liz-Marzán, L. M.; Farle, M. *Advanced Functional Materials* **2006**, *16*, 509–514.

[52] Yang, H.; Santra, S.; Walter, G. A.; Holloway, P. H. *Advanced Materials* **2006**, *18*, 2890–2894.

[53] Ow, H.; Larson, D. R.; Srivastava, M.; Baird, B. A.; Webb, W. W.; Wiesner, U. *Nano Letters* **2005**, *5*, 113–117.

[54] Burns, A.; Ow, H.; Wiesner, U. *Chemical Society Reviews* **2006**, *35*, 1028–1042.

[55] Wang, L.; Wang, K.; Santra, S.; Zhao, X.; Hilliard, L. R.; Smith, J. E.; Wu, Y.; Tan, W. *Analytical Chemistry* **2006**, *78*, 646–654.

[56] Rampazzo, E.; Bonacchi, S.; Montalti, M.; Prodi, L.; Zaccheroni, N. *Journal of the American Chemical Society* **2007**, *129*, 14251–14256.

[57] Kim, O.-H.; Ha, S.-W.; Kim, J. I.; Lee, J.-K. *ACS Nano* **2010**.

[58] Liz-Marzán, L. M.; Giersig, M.; Mulvaney, P. *Langmuir* **1996**, *12*, 4329–4335.

[59] Bruchez, M., JR.; Moronne, M.; Gin, P.; Weiss, S.; Alivisatos, A. P. *Science* **1998**, *281*, 2013–2016.

[60] Kobayashi, Y.; Correa-Duarte, M. A.; Liz-Marzán, L. M. *Langmuir* **2001**, *17*, 6375–6379.

[61] Schroedter, A.; Weller, H. *Angewandte Chemie International Edition* **2002**, *41*, 3218–3221.

[62] Liu, S.; Zhang, Z.; Ha, M. *Analytical Chemistry* **2005**, *77*, 2595–2600.

[63] Piao, Y.; Burns, A.; Kim, J.; Wiesner, U.; Hyeon, T. *Advanced Functional Materials* **2008**, *18*, 3745–3758.

[64] Guerrero-Martínez, A.; Pérez-Juste, J.; Liz-Marzán, L. M. *Advanced Materials* **2010**, *22*, 1182–1195.

[65] Chan, Y.; Zimmer, J. P.; Stroh, M.; Steckel, J. S.; Jain, R. K.; Bawendi, M. G. *Advanced Materials* **2004**, *16*, 2092–2097.

[66] Yi, D. K.; Selvan, S.; Lee, S. S.; Papaefthymiou, G. C.; Kundaliya, D.; Ying, J. Y. *Journal of the American Chemical Society* **2005**, *127*, 4990–4991.

[67] Yang, Y.; Gao, M. Y. *Advanced Materials* **2005**, *17*, 2354–2357.

[68] Lee, D. C.; Mikulec, F. V.; Pelaez, J. A. M.; Koo, B.; Korgel, B. A. *Journal of Physical Chemistry B* **2006**, *110*, 11160–11166.

[69] Darbandi, M.; Lu, W.; Fang, J.; Nann, T. *Langmuir* **2006**, *22*, 4371–4375.

[70] Li, Y.; Zhang, X. L.; Qiu, R.; Qiao, R.; Kang, Y. S. *Journal of Physical Chemistry C* **2007**, *111*, 10747–10750.

[71] Koole, R.; van Schooneveld, M. M.; Hilhorst, J.; de Mello Donegá, C.; t' Hart, D. C.; van Blaaderen, A.; Vanmaekelbergh, D.; Meijerink, A. *Chemistry of Materials* **2008**, *20*, 2503–2512.

[72] Yeo, K. M.; Shin, J.; in Lee, S. *Chemical Communications* **2010**, *46*, 64–66.

[73] Yang, H.; Zhuang, Y.; Hu, H.; Du, X.; Zhang, C.; Shi, X.; Wu, H.; Yang, S. *Advanced Functional Materials* **2010**, *20*, 1733–1741.

[74] Stöber, W.; Fink, A.; Bohn, E. *Journal of Colloid and Interface Science* **1968**, *26*, 62–69.

[75] Skoog, B. *Vox Sanguinis* **1979**, *37*, 345–349.

[76] Zhang, G.; Wang, X.; Wang, Z.; Zhang, J.; Suggs, L. *Tissue Engineering* **2006**, *12*, 9–19.

[77] Natarajan, A.; Xiong, C.-Y.; Albrecht, H.; DeNardo, G. L.; DeNardo, S. J. *Bioconjugate Chemistry* **2005**, *16*, 113–121.

[78] Nag, A.; Mitra, G.; Ghosh, P. C. *Analytical Biochemistry* **1996**, *237*, 224–231.

[79] Zillies, J. C.; Zwiorek, K.; Winter, G.; Coester, C. *Analytical Chemistry* **2007**, *79*, 4574–4580.

[80] Jana, N. R.; Chen, Y.; Peng, X. *Chemistry of Materials* **2004**, *16*, 3931–3935.

[81] Tan, H.; Xue, J. M.; Shuter, B.; Li, X.; Wang, J. *Advanced Functional Materials* **2010**, *20*, 722–731.

[82] Ghosh, M.; Biswas, K.; Sundaresan, A.; Rao, C. N. *Journal of Materials Chemistry* **2006**, *16*, 106–111.

[83] Seo, W. S.; Jo, H. H.; Lee, K.; Kim, B.; Oh, S. J.; Park, J. T. *Angewandte Chemie International Edition* **2004**, *43*, 1115–1118.

[84] Santra, S.; Yang, H.; Dutta, D.; Stanley, J. T.; Holloway, P. H.; Tan, W.; Moudgil, B. M.; Mericle, R. A. *Chemical Communications* **2004**, *40*, 2810–2811.

[85] Radsak, M. P.; Salih, H. R.; Rammensee, H.-G.; Schild, H. *Journal of Immunology* **2004**, *172*, 4956–4963.

[86] Warger, T.; Osterloh, P.; Rechtsteiner, G.; Fassbender, M.; Heib, V.; Schmid, B.; Schmitt, E.; Schild, H.; Radsak, M. P. *Blood* **2006**, *108*, 544–550.

CHAPTER 11

Synthesis and Magnetic Properties of FePt@MnO Nano-*hetero*-Particles

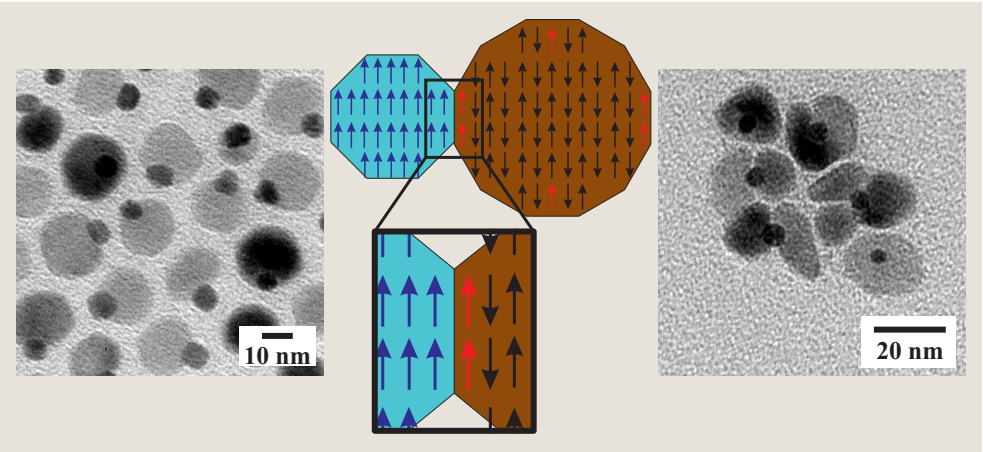

11.1 Abstract

Monodisperse FePt@MnO nano-*hetero*-particles with different sizes and morphologies were prepared by a seed-mediated nucleation and growth technique. Both, size and morphology, could be controlled by adjustment of the synthetic parameters. The FePt nano-*hetero*-particles were thoroughly characterized by TEM- and XRD analysis and SQUID magnetometry. The surface spins of the antiferromagnetic MnO domains pin the magnetic moments of the ferromagnetic FePt NPs which leads to an exchanged biased magnetic hysteresis.

11.2 Introduction

Recent efforts in nanoscale science and technology are focused on the development of novel multifunctional materials which exhibit several beneficial properties at the same time. In this context, the synthesis and design of hybrid nanomaterials which consist of two or more individual inorganic components has attracted considerable interest. The controlled combination of different materials, which themselves exhibit distinct chemical and physical properties, offers several advantages.[1, 2] In fact, the combination of magnetic NPs with optically active materials, such as gold[3–5], silver[6, 7] or semiconductor NPs[8], has led to many interesting discoveries in recent years.[9, 10]

Magnetic NPs have been among the most intensively studied material classes for more than two decades. Owing to their interesting properties they have found applications in a vast range of different scientific areas, including mass data storage, catalysis,[11–14] protein separation,[15–17] specific cell targeting, drug delivery,[18, 19] and magnetic resonance imaging (MRI).[4, 20–22]

Among these magnetic nanomaterials, FePt NPs containing a near-equal atomic percentage of Fe and Pt, play an outstanding role, not only because they were one of the first nanomaterials which could be prepared with an exceptionally narrow particle size distribution, but also because they have interesting magnetic properties which are promising for a variety of applications.[12, 14] FePt occurs in two different modifications, an ordered *fct* (or $L1_0$) phase, in which the Fe and Pt atoms form alternating atomic layers in the $\{001\}$ direction of the crystal lattice, and a

disordered *fcc* phase, in which the atoms are randomly distributed.[23–25] Much research effort has been devoted in the preparation of ordered *fct* FePt NPs, since they exhibit a high magneto-crystalline anisotropy (K), high saturation magnetization, as well as a high maximum energy product.[26–28] This makes them ideal candidates for many different applications ranging from high density data storage devices,[12] nanocomposites for permanent magnets,[29] or even biomedical probes.[30–34] However, since as-prepared FePt NPs usually exhibit the disordered *fcc* structure, their magneto-crystalline anisotropy and saturation magnetization are reasonably low, leading to superparamagnetic behavior at room temperature.[25]
MnO NPs, on the other hand, have served as a model compound to explain the magnetic properties of 3d transition metal oxides.[35, 36] Just like other binary oxides, including FeO, NiO and CoO, they are part of a special class of magnetic materials in which the bulk phase exhibits antiferromagnetic properties, but superparamagnetic behavior is observed in nanoparticulate samples.[37–39] This phenomenon is often explained by the presence of uncompensated spins on the surface of the crystallites which leads to a measurable net magnetic moment.[40–42] Since the surface to volume ratio increases with decreasing particle size, the magnetic moment of the NPs grows when the particle size is reduced.[42] These circumstances have lead to a growing interest of MnO NPs for biomedical applications. Especially, they have shown to shorten the spin-lattice relaxation time T_1, and therefore, show strong potential as positive contrast agents for magnetic resonance imaging (MRI).[43–49]
The combination of FePt and MnO on the nanolevel has so far only been reported for FePt-MnO core-shell structures by Kang et *al.*[50] where the authors demonstrated an enhancement of the magnetic coercivity and blocking temperature. In this contribution we report on the successful synthesis of FePt@MnO nanocomposites, which combine the individual properties of both material classes. We were able to selectively vary the size and morphology of the nano-*hetero*-particles from dimers to flower-like by adjustment of the individual experimental parameters based on the mechanisms presented in chapter 4. Furthermore, the magnetic behavior of the FePt domains was significantly altered upon attachment to MnO. We reveal, that the surface spins of the antiferromagnetic MnO domains pin the magnetic moments of the ferromagnetic FePt NPs, which leads to an exchanged biased magnetic hysteresis.

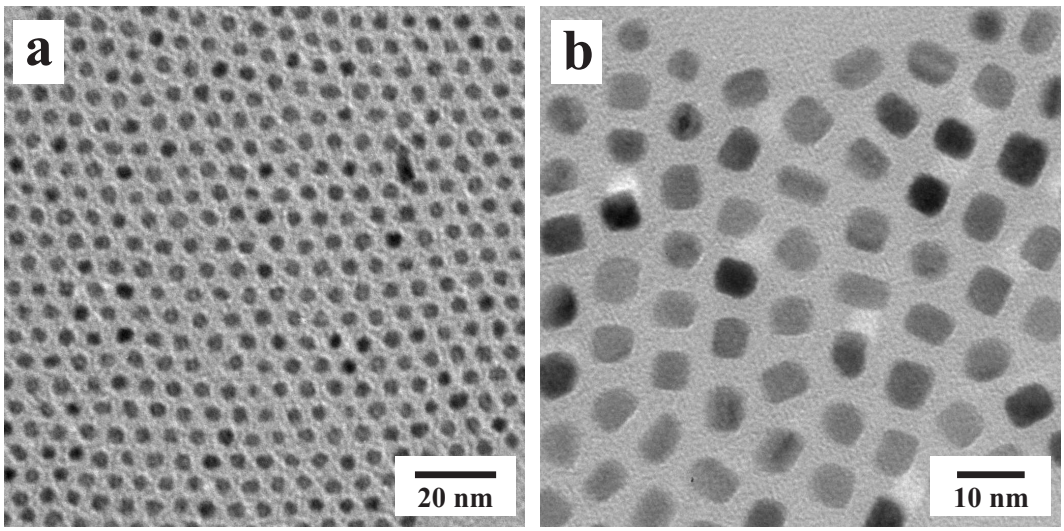

Figure 11.1: TEM images of monodisperse FePt NPs with an average size of (a) 3 nm and (b) 6 nm.

11.3 Results and Discussion

Synthesis. FePt@MnO nanocomposites, consisting of an antiferromagnetic MnO domain and a ferromagnetic FePt domain, were prepared by a simple two step procedure. In the first step monodisperse FePt NPs of 3 nm[12] or 6 nm[51] in size were prepared by the decomposition of platinum acetylacetonate and iron pentacarbonyl as precursors. The size of the NPs could be controlled by varying the individual synthetic parameters, such as precursor ratio, temperature, or surfactant ratio. Figure 11.1 shows representative TEM images of monodisperse FePt NPs with an average size of 3 nm and 6 nm. The 3 nm FePt particles are spherical, whereas the larger particles in Figure 11.1b have a cube-like shape. In the second step, manganese oxide domains were heterogeneously nucleated on the FePt seeds by the decomposition of a manganese oleate precursor.[42] As mentioned in chapter 4, a successful formation of nano-*hetero*-particles can only be achieved by suppressing homogeneous nucleation and simultaneously promoting heterogeneous nucleation. In fact, suppression of homogeneous nucleation can be obtained by keeping the precursor concentration under the critical supersaturation value (see section 3.1). This can be achieved by precise control of the precursor ratio, amount of seed particles

and heating profile. Dimeric FePt@MnO NPs with different FePt and MnO domain sizes are shown in Figure 11.2. Figure 11.2a, d and g show FePt@MnO dimers prepared with 3 nm FePt seeds, whereas the other images in Figure 11.2 present FePt@MnO nanodimers synthesized with 6 nm FePt seeds. Figure 11.2 clearly demonstrates that the size of the MnO domain can be controlled by adjusting the molar ratio of Mn precursor to FePt seeds. For example, 6 nm@12 nm FePt@MnO NPs (Figure 11.2h) were prepared with 10 mg FePt and 0.25 mmol Mn oleate, while 6 nm@9 nm FePt@MnO NPs (Figure 11.2i) were synthesized with 10 mg FePt and 0.1 mmol Mn oleate.

By changing the "polarity" of the solvent different morphologies could be obtained. Figure 11.3 shows TEM images of flowerlike FePt@MnO NPs with multiple MnO domains being attached to each FePt core. These particles were prepared in the same way as the particles presented in Figure 11.2, however, benzyl ether was used as solvent instead of 1-octadecene. It is obvious that the change of solvent had a major influence on the particle morphology. A similar behavior was reported by Yu et *al.* for Au@Fe_3O_4 nano-*hetero*-particles.[3] The authors proposed that the nucleation of Fe_3O_4 on the Au surface leads to a charge polarization at the nucleation interface. However, the free electrons of the Au nanoparticle must compensate the electron loss at the interface and are, therefore, withdrawn from the remaining surface. On the other hand, further nucleation is only possible if a sufficient number of free electrons is available on the Au surface. Therefore, further growth of the metal oxide domain will lead to dimeric structures, if the electron deficiency cannot be compensated. By using a solvent which carries a considerably amount of electron density by itself, a charge transfer from the solvent to the metal surface can replenish the free electrons and, therefore, allow additional nucleation. As a result, multiple nucleation sites are can occur on each metal seed leading to the formation of flowerlike nano-*hetero*-particles.

The results shown in Figures 11.2 and 11.3 confirm these assumptions in an impressive way. Just as Au, FePt NPs possess free electrons, that are depleted by the nucleation of MnO on the seed surface. If 1-octadecene is used as solvent during the reaction, the electrons deficiency cannot be compensated and the growth of the MnO domain results in FePt@MnO dimers. Benzyl ether, on the other hand, is a typical example for a "polar" solvent which contains a sufficient amount of electron

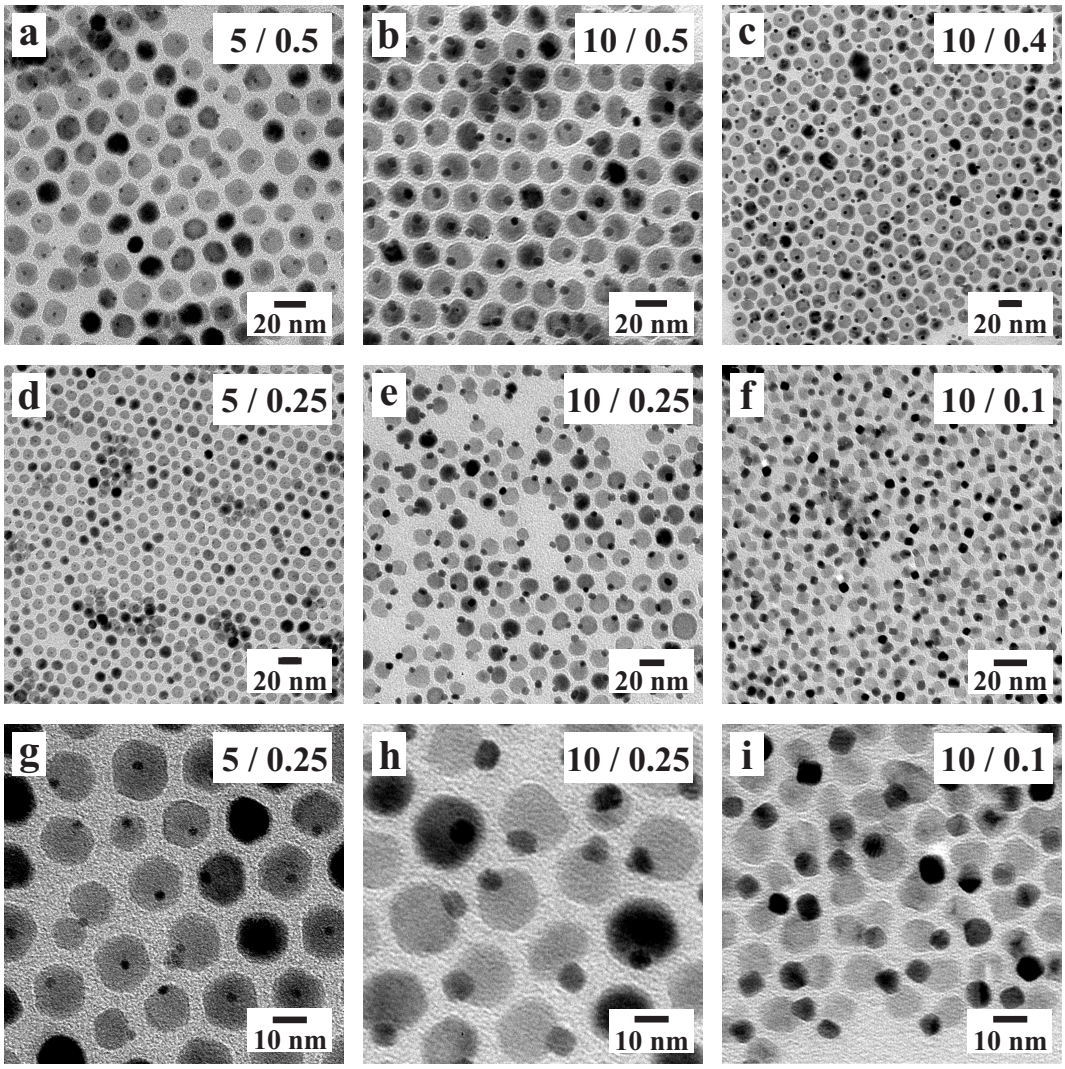

Figure 11.2: TEM images of monodisperse FePt@MnO NPs prepared with different precursor ratios (the ratios are indicated with mg FePt/mmol Mn oleate).(a) 3 nm@17 nm, (b) 6 nm@17 nm, (c) 6 nm@15 nm, (d) 3 nm@15 nm, (e), 6 nm@12 nm, (f) 6 nm@9 nm, (g - h) enlarged images of (d - f).

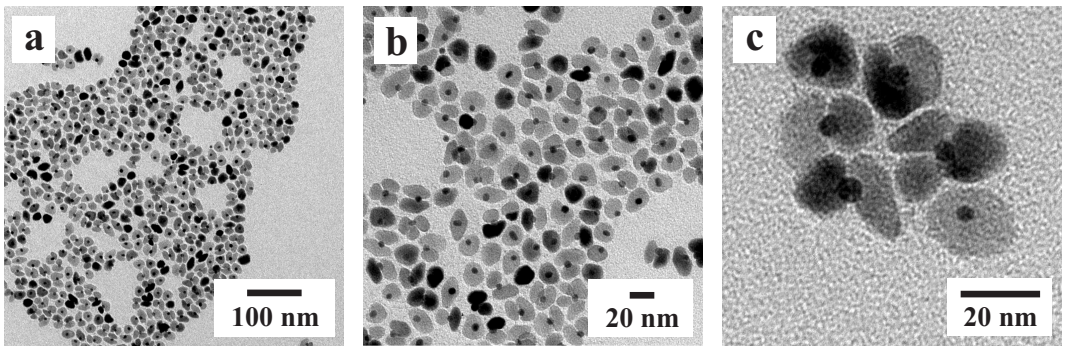

Figure 11.3: TEM images of flower-like FePt@MnO NPs prepared in benzyl ether.

density owing the delocalized π-electron system in the benzyl ring. It can transfer electron density to the FePt surface, leading to further nucleation of MnO on suitable crystal facets and, therefore, the formation of flower-like FePt@MnO NPs.
The FePt@MnO nano-*hetero*-structure is likely derived from the epitaxial growth of MnO on the FePt seeds, as FePt has an disordered *fcc* structure with a d-spacing in $\{111\}$ direction of 2.2002 Å, while MnO has a cubic rock salt structure with lattice constant a = 4.44 Å, which is within 1% of being exactly double the value of $d_{\{111\}}$(FePt). Therefore, it has to be estimated that nucleation of MnO preferably occurs on the $\{111\}$ crystal facets of the FePt seeds. This assumption becomes obvious when larger FePt NPs are used as seeds (see Figure 11.4). An example for larger FePt (13 nm) NPs is shown in Figure 11.4a. The cubic structure of FePt is clearly reflected in the nanoparticle morphology, although the corners appear rounded off, displaying the $\{111\}$ crystal surfaces. The cubic morphology of larger FePt NPs can be ascribed to a faster growth rate of the $\{111\}$ facets compared to the $\{100\}$ crystal surfaces during the synthesis.[52] However, if these NPs are used as seeds, flower-like FePt@MnO structures are obtained even if strictly non-polar solvents, such as 1-octadecene or octyl ether, are used. The reason for this behavior is presumably the presence of residual electron densities in the larger FePt particles. Compared to the smaller FePt seeds, the 13 nm nanocubes have a reduced surface-to-volume ratio and, therefore, more electrons can be retained inside the particles. Since the surface areas of the $\{111\}$-facets are considerably small (compared to the $\{100\}$ surfaces, a relatively large amount of electron density is provided for further nucleation on

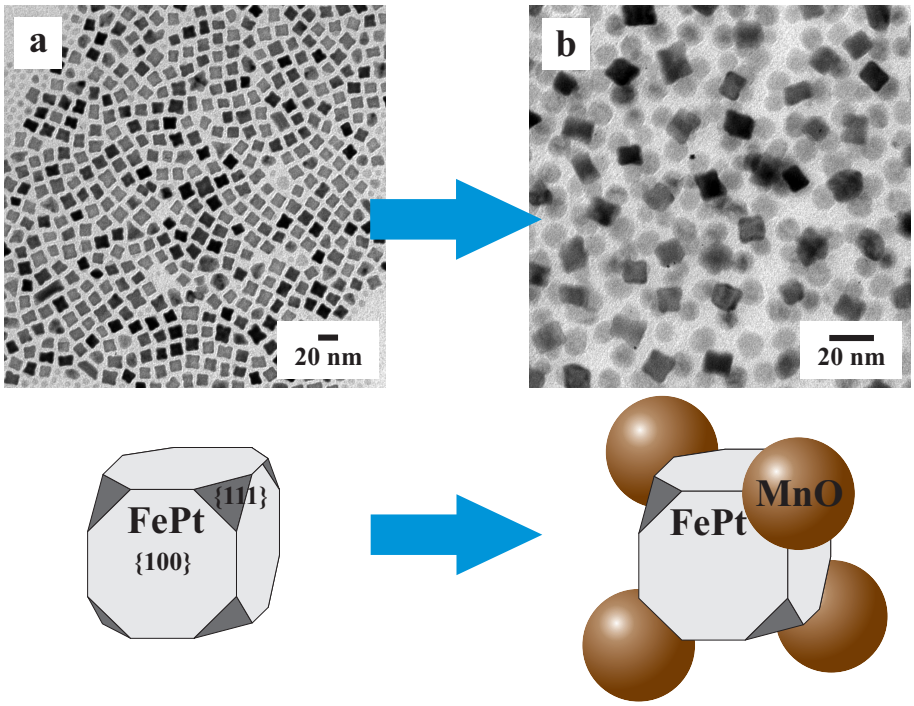

Figure 11.4: (a) Larger FePt NPs with an average diameter of 13 nm with a cube-like shape. However, the remaining $\{111\}$ crystal facets permit the nucleation of MnO. (b) Flower-like FePt@MnO NPs synthesized with FePt nanocubes from (a) as seeds. The MnO domains are mostly located at the corners of the cubes, which is in accordance with the proposed nucleation of MnO on the $\{111\}$ surfaces of FePt. Due to steric hindrance, not all corners are occupied by MnO, they are rather arranged in a tetrahedral manner.

the $\{111\}$ surfaces. As result, FePt NPs with multiple MnO domains are obtained. However, not all corners of the FePt cubes are occupied by MnO, since due to steric hindrance, a tetrahedral arrangement is preferred (see Figure 11.4b).

XRD analysis. The phase composition of the product was investigated with powder X-ray diffraction. Figure 11.5 displays typical powder XRD patterns of FePt@MnO nano-dimers with 3 nm FePt/17 nm MnO (Figure 11.5a) and 6 nm FePt/17 nm MnO (Figure 11.5b) domains. The positions and relative intensities of all diffraction peaks match well with expected patterns for *fcc* FePt and rock-salt MnO. The peak broadness resembles the average particle size distribution of both components: The shape of the FePt peaks is much broader than that of the MnO,

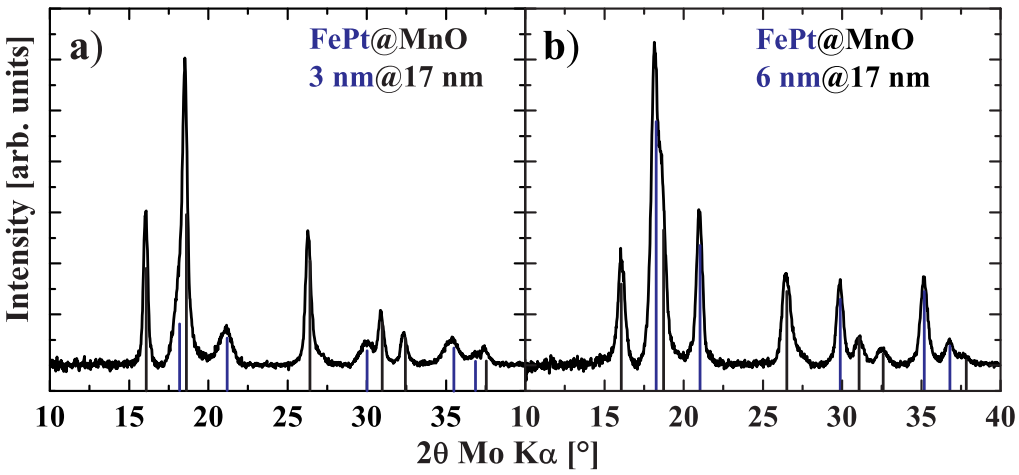

Figure 11.5: Powder XRD pattern of FePt@MnO nano-*hetero*-particles. (a) 3 nm@17 nm FePt@MnO and (b) 6 nm@17 nm. The expected reflection positions of FePt and MnO are indicated by the blue and black bars, respectively.

which is in accordance with the expected appearance derived from Scherrer's equation.

Magnetic properties. Magnetic measurements performed on 3 nm@17 nm, 6 nm@17 nm and 6 nm@9 nm FePt@MnO NPs revealed superparamagnetic behavior at room temperature in all investigated samples (see Figure 11.6). However, the individual magnetic properties differ substantially from each other in measurements carried out at 5 K which indicates a considerable magnetic interaction between the FePt and MnO domains. An explanation for this behavior can be derived by considering two key contributions: (1) the magnetic volume of each sample, or rather the ratio of magnetic volumes of both parts: $r = V_{\mathrm{FePt}}/V_{\mathrm{MnO}}$, and (2) the ferromagnetic-antiferromagnetic (FM-AFM) interaction between the surface spins of FePt and MnO. In sample (a), r is comparatively small and the FM-AFM spin interaction is low due to a small FePt-MnO interface area. As a result, the magnetic hysteresis is mainly dominated by MnO and resembles a typical paramagnet with low values for remanence magnetization M_R = 0.28 emu g^{-1}, coercitive field H_C = 1700 Oe, as well as the magnetization M(5 T) = 5.01 emu g^{-1}, and does not reach saturation. In sample (b) larger FePt NPs are connected to MnO domains of

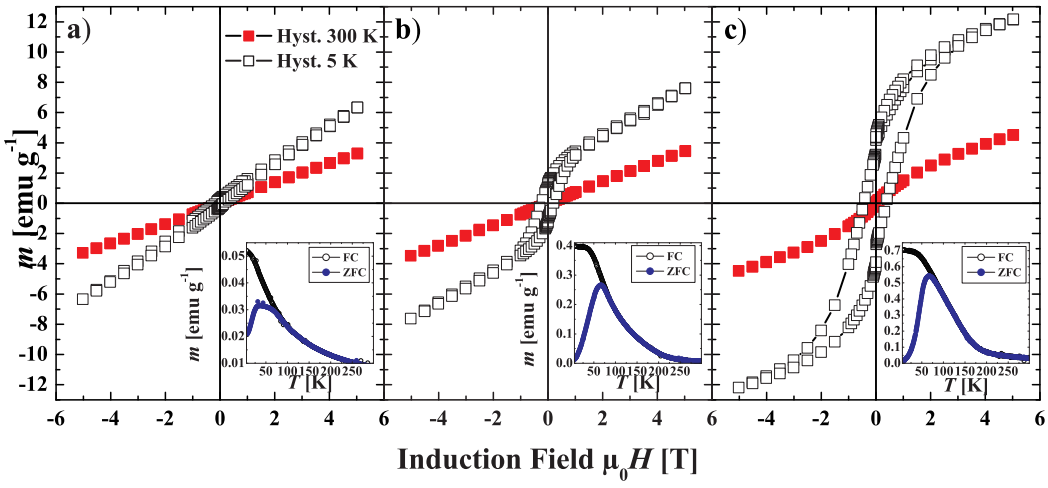

Figure 11.6: Magnetic data of FePt@MnO nano-*hetero*-particles. Magnetic hysteresis loops (a) 3 nm@17 nm, (b) 6 nm@17 nm and (c) 6 nm@9 nm FePt@MnO NPs. The insets show the corresponding temperature dependent magnetization curves (ZFC-FC) under an applied field of 100 Oe.

the same size as in sample (a). Consequently, r is larger leading to enhanced values for M_R (1.27 emu g^{-1}), H_C (2500 Oe) and M(5 T) (7.60 emu g^{-1}). Additionally, the higher interface area between the FePt and MnO domains results in increased interactions between the corresponding surface spins (see Figure 11.7). It was reported previously, that such interactions can lead to enhanced magnetic properties, since the thickness of the magnetic dead layer in the FePt domain (or "canted spin" layer, which occurs due to broken symmetry at the FePt nanoparticle surface) is reduced.[50, 53, 54] Finally, in sample (c) FePt NPs of the same size as in sample (b) are used, but the domain size of MnO is reduced from 17 to 9 nm. Hence, r is largest of all samples and the magnetic hysteresis is mainly dominated by FePt, resembling almost that of a typical hard ferromagnet, with M_R = 4.57 emu g^{-1}, H_C = 4509 Oe, and M_S = 12.10 emu g^{-1}.

The interaction of the ferromagnetic FePt and the antiferromagnetic MnO domains is also observable in the magnetic blocking temperature T_B of the FePt@MnO nano-*hetero*-particles. For this purpose, temperature dependent magnetization (zero-field-cooled/field-cooled (ZFC/FC)) measurements were performed to establish a

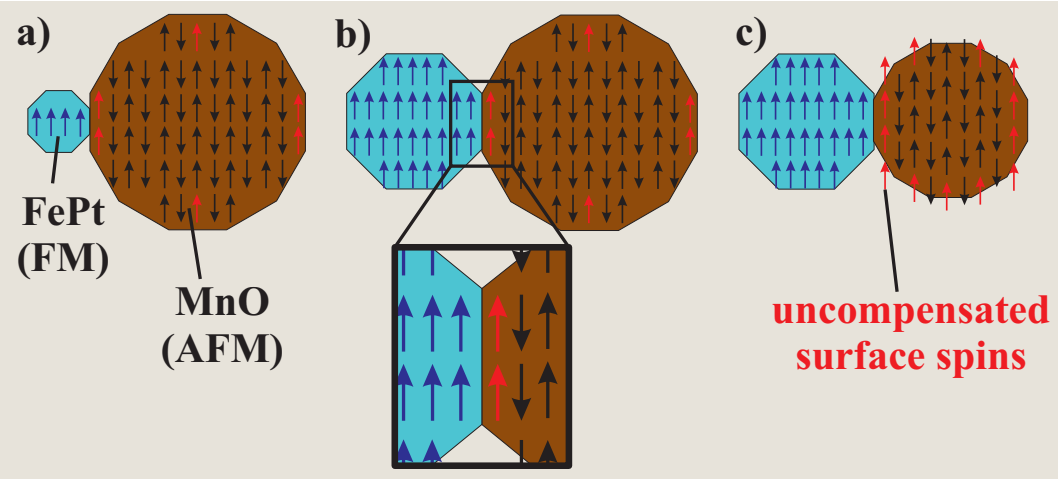

Figure 11.7: Illustration of the pinning effect of the antiferromagnetic MnO domain at the FePt-MnO interface. (a) For 3 nm FePt NPs the interface area is small and as a consequence the pinning effect of the AFM MnO domain is low. (b) The interface are for 6 nm FePt NPs is larger and, therefore, the influence of the FePt-MnO interface is greater. (c) With reduction of the MnO domain size the number of uncompensated surface spins, and with that, the magnetic moment of MnO is increased. Consequently, the influence of the MnO NPs on the FePt domains is higher.

quantitative evaluation of these interactions. The results are displayed in the respective insets of Figure 11.6. The maximum in the ZFC curves indicates the temperature T_B above which the system behaves like a paramagnet. Above T_B the thermal energy of the system k_BT is sufficient to freely flip the particle moments. At lower temperatures, on the other hand, k_BT is too small and the magnetic moments of the particles are aligned in direction of the external magnetic field. Consequently, the system behaves like a ferromagnet. The latter case is often referred to as "blocked" state and, therefore, the temperature, at which the transition from the superparamagnetic to the ferromagnetic state occurs, is called magnetic blocking temperature T_B. The ZFC curve in the inset of Figure 11.6a reveals a T_B of 40 K. However, "naked" FePt NPs of 3 nm in diameter were reported to have a T_B of 25 K.[12] A similar observation was reported for FePt-MnO core-shell NPs with FePt domains of 3 nm in size.[50] The increase in T_B in the FePt@MnO sample can be ascribed to two factors. First, the larger effective mass of the FePt@MnO composite NPs

compared to "naked" FePt NPs requires a higher thermal energy to overcome the blocked magnetic state. Secondly, the presence of an AFM MnO domain, which is connected via a common interface, pins the magnetic moments in FePt resulting in a higher stability against thermal fluctuations (see Figure 11.7).[55] In samples (b) and (c), T_B has increased to 65 K and 66 K, respectively. This increase can clearly be ascribed to the higher magnetic moment of 6 nm FePt NPs compared to FePt NPs with an average size of 3 nm. Again, pinning effects induced by the MnO domains lead to a higher T_B than the expected value of $T_B \approx 50$ K. Furthermore, the present ZFC-FC plots exhibit considerably narrow shapes which is, again, a clear indication for an exceedingly narrow particle size distribution.
Finally, the magnetic exchange bias, a phenomenon, which occurs in systems where ferromagnetic and antiferromagnetic materials share a common interface, can also be observed in the present system. In sample (a) the hysteresis loop at 5 K is shifted by 200 Oe from the origin. This can be, again, explained by the interaction between FM FePt and AFM MnO, if the history of the sample is taken into account. The hysteresis measurements were performed in a field cooled state with an applied field of 100 Oe. Therefore, the magnetic moment of MnO is aligned parallel to the external field. The magnetic moment of the FePt domains points parallel to the MnO moment, since the surface spins pin the magnetization of FePt. When the direction of the applied field is reversed, the magnetization of the FePt domains remains pinned until the external field exceeds the pinning field of the MnO domain. Consequently, the magnetization flips at lower fields, compared to "naked" FePt particles if the external field points in the original direction. As a result, the hysteresis loop is shifted from the origin. Increasing the size of the FePt domain (sample (b)), results in a stronger exchange bias due to an increased common surface area, i.e. a larger shift of the hysteresis curve of 400 Oe. The size reduction of the MnO domain (sample (c)), leads to an even stronger exchange bias (≈800 Oe). This is caused by the enhanced magnetic moment of the reduced MnO particle size.[42]

11.4 Conclusion

In summary, we were able to prepare monodisperse FePt@MnO nano-*hetero*-particles of different shapes and sizes by a two-step seed-mediated growth technique.

The size of each domain could be controlled by adjusting the individual synthetic parameters. Moreover, the particle morphology could be varied from dimers to flower-like particles by changing the "polarity" of the solvent from non-polar to polar. Additionally, FePt@MnO nano-*hetero*-particles prepared with large (13 nm) FePt nanocubes as seeds showed a predominant formation of MnO on the corners of the cubes, which suggests a preferential nucleation of MnO on the $\{111\}$ crystal facets of FePt. Furthermore, magnetic measurements revealed strong interactions between both magnetic domains resulting in increased M_R, H_C, M_S and T_B compared to "naked" FePt NPs. Finally, a shift in the hysteresis can be attributed to a magnetic exchange bias at the ferromagnetic-antiferromagnetic FePt-MnO interface.

11.5 Experimental Section

Materials. Manganese chloride tetrahydrate ($MnCl_2 \times 4H_2O$, 99%), oleic acid (techn. 90%), sodium hydroxide (p.A.), platinum acetylacetonate (99%), iron pentacarbonyl (99.999%), 1,2-hexadecanediol (techn. 90%), dioctylether (99%), benzylether (99%), and 1-octadecene (techn. 90%) were purchased from Aldrich and used without further purification. Oleylamine (80-90%) was from ACROS.

Synthesis of 3 nm FePt NPs. The preparation of monodisperse FePt NPs, with an average size of 3 nm, was carried out according to the procedure by Sun et al.[12] Under standard airless conditions platinum acetylacetonate ($Pt(acac)_2$, 196.7 mg, 0.5 mmol), 1,2-hexadecandiol (387.7 mg, 1.5 mmol), oleic acid (159 μL, 0.5 mmol), and oleylamine (165 μL, 0.5 mmol) were mixed in dioctylether (20 mL) and degassed at 70 °C for one hour with intermittent argon backfilling. After that, the mixture was heated to 120 °C and iron pentacarbonyl ($Fe(CO)_5$, 132 μL, 1 mmol) was added before raising the temperature rapidly to reflux (298 °C). After 30 minutes the reaction mixture was cooled to room temperature and the product was washed by repeated cycles of precipitation with ethanol, centrifugation (9000 rpm for 10 minutes), resuspension in hexane. The final product was stabilized with 25 μL of oleic acid and 25 μL of oleylamine and stored in hexane in a fridge.

Synthesis of 6 nm FePt NPs. For the preparation of monodisperse FePt NPs with an average size of 6 nm, a reported method by Chen et al. was employed.[51] In a

typical reaction, $Pt(acac)_2$ (196.7 mg, 0.5 mmol) was mixed with 10 mL of benzyl ether and 5 mL of 1-octadecene, and degassed at 70 °C for one hour and regularly backfilled with argon. Subsequently, the solution was heated to 120 °C and $Fe(CO)_5$ (264 μL, 2 mmol) and oleic acid (1588 μL, 5 mmol) were added simultaneously. After five minutes, oleylamine (1650 μL, 5 mmol) was injected and the mixture was heated to 205 °C and kept at this temperature for one hour. After cooling to room temperature, the product was washed and stored in the same way as mentioned above.

Synthesis of 13 nm FePt nanocubes. Larger FePt nanocubes were prepared according to a procedure by Chou et *al.*[52] $Pt(acac)_2$ (40 mg, 0.1 mmol) was mixed with 1,2-hexadecanediol (1033.8 mg, 4 mmol), oleic acid (4 mL, 12.6 mmol), oleylamine (4 mL, 12.1 mmol) and 4 mL dioctyl ether. The mixture was degassed and backfilled with argon at 80 °C for 45 minutes and subsequently heated to 115 °C. $Fe(CO)_5$ (66 μL, 0.5 mmol) was injected and the reaction mixture was heated to 240 °C for 60 minutes. After cooling to room temperature, the FePt nanocubes were isolated and washed with ethanol. Finally, the NPs were stored in hexane with oleic acid and oleylamine (50 μL).

Preparation of manganese oleate. Manganese oleate was prepared according to a published procedure.[42, 56] Briefly, 40 mmol of $MnCl_2 \times 4H_2O$ and 80 mmol oleic acid were dissolved in 200 mL methanol before 80 mmol of NaOH (in 200 mL methanol) were added dropwise to precipitate Mn-oleate. The product was washed with water, ethanol and acetone and subsequently dried in high vacuum at 120 °C to produce a waxy deep red solid.

Synthesis of 3 nm@17 nm FePt@MnO nanodimers. For the synthesis of 3@17 nm nanodimers, 3 nm sized FePt NPs (5 mg) were used as seeds, and dissolved in 0.5 mL 1-octadecene with 25 μL of oleic acid and oleylamine. Manganese oleate (309 mg, 0.5 mmol) was dissolved together with oleic acid (953 μL, 3 mmol), oleylamine (1980 μL, 6 mmol), and the FePt nanoparticle solution in 15 mL 1-octadecene and degassed/backfilled with argon at 80 °C for 30 minutes. After that the reaction mixture was heated to reflux (315 °C) within 8 minutes and kept at this temperature for 30 minutes. After cooling to room temperature, the product was washed by repeated precipitation with acetone, centrifugation (9000 rpm for ten minutes), and redispersion in hexane.

Synthesis of 6 nm@17 nm FePt@MnO nanodimers. FePt@MnO nanodimers of 6 nm@17 nm in size were prepared in the same way. However, the 6 nm FePt NPs (10 mg) were used as seeds instead.

Synthesis of 6 nm@17 nm FePt@MnO nanoflowers. According to principle synthetic mechanisms introduced in chapter 4 more nucleation sites on the FePt seeds can be obtained by increasing the polarity, i.e. the amount of available electron density in the solvent. For this purpose the FePt NPs (10 mg) were dissolved in benzyl ether by ultra sonication and added to a Mn-oleate, oleic acid, oleylamine, benzyl ether (15 mL) mixture. Subsequently, the reaction mixture was treated in the same way as described above.

Synthesis of 13 nm@9 nm FePt@MnO nanocubes The preparation of FePt@MnO nano-*hetero*-particles follows the same rules as described above. 25 mg of FePt nanocubes were dispersed in 1 ml 1-octadecene with 25 μL oleic acid and oleylamine and mixed with 0.1 mmol Mn oleate, 953 μL, 3 mmol oleic acid, 1980 μL, 6 mmol oleylamine and 15 mL 1-octadecene. After degassing at 80 °C, the mixture was refluxed for 30 minutes and the NPs were retrieved in the same way as mentioned above.

Nanoparticle Characterization. The particles were characterized by means of powder X-ray diffraction (XRD) and transmission electron microscopy (TEM). The magnetic properties of the MnO NPs were investigated with a superconducting quantum interference device (SQUID). XRD measurements were performed on a Bruker D8 Advance diffractometer equipped with a Sol-X energydispersive detector and operating with Mo Kα radiation. Full pattern profile fits were performed with TOPAS Academic V1.0 applying the fundamental parameter approach.[57] Samples for transmission electron microscopy were prepared by placing a drop of dilute nanoparticle solution in hexane on a carbon coated copper grid. Low-resolution TEM images and ED patterns were recorded on a Philips EM420 microscope operating at an acceleration voltage of 120 kV. Magnetic measurements were carried out using a Quantum Design MPMS-XL SQUID magnetometer.

11.6 References

[1] Zeng, H.; Sun, S. *Advanced Functional Materials* **2008**, *18*, 391–400.

[2] Frey, N. A.; Peng, S.; Cheng, K.; Sun, S. *Chemical Society Reviews* **2009**, *38*, 2532–2542.

[3] Yu, H.; Chen, M.; Rice, P. M.; Wang, S. X.; White, R.; Sun, S. *Nano Letters* **2005**, *5*, 379–382.

[4] Xu, C.; Xie, J.; Ho, D.; Wang, C.; Kohler, N.; Walsh, E.; Morgan, J.; Chin, Y.; Sun, S. *Angewandte Chemie International Edition* **2008**, *47*, 173–176.

[5] Xu, C.; Wang, B.; Sun, S. *Journal of the American Chemical Society* **2009**, *131*, 4216–4217.

[6] Gu, H.; Yang, Z.; Gao, J.; Chang, C.; Xu, B. *Journal of the American Chemical Society* **2005**, *127*, 34–35.

[7] Choi, S.-H.; Na, H. B.; Park, Y. I.; An, K.; Kwon, S. G.; Jang, Y.; Park, M.-h.; Moon, J.; Son, J. S.; in Song, C.; Moon, W. K.; Hyeon, T. *Journal of the American Chemical Society* **2008**, *130*, 15573–15580.

[8] Gu, H.; Zheng, R.; Zhang, X.; Xu, B. *Journal of the American Chemical Society* **2004**, *126*, 5664–5665.

[9] Cozzoli, P. D.; Pellegrino, T.; Manna, L. *Chemical Society Reviews* **2006**, *35*, 1195–1208.

[10] Jun, Y.-w.; Choi, J.-s.; Cheon, J. *Chemical Communications* **2007**, 1203–1214.

[11] Raj, K.; Moskowitz, R. *Journal of Magnetism and Magnetic Materials* **1990**, *85*, 233–245.

[12] Sun, S.; Murray, C. B.; Weller, D.; Folks, L.; Moser, A. *Science* **2000**, *287*, 1989–1992.

[13] Hyeon, T. *Chemical Communications* **2003**, 927–934.

[14] Sun, S. *Advanced Materials* **2006**, *18*, 393–403.

[15] Gu, H.; Xu, K.; Xu, C.; Xu, B. *Chemical Communications* **2006**, 941–949.

[16] Shukoor, M. I.; Natalio, F.; Tahir, M. N.; Ksenofontov, V.; Therese, H. A.; Theato, P.; Schroder, H. C.; Muller, W. E. G.; Tremel, W. *Chemical Communications* **2007**, 4677–4679.

[17] Schröder, H. C.; Natalio, F.; Wiens, M.; Tahir, M. N.; Shukoor, M. I.; Tremel, W.; Belikov, S. I.; Krasko, A.; Müller, W. E. G. *Molecular Immunology* **2008**, *45*, 945–953.

[18] Liong, M.; Lu, J.; Kovochich, M.; Xia, T.; Ruehm, S. G.; Nel, A. E.; Tamanoi, F.; Zink, J. I. *ACS Nano* **2008**, *2*, 889–896.

[19] Park, H.; Yang, J.; Seo, S.; Kim, K.; Suh, J.; Kim, D.; Haam, S.; Yoo, K. H. *Small* **2008**, *4*, 192–196.

[20] Kim, J.; Park, S.; Lee, J. E.; Jin, S. M.; Lee, J. H.; Lee, I. S.; Yang, I.; Kim, J. S.; Kim, S. K.; Cho, M. H.; Hyeon, T. *Angewandte Chemie International Edition* **2006**, *45*, 7754–7758.

[21] Hu, F. Q.; Wei, L.; Zhou, Z.; Ran, Y. L.; Li, Z.; Gao, M. Y. *Advanced Materials* **2006**, *18*, 2553–2556.

[22] Jun, Y.-w.; Lee, J.-H.; Cheon, J. *Angewandte Chemie International Edition* **2008**, *47*, 5122–5135.

[23] Dai, Z.; Sun, S.; Wang, Z. *Nano Letters* **2001**, *1*, 443–447.

[24] Klemmer, T. J.; Shukla, N.; Liu, C.; Wu, X. W.; Svedberg, E. B.; Mryasov, O.; Chantrell, R. W.; Weller, D.; Tanase, M.; Laughlin, D. E. *Applied Physics Letters* **2002**, *81*, 2220–2222.

[25] Ulmeanu, M.; Antoniak, C.; Wiedwald, U.; Farle, M.; Frait, Z.; Sun, S. *Physical Reviews B* **2004**, *69*, 054417.

[26] Weller, D.; Moser, A. *IEEE Transactions on Magnetics* **1999**, *35*, 4423–4439.

[27] Zeng, H.; Li, J.; Wang, Z.; Liu, J.; Sun, S. *Nano Letters* **2004**, *4*, 187–190.

[28] Lee, D. C.; Mikulec, F. V.; Pelaez, J. A. M.; Koo, B.; Korgel, B. A. *Journal of Physical Chemistry B* **2006**, *110*, 11160–11166.

[29] Zeng, H.; Li, J.; Liu, J.; Wang, Z. L.; Sun, S. *Nature* **2002**, *420*, 395–398.

[30] Gu, H.; Ho, P.-L.; Tsang, K. W. T.; Yu, C.-W.; Xu, B. *Chemical Communications* **2003**, 1966–1967.

[31] Gu, H.; Ho, P.-L.; Tsang, K. W. T.; Wang, L.; Xu, B. *Journal of the American Chemical Society* **2003**, *125*, 15702–15703.

[32] Xu, C.; Xu, K.; Gu, H.; Zhong, X.; Guo, Z.; Zheng, R.; Zhang, X.; Xu, B. *Journal of the American Chemical Society* **2004**, *126*, 3392–3393.

[33] Xu, C.; Yuan, Z.; Kohler, N.; Kim, J.; Chung, M. A.; Sun, S. *Journal of the American Chemical Society* **2009**, *131*, 15346–15351.

[34] Chou, S.-W.; Shau, Y.-H.; Wu, P.-C.; Yang, Y.-S.; Shieh, D.-B.; Chen, C.-C. *Journal of the American Chemical Society* **2010**, doi:10.1021/ja1035013.

[35] Hill, R. J.; Howard, C. J. *Journal of Applied Crystallography* **1987**, *20*, 467–474.

[36] Rao, C. N. R.; Raveau, B. *Transition metal oxides*; VCH: New York, NY, 1995.

[37] Makhlouf, S. A.; Parker, F. T.; Spada, F. E.; Berkowitz, A. E. *Journal of Applied Physics* **1997**, *81*, 5561–5563.

[38] Kodama, R. H.; Makhlouf, S. A.; Berkowitz, A. E. *Physical Review Letters* **1997**, *79*, 1393–1396.

[39] Kodama, R. H. *Journal of Magnetism and Magnetic Materials* **1999**, *200*, 359–372.

[40] Seo, W. S.; Jo, H. H.; Lee, K.; Kim, B.; Oh, S. J.; Park, J. T. *Angewandte Chemie International Edition* **2004**, *43*, 1115–1118.

[41] Ghosh, M.; Biswas, K.; Sundaresan, A.; Rao, C. N. *Journal of Materials Chemistry* **2006**, *16*, 106–111.

[42] Schladt, T. D.; Graf, T.; Tremel, W. *Chemistry of Materials* **2009**, *21*, 3183–3190.

[43] Na, H. B.; Lee, J. H.; An, K.; Park, Y. I.; Park, M.; Lee, S.; Nam, D. H.; Kim, S. T.; Kim, S. H.; Kim, S. W.; Lim, K. H.; Kim, K. S.; Kim, S. O.; Hyeon, T. *Angewandte Chemie International Edition* **2007**, *46*, 5397–5401.

[44] Shapiro, E. M.; Koretsky, A. P. *Magnetic Resonance in Medicine* **2008**, *60*, 265–269.

[45] Gilad, A. A.; Walczak, P.; McMahon, M. T.; Bin Na, H.; Lee, J. H.; An, K.; Hyeon, T.; van Zijl, P. C. M.; Bulte, J. W. M. *Magnetic Resonance in Medicine* **2008**, *60*, 1–7.

[46] Na, H. B.; Hyeon, T. *Journal of Materials Chemistry* **2009**, *19*, 6267–6273.

[47] Na, H. B.; Song, I. C.; Hyeon, T. *Advanced Materials* **2009**, *21*, 2133–2148.

[48] Schladt, T. D. et al. *Angewandte Chemie International Edition* **2010**, *49*, 3976–3980.

[49] Schladt, T. D.; Schneider, K.; Shukoor, M. I.; Natalio, F.; Bauer, H.; Tahir, M. N.; Weber, S.; Schreiber, L. M.; Schröder, H. C.; Müller, W. E. G.; Tremel, W. *Journal of Materials Chemistry* **2010**, DOI: 10.1039/c0jm01465f.

[50] Kang, S.; Miao, G.; Shi, S.; Jia, Z.; Nikles, D. E.; Harrell, J. *Journal of the American Chemical Society* **2006**, *128*, 1042–1043.

[51] Chen, M.; Kim, J.; Liu, J.; Fan, H.; Sun, S. *Journal of the American Chemical Society* **2006**, *128*, 7132–7133.

[52] Chou, S.-W.; Zhu, C.-L.; Neeleshwar, S.; Chen, C.-L.; Chen, Y.-Y.; Chen, C.-C. *Chemistry of Materials* **2009**, *21*, 4955–4961.

[53] Wu, X. W.; Liu, C.; Li, L.; Jones, P.; Chantrell, R. W.; Weller, D. *Journal of Applied Physics* **2004**, *95*, 6810–6812.

[54] Thomson, T.; Toney, M. F.; Raoux, S.; Lee, S. L.; Sun, S.; Murray, C. B.; Terris, B. D. *Journal of Applied Physics* **2004**, *96*, 1197–1201.

[55] Skumryev, V.; Stoyanov, S.; Zhang, Y.; Hadjipanayis, G.; Givord, D.; Nogues, J. *Nature* **2003**, *423*, 850–853.

[56] Jana, N. R.; Chen, Y.; Peng, X. *Chemistry of Materials* **2004**, *16*, 3931–3935.

[57] Cheary, R. W.; Coelho, A. *Journal of Applied Crystallography* **1992**, *25*, 109–121.

CHAPTER 12

Conclusion and Outlook

The present dissertation demonstrated how magnetic nanoparticles can be designed to meet the individual needs of future biomedical applications. The first part covered general considerations concerning the use of magnetic NPs in nano-biotechnology and nanomedicine. It showed how the unique physical properties of the NPs can be specifically tuned by variation of the corresponding synthetic parameters. Moreover, a variety of efficient surface modification strategies were presented that allow a precise control of the particle properties *in vitro* and *in vivo*. Furthermore, the basic biological concepts that determine the fate and behavior of magnetic NPs inside living organisms, including blood half-life, passive and active cellular targeting, and NP toxicity were shortly addressed. Furthermore, nano-*hetero*-particles, a new class of materials, were also introduced and the basic physical principles which lead to the evolution of novel physical properties in these systems, were briefly discussed.
The second part of this thesis covered specific examples in which the concepts of part I were used to design nanoparticulate probes for biomedical applications:
It was shown that MnO NPs can easily be synthesized by a simple one-pot heating-up method involving manganese oleate as a single source precursor. Moreover, the nucleation and growth processes of the particles was studied by TEM, FT-IR, and AAS analysis and the results suggest a single nucleation event followed by uniform

growth on the existing nuclei. Because nucleation and growth are clearly separated, the crystals grow uniformly, leading to a narrow size distribution, which is in accordance to the LaMer concept. The particle size can easily be controlled by adjusting the reaction time and temperature, the solvent and the heating rate. It was demonstrated that the particle size increased with temperature, reaction time, and chain length (boiling point) of the solvent. Investigation of the surface of the MnO nanocrystals by FT-IR and NMR revealed that oleate molecules bind to the surface in a bidentate manner. In addition, XPS measurements indicate that no significant oxidation of Mn^{2+} to Mn^{3+} occurred even after several days. Magnetic measurements showed that the magnetic properties strongly depend upon the size of the NPs. Both magnetic moment and blocking temperature increase when the particle size is decreased.

Furthermore, the synthesis and characterization of a group of flowerlike Au@MnO NPs was described. They are an example for nano-*hetero*-material and follow the synthetic principles explained in chapter 4. We showed, that the size of the MnO petals could be precisely tuned by variation of the amount of manganese precursor. By taking advantage of their constituent properties, different functional molecules were loaded onto each component of the heterostructure, including a catechol-containing ligand, that was attached to the MnO domain, whereas a thiol-modified oligonucleotide was used to functionalize the Au core. The NPs are magnetically and optically active, and they are therefore useful for simultaneous magnetic and optical detection by MR and optical imaging. The fact that the nanoflowers are capable of imaging the same tissue area with both MRI and an optical source without the fast signal loss observed in the common fluorescent labeling, implies, that they can be used to achieve high sensitivity in diagnostic imaging applications. It would be interesting to extend this synthetic method to nanoflowers made of different materials, such as Cu@MnO, Ag@MnO, or Pt@MnO, and to use these multidomain particles as building blocks of higher-order structures, the symmetries of which would derive from "directional" interactions between NP petals (for example, linear particle chains from nanoflowers having two leaves). Work on attaching therapeutic molecules to these dumbbell NPs for target-specific imaging and delivery is currently underway.

Additionally, we showed the "theragnostic" potential of PP functionalized MnO

NPs. For this purpose, hydrophobic superparamagnetic MnO NPs were functionalized using a novel hydrophilic DA-PEG-PP ligand containing protoporphyrin IX (PP) as photosensitizer. The presence of a dopamine moiety permitted a strong attachment on the MnO surface. Efficient surface binding of the ligand molecules was confirmed by FT-IR and UV-Vis analysis. We showed that the optical properties of protoporphyrin IX are not significantly changed by binding to the MnO surface. Internalization of well dispersed protoporphyrin functionalized MnO NPs by human renal cell carcinoma (Caki-1) cells was demonstrated by fluorescence microscopy. We further demonstrated that laser light radiation (PDT) irradiation (635 nm, incident dose of 72 Jcm^{-2}) of Caki-1 cells incubated with protoporphyrin IX-functionalized MnO NPs led to cell death by apoptosis due to formation of reactive singlet oxygen ($^1O_2$) initiated by photoactivation of protoporphyrin IX. Furthermore, the presence of protoporphyrin IX on the MnO NPs permits detection of the particles by fluorescence microscopy due to its intrinsic fluorescence. Finally, we demonstrated that by virtue of their magnetic properties functionalized MnO NPs exhibit a strong T_1 contrast enhancement effect for MRI. Hence, hydrophilic protoporphyrin IX functionalized MnO NPs show potential for application not only as imaging agents for MRI and fluorescence microscopy but also as target systems for photodynamic therapy.

Moreover, we have demonstrated a novel way to prepare biocompatible multifunctional MnO@SiO_2 core-shell NPs. The procedure combines a water-in-oil microemulsion technique, to create an initial silica shell around MnO, and common Stöber-like processes to condense further functionalities, such as PEG or NH_2-groups, on the preformed silica surface. The silica encapsulated MnO NPs showed excellent stability in various aqueous solutions, including physiological saline solution and human blood serum. Furthermore, by virtue of their magnetic properties, MnO@SiO_2-PEG/NH_2 NPs showed a considerable T_1 MR contrast enhancement, and, since a fluorescent dye was also incorporated into the silica shell during the synthesis, our silica coated MnO NPs may serve as multimodal imaging agents for both, optical and MR imaging. We also demonstrated that silica encapsulated MnO NPs are less prone to manganese leaching in aqueous solution, compared to simple PEGylated NPs. Finally, the vast and well-established silane chemistry permits additional modification of the NPs, which leads to numerous further applications

which is also confirmed by their low toxicity and their cellular uptake.
A further example for the exciting field of nano-*hetero*-materials was given by FePt@MnO nano-*hetero*-particles. Monodisperse FePt@MnO NPs could be prepared in various shapes and sizes by alteration of the individual synthetic parameters according to the concepts introduced in chapter 4. By changing the solvent from "non-polar" to "polar" the morphology of the resulting NPs could be transformed from dimeric to flower-like. Magnetic measurements revealed a significant influence of the MnO domains on the FePt NPs. Being an antiferromagnetic material, MnO is able to pin the magnetic moments in the ferromagnetic FePt cores, a phenomenon generally referred to as magnetic exchange bias. As a result the magnetic hysteresis loop at 5 K is shifted $\approx$ 500 Oe from the origin.
Future work comprises further studies of our functionalized magnetic NPs in different biomedical areas. Recent results suggest a potential superoxide dismutase (SOD) biomimetic behavior of MnO NPs. Possible applications of these particles in this context may include probes to measure and regulate cellular oxidative stress. Furthermore, the excellent stability, easy modifiability and low toxicity of MnO@SiO_2 NPs enable the opportunity for cell targeting and imaging *in vivo*. Besides, the use of silica also offers the possibility to create mesoporous SiO_2 shells, which can entrap certain reactive molecules (e.g. drugs, peptides) and release them at a designated site in a controlled manner due to concentration gradients.
Another area for intensive work will be devoted to nano-*hetero*-structures. In this respect, not only the preparation of novel nano-*hetero*-combinations, but also the selective functionalization of such particles is of great importance. From a fundamental point of view, it will be interesting to selectively functionalize the individual surfaces of dimeric nano-*hetero*-particles with hydrophilic and hydrophobic ligands, respectively, and thus creating giant inorganic/organic amphiphiles and to study their aggregation behavior. Additionally, combinations of metallic NPs of heavy elements, such as FePt, Pt, or Au, and metal oxide NPs, such as MnO or Fe_3O_4, are interesting as dual contrast agents for both, CT and MRI.

List of Publications

1. E. S. Toberer, T. D. Schladt, R. Seshadri, "Macroporous Manganese Oxides with Regenerative Mesopores", *Journal of the American Chemical Society*, **2006**, *128*, 1462-1463.

2. E. S. Toberer, M. Grossman, T. D. Schladt, F. F. Lange, R. Seshadri, "Epitaxial Manganese Oxide Thin Films with Connected Porosity: Topotactic Induction of Crystallographic Pore Alignment", *Chemistry of Materials*, **2007**, *19*, 4833-4838.

3. J. Li, U. G. Singh, T. D. Schladt, J. K. Stalick, S. L. Scott, R. Seshadri, "Hexagonal $YFe_{1-x}Pd_xO_{3-\delta}$: Non-Perovskite Host Compounds for Pd^{2+} and Their Catalytic Activity for CO Oxidation", *Chemistry of Materials*, **2008**, *20*, 6567-6576.

4. T. D. Schladt, T. Graf, W. Tremel: "Synthesis and Characterization of Monodisperse Manganese Oxide Nanoparticles - Evaluation of the Nucleation and Growth Mechanism", *Chemistry Materials*, **2009**, *21*, 3183-3190.

5. T. D. Schladt, M. I. Shukoor, K. Schneider, M. N. Tahir, F. Natalio, I. Ament, J. Becker, F. D. Jochum, S. Weber, O. Köhler, P. Theato, L. M. Schreiber, C. Sönnichsen, H. C. Schröder, W. E. G. Müller, W. Tremel: "Au@MnO Nanoflowers: Hybrid Nanocomposites for Selective Dual Functionalization

and Imaging", *Angewandte Chemie*, **2010**, *122*, 4068-4072; *Angewandte Chemie International Edition*, **2010**, *49*, (23), 3976-3980.

6. T. D. Schladt, K. Schneider, W. Tremel: "Magnetische Nanopartikel als Kontrastmittel in der MRT", *Natur und Geist (Forschungsmagazin der Johannes Gutenberg Universität Mainz)*, **2010**, *26*, 24-27.

7. T. D. Schladt, K. Schneider, M. I. Shukoor, F. Natalio, M. N. Tahir, S. Weber, L. M. Schreiber, H. C. Schröder, W. E. G. Müller, W. Tremel: "Highly Soluble Multi-functional MnO Nanoparticles for Simultaneous Optical and MRI Imaging and Cancer Treatment using Photodynamic Therapy", *Journal of Materials Chemistry*, **2010**, *20*, DOI: 10.1039/c0jm01465f.

8. T. D. Schladt, K. Schneider, M. I. Shukoor, H. Schild, W. Tremel: "Engineered Multifunctional Nanotools for Biological and Cancer Applications", *RSC Dalton Transactions*, **submitted.**

9. T. D. Schladt, K. Schneider, S. Prüfer, H. Bauer, F. Natalio, O. Dumele, R. Raidoo, S. Weber, L. M. Schreiber, M. P. Radsak, H. J. Schild, W. Tremel: "Multifunctional Superparamagnetic MnO@SiO_2 Core/Shell Nanoparticles and their Application for Optical and Magnetic Resonance Imaging", *Advanced Functional Materials*, **submitted**.

10. J. K. Sahoo, M. N. Tahir, A. Yella, T. D. Schladt, E. Mugnaoli, U. Kolb, W. Tremel: "Rational Reversible Self-Assembly of Heterogeneous Metal Chalcogenide/ Metal Oxide Nanostructures Based on Pearson Hardness", *Angewandte Chemie*, **2010**, *122*, DOI: 10.1002/ange.201000774; *Angewandte Chemie International Edition*, **2010**, *49*, DOI: 10.1002/anie.201000774.

11. M. I. Shukoor, M. Barz, M. N. Tahir, F. Natalio, T. D. Schladt, S. Weber, R. Zentel, L. M. Schreiber, J. Brieger, W. E . G. Müller, W. Tremel, "Functionalized Magnetic Nanoparticles for Selective Targeting of Cells", *Materials Research Society Symposium Proceedings*, **2010**, **in press**.

12. B. Nakhjavan, M. N. Tahir, H. Gao, T. D. Schladt, F. Natalio, I. Ament, R. Branscheid, S. Weber, U. Kolb, C. Sönnichsen, L. M. Schreiber, W. Tremel: "Cu@Fe3O4 Nanodimers as Contrast Agents for Magnetic Resonance

Imaging with Selective Dual-Functionalization Capability", *Chemistry of Materials*, **submitted**.

13. F. Natalio, T. D. Schladt, K. Schneider, W. Tremel: "MnO Nanoparticles as Superoxide Dismutase (SOD) Biomimetic", *Angewandte Chemie International Edition*, **submitted**.

14. F. Natalio, K. Schneider, T. D. Schladt, S. Weber, J. Brieger, L. M. Schreiber, W. Tremel: "Live Monitoring of the SOD Activity of MnO Nanoparticles in Lymphatic Cells", **in preparation**.

15. T. D. Schladt, K. Schneider, F. Natalio, H. Bauer, S. Weber, J. Brieger, L. M. Schreiber, W. Tremel: "*In Vivo* MR Imaging of Tumors Using Multifunctional and Highly Soluble MnO@SiO_2 Core-Shell Nanoparticles", **in preparation**.

16. T. D. Schladt, T. Graf, O. Köhler, H. Bauer, K. Schneider, C. Herold, J. Mertins, W. Tremel: "Synthesis and Magnetic Properties of FePt@MnO Nano-*hetero*-Particles", **in preparation**.

17. T. D. Schladt, H. Bauer, K. Schneider, F. Natalio, J. Mertins, S. Weber, L. M. Schreiber, W. Tremel, "Multifunctional Pt@MnO@SiO_2 Nano-*hetero*-Particles as Novel Multimodal Agents for Optical, MR and CT imaging", **in preparation**.

18. T. D. Schladt, K. Schneider, H. Bauer, R. Raidoo, F. Natalio, W. Tremel: "Superparamagnetic Fe_3O_4 and MnO Nanoparticles Coated with a Multifunctional Mesoporous Silica Shell for the Controlled Delivery of Reactive Agents", **in preparation**.

19. J. Rother, A. Pietuch, T. D. Schladt, K. Schneider, W. Tremel, A. Janshoff: "Impact of TLR9 agonistic Nanoparticles on Pulmonary Cancer Cells", *ACS Nano*, **in preparation**.

20. J. Rother, A. Pietuch, K. Schneider, T. D. Schladt, W. Tremel, A. Janshoff: "Effect of Immunostimulating MnO and Fe_3O_4 Nanoparticles on Human Cancer Cells" **in preparation**.

21. T. D. Schladt, K. Schneider, H. Bauer, C. Mangold, M. Dietzsch, W. Steffen, H. Frey, G. Fytas, W. Tremel: "Self-Assembly of Inorganic/Organic Janus Nanoparticles with Orthogonal Polarity", **in preparation**.